IAEA TECDOC SERIES

IAEA-TECDOC-1807

IAEA-TECDOC-1807

Utilization of a Network of Small Magnetic Confinement Fusion Devices for Mainstream Fusion Research

IAEA
International Atomic Energy Agency

UTILIZATION OF A NETWORK OF SMALL MAGNETIC CONFINEMENT FUSION DEVICES FOR MAINSTREAM FUSION RESEARCH

The following States are Members of the International Atomic Energy Agency:

AFGHANISTAN
ALBANIA
ALGERIA
ANGOLA
ANTIGUA AND BARBUDA
ARGENTINA
ARMENIA
AUSTRALIA
AUSTRIA
AZERBAIJAN
BAHAMAS
BAHRAIN
BANGLADESH
BARBADOS
BELARUS
BELGIUM
BELIZE
BENIN
BOLIVIA, PLURINATIONAL STATE OF
BOSNIA AND HERZEGOVINA
BOTSWANA
BRAZIL
BRUNEI DARUSSALAM
BULGARIA
BURKINA FASO
BURUNDI
CAMBODIA
CAMEROON
CANADA
CENTRAL AFRICAN REPUBLIC
CHAD
CHILE
CHINA
COLOMBIA
CONGO
COSTA RICA
CÔTE D'IVOIRE
CROATIA
CUBA
CYPRUS
CZECH REPUBLIC
DEMOCRATIC REPUBLIC OF THE CONGO
DENMARK
DJIBOUTI
DOMINICA
DOMINICAN REPUBLIC
ECUADOR
EGYPT
EL SALVADOR
ERITREA
ESTONIA
ETHIOPIA
FIJI
FINLAND
FRANCE
GABON
GEORGIA
GERMANY
GHANA
GREECE
GUATEMALA
GUYANA
HAITI
HOLY SEE
HONDURAS
HUNGARY
ICELAND
INDIA
INDONESIA
IRAN, ISLAMIC REPUBLIC OF
IRAQ
IRELAND
ISRAEL
ITALY
JAMAICA
JAPAN
JORDAN
KAZAKHSTAN
KENYA
KOREA, REPUBLIC OF
KUWAIT
KYRGYZSTAN
LAO PEOPLE'S DEMOCRATIC REPUBLIC
LATVIA
LEBANON
LESOTHO
LIBERIA
LIBYA
LIECHTENSTEIN
LITHUANIA
LUXEMBOURG
MADAGASCAR
MALAWI
MALAYSIA
MALI
MALTA
MARSHALL ISLANDS
MAURITANIA
MAURITIUS
MEXICO
MONACO
MONGOLIA
MONTENEGRO
MOROCCO
MOZAMBIQUE
MYANMAR
NAMIBIA
NEPAL
NETHERLANDS
NEW ZEALAND
NICARAGUA
NIGER
NIGERIA
NORWAY
OMAN
PAKISTAN
PALAU
PANAMA
PAPUA NEW GUINEA
PARAGUAY
PERU
PHILIPPINES
POLAND
PORTUGAL
QATAR
REPUBLIC OF MOLDOVA
ROMANIA
RUSSIAN FEDERATION
RWANDA
SAN MARINO
SAUDI ARABIA
SENEGAL
SERBIA
SEYCHELLES
SIERRA LEONE
SINGAPORE
SLOVAKIA
SLOVENIA
SOUTH AFRICA
SPAIN
SRI LANKA
SUDAN
SWAZILAND
SWEDEN
SWITZERLAND
SYRIAN ARAB REPUBLIC
TAJIKISTAN
THAILAND
THE FORMER YUGOSLAV REPUBLIC OF MACEDONIA
TOGO
TRINIDAD AND TOBAGO
TUNISIA
TURKEY
TURKMENISTAN
UGANDA
UKRAINE
UNITED ARAB EMIRATES
UNITED KINGDOM OF GREAT BRITAIN AND NORTHERN IRELAND
UNITED REPUBLIC OF TANZANIA
UNITED STATES OF AMERICA
URUGUAY
UZBEKISTAN
VANUATU
VENEZUELA, BOLIVARIAN REPUBLIC OF
VIET NAM
YEMEN
ZAMBIA
ZIMBABWE

The Agency's Statute was approved on 23 October 1956 by the Conference on the Statute of the IAEA held at United Nations Headquarters, New York; it entered into force on 29 July 1957. The Headquarters of the Agency are situated in Vienna. Its principal objective is "to accelerate and enlarge the contribution of atomic energy to peace, health and prosperity throughout the world".

IAEA-TECDOC-1807

UTILIZATION OF A NETWORK OF SMALL MAGNETIC CONFINEMENT FUSION DEVICES FOR MAINSTREAM FUSION RESEARCH

REPORT OF A COORDINATED RESEARCH PROJECT 2011–2016

INTERNATIONAL ATOMIC ENERGY AGENCY
VIENNA, 2016

Marketing and Sales Unit, Publishing Section
International Atomic Energy Agency
Vienna International Centre
PO Box 100
1400 Vienna, Austria
fax: +43 1 2600 29302
tel.: +43 1 2600 22417
email: sales.publications@iaea.org
http://www.iaea.org/books

For further information on this publication, please contact:

Physics Section
International Atomic Energy Agency
Vienna International Centre
PO Box 100
1400 Vienna, Austria
Email: Official.Mail@iaea.org

Printed by the IAEA in Austria
December 2016

IAEA Library Cataloguing in Publication Data

Names: International Atomic Energy Agency.
Title: Utilization of a network of small magnetic confinement fusion devices for mainstream fusion research / International Atomic Energy Agency.
Description: Vienna : International Atomic Energy Agency, 2016. | Series: IAEA TECDOC series, ISSN 1011–4289 ; no. 1807 | Includes bibliographical references.
Identifiers: IAEAL 16-01073 | ISBN 978–92–0–1104168–9 (paperback : alk. paper)
Subjects: LCSH: Nuclear fusion — Research. | Plasma confinement. | Controlled fusion.

FOREWORD

The IAEA actively promotes the development of controlled fusion as a source of energy. Through its coordinated research activities, the IAEA helps Member States to exchange and establish scientific and technical knowledge required for the design, construction and operation of a fusion reactor. Due to their compactness, flexibility and low operation costs, small fusion devices are a great resource for supporting and accelerating the development of mainstream fusion research on large fusion devices such as the International Thermonuclear Experimental Reactor. They play an important role in investigating the physics of controlled fusion, developing innovative technologies and diagnostics, testing new materials, training highly qualified personnel for larger fusion facilities, and supporting educational programmes for young scientists.

This publication reports on the research work accomplished within the framework of the Coordinated Research Project (CRP) on Utilization of the Network of Small Magnetic Confinement Fusion Devices for Mainstream Fusion Research, organized and conducted by the IAEA in 2011–2016. The CRP has contributed to the coordination of a network of research institutions, thereby enhancing international collaboration through scientific visits, joint experiments and the exchange of information and equipment. A total of 16 institutions and 14 devices from 13 Member States participated in this CRP (Belgium, Bulgaria, Canada, China, Costa Rica, the Czech Republic, the Islamic Republic of Iran, Kazakhstan, Pakistan, Portugal, the Russian Federation, Ukraine and the United Kingdom).

The IAEA acknowledges the valuable contributions of the participants to this publication and their efforts during the CRP. The IAEA officers responsible for this publication were R. Kamendje, A. Botrugno and O. Stasyuk of the Division of Physical and Chemical Sciences.

EDITORIAL NOTE

This publication has been prepared from the original material as submitted by the contributors and has not been edited by the editorial staff of the IAEA. The views expressed remain the responsibility of the contributors and do not necessarily represent the views of the IAEA or its Member States.

Neither the IAEA nor its Member States assume any responsibility for consequences which may arise from the use of this publication. This publication does not address questions of responsibility, legal or otherwise, for acts or omissions on the part of any person.

The use of particular designations of countries or territories does not imply any judgement by the publisher, the IAEA, as to the legal status of such countries or territories, of their authorities and institutions or of the delimitation of their boundaries.

The mention of names of specific companies or products (whether or not indicated as registered) does not imply any intention to infringe proprietary rights, nor should it be construed as an endorsement or recommendation on the part of the IAEA.

The IAEA has no responsibility for the persistence or accuracy of URLs for external or third party Internet web sites referred to in this publication and does not guarantee that any content on such web sites is, or will remain, accurate or appropriate.

CONTENTS

SUMMARY

1. BACKGROUND

The beginning of construction of the ITER reactor is accompanied by an apparent increase in fusion research activities all over the world. Many countries have or would like to have a National Fusion Programme and experimental fusion facilities. Without such facilities it is difficult to develop the required expertise in fusion science and technology in order to be able to take advantage from the progress leading to the use of fusion power in the future. Today, more than 55 magnetic confinement fusion devices (tokamaks, stellarators and others) are operational, under construction or upgrade[1], of which more than 40 are small fusion devices. About 50 IAEA Member States are involved in plasma physics and fusion research.

Small magnetic confinement fusion devices have played and continue to play an important role in fusion research. Thanks to their compactness, flexibility, low operation costs and the high skill of their personnel they contribute to a better understanding of phenomena in a wide range of fields such as plasma confinement and energy transport, plasma stability in different magnetic configurations, plasma turbulence and its impact on local and global plasma parameters, processes at the plasma edge and plasma-wall interaction, scenarios with additional heating and non inductive current drive, etc. Research on small fusion devices has created the scientific basis for the scaling-up to larger facilities. In addition, small fusion devices offer the attractive possibility for developing and testing new diagnostics, materials and technologies in the most efficient manner (in terms of time and cost). Moreover, the experimental work on small fusion devices is very appropriate for educating students, scientific activities of postgraduate students and for training of personnel for larger fusion devices. Previous IAEA efforts in this area have strived to establish a framework of co-operation of small magnetic fusion devices with the aim to co-ordinate research through the exchange of information and equipment, scientific visits, and joint experiments. This concept has clearly demonstrated its value and potential for enhancing international collaborations and increased the impact of the small fusion devices.

The purpose of the CRP on “Utilisation of a Network of Small Magnetic Confinement Fusion Devices for Mainstream Fusion Research” was to continue the promotion of coordinated research activities on small magnetic confinement fusion devices with the view to streamline their contribution to next step fusion facilities.

2. CRP OVERALL OBJECTIVE

The overall objective of this CRP has been to contribute to streamlining the contributions of small magnetic confinement fusion devices in various Member States to mainstream fusion research by establishing a network of cooperation enabling coordinated investigations of topics of relevance to physics, diagnostics and technology issues of next step fusion devices such as ITER and DEMO.

A total of 16 institutions and 14 devices from 13 Member States participated in this CRP.

- Institute of Plasma Physics, Prague, Czech Republic (COMPASS)

---

[1] http://www.tokamak.info/, accessed 9 May 2016

- Czech Technical University, Prague, Czech Republic (GOLEM)
- Instituto Superior Tecnico, Lisbon, Portugal (ISTTOK)
- Tsinghua University, Beijing, China (SUNIST)
- Plasma Physics Research Center, Islamic Azad University, Teheran, Iran (IR-T1)
- Faculty of Physics of Sofia University, Sofia, Bulgaria
- Institute of Plasma Physics, National Science Center “Kharkov Institute of Physics and Technology”, Kharkov, Ukraine (URAGAN-2, URAGAN-3)
- Ghent University, Belgium
- Plasma Physics Laboratory of University of Saskatchewan, Canada (STOR-M)
- Tokamak Energy Ltd, UK (ST-25, ST-HTS)
- Oxford Instruments, UK
- National Tokamak Fusion Program, Pakistan (GLAST-2, GLAST-3)
- NRC Kurchatov Institute, Moscow, Russian Federation (T-10)
- Institute of Atomic Energy, Kurchatov, Kazakhstan (KTM)
- Saint-Petersburg State University, Russian Federation
- Instituto Tecnológico de Costa Rica, Costa Rica

3. SPECIFIC RESEARCH OBJECTIVES

The specific objectives of this CRP were as follows:

- Establishment of a Network of Small magnetic confinement Fusion Devices
- Utilization of the network to perform joint and comparative experiments on a number of selected devices
- Utilization of the network to support technology development, e.g. novel diagnostics, materials and techniques
- Utilization of the network to support modelling analysis and the development of simulation and communication tools
- Provide training and education activities to members of the network

4. EXPECTED RESEARCH AND EDUCATION OUTPUTS

The expected outputs of this CRP were as follows:

- Detailed documentation and publication of results of joint experiments investigating dedicated topics together with the necessary analysis and conclusions
- Development of prototypes of specific (i) fusion-relevant diagnostics, (ii) partial or full in-vessel components, and (iii) components of systems auxiliary to the main confinement device
- Development of prototypes of applicable fusion-relevant simulation and communication tools
- Provision of training courses to participants from participating countries.
- Provision of support to complete doctoral & master degrees.

5. MAJOR CRP ACTIVITIES

The network of 14 small magnetic confinement fusion devices successfully established within this CRP was used to conduct collaborative studies of relevance to main stream fusion research. In particular, the network was used to perform annual Joint Experiments at different facilities. Joint Experiments offer the advantage of increasing the intellectual diversity in the scientific exploitation of the targeted facilities. In addition, various scientific research and development activities were conducted at participating Institutions. These include experiments to characterize the edge and core plasmas using a unique set of dedicated diagnostics; the development of new technologies such as high temperature superconducting coils for fusion magnets and affordable microwave sources for plasma preionisation; the development of novel diagnostics; and the application of modelling tools to support experimental activities. Also, the established network facilitated contributions towards capacity building through the provision of training and education activities conducted at various devices within the network.

5.1. Joint Experiments on dedicated devices

A total of 4 Joint Experiment events (each lasting one week) were organized during the lifetime of this CRP.

In 2012, Joint Experiments were organized on COMPASS and GOLEM tokamaks in Prague. Experiments at the COMPASS tokamak aimed at (i) investigating the effects of strong gas puff on the suppression of plasma edge fluctuations and on particle confinement time, (ii) characterization of edge turbulent transport in limiter and divertor configuration, (iii) evaluation of the plasma potential and electron energy distribution function. Experiments at the GOLEM tokamak were devoted to (i) first tests of High Temperature Superconductors in poloidal field coils in the real tokamak operation, (ii) studies of plasma pre-ionization using electron cyclotron waves from an adapted commercial microwave source. A total of 14 foreign participants from 9 institutions contributed to these Joint Experiments, in addition to ~ 15 local scientists and supporting staff.

In 2013, Joint Experiments were again organized on COMPASS and GOLEM tokamaks in Prague. Experiments at the COMPASS tokamak aimed at (i) measurement of the parallel heat flux profiles in the plasma scrape off layer; (ii) comparison of electron temperature and plasma potential measurements with the Ball Pen and Langmuir Probes, respectively; (iii) determination of the power heat flux to divertor during high density high confinement mode operation; (iv) studies of toroidal asymmetry effects of plasma disruptions; (v) investigation of magnetohydrodynamic activity in the Alfvén frequency range during ohmic and Neutral Beam injection heating; (vi) investigation of the electrostatic turbulence in the frequency range of Geodesic Acoustic Modes using Ball Pen and Langmuir Probes in combination with magnetic measurements. Experiments at the GOLEM tokamak were devoted to further testing of High Temperature Superconductors in poloidal field coils including detailed coil current quench studies. A total of 18 foreign participants from 12 institutions contributed to these Joint Experiments, in addition to ~ 16 local scientists and supporting staff.

In 2014, Joint Experiments were also organized on COMPASS and GOLEM tokamaks in Prague. Experiments at the COMPASS tokamak aimed at (i) study of the spatial structure of Geodesic Acoustic Modes with core and edge diagnostics; (ii) identification and characterisation of various types of plasma fluctuations (quasicoherent modes) including Alfvén Eigenmodes in ohmic plasmas and in different confinement regimes with ohmic and NBI heating (low confinement L-mode and high confinement H-mode); (iii) characterization of the transition to high confinement mode using reciprocating probe measurements; (iv) measurements of MHD precursor poloidal and toroidal mode structure during disruptions in high plasma density regimes (with average densities above $10^{20}m^{-3}$); (v) study of effects of the externally applied resonant magnetic perturbation by magnetics and Langmuir probes located at the divertor tiles; (vi) studies of electron energy distribution function at the plasma periphery using divertor Langmuir probes. Experiments at the GOLEM tokamak were devoted to (i) further quench studies in High Temperature Superconducting poloidal field coils using modified bridge scheme to increase sensitivity of the measurements; (ii) further studies of the plasma pre-ionization using electron cyclotron waves from a modified commercial microwave source. A total of 13 foreign participants from 11 institutions contributed to these Joint Experiments, in addition to ~ 15 local scientists and supporting staff.

In 2015, Joint Experiments were organized on STOR-M tokamak at the University of Saskatchewan, Canada, aimed at (i) investigation of the interplay between magnetohydrodynamic and turbulence under edge biasing and resonant magnetic perturbations, (ii) effect of biasing on Geodesic Acoustic Modes and plasma confinement, (iii) study of the edge potential and Geodesic Acoustic Modes under the influence of magnetohydrodynamic activity, (iv) investigation of effects of compact torus injection, resonant magnetic perturbations and biasing on the edge plasma, (v) measurements of high-frequency magnetohydrodynamic oscillations, (vi) study of vertical displacement events, (vii) comparison of magnetic measurements with numerical modelling of magnetic field due to image currents in the iron core. A total of 8 foreign participants from 6 institutions contributed to these Joint Experiments, in addition to ~ 10 local scientists and supporting staff.

5.2. Activities at participating Institutions

Activities performed at different participating institutions fall into the following topic categories:

- Studies of phenomena at the edge of the tokamak plasma

It is known that, for similar magnetic configurations, properties and parameters in the plasma edge (in particular in the scrape-off layer region) are similar in magnetic confinement fusion devices regarless the size. Therefore studies of the edge plasma properties in small magnetic fusion devices are directly relevant to larger fusion facilities.

At the Institute of Plasma Physics (IPP), Prague, Czech Republic, the COMPASS tokamak was used to conduct various studies pertaining to the characterization of the plasma edge region. The goal of the investigations was to perform detailed measurements of the edge plasma parameters in different confinement regimes and heating methods using advanced diagnostics with high temporal and spatial resolution. These studies have particular relevance to larger tokamaks such as ITER as far as COMPASS shares the same magnetic configuration and methods of auxiliary heating.

At the Faculty of Physics of Sofia University, Sofia, Bulgaria, the advanced Langmuir probe analysis technique (first derivative probe technique) has been developed for evaluating the plasma potential and electron energy distribution function in magnetized plasma. This technique was applied to derive the electron energy distribution function from the Langmuir probe measurements in the plasma boundary region in the COMPASS and ISTTOK tokamaks, as well as in the TJ-II stellarator.

At the Institute of Plasma Physics, National Science Center “Kharkov Institute of Physics and Technology”, Kharkov, Ukraine, the URAGAN-3M stellarator was used to perform studies of turbulent particle flux at the plasma edge during transition to a better confinement regime using Langmuir probes.

- Studies of plasma transport and instabilities related phenomena in magnetic fuson device (electrostatic turbulence, MHD instabilities, effects of application of the resonant magnetic perturbations and compact torus injection).

Performance of plasmas in magnetic fusion devices is dictated by particle and energy confinement as well as stability properties. Small fusion magnetic confinement devices provide excellent conditions for performing dedicated experiments aimed at elucidating the physics governing these processes.

At the NRC Kurchatov Institute, Moscow, Russian Federation, a multi-channel Heavy Ion Beam diagnostics has been used to measure the time evolution of the radial profiles and/or local values of plasma parameters in wide radial range (plasma potential, density, poloidal and radial electic fields, turbulent particle flux, plasma turbulence poloidal rotation and poloidal mode number).

At the Plasma Physics Laboratory of University of Saskatchewan, Canada, the STOR-M tokamak was used to conduct various studies such as alternating current operation, Ohmic H-mode formation by rapid edge heating and Compact Torus Injection (CTI), plasma flow control by applying resonant magnetic perturbation and CTI, and detection of Geodesic Acoustic Modes.

At the Institute of Plasma Physics, National Science Center “Kharkov Institute of Physics and Technology”, Kharkov, Ukraine, a new method for avoiding the appearance of runaway electrons in torsatrons was tested on Uragan-2M and Uragan-3M devices.

- Radio frequency and microwave assisted plasma start up and current drive

Plasma initiation in tokamaks requires the application of a toroidal electric field. In future devices, such as ITER, the available electric field to perform this task is limited, therefore auxiliary means have to be applied to assist in the breakdown phase. The application of radio frequency waves or microwaves provides an opportunity to produce an effective preionization thereby reducing the requirements on the magnitude of the needed toroidal electic field. Research on small fusion magnetic confinement devices provides possibilities to perform optimisation of plasma start-up scenarios.

At the Tsinghua University, Beijing, China, on SUNIST tokamak, research on plasma startup by high frequency electron cyclotron and electron Bernstein waves, and low frequency Alfven waves were performed.

At the Institute of Atomic Energy, Kurchatov, Kazakhstan, experiments on the KTM tokamak have been carried out to study plasma formation. Two options were used to initiate the plasma current by varying the polarity of the voltage in the central solenoid. A preionization system based on a microwave magnetron has been used. A similar system was also used on GLAST-2 and GLAST-3 tokamaks at the National Tokamak Fusion Program, Pakistan.

At the Czech Technical University, Prague, Czech Republic, on the GOLEM tokamak experiments were performed on comparison of the microwave assisted preionization with the preionization assisted by an electron gun.

At the Institute of Plasma Physics, National Science Center “Kharkov Institute of Physics and Technology”, Kharkov, Ukraine, on Uragan-3M device experiments were performed on study of plasma produced by radio frequency (RF) power supplied to two RF antennae.

- High Temperature Superconductors (HTS) in Fusion Devices

High Temperature Superconductors offer the prospects for more compact magnet systems as compared to conventional low temperature supeconductors. Hence, HTS coil systems open the way to more compact and potentially economical reactor. Naturally, small magnetic fusion devices are perfect testbed for the application of HTS coils in fusion environment.

At the tokamaks GOLEM (Czech Technical University in Prague, Czech Republic), ST-25 (Oxford Instruments, Tokamak Energy Ltd, UK) and ST-25 HTS (Oxford Instruments, Tokamak Energy Ltd, UK), the use of HTS in magnets was tested for the first time ever on a fusion device. The work included: (i) design, manufacture and tests of cryostats for HTS magnets and HTS coil feeds, (ii) studies of properties of HTS (critical current dependence on magnetic field, temperature and current quench characteristics), (iii) tests of HTS magnets on GOLEM and ST-25, (iv) operation of ST-25 HTS with a complete set of HTS coils up to 29 hours. In addition, HTS poloidal field coils for the GLAST-3 tokamak (National Tokamak Fusion program, Islamabad, Pakistan) were designed and constructed.

- Diagnostics, data analysis and plasma control

Small magnetic fusion devices are very suitable for the development and testing of new plasma diagnostics that then find use in the mainstream fusion research.

At the NRC Kurchatov Institute, Moscow, Russian Federation, Heavy Ion Beam Probing (HIBP), a unique diagnostics for core plasma potential, was developed. Advanced multi-channel HIBP is operating now on the T-10 tokamak and on TJ-II flexible heliac with high spatial (~1cm) and temporal (< 500 kHz) resolution. The developed HIBP has no limitations with respect to magnetic configurations, plasma density and magnetic field within operational limits of T-10 tokamak. HIBP becomes multipurpose diagnostics to study plasma electric potential and turbulence properties in the middle size toroidal devices.

The Heavy Ion Beam Probe diagnostics on the tokamak ISTTOK, Instituto Superior Tecnico, Lisbon, Portugal, has been modified to measure the local density/temperature fluctuations along the tokamak minor diameter, enable the identification of tearing modes. HIBP was developed and installed on the Uragan-2M stellarator at Institute of Plasma Physics, National Science Center “Kharkov Institute of Physics and Technology”, Kharkov, Ukraine.

Several advanced electric probes have been designed, installed and used in experiments to measure edge plasma parameters with a high spatial (<3mm) and temporal (<1MHz) resolution. They are arrays of Ball Pen probes and Langmuir probes, ExB analyzers and U-shaped probe on the COMPASS tokamak; triple Langmuir probes on the GLAST-3 tokamak; combined Ball Pen probes and Langmuir probes on the IR-T1 tokamak; multipin probe on the URAGAN-3M stellarator, a set of arrays of Langmuir probes on the STOR-M tokamak.

High-frequency (up to 2MHz) magnetic probes arrays were exploited in a number of devices: COMPASS, GLAST-3, SUNIST, IR-T1 and STOR-M tokamaks, and URAGAN-3M stellarator.

6. CRP ACHIEVEMENTS

6.1. Outputs of Joint Experiments

Analyses of the experimental data obtained during Joint Experiments performed in 2012, 2013, 2014 and 2015 have made possible the following scientific publications in peer-reviewed journals and conference proceedings:

- DIMITROVA, M., DEJARNAC, R, POPOV, TSV. K., IVANOVA, P., VASILEVA, E., KOVAČIČ, J., STÖCKEL, J., HAVLICEK, J., JANKY, F., AND PANEK, R., Plasma Parameters on COMPASS Divertor during Ohmic D-Shaped Plasmas Contrib. Plasma Phys. # 3 54, (2014) 255 – 260
- POPOV, TSV. K., DIMITROVA, M., IVANOVA, P., HASAN, E., HORACEK, J., DEJARNAC, R., STÖCKEL, J., WEINZETTL, V., AND KOVAČIČ, J., Langmuir Probe Evaluation of the Plasma Potential in Tokamak Edge Plasma at non-Maxwellian EEDF, Contrib. Plasma Phys. # 3 54, (2014), 267 – 272
- DIMITROVA, M., VASILEVA, E., HASAN, E., HORÁČEK, J., POPOV, TSV. K., IVANOVA, P., VONDRÁČEK, P., DEJARNAC, R., STÖCKEL, J., WEINZETTL, V., HAVLICEK, J., JANKY, F. AND PANEK, R., Evaluation of the scrape-off-layer plasma parameters by a horizontal reciprocating Langmuir probe in the COMPASS tokamak, Journal of Physics: Conference series 514 (2014) 012049
- POPOV, TSV. K., DIMITROVA, M., IVANOVA, P., KOVAČIČ, J., GYERGYEK, T., STÖCKEL, J., PANEK, R., Langmuir probe diagnostics of the plasma potential and electron energy distribution function in magnetized plasma, Proc. of 32nd International Conference on Phenomena in Ionized Gases, 26th – 31st July 2015, Iasi, Romania
- POPOV, TSV. K., DIMITROVA, M., PEDROSA, M. A., LÓPEZ-BRUNA, D., HORACEK, J., KOVAČIČ, J., DEJARNAC, R., STÖCKEL, J., AFTANAS, M., BÖHM, P., BÍLKOVÁ, P., HIDALGO, C., AND PANEK, R., Bi-Maxwellian electron energy distribution function in the vicinity of the last closed flux surface in fusion plasma, Plasma Phys. Control. Fusion 57 (2015) 115011
- GRYAZNEVICH, M., VAN OOST, G., STOCKEL, J., KAMENDJE, R., KUTEEV, B.N., MELNIKOV, A., POPOV, TSV. K., SVOBODA V., and the IAEA CRP Teams, Contribution to fusion research from IAEA coordinated research projects and joint experiments, Nuclear Fusion 55 (2015) 104019
- GRYAZNEVICH, M., SVOBODA, V., STOCKEL, J., SYKES, A., SYKES, N., KINGHAM, D., HAMMOND, G., APTE, P., TODD, T.N., BALL, S., CHAPPELL, S., MELHEM, Z., ĎURAN, I., KOVARIK, K., GROVER, O., MARKOVIC, T., ODSTRCIL, M., ODSTRCIL, T., SINDLERY, A., VONDRASEK, G., KOCMAN, J., LILLEY, M.K., DE GROUCHY, P., KIM, H.-T., Progress in application of high

temperature superconductor in tokamak magnets, Fusion Engineering and Design, 88 (2013) 1593–1596.

- MELNIKOV, A.V., MARKOVIC, T., ELISEEV, L.G., GRYAZNEVICH, M., IMRISEK, M., KOVARIK, K., LYSENKO, S.E., MEDVEDEV, S.YU., PETERKA, M., SEIDL, J., STOCKEL, J., WEINZETTL, W. and the COMPASS team, Quasicoherent modes in the COMPASS tokamak, Plasma Physics and Controlled Fusion 57 (2015) 065006 (13pp)
- MARKOVIC, T., SEIDL, J., MELNIKOV, A., HÁCEK, P., HAVLICEK, J., HAVRÁNEK, A., HRON, M., HRONOVA, O., IMRÍŠEK, M., JANKY, F., KOVARÍK, K., MIKULÍN, O., PÁNEK, R., PAPROK, R., PIPEK, J., VONDRÁCEK, P., WEINZETTL, V., Alfvén-wave character oscillations in tokamak COMPASS plasma, 42nd EPS Conference on Plasma Physics P4.104, http://ocs.ciemat.es/EPS2015PAP/pdf/P4.104.pdf
- SEIDL, J., HRON, M., ADAMEK, J., VONDRACEK, P., HORACEK, J., HIDALGO, C., MELNIKOV, A., ELISEEV, L., MARKOVIC, T., STÖCKEL, J., BASU, D., HACEK, P., HAVLICEK, J., IMRÍŠEK, M., KOVARIK, K., WEINZETTL, V., PANEK, R. and COMPASS Team, Observation of geodesic acoustic mode-like oscillations on COMPASS, 42-nd EPS Conference on Plasma Physics P4.103, http://ocs.ciemat.es/EPS2015PAP/pdf/P4.103.pdf
- GERASIMOV, S.N., ABREU, P., BARUZZO, M., DROZDOV, V., DVORNOVA, A., HAVLICEK, J., HENDER, T.C., HRONOVA, O., KRUEZI, U., LI, X., MARKOVIČ, T., PÁNEK, R., RUBINACCI, G., TSALAS, M., VENTRE, S., VILLONE, F., ZAKHAROV, L.E., and JET Contributors. JET and COMPASS asymmetrical disruptions. Nuclear Fusion, 55 (2015) 113006.
- LOUREIRO, J., SILVA, C., HORACEK, J., ADAMEK, J., STOCKEL, J., Scrape-off layer width of parallel heat flux on tokamak COMPASS, Plasma Physics and Technology, 2014, 1, 3, 121-123
- ADAMEK, J., MÜLLER, H.W., SILVA, C., SCHRITTWIESER, R., IONITA, C., MEHLMANN, F., COSTEA, S., HORACEK, J., KURZAN, B., BILKOVA, P., BÖHM, P., AFTANAS, M., VONDRACEK, P., STÖCKEL, J., PANEK, R., FERNANDES, H., FIGUEIREDO, H., COMPASS Team and ASDEX Upgrade Team, Profile measurements of the electron temperature on the ASDEX Up-grade, COMPASS and ISTTOK tokamak using ball-pen probes, accepted for publication in Review of Scientific Instruments
- POPOV, TSV. K., DIMITROVA, M., IVANOVA, P., KOVAČIČ, J., GYERGYEK, T., DEJARNAC, R., STOCKEL, J., PEDROSA, M., LOPEZ-BRUNA, D. AND HIDALGO, C., Advances in Langmuir probe diagnostics of the plasma potential and electron energy distribution function in magnetized plasma, Plasma Sources Sci. Technol. 25 (2016) 033001 (18pp)
- IVANOVA, P, DIMITROVA, M., VASILEVA, E., POPOV, TSV. K., DEJARNAC, R., STÖCKEL, J., IMRÍŠEK, M., HACEK P., AND PANEK, R., Determination of the plasma potential and the EEDF by Langmuir probes in the divertor region of COMPASS tokamak, Journal of Physics: Conference series (2016).

6.2. Diagnostics and technology development (HTS, probes etc)

During the CRP lifetime participants have been able to demonstrate the following achievements:

- Design, fabrication and first tests on tokamaks of high temperature superconducting magnets:

  - ✓ Design of cryostat (by IPP Prague and Tokamak Energy), feeds (by IPP Prague, Tokamak Energy and Oxford Instruments) and power supplies (by IPP Prague, Czech Technical University and National Fusion Tokamak Program) for initial test performed on GOLEM, ST-25, ST-25 HTS and GLAST-3 tokamaks.
  - ✓ First test of high temperature superconducting coils on GOLEM tokamak performed by Tokamak Energy, Oxford Instruments UK, the Czech Technical University and IPP Prague.
  - ✓ Construction of high temperature superconducting magnets for ST-25, ST-25 HTS and GLAST-3.
- Design and tests of Li evaporator for ST-25 and STOR-M tokamaks.
- Design and manufacturing of a probe array embedded in divertor tiles of COMPASS tokamak (equipped with 55 Ball Pen Probes and 55 Langmuir Probes) to measure plasma parameters in the divertor region with a high spatial and temporal resolution.
- Design and manufacturing of an ExB analyser for measurements of the ion temperature with a high temporal resolution on COMPASS tokamak.
- Design and manufacturing of a U-shaped novel probe to measure current filaments at the plasma edge on COMPASS tokamak.
- Design, development and completion of a dielectric vacuum vessel for GLAST-3 tokamak.
- Design construction and installation of a Triple Langmuir probe on GLAST-3 tokamak for the edge electron temperature measurement.
- Design and installation of a line of sight arrangement for spatial and temporal measurement of H-alpha emission on GLAST-3 tokamak.
- Design and implementation of a twisted toroidal field inner column for the ease of connection on GLAST-3 tokamak.
- Modification and installation of a 2.45 GHz, 1 kW microwave magnetron on GLAST-3 and GOLEM tokamaks to generate a radio frequency pulse of 4–6 ms for pre-ionization in presence of toroidal magnetic field.
- Design and construction of a flexible orthogonal probes array to measure eddy current in SUNIST tokamak.
- Design and construction of a high frequency magnetic probes array based on small chip inductors to investigate high frequency magnetohydrodynamic activities in SUNIST tokamak.
- Design, construction and installation of an ion Doppler spectroscopy system on STOR-M tokamak to measure toroidal and poloidal flow velocity of tokamak plasma with a sufficiently high resolution.
- A compact torus injector operated at high repetition rate (10 Hz) has been developed and installed on STOR-M tokamak.
- The ISTTOK tokamak Heavy Ion Beam diagnostic signal conditioning system was improved with novel low noise, broad band amplifiers to allow simultaneous amplification of all the signals coming from the detectors.
- Faculty of Physics of Sofia University designed, built and installed a new Langmuir probe heads with 60-chanels electronic circuit for probe measurements on the COMPASS and ISTTOK tokamaks.
- Development and installation of a heavy ion beam probe diagnostic on the Uragan-2M stellarator.
- A new method of wall conditioning was implemented on the Uragan-2M stellarator.
- A new method for avoiding the appearance of runaway electrons in torsatrons was tested in both Uragan-2M and Uragan-3M.

- Design and fabrication of combined Langmuir and Ball-Pen probes for direct measurements of the plasma potential in the IR-T1 tokamak.
- Design, construction and installation of an emissive biased limiter on IR-T1 tokamak for edge plasma investigation.

6.3. Development of prototypes of applicable fusion-relevant simulation tools

- The optimization of two self-consistent codes for modelling of RF plasma production was provided in close cooperation between Kharkov IPP and Plasma Physics Laboratory (Brussels, Belgium).
- The ASTRA transport simulation code has been adapted to the COMPASS configuration to validate the hypothesis of ionization as a main reason for appearance of bi-Maxwellian electron energy destitution function in the vicinity of the last closed flux surface.
- The KINX MHD simulation code has been adapted to the COMPASS configuration to calculate the Alfven continuum gaps and identify the Alfven Eigenmodes and Alfven-sound modes in the core plasma.
- A First Derivative Probe Techniques for evaluation of the electron energy distribution function in the edge plasma was developed by Faculty of Physics of Sofia University and applied to the analysis of the probe data from the COMPASS and ISTTOK tokamaks.

6.4. Improved networking among CRP participating Institutions

Within the framework of the CRP a number of collaborative initiatives among different institutions were undertaken to address specific research and development issues.

- Through the collaboration among CRP participants from University of Sofia, Institute of Plasma Physics in Prague and IST Lisbon the capability of a Langmuir probe technique to determine the electron energy distribution function was optimized and confirmed.
- Through the collaboration among CRP participants from Kurchatov Institute Moscow, Institute of Plasma Physics in Prague, IST Lisbon and Kharkov Institute of Physics and Technology the conceptual design of a Heavy Ion Beam Probe diagnostic for the COMPASS tokamak in Prague was done. Through bilateral collaboration between Kurchatov Institute Moscow and Kharkov Institute of Physics and Technology a new Heavy Ion Beam Probe diagnostic has been developed and installed on the URAGAN-2M stellarator in Kharkov.
- Through the collaboration among CRP participants from the Institute of Plasma Physics in Prague and Plasma Physics Research Centre in Islamic Azad University in Tehran, a Ball Pen and a rake probe were designed, fabricated and installed on the IR-T1 tokamak in Tehran.
- Through the collaboration among CRP participants from the Institute of Plasma Physics in Prague and IST in Lisbon, a Ball Pen probe was designed, fabricated and installed on the ISTTOK tokamak in Lisbon.
- Through the collaboration among CRP participants from Plasma Physics Institute in Prague and National Tokamak Fusion program Islamabad, a triple Langmuir and an emissive probe were designed, fabricated and installed on the GLAST-3 tokamak in Islamabad.

- The collaboration between the St. Petersburg State University and Czech Technical University in Prague enabled the manufacturing and installation of a new microwave launcher (based on 2.45GHz 1kW magnetron) as a pre-ionisation source for the GOLEM tokamak in Prague.
- The collaboration between the St. Petersburg State University and National Tokamak Fusion program Islamabad enabled the manufacturing and installation of a new microwave launcher (based on 2.45GHz 1kW magnetron) as a pre-ionisation source for the GLAST-3 tokamak in Islamabad.
- The collaboration between Oxford Instruments, UK, Tokamak Energy Ltd, Institute of Plasma Physics in Prague and Czech Technical University in Prague the development of high temperature superconductor magnets (HTS) for tokamaks was pursued.
- Within the collaboration between Oxford Instruments, UK and Tokamak Energy, Ltd. ST-25 HTS and ST-60, ST-140 tokamaks with HTS magnets have been designed. In addition full HTS tokamak (ST-25 HTS) has been constructed and put into operation.
- Through the collaboration among Oxford Instruments, UK, Tokamak Energy Ltd., and National Tokamak Fusion program Islamabad high temperature superconductor poloidal field coils for GLAST-3 were developed.
- Through the collaboration of IST Lisbon and National Tokamak Fusion Program, Islamabad, Data Acquisition System for GLAST-3 was developed.
- The collaboration between Kurchatov Institute and Institute of Plasma Physics in Prague enabled the use of the KINX magnetohydrodynamic numerical code (developed by collaboration with Keldysh Institute of Applied Mathematics Russian Academy of Sciences) to study Alfvén Eigenmodes in COMPASS plasmas. In addition, the ASTRA transport code was used to study particle and energy transport to model experiments dedicated to the confinement transition on the COMPASS tokamak in Prague.
- Through the collaboration among Kurchatov Institute and Institute of Plasma Physics in Prague and IST Lisbon the modelling of the probing beam attenuation for the conceptual design of the Heavy Ion Beam Probe diagnostic for the tokamak COMPASS in Prague was performed.
- In collaboration among Plasma Physics Laboratory at University of Saskatchewan, Czech Technical University in Prague, Institute of Plasma Physics in Prague and Tokamak Energy, Ltd., a newly developed 3D model of the ferromagnet effect on the magnetic field has been introduced for ion core based GOLEM and STOR-M tokamaks.
- Through the collaboration between National Nuclear Centre in Kurchatov, Kazakhstan and National Tokamak Fusion Program, Islamabad, modelling of equilibrium in the presence of poloidal field coils in the GLAST-3 tokamak using the code TOKAMEQ (developed in collaboration with Lomonosov Moscow State University) was done.

6.5. Contribution to capacity building and human resource development

The network was instrumental in providing opportunities for training and education of students and young researchers through several programmes:

- Joint experiments provided a platform for young researchers to interact with and benefit from experts in the field.
- A series of summer training courses (SUMTRAIC) have been held on the COMPASS tokamak in Prague in 2012, 2013, 2014 and 2015 (12–16 students each year, including CRP members). The objective of SUMTRAIC was to acquaint students with important aspects of experimental research (planning and execution of experiment, data

processing, discussion of achieved results within experimental groups and presentation thereof).

- The series of winter training courses (EMTRAIC) held on the COMPASS tokamak in Prague within the framework of European Master of Science in Nuclear Fusion and Engineering Physics (FUSION-EP) was open to CRP participants. CRP participants attended the corresponding Joint Experimentation and Analysis Sessions organized in 2013, 2014 and 2015.
- Experts from CRP members were invited to give lectures on Tokamak Physics and technology to students and young researchers within the framework of the Tokamak Workshops, during International Nathiagali Summer College (INSC), Islamabad. On-site hands-on training and discussions were also arranged on the GLAST-3 tokamak in Islamabad.
- Experts from CRP members delivered a series of lectures at various summers schools (Kudowa Summer School, Poland 2012, 2013 and 2014, International Workshop & Summer School on Plasma Physics, Kiten, Bulgaria 2012 and 2014, Conference and school on plasma physics (held at Alushta in 2012 and at Kharkiv in 2014), Summer school on plasma diagnostics, Bezmiechova, Poland in 2015, Erasmus Mundus Winter Event – Cadarache in 2013, 2014 and 2015, ICPT-IAEA College, Trieste, Italy 2012, Summer school on plasma physics in Costa Rica 2014)
- A series of summer training courses on plasma physics and nuclear fusion (PLASMASURF) have been held in Lisbon with a visit to the ISTTOK tokamak in 2013, 2014 and 2015 attracting more than 20 students each year, some of them coming from CRP members. The objective of the course was to give an overview of plasma physics and motivate the students for a master and Ph.D. programmes in the field.
- The network has proven a conducive environment for providing mobility opportunities to students from participating countries. This includes e.g. co-supervision of thesis works and scientific stays at different laboratories and facilities.
- The CRP contributed to the development of the unique ability to remotely operate the GOLEM and ST-25 tokamaks through on-line access. The remote operation of GOLEM by students from several foreign universities including CRP partners has been successfully performed.

7. IMPACT OF THE CRP

This CRP provided a unique possibility to strengthen the links among the various institutions hosting devices that are part of the network. It also provided opportunities for scientific cooperation among developed and developing countries. In addition, developing countries have been able to benefit from a large number of capacity building and human resource development activities offered throughout the CRP. The Joint Experiments organized on different devices played a key role in enabling the exchange of information as well as experience and was instrumental in broadening the scientific scope of the exploitation of the devices involved. Finally, the CRP has considerably contributed to streamlining the contributions of smaller devices to the science and technology of larger devices.

REPORTS OF THE COORDINATED RESEARCH PROJECT PARTICIPANTS

ADVANCES IN LANGMUIR PROBE DIAGNOSTICS OF THE PLASMA POTENTIAL AND ELECTRON-ENERGY DISTRIBUTION FUNCTION IN FUSION PLASMAS

Tsv. K. POPOV[1], M. DIMITROVA[2,3], P. IVANOVA[3], J. KOVACIC[4], T. GYERGYEK[4,5], R. DEJARNAC[2], J. STOCKEL[2], M. A. PEDROSA[6], D. LOPEZ-BRUNA[6], C. HIDALGO[6]

[1] Faculty of Physics, St. Kliment Ohridski University of Sofia, 5, J. Bourchier Blvd., 1164 Sofia, Bulgaria
[2] Institute of Plasma Physics, Academy of Sciences of the Czech Republic, Za Slovankou 3, 182 00 Prague 8, CR
[3] Emil Djakov Institute of Electronics, Bulgarian Academy of Sciences, 72, Tsarigradsko Chaussee, 1784 Sofia, Bulgaria
[4] Jožef Stefan Institute, 39, Jamova, 1000 Ljubljana, Slovenia
[5] University of Ljubljana, Faculty of Electrical Engineering, 1000 Ljubljana, Slovenia
[6] Laboratorio Nacional de Fusión, CIEMAT, Complutense 40 – 28040 Madrid, Spain

Abstract
Advanced Langmuir probe techniques are reviewed for evaluating the plasma potential and electron-energy distribution function in magnetized plasma. The classical, the triple probe and the first derivative probe technique are reviewed and discussed. The first-derivative probe technique was applied to derive data for plasma parameters from the *IV* Langmuir probe characteristics measured in the plasma boundary region in the COMPASS and ISTTOK tokamaks, as well as in the TJ-II stellarator. It is shown that in the COMPASS tokamak in the vicinity of the last closed flux surface (LCFS) the electron energy distribution function (EEDF) is bi-Maxwellian with the low-temperature electron fraction predominating over the higher temperature one, whereas in the far scrape off layer (SOL) the EEDF is Maxwellian. In the TJ-II stellarator during NBI heated plasma, the EEDF in the confined plasma and close to the LCFS is bi-Maxwellian while in the far SOL the EEDF is Maxwellian. In contrast, during the ECR heating phase of the discharge both in the confined plasma and in the SOL the EEDF is bi-Maxwellian. The mechanism for the appearance of a bi-Maxwellian EEDF in the vicinity of the LCFS is discussed. The comparison of the results from probe measurements with the ASTRA package and EIRENE code calculations suggests that the main reason of the appearance of a bi-Maxwellian EEDF in the vicinity of the LCFS is the ionization of the neutral atoms. Results for the electron temperatures and densities obtained by the first-derivative probe technique in the COMPASS tokamak and in the TJ-II stellarator were used to evaluate the radial distribution of the parallel power flux density. It is shown that in the SOL the radial distribution of the parallel power flux density is a double exponential. It is pointed out that in the calculations of the parallel power flux density at the LCFS the energy losses from inelastic processes (excitation and ionization) must be taken into account.

Tsv. K. Popov et al Plasma Sources Sci. Technol. (2016) **25** 033001
http://iopscience.iop.org/article/10.1088/0963-0252/25/3/033001/meta

CONTROL OF TOROIDAL PLASMA FLOW IN THE STOR-M TOKAMAK AND INVESTIGATION OF THE GEODESIC ACOUSTIC MODE

A. ROHOLLAHI*, T. ONCHI**, D. BASU*, S. ELGRIW*, M.B. Dreval*, D. MCCOLL*, M. NAKAJIMA*, J.A. ADEGUN*, M. PATTERSON*, C. XIAO*, A. HIROSE*

*Plasma Physics Laboratory of University of Saskatchewan, Saskatoon, Saskatchewan, Canada
**Research Institute for Applied Mechanics, Kyushu University, Fukuoka 816-8580, Japan

Abstract
The Saskatchewan Torus Modified (STOR-M) is an iron core tokamak and the only operating tokamak in Canada which has been in operation since 1987. The major and minor radius of the STOR-M are 46 cm and 12 cm respectively. Different types of experiments such as AC operation, Ohmic H-modes by rapid edge heating and Compact Torus Injection (CTI), plasma flow control by applying Resonant Magnetic Perturbation (RMP) and CTI, and recently detection of Geodesic Acoustic Modes (GAM) have been conducted in this tokamak. Experimental data indicate that toroidal rotational flow of the tokamak plasma is controllable by applying a RMP and a tangential CTI. On the other hand experimental results indicate presence of GAM like oscillation in this machine. Detailed discussions have been done in the following sections.

1. INTRODUCTION

The toroidal flow velocity of tokamak plasma plays a critical role in plasma confinement and the mitigation of disruptions [1–3]. Toroidal flow depends on radial electric field (E_r) and the gradient of the ion pressure among other parameters. It has been shown that by enhancement of the radial shear, in toroidal and poloidal plasma flow, the transition to H-mode is achievable. Also, toroidal rotational flow plays a critical role in maintaining high β and stability in tokamaks in addition to the generation of the internal transport barrier due to the change in the radial electric field [2,4,5]. An unbalanced neutral beam injection (NBI) is one of the methods to induce a substantial plasma flow in large tokomaks. NBI requires a large amount of stored energy to accelerate particles to sufficiently high velocity in order to inject momentum and rotational flow into the tokamak plasma in addition to plasma heating [6]. Besides fuelling purposes for Compact Torus Injection (CTI), it has been demonstrated during our experiments that tangential compact torus injection is able to control tokamak plasma flow. Also, flow change and the suppression of magnetic fluctuations by applying RMP are examined in recent experiments [7].

CTI is one of the advanced methods for the fuelling of tokamak reactors and deposits fuel directly into the core of a tokamak. It is also possible to control the plasma density profile by CTI. Steady state operation of a reactor needs a repetitive CTI for fueling. The injection frequency of 10 Hz has been achieved through development of the charging system and associated capacitor banks. All of this progress -the toroidal flow control and the repetitive CTI- has been made in the last four years.

We also start elaborate turbulence studies experimentally in STOR-M machine. One of the major aims of this project is to detect GAM and zonal flows. Recent experimental results demonstrate GAM like oscillations present in this tokamak.

2. CONTROL OF TOROIDAL PLASMA FLOW

2.1. Toroidal Plasma Flow Measurement

An Ion Doppler Spectrometer (IDS) system has been developed and installed on STOR-M. The IDS system is a non-invasive and standard diagnostic tool in fusion devices for impurity ion flow and temperature measurement. To measure plasma flow, we chose emission lines of impurities with the highest brightness such as Oxygen and Carbon. Three different line emissions, C_{III}(4647.4 Å), C_{VI}(5290.5Å) and O_{V}(2728Å), were selected because they are in different ionization states and are located in the different radial locations of the tokamak plasma. Experimental data show that C_{III} ions are concentrated at the periphery region of the tokamak plasma (r = 7 cm) and C_{VI} ions are in the core (r = 0 cm) of the tokamak plasma. The most probable location for O_{V} ions is around r = 3 cm. The schematic of the IDS system for STOR-M is illustrated in Figure 1. It consists of a fibre optic cable with collimators on both ends, a Czerny-Tuner-type spectrometer (SPEX 1702) with a spectral resolution of 0.3 Å which operates in the range 0–15000 Å, a cylindrical rod lens and a multi-anode photomultiplier (PMT) array. The resolution of the velocity measurement for this system is $\tilde{v} \approx 1–2\ \mathrm{kms^{-1}}$.

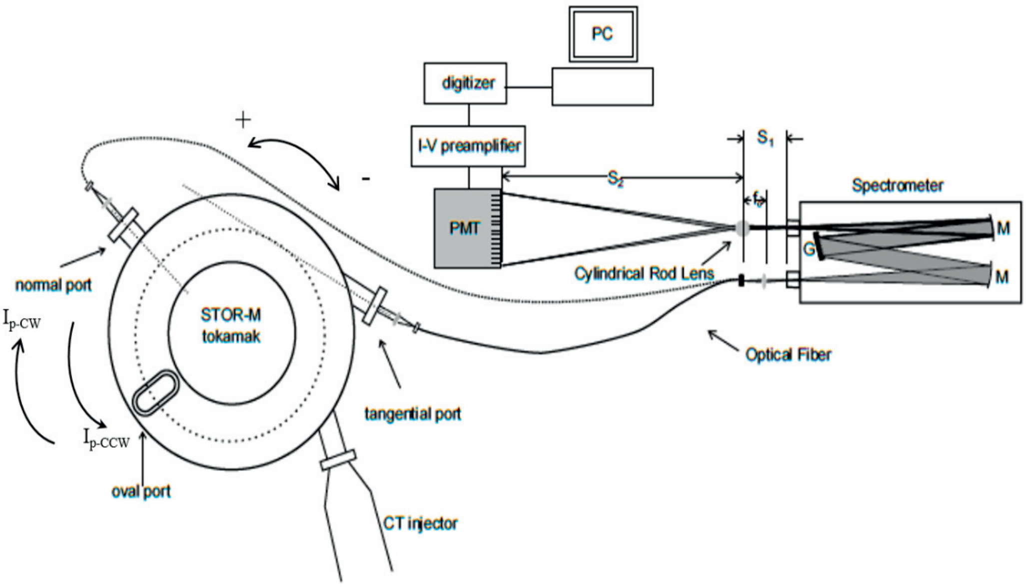

FIG. 1. Schematic diagram of the IDS system.

As shown in Figure 1, the light collected from the tokamak ports is conveyed by an optical fibre to the spectrometer input slit. It is collimated by a concave mirror, diffracted by a diffraction grating, and focused by another concave mirror to the exit of the spectrometer. A cylindrical rod lens magnifies the spectrum to the PMT surface. The PMT signals are transmitted by twisted pair cables to pre-amplifier and then digitizer to record. The rotational flow of impurity ions is calculated by measuring the wavelength shift between the line emission gathered from the tangential port and that from the normal port (Figure 1).

Keeping the toroidal field in the same counter clockwise (top view), the toroidal plasma rotational flow for counter-clockwise (CCW) and clockwise (CW) tokamak discharges currents has been measured. The toroidal flow velocities of C_{III}, O_{V} and C_{VI} ions for CCW current during normal ohmic discharge are shown in Figure 2a. They represent the difference in magnitude and direction of flow at different radial locations of the tokamak and suggest a toroidal rotational flow shear. The C_{III} flow velocity at the periphery (r = 7 cm) is in the counter clockwise direction (co-current) and decreases from 6 $\mathrm{kms^{-1}}$ to 1 $\mathrm{kms^{-1}}$ over time. The O_{V} flow velocity at r = 3 cm is in the clockwise direction (anti-current) and changes from -0.5 $\mathrm{kms^{-1}}$ to -7.5 $\mathrm{kms^{-1}}$. The C_{VI} flow velocity in the core (r = 0 cm) is also in the clockwise direction (anti-current) and changes from -5 $\mathrm{kms^{-1}}$ to -12.5 $\mathrm{kms^{-1}}$.

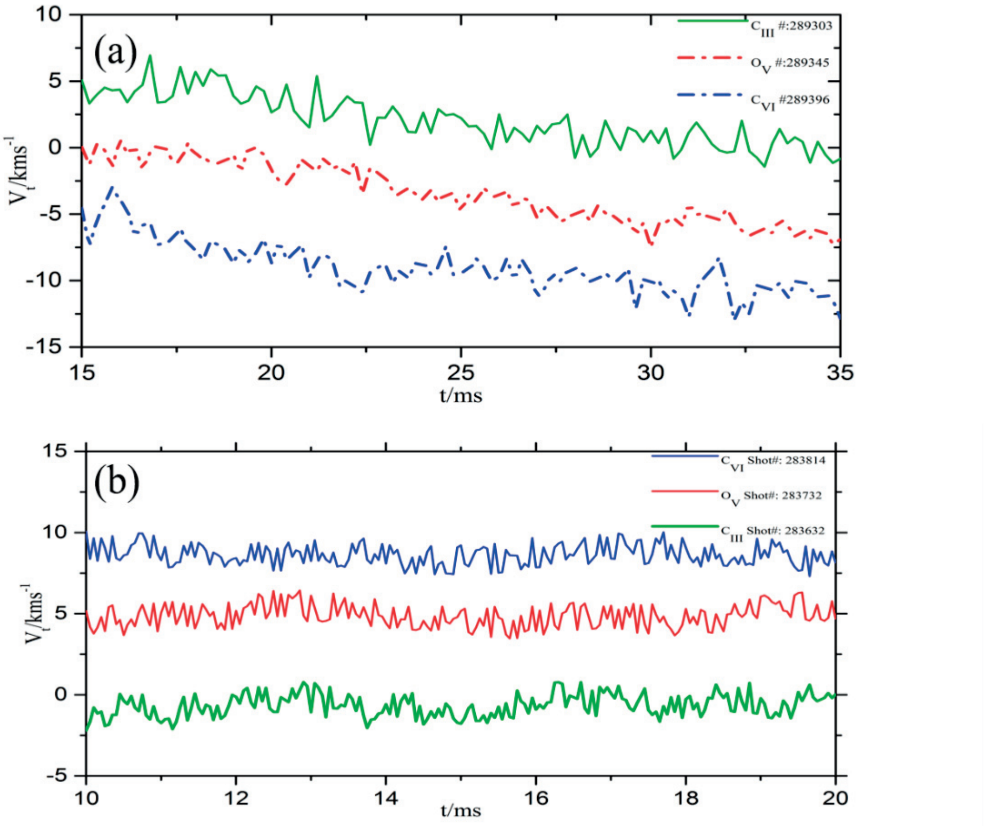

FIG. 2. The plasma toroidal flow velocities measurement for CCW (a) and CW current (b) tokomak discharge current directions.

Figure 2b shows the velocities of ions for CW current directions. As illustrated, flow velocity of C_{III} ions is in the co-current direction while O_V and C_{VI} rotate in the anti-current direction. Also in both scenarios, CCW current and CW current, the plasma rotational flow has a shear in the *r* direction.

2.2. Plasma Flow Control by Tangential CTI

A Compact Torus (CT) is a fully ionized high density plasmoid magnetically confined by its own magnetic field which can withstand a large acceleration. STOR-M is equipped with a tangential CT injector which accelerates the CT to v_{inject} = 90–210 kms^{-1}. CTI is a non-distributive central fuelling method which has the capability to perform localized fuelling. The localized central fuelling provides a means to control the plasma density and pressure profiles which may also enhance bootstrap current density leading to modification of magnetic shear in the plasma core [8]. Improvement in plasma confinement and suppression of magnetic fluctuation have been reported as a result of CTI [9–12]. In this study, we have concentrated on effects of CTI on plasma flow and the momentum transferred from CTI to the tokamak plasma. Figure 3 shows a schematic diagram of the University of Saskatchewan Compact Torus Injector (USCTI). USCTI has a coaxial configuration with formation, compression and acceleration sections.

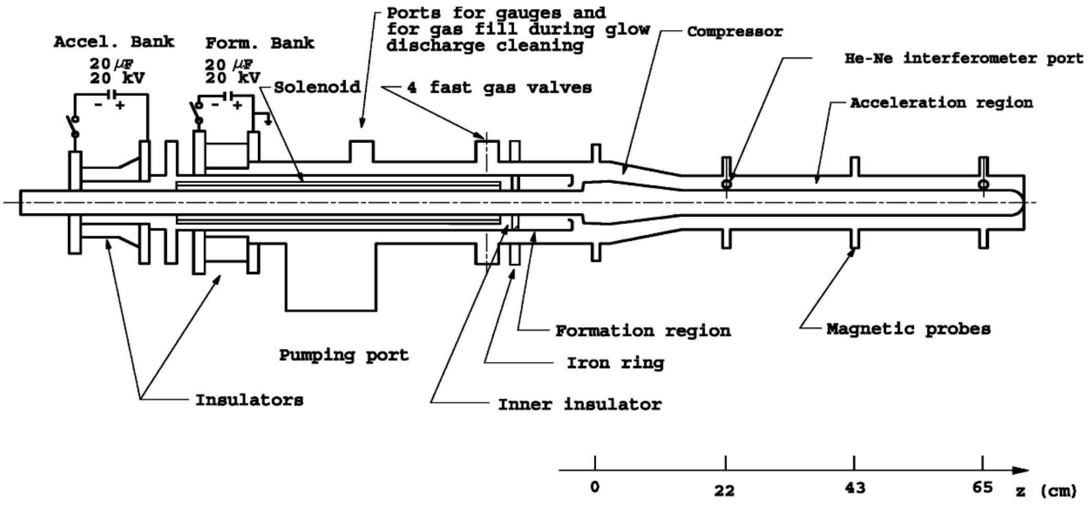

FIG. 3. Schematic Diagram of USCTI.

The injection velocity of the CT is a function of the acceleration bank voltage. There are one magnetic probe (Z=0) in the formation region and three along the acceleration section. The injection velocity of the CT is measured by measuring the time of flight of the CT along the acceleration section. The sample magnetic probe signals are shown in Figure 4a.

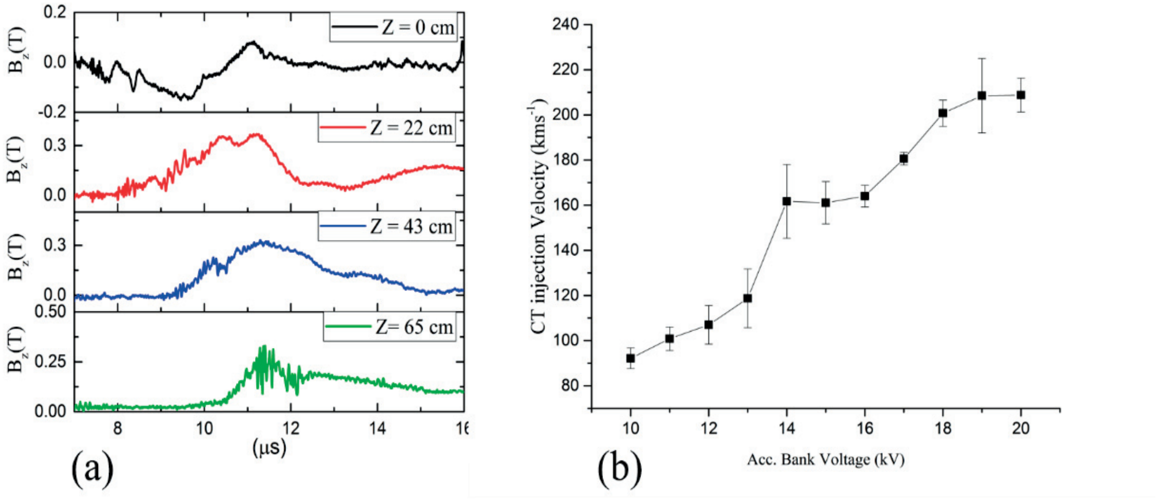

FIG. 4. Magnetic probes signals along the acceleration region (a), and the injection velocity vs. acceleration bank voltage (b).

Figure 4b shows the change in the injection velocity with respect to the acceleration bank voltage. For each of the acceleration voltages, the injection velocity is calculated by averaging over 15 CT injections. For the acceleration bank voltages lower than 18 kV ($V_{acc} \leq 18$ kV), the injection velocity increases with acceleration bank voltage. The injection velocity measurement results show that for $V_{acc} \geq 18$ kV, the injection velocity becomes saturated and the maximum achievable injection velocity for the USCTI is $v_{inject} = 210$ kms^{-1}. This magnitude of the velocity is large enough to overcome the magnetic field barrier and deposit fuel into the core of the tokamak plasma.

The waveforms of the STOR-M plasma parameters are shown in Figure 5 for a CW plasma current discharge. The CT is injected at the flat top of the plasma current at $t = 15$ ms. The line-averaged electron density (n_e) has increased from 3.2×10^{13} cm^{-3} to 5.87×10^{13} cm^{-3} within 1.8 ms after CTI. It is also shown that the horizontal plasma position (ΔH) starts to move outward at the time when density starts to increase which may be a result of an increase in the thermal energy content in the tokamak plasma.

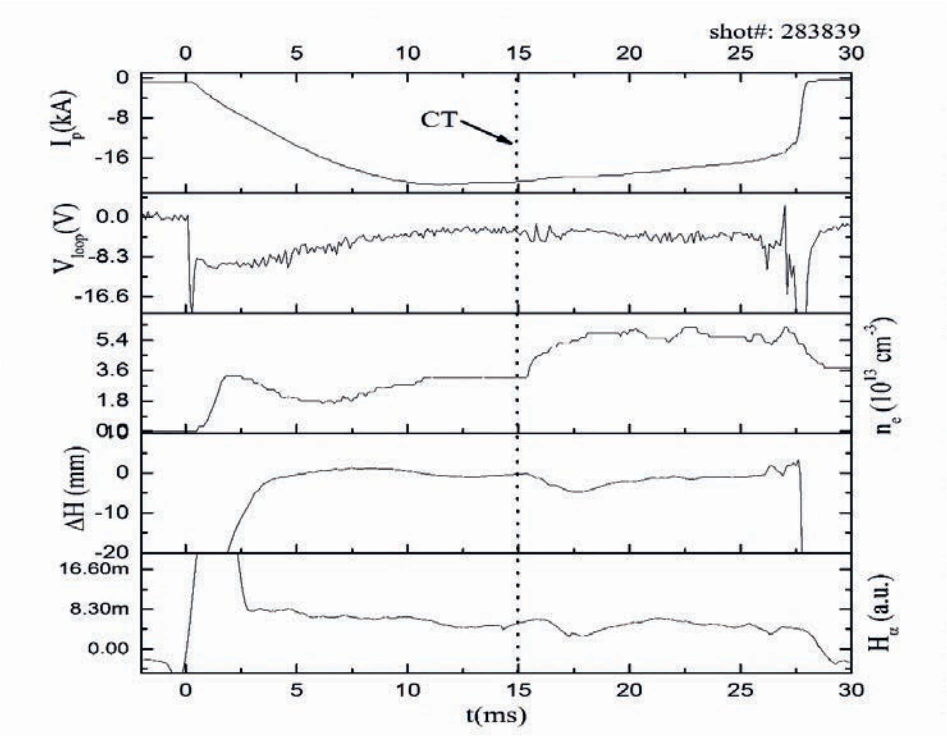

FIG. 5. Wave forms of plasma parameters in a STOR-M tokamak discharge during the preliminary CT injection experiments. The discharge current I_p is in the CW direction.

As shown in the last trace of the Figure 5, H_α radiation level decreases by ≈30% 2 ms after CTI and returns to a nominal level after 3 ms. Improvement of the particle confinement and an increase in the global energy confinement in the STOR-M tokamak after CTI have been reported previously and the recent results confirm those previous observations [10].

The change in the line-averaged electron density with respect to the acceleration bank voltage of the CT injector is illustrated in Figure 6a. Figure 6b shows the time delay between CTI and the increase of the density. For the $V_{acc} = 10$ kV, the density change is small and the delay is long, indicating that penetration of the CT into the tokamak plasma has not occurred and the density increases due to gass puffing in CTI. The change in the density increases with V_{acc} and for $V_{acc} \geq 16$ kV it is almost constant with $\Delta n_e \approx 1.5 \times 10^{13}$ cm^{-3}. It has been expected that for deposition of the fuel into the core of the tokamak plasma the condition $\rho v_{\mathrm{inject}}^2/2 > B_0^2/2\mu_0$ must be met, here ρ is the electron line-averaged density of the CT, v_{inject} is the injection velocity and B_o is the toroidal magnetic field at the tokamak centre.

The line-averaged density of the CT has been measured $\rho \approx 3 \times 10^{15}$ cm^{-3} by a He-Ne laser interferometer at the exist point of the injector. The length of the CT at the end of the injector is 17 cm. The CT mass has been estimated about 1 μg corresponding to 50% the particle inventory in the STOR-M discharges [10].

The USCTI was also injected into the tokamak discharge with current in the CCW direction to clarify whether the flow change is due to CT momentum injection to the tokamak discharge.

In both cases, CT was injected in the same CCW direction. IDS measurements for both of the CCW (Figure 7a) and the CW plasma current (Figure 7b) directions show that the toroidal flow has been changed toward positive direction for both cases. The positive (negative) flow velocity is defined in the CCW (CW) direction. USCTI always injects CTs in the positive (CCW) direction so the injected CT momentum of the CT is in the positive direction (CCW).

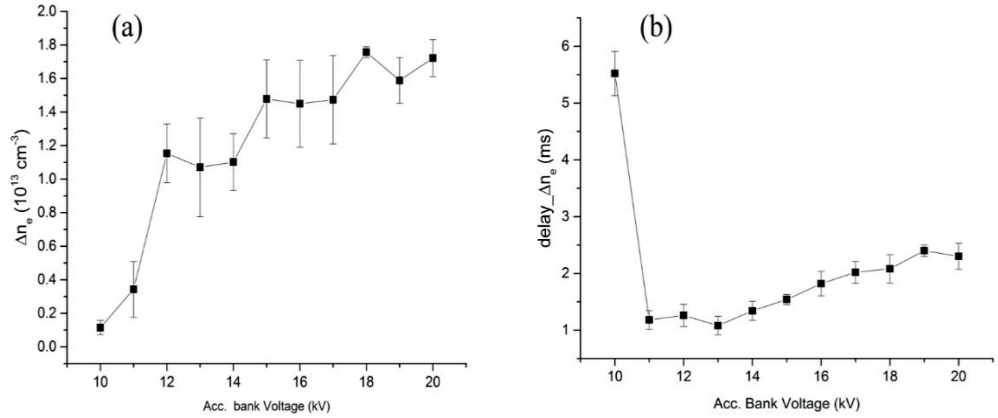

FIG. 6. The change in the line average electron density after CTI (a), the delay time between CTI and the start of the tokamak plasma density change (b).

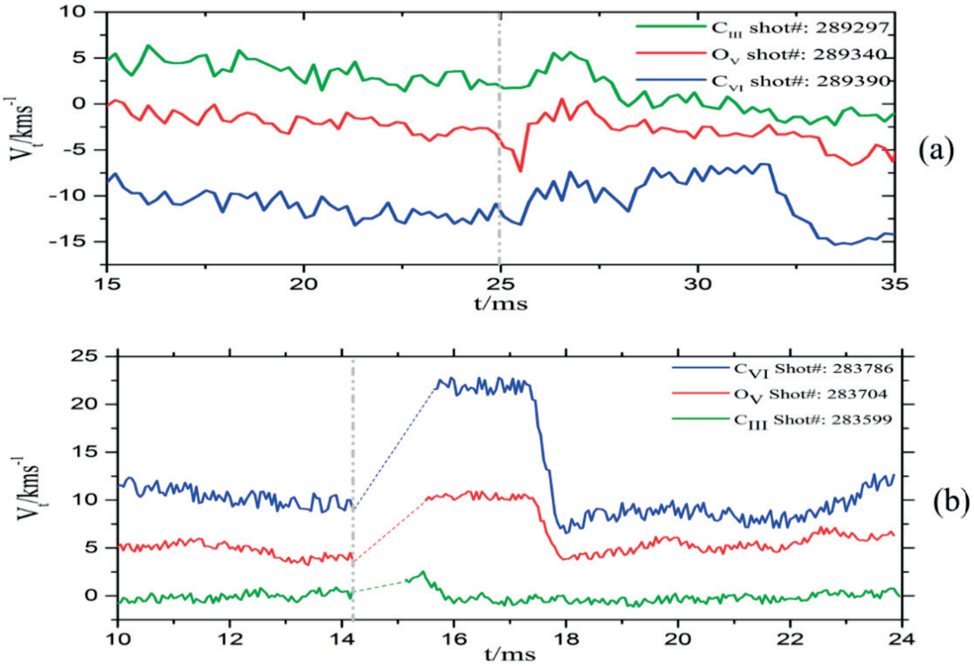

FIG.7. The plasma rotational flow measurement after the CTI for CCW current(a), and CW current(b)

As shown in Figure 7 (both cases), the velocity of the C_{III} ions, which are outer tokamak region, increases ≈ 2 kms^{-1} after injection and lasts for 2 ms before dropping back to the normal level. The velocity of the O_V and C_{VI} increases about 5 kms^{-1} and 8 kms^{-1} respectively and last longer compared to the C_{III} ions. The change in the toroidal flow in the outer area is short lived, possibly due higher collisionality in that outer region.

Figure 8 shows the change in the toroidal rotational flow of the impurity ions after the CT injection with respect to the acceleration bank voltage of the CT injector.

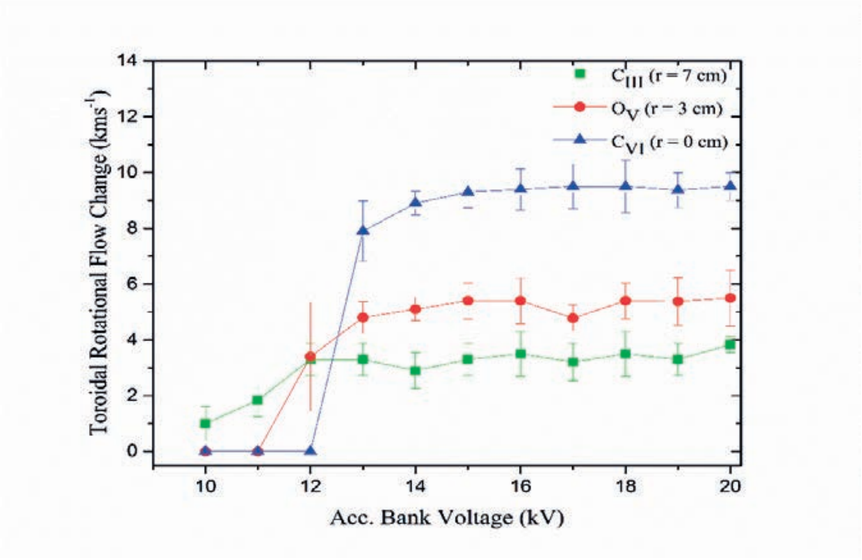

FIG. 8. Toroidal Rotational Flow change for C_{III}, O_V and C_{VI} ions respect to the acceleration bank voltage of the CT injector.

For low acceleration bank voltages corresponded to low injection velocities, there is no change in the flow velocity of C_{VI} ions which are concentrated at the core of tokamak plasma. It is possible that the CT does not reach the core of the tokamak plasma with a low acceleration voltage and low injection velocity. For the flow of C_{III} ions at the outer region of the tokamak plasma, changes in the rotational flow velocity have been observed even at low acceleration voltage. The change in the rotational flow velocity for all of the impurity ions has been saturated after V_{acc} = 15 kV. We anticipated that momentum injection will be increased by increasing the injection velocity of the CT, but our results show the increase of the momentum injection does not follow the increase of the injection velocity of the CT. As reported before, the mass loss of the accelerated CT is related to the injection velocity [13]. Either the increase of the mass loss or other unknown effects might be the reason of the saturation of the momentum injection at the high CT injection velocities.

It has been confirmed that the injection of CT into the tokamak plasma changes the toroidal flow velocity through the injection of the momentum into the tokamak plasma. The CTI is one of the advanced core-fuelling methods for fusion reactors. In addition to the fuelling purposes, CTI is possible to control the toroidal flow of the tokamak plasma.

2.3. Plasma Flow Control by Resonant Magnetic Perturbation

It is known that major disruptions are serious problems for a tokamak reactor. Different techniques have already been proposed to avoid disruptions. One of the proposed techniques is application of a radial magnetic fields called resonant magnetic perturbations (RMP) produced by external helical coils with low poloidal (m) and toroidal (n) modes. The produced RMP counteracts magnetic islands of the same helicity. On one hand, application of moderate RMP showed that Mirnov oscillations could be strongly suppressed and the onset of the disruptive instability could be delayed [14–16]. On the other hand, the external helical coils have been used to study the nature of major disruptions since the disruptions can be artificially triggered if the coils are fed with substantially higher RMP current (IRMP).

The RMP fields have been successfully utilized to control plasma rotation in tokamaks. Previous experiments have shown that tokamak plasmas can be confined and stabilized by plasma rotation [15]. It is well known that both RMP and non-resonant magnetic perturbations (NRMP) can influence the plasma rotation and the radial electric field (E_r) in tokamaks through either electromagnetic (EM) torque mechanism in the resonant configurations, or via the neoclassical toroidal viscosity (NTV) effect in the non-resonant configurations. The NTV torque is believed to be caused by a nonambipolar radial particle flux resulted from the breaking of the toroidal magnetic symmetry in low collisionality plasmas.

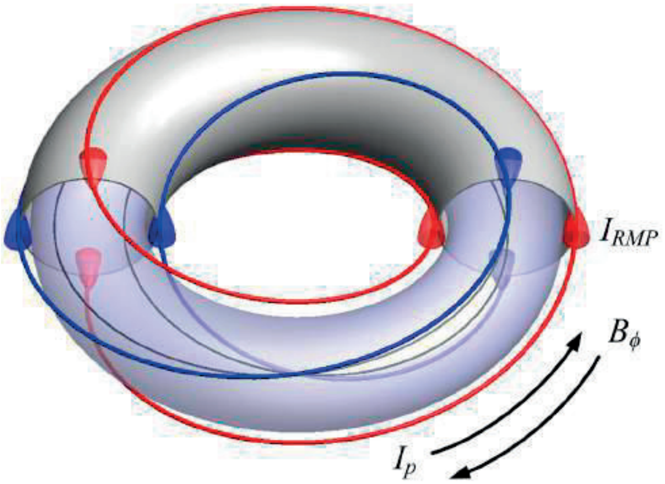

FIG. 9. The layout of RMP coils in STOR-M. The blue and red lines illustrate the helical configuration of RMP coils used to control (2, 1) magnetic islands (the black line).

The RMP system in STOR-M consists of RMP coils, power supplies, trigger circuits, IGBT and SCR switches. The RMP coil is a 30 m long wire formed by two sets of 8 AWG wires with an (l = 2, n = 1) configuration connected in series. The two sets of helical windings are poloidally separated by 90° illustrated in Figure 9 by the blue and red lines. The coils are externally wound and secured against the outer surface of the vacuum chamber at a radius of 17 cm. The total resistance and inductance of the RMP windings are about 100 mΩ and 15 μH, respectively.

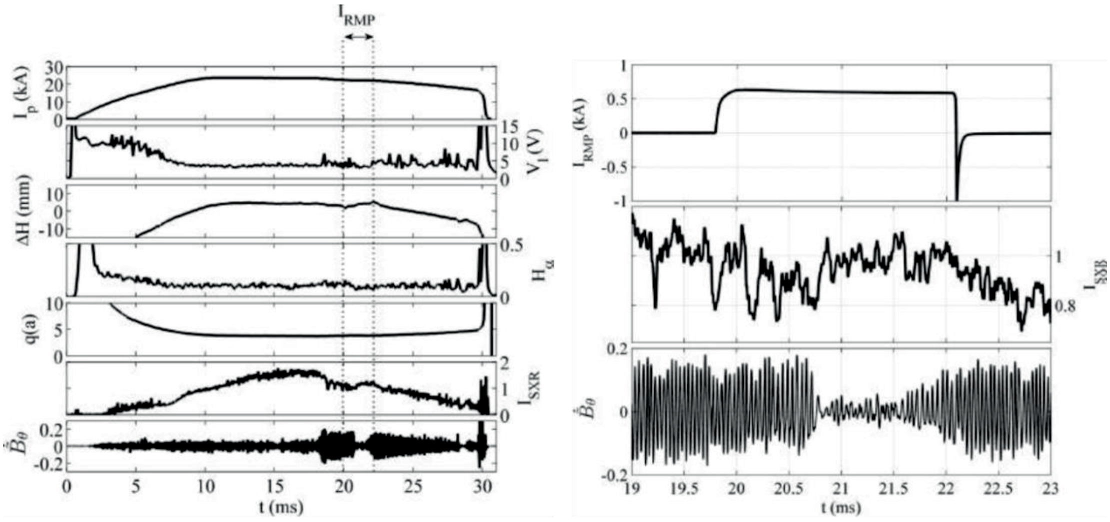

(a) (b)

FIG. 10. Effect of RMP on plasma parameters during STOR-M discharge.

The effects of RMP on tokamak plasma parameters have been studied experimentally. Figure 10a shows plasma parameters and the influence of RMP. The current of RMP coils is 600 A and the plasma current is 23.5 kA.

There is not a significant change in the plasma current, while a small reduction in loop voltage and a clear suppression in H_α line emission are observed after applying RMP. The plasma column is also shifted by 3 mm outwards. The main effect of RMP on the discharge is the significant suppression in the MHD fluctuation signal and the increased in the SXR emission from the plasma core. Figure 10b shows three expanded waveforms of I_{RMP}, central SXR and Mirnov fluctuation signals. The frequency analysis of the Mirnov signal shows a gradual decrease in MHD amplitude and frequency. The MHD frequency reduces from 20 kHz to 25 kHz. This gradual change is not seen in the frequency analysis of the SXR signal but it's clear that both of the signals are highly coherent (Figure 11).

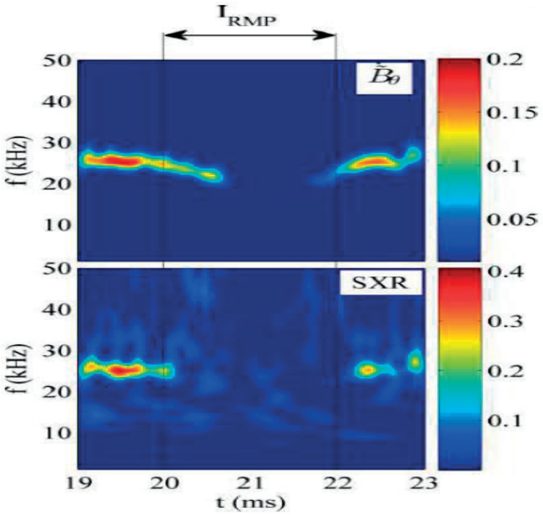

FIG. 11. Wavelet power spectra of the Mirnov and SXR signals.

The Fourier analysis of Mirnov coil signal shows, during RMP current, the magnitude of the harmonics with low *m* numbers drop 0.7 ms after applying RMP. The mode magnitudes are plotted in Figure 12. As shown in Figure 12, the $m = 2$ mode has the highest magnitude before RMP and the highest drop (~ 90%) after RMP. The magnitude of the mode $m = 3$ drops by ~50% after RMP. However, the magnitude of the weak mode $m = 4$ is hardly affected by RMP.

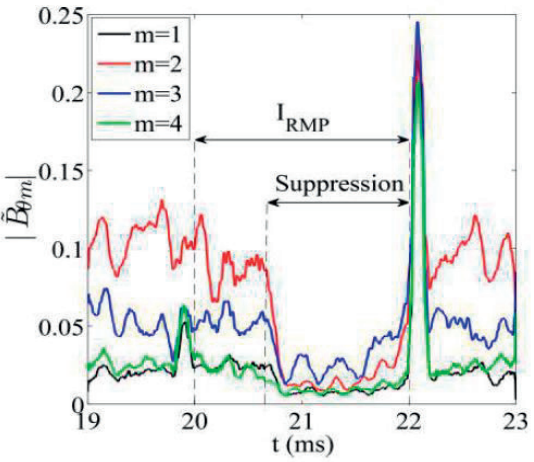

FIG. 12. Mode magnitudes for MHD modes up to m = 4 around the time of firing RMP.

Before discussions on the flow velocities, if should be pointed out that the positive (negative) flow direction pertinent to the RMP experiments is defined in the CW (CCW) direction, in contrast to the definition in the CT Injection experiments. The influence of RMP on the rotational toroidal flow of C_{III}, O_V and C_{VI} is illustrated in Figure 13a. The RMP current is about 600 A and applied between 20 and 28 ms. As mentioned before, the O_V and C_{VI} impurities are respectively located at r = 3 cm and 0 cm. Figure 13b shows the flow velocity of O_V and C_{VI} impurities for the cases with zero RMP current and with three other I_{RMP} values. Without I_{RMP} (black curves), the direction of the toroidal flow is in the counter-current direction (positive). Once the current of the RMP pulse, applied between 20 and 28 ms, exceeds a threshold, the magnitude of toroidal flow velocity of O_V and C_{VI} impurities is reduced and the change is more significant with the increase of the RMP current. The toroidal O_V and C_{VI} flows even reverse their directions at I_{RMP} = 850 A and 1.1 kA to the co-current direction (negative).

The possibility of the continuous modulation of toroidal flow by double RMP (DRMP) has been investigated during ohmic discharge of STOR-M tokamak. The first RMP pulse was turned on at 15 ms for 3 ms and the second one at 20 ms for 3 ms. Figure 14 shows the modulation of toroidal flow velocities of O_V and C_{VI} impurities induced by the DRMP pulse. For the CCW plasma current, the O_V and C_{VI} impurity ions rotate in the CW direction before applying the DRMP pulse. As the first RMP pulse is turned on at 15 ms, the directions of O_V and C_{VI} flow velocities change towards the CCW direction, the same as the plasma current direction and a greater change is observed with a larger RMP current. When the first RMP pulse is switched off at 18 ms, the toroidal flow velocities return to the initial direction and amplitude. The second RMP pulse applied at 20 ms induces a change in the flow velocities similar to that induced by the first RMP pulse. It is expected that a continuous modulation of flow velocity can be achieved with additional RMP pulses.

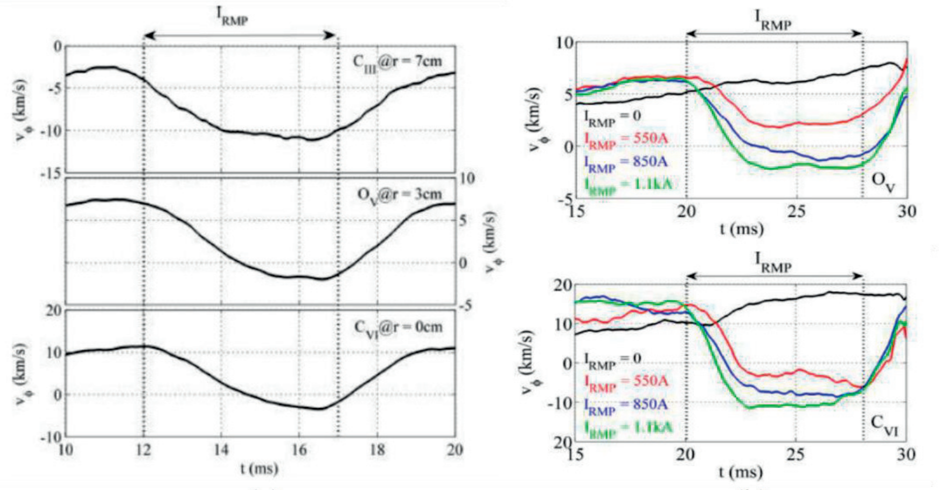

(a) (b)

FIG.13. (a) Effect of a 600 A RMP pulse on the toroidal velocities of CIII, OV and CVI impurities. (b) Modification of the toroidal flow velocities of OV and CVI impurities at several RMP current.

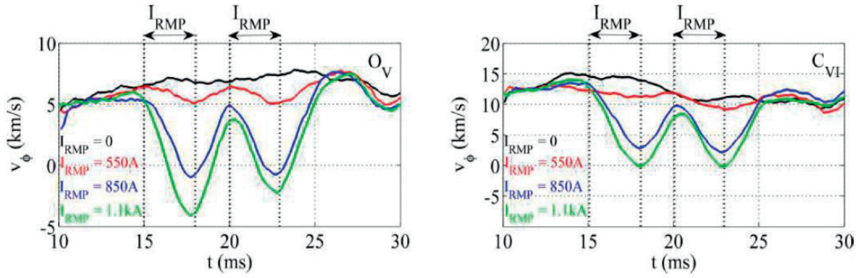

FIG. 14. Modulation of toroidal flow velocities of OV and CVI impurities by the DRMP pulse.

Results of the toroidal flow velocity measurement by IDS show effect of RMP on toroidal flow. It has been confirmed by our result that RMP has capability to control toroidal flow. It was observed that the toroidal flow in STOR-M could be significantly modified by RMP fields. It was observed that RMP not only reduced the amplitude and rotational frequency of magnetic islands, but also modified the toroidal plasma flow. The flow measurements of C_{III}, O_V and C_{VI} impurity lines revealed that the flow direction changed towards the co-current direction during RMP. Also the capability of the continuous modulation of the toroidal flow by applying DRMP has been demonstrated.

3. REPETETIVE COMPACT TORUS INJECTION

A steady state and continuous operation of a tokamak reactor needs a continuous and consistent fuelling method, so the CTI must be operated in a repetitive mode either for fuelling purposes or for control of the plasma toroidal flow and the density profile. In order to fuel a tokamak reactor in a quasi-steady-state fashion, repetitive CTI (RCTI) is required. In the University of Saskatchewan, RCTI was demonstrated using high-power and high-voltage (HV) power supplies. The 8 kW power supply with a current of 600 mA is capable of charging capacitors quickly so that CTs are repetitively formed and accelerated with 3 s intervals (1/3 Hz). To increase the injection rate, a novel charging circuit for the RCTI has been developed recently. In the new design, the power supply slowly charges a storage bank (slow bank) with a large capacity and the slow bank quickly charges the CTI bank through a stack of insulated-gate bipolar transistors (IGBTs). After the fast bank is fully charged, the IGBT stack between banks is turned OFF and the CT formation sequence starts. The circuit with slow bank and IGBT stack is added to all of the CTI banks. The repetition rate of the CTI is increased to 1.7 Hz by these changes. A schematic of the circuit with slow bank and IGBT stacks is illustrated in Figure 15.

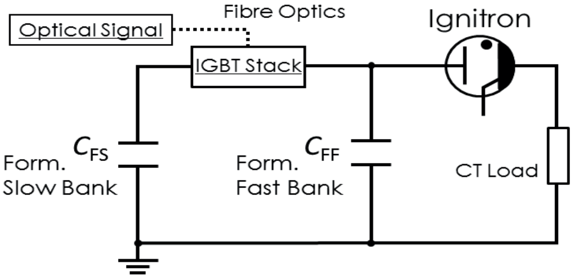

FIG. 15. Basic circuit Diagram for RCT Formation.

In order to increase repetition rate of RCTI, the Krytron switch used previously to trigger ignitrons was replaced with silicon-controlled rectifiers (SCRs). The Krytron is a compact switching device which uses gas breakdown to rapidly conduct high current to trigger ignitrons. The limitation with the Krytron is long recovery time for the switch. It takes about 500 ms for flowing current through the Krytron to stop and goes to OFF mode. It limits the repetition rate of CT formation to 1.7 Hz. Figure 16a shows the ignitron trigger circuit with the Krytron which is replaced later by SCR now (Figure 16b).

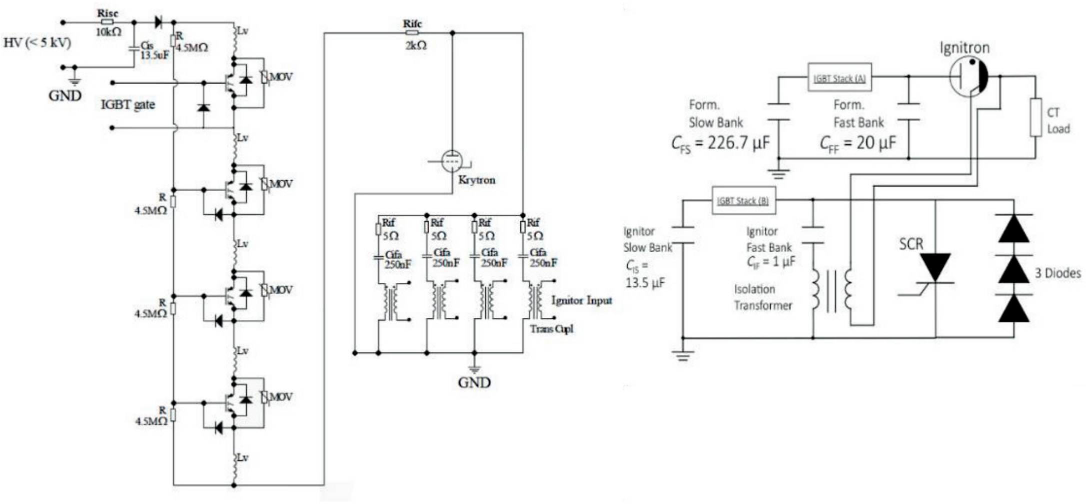

(a) (b)

FIG. 16. (a) Circuit diagram of the Krytron ignitor circuit used to provide high voltage trigger pulses, isolated by transformers, to ignitrons. (b) Simplified circuit diagram for repetitive CT formation. Ignitron with formation fast bank is triggered by ignitor circuit.

The bench test result indicates that the CT is repetitively formed and accelerated with the frequency up to 10 Hz after replacing of the Krytron with SCR in the ignitron trigger circuit. Table 1 shows the parameters of the modified circuit for the RCTI.

TABLE 1. THE LIST OF PARAMETERS FOR THE MODIFIED CIRCUITS USED IN RCT OPERATION

	CT formation CT acceleration	Ignitron trigger Circuit	Bias field	Gas puffing
Fast bank Capacitance	20 µF	1 µF	5 mF	1.29 mF
Slow bank Capacitance	226.7 µF	13.5 µF	108.0 mF	10.0 mF
Charging voltage	-20 kV	5 kV	400 V	1 kV
IGBT type	IXBH32N300	IXBH32N300	CM600HA-24H	CM600HA-24H
Number of IGBTs	10	4	1	1

The circuit diagrams and pictures of the CT formation and acceleration bank are shown in Figs 17 and 18 respectively. A charge and discharge control system has been developed and installed on the CTI to control charging time of the fast banks through slow banks. Also it controls time delay between firing of each of the fast banks to form and accelerate the CT. Optical fibres are used to send control signals to IGBT switches and SCRs.

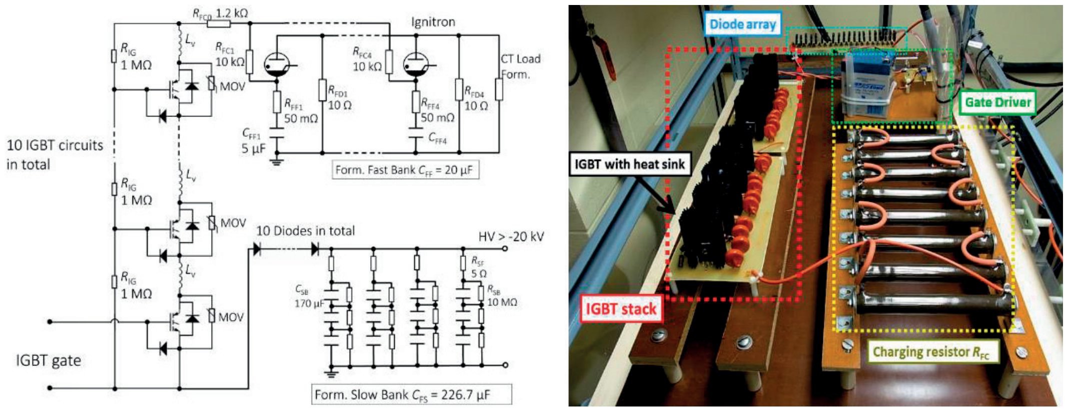

FIG. 17. Circuit diagram of the formation banks. Abbreviations are to show Formation Fast bank (FF), Formation Slow bank (FS), Formation Current limiter (FC), Formation Dummy load (FD), IGBT (IG), Slow bank Fault (SF) and Slow Bank(SB).

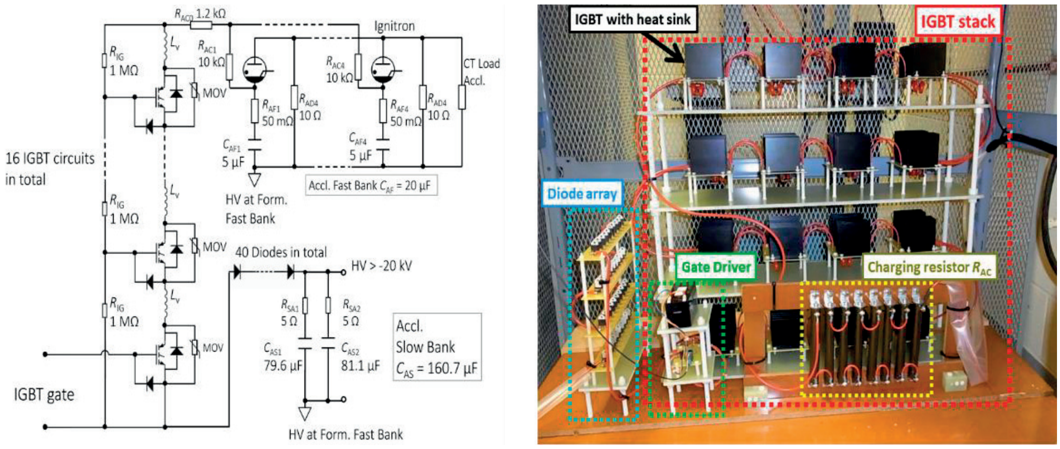

FIG.18. Circuit diagram of the acceleration banks. Abbreviations are to show Acceleration Fast bank (AF), Acceleration Slow bank (AS), Acceleration Current limiter (AC), Acceleration Dummy load (AD), IGBT (IG), and Slow bank fault on Acceleration (SA).

For a bench test of RCTI, all six systems (CT formation, CT acceleration, two ignitors, bias field and gas injection) need to be synchronized. For the test shots presented below, the repetition rate was set to 10 Hz (charging/discharging time and the rest time are 50 ms). The numbers of CT pulses are set to three. The charging voltages at the slow banks are as follows: V_{fs} = -14kV for formation, V_{as} = -12 kV for acceleration, V_{scrs} = 4 kV for ignitor, V_{sols} = 380 V for solenoid and V_{gps} = 900 V for gas valves. Figure 19a shows the voltage measured at each fast bank. The charging time of the fast banks depends to the capacitance and the charging resistor in each charging system. The final voltages of the fast banks are not fixed and drop after each shot as the stored charges of the slow banks decrease. As shown in the top trace in Figure 19a, the fast bank of the formation bank is charged through resistor R_{IG} before starting the charging and discharging sequence. Because of that, the final voltage of the first shot is much higher than the second and third one. The difference between final voltages of the second and third shot is negligible. A voltage regulator system is developed and installed on the RCTI to control the final voltages of the fast banks.

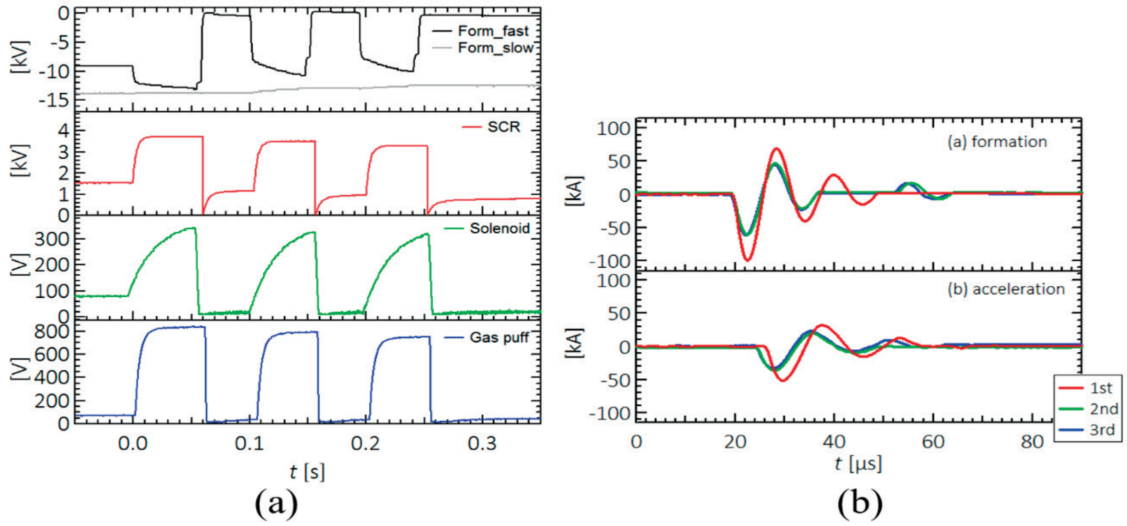

FIG. 19. (a) Waveforms of voltages at each discharge circuit in the bench test of RCTI. (b) Discharge current at electrodes on CT formation and acceleration.

The discharge currents of formation and acceleration electrodes for the first three shots are illustrated in Figure 19b. The discharge currents of the formation and acceleration electrodes oscillate through an equivalent *RLC* circuit. As shown in the circuit diagrams of the formation and acceleration banks, a 10 Ω resistor is in parallel to CT load as a dummy load. If CT is not generated, the discharge current flows through the dummy load. The current drops monotonically through an equivalent *RC* circuit. Therefore, the oscillation of the discharge current is an indication of CT formation.

In this research, RCTI with the repetition frequency of 10 Hz has been developed. The new charging system which contains slow bank and IGBT stacks is added to all of the capacitor banks. The Krytron in the ignitron trigger circuits have been replaced with SCRs. These two changes enhance the repetition frequency of the RCTI from 0.2 Hz to 10 HZ. Multiple CTI in a tokamak discharge is the key for steady-state operation of a practical reactor. With repetition rate higher than 100 Hz, multiple CTI into STOR-M tokamak will be feasible since the discharge duration of the tokamak is 30–40 ms. Therefore, two to three CTs can be injected in the current flat top phase of the STOR-M discharge. Incidentally, the required repetition rate for fuelling ITER is also about 100 Hz.

4. SIGNS OF GEODESIC ACOUSTIC MODE IN STOR-M

4.1. Introduction

Drift wave turbulence has plagued magnetic confinement devices, making up the major plasma transport. This turbulence, however, is self-limiting; the size of turbulence eddies does not grow to sizes comparable to the device. This is due to flows perpendicular to the radial direction whose direction reverses with radial dependence. Such flows are called zonal flows. Zonal flow is a zero-frequency mode with mode numbers $n = 0$ and $m = 0$. Excited by drift wave turbulence, zonal flows tear up the turbulent eddies into smaller sized by the velocity shear, limiting the growth of turbulent [17]. A high-frequency branch of zonal flow is called geodesic acoustic mode (GAM). GAM is supported by plasma compressibility and toroidal geometry [18]. This mode is characterized by:

- Potential oscillation ($n = 0$, $m = 0$)
- Density oscillation ($n = 0$, $m = 1$)

- $\omega_{GAM}{}^2 = \left(\frac{C_s}{R}\right)^2 \left(2 + \frac{1}{q^2}\right)$ (1)

where C_s is the speed of the ion acoustic wave, R the major radius, and q the safety factor. Including the effect of ion temperature, the GAM frequency is corrected as

$$\omega_{GAM}{}^2 = \frac{2}{R^2}\left(\frac{T_e + 7/4T_i}{m_i}\right), \text{ [19]} \qquad (2)$$

Similar to zonal flow, GAM is believed to be excited by drift wave turbulence. GAM is a topic of active research for its relationship with drift wave turbulence as well as other modes present in toroidal plasmas.

4.2. Experimental Set-up

The primary aim of our study was to detect GAM oscillations in plasma potential and density at the edge. Thus, we placed Langmuir probe systems in two locations, top and bottom, of a poloidal plane (Figure 20a) with radial adjustability. The Langmuir probe pins are cylindrical (Figure 20b).

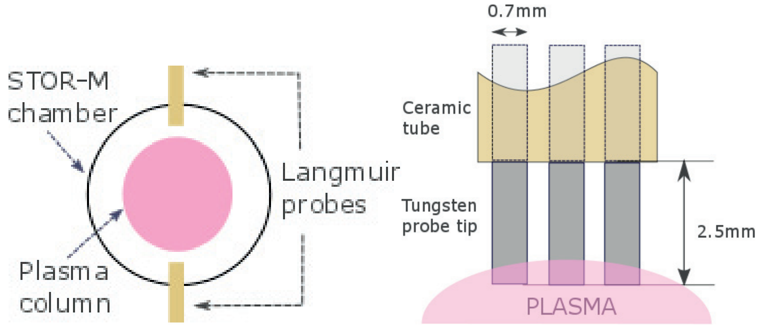

a) *b)*

FIG.20. Langmuir probe systems: a) poloidal cross section with two Langmuir probe systems, top and bottom, with adjustable radial locations, b) dimensions of cylindrical probe tips.

At each location, two measurements were made: floating potential (V_f) and ion saturation current (I_{sat}). The two parameters are related to plasma potential and density as:

- $kT_e \, ln(2m_i/\pi m_e) = 2e\left(V_p - V_f\right)$ (3)
- $n = I_{sat}/\left(eAexp(-{}^{1}\!/_{2})\sqrt{T_e/m_i}\right)$ (4)

Assuming a constant T_e, fluctuations $\widetilde{V_p}$ and $\tilde{n}$ can be approximated by $\widetilde{V_f}$ and $\tilde{I}_{sat}$, respectively.

4.3. Results

The Langmuir probe measurements were taken during a typical ohmic STOR-M discharge. Figure 21 shows the plasma current (I_p), loop voltage (V_L) and the horizontal position of the plasma column (ΔH). For the horizontal position, ΔH = - 10 mm corresponds to the geometrical centre. The spectral analysis of the probe data was carried out for the 6 ms window on the current plateau (from 24 ms to 30 ms).

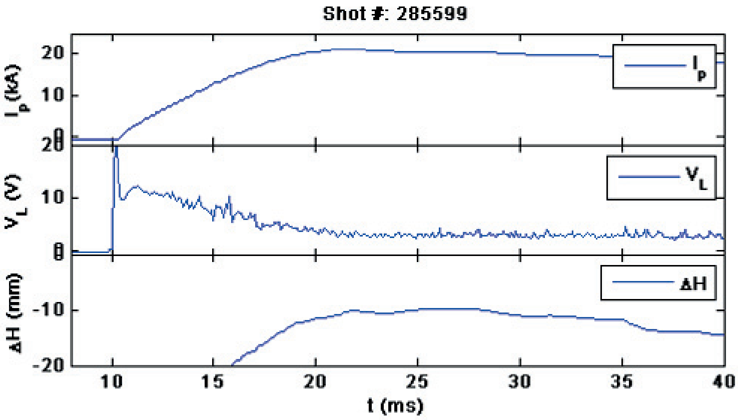

FIG. 21. Typical STOR-M ohmic discharge. A time window indicated in yellow was used for the spectral analysis.

Figure 22 shows the power spectral densities of V_f and I_{sat} signals at each location. For V_f, 14 kHz and 30 kHz were dominant at the top, while 10–14 kHz was dominant at the bottom. This pattern was also observed for I_{sat} signals.

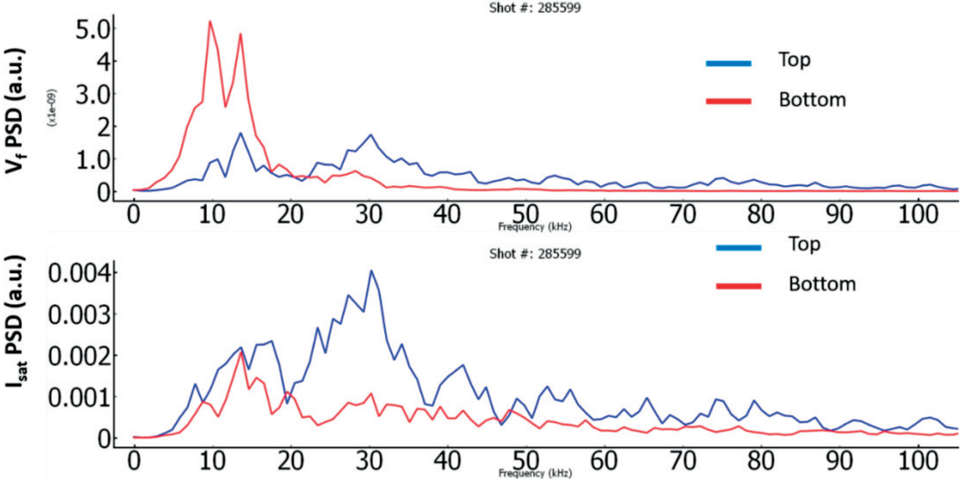

FIG. 22. Power Spectral Density of V_f and I_{sat} Signals.

Figure 23 shows the coherence and phase of the V_f signals at the top and bottom. A peak in coherence (~ 0.6) was observed around 25 – 30 kHz. The corresponding phase was ~ 0.3 π.

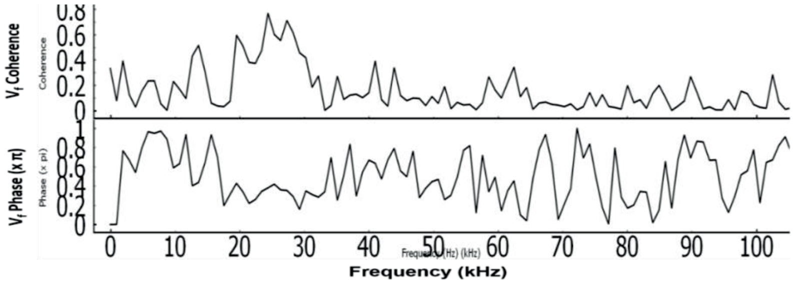

FIG.23. Coherence and Phase of the V_f Signals at Top and Bottom.

Figure 24 shows the coherence and phase of theI_{sat} signals at the top and bottom. A peak in coherence (~ 0.4) was observed around 25 – 30 kHz. The corresponding phase was ~ 0.7 π.

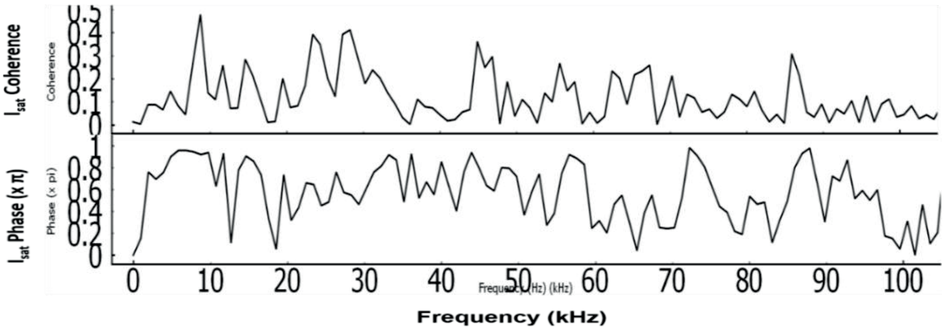

FIG. 24. Coherence and Phase of the I_{sat} Signals at Top and Bottom.

4.4. Conclusion

- In both V_f and I_{sat} signals, 14 kHz and 30 kHz were present.
- It was only the 30 kHz band that was coherent (> 0.4) in both V_f and I_{sat} , suggesting that the potential GAM frequency is 30 kHz.
- At 30 kHz, the phases between top and bottom for V_f and I_{sat} were 0.3 π and 0.7 π, respectively.
- The results suggest that the mode numbers m = 0 for V_f and m = 1 for n are possible around 30 kHz.

4.5. Future Work

- Noise may have contaminated the signals, adding uncertainty in coherence and phase. Noise reduction can provide better signal quality.
- Current study has been carried out on one poloidal plane. More probes at different toroidal locations will help determine toroidal mode number.
- Another probe in the same poloidal plane will help distinguish poloidal modes.

GAM has also been found to couple with magnetic fluctuation. Signals from Mirnov coil can help determine magnetic mode numbers.

ACKNOWLEDGMENT

This work was sponsored by the Natural Sciences and Engineering Research Council of Canada (NSERC), Canada Research Chair (CRC) program and the Sylvia Fedoruk Canadian Center for Nuclear Innovation.

REFERENCES

[1] WARE, A.S., TERRY, P.W., DIAMOND, P.H., CARRERAS, B.A., Transport reduction via shear flow modification of the cross phase, Plasma Phys. Control. Fusion. **38** (1996) 1343–1347.

[2] ERNST, D.R., BELL, M.G., BELL, R.E., BUSH, C.E., CHANG, Z., FREDRICKSON, E. et al., Notched velocity profiles and the radial electric field in high ion temperature plasmas in the Tokamak Fusion Test Reactor notched velocity profiles and the radial electric field in high ion temperature plasmas in the Tokamak Fusion Test Reactor, Phys. Plasmas **5** (1998) 665–681.

[3] BURRELL, K.H., Effects of E × B velocity shear and magnetic shear on turbulence and transport in magnetic confinement devices effects of E x B velocity shear and magnetic shear on turbulence and transport in magnetic confinement devices, Phys. Plasmas **4** (1997) 1499–1518.

[4] TERRY, P.W., Suppression of turbulence and transport by sheared flow, Rev. Mod. Phys. **72** (2000) 109–165.

[5] STRAIT, E.J., TAYLOR, T.S., TURNBULL, A.D., FERRON, J.R., LAO, L.L., RICE, B., SAUTER, O., THOMPSPON, S.J., WRÓBLEWSKI, D., Wall stablization of high beta tokamaks discharges in DIII-D, Phys. Rev. Lett. **74** (1995) 2483–2486.

[6] IDA, K., MIURA, Y., MATSUDA, T., ITOH, K., Evidence for a toroidal-momentum-transport nondifusive term from the JFT-2M tokamaks, Phys. Rev. Lett. **74** (1995) 1990–1993.

[7] ELGRIW, S., LIU, Y., HIROSE, A., XIAO, C., Modification of plasma rotation with resonant magnetic perturbations in the stor-m tokamak, Plasma Phys. Control. Fusion. **58** (2016).

[8] SUZUKI, Y., WATANABE, T., SATO, T., HAYASHI, T., Three dimensional simulation study of spheromak injection into magnetized plasmas, Nucl. Fusion. **40** (2000) 277–288.

[9] XIAO, C., HIROSE, A., Saskatchewan torus-modified (stor-m) tokamak improved confinement induced by tangential injection of compact torus into the Saskatchewan torus-modified, stor-m tokamak, Phys. Plasmas **11** (2004) 4041.

[10] CHIJIN, X., LIU, D., LIVINGSTONE, S., SINGH, A.K., ZHANG, E., HIROSE, A., Tangential and vertical compact torus injection experiments on the stor-m tokamak, Plasma Sci. Technol. **7** (2005) 2701–2704.

[11] XIAO, C., DING, W.X., MCCOLL, D.R., WHITE, D., HIROSE, A., Improved confinement induced by tangential ct injection in stor-m, (n.d.) 1–4.

[12] LIU, D., LIVINGSTONE, S., SINGH, A.K., ZHANG, E., HIROSE, A., Tangential and vertical compact torus injection experiments on the stor-m tokamak, Plasma Sci. Technol. **7** (2005) 2701–2704.

[13] LOEWENHARDT, P.K., BELLAN, P.M., Introduction, characterization of the caltech corn act torus injector, Rev. Sci. Instrum. **66** (1995) 1050–1055.

[14] JANZER, A., HERRMANN, A., KALLENBACH, A., LANG, P.T., LUNT, T., SUTTROP, W. et al., First observation of edge localized modes mitigation with resonant and nonresonant magnetic perturbations in asdex upgrade, Phys. Rev. Lett. **106** (2011).

[15] HENDER, T.C., FITZPATRICK, R., MORRIS, A.W., CAROLAN, P.G., DURST, R.D., EDLINGTON, T., FERREIRA, J., FIELDING, S.J., HAYNES, P.S., HUGILL, J., Effect of resonant magnetic perturbation on COMPASS-C tokamak discharges, Nucl. Fusion. **32** (1992) 2091–2117.

[16] EVANS, T.E., MOYER, R.A., THOMAS, P.R., WATKINS, J.G., OSBORNE, T.H., BOEDO, J.A. et al., Suppression of large edge localized modes in high-confinement DIII-D plasmas with a stochastic magnetic boundary, Phys. Rev. Lett. **92** (2004).

[17] DIAMOND, P.H., ITOH, S.-I., ITOH, K., HAHM, T.S., Zonal flows in plasma: a review, Plasma Phys. Control. Fusion **47** (2005) 35–161.

[18] WINSOR, N., JOHNSON, J.L., DAWSON, J.M., Geodesic acoustic waves in hydromagnetic systems, Phys. Fluids **11** (1968) 2448–2450.

[19] DREVAL, M.B., YAKOVENKO, Y.V., SOROKOVOY, E.L., SLAVNYJ, A.S., PACLINCHENKO, R.O., KULAGA, A.E., et al., Observation of 20 – 400 kHz fluctuations in the U-3M torsatron, Phys. Plasmas (2016).

PLASMA STARTUP BY RF WAVES IN SPHERICAL TOKAMAK

Z. GAO*, Y. TAN*, W. H. WANG*, H. Q. XIE*, Y. Q. LIU*, Y. Z. JIANG*, R. KE*, S. CHAI*, C. H. FENG**, L. WANG**, X. Z. YANG**

* Department of Engineering Physics, Tsinghua University, Beijing 100084, China
** Institute of Physics, Chinese Academic of Science, Beijing 100083, China

Abstract
RF startup is of great importance in present devices and ITER. The same problem was faced by spherical tokamaks, and even more urgent. This report is a summary of research activities on plasma startup by high frequency ECWs/EBWs and low frequency Alfven waves in the SUNIST device in the framework of the Co-ordinated Research Project (CRP) of the International Atomic Energy Agency (IAEA) “Utilization of the Network of Small Magnetic Confinement Fusion Devices for Main Stream Fusion Research”.

1. INTRODUCTION

Non-inductive plasma startup presents a challenge to ITER due to its limited inductive electric field. This problem is also urgent in spherical tokamaks or in stellarators due to the Ohmic powers in these configurations are not enough or undesirable. Since one prefers to employ one system to realize both the processes of plasma startup and the discharge maintaining, RF waves might be a promising technique. In fact, RF startup has been demonstrated in many experiments.

Among different frequency domains of RF, electron cyclotron wave (ECW) startup is most popular since ECW startup is very effective and reliable. [1–5] However, the efficiency of ECW-startup varies in many experimental results. It may be influenced by gas species and pressure, RF power and pulse duration, toroidal equilibrium construction, structure of vacuum vessel, and many other factors. It still needs further and comprehensive investigations in different devices and more theoretical and modeling analysis as well. Since conventional ECR-startup experiences the limitation of plasma density, the ECW-converted Bernstein waves (EBW) is proposed to startup the plasma and then heat the initial plasma or ramp-up the plasma current. In practice, the LFS injected ECW should experience the O-X-B conversion to become the EBW. The window for O-X conversion is narrow and sensitive, therefore it needs precise experimental setup and precise theoretical calculations. It is noted that the mechanism of ECW startup depends on the resonance, therefore, its operation region is limited to specific values of the magnetic field. Comparatively, using RF wave in ion cyclotron range of frequencies (ICRF) can be operated in a relatively wide range of magnetic field for a given frequency. The whole process is not fully understood yet. It may include both the non-resonant mechanism (depending on ionization by RF electric field) and the resonant mechanism. Using RF wave in Alfven frequency ranges (AW) is expected effective to startup the plasma. In this case, non-resonant mechanism may be dominant. In summary, different RF waves can assist the plasma startup depending on resonant and/or nonresonant mechanisms. Such processed as equilibrium construction, wave propagation and plasma diffusion will influence the startup. Further experimental researches should be performed with different conditions in different devices, and, also complete modeling for RF startup remains to be developed.

The SUNIST [5] is a spherical tokamak with major and minor radius of 0.3 m and 0.23 m respectivelly, on-axis magnetic field of 1500 Gauss and typical current of 30~50 kA, which is operated by Tsinghua University, Beijing, China. In the framework of the current Co-ordinated Research Project (CRP) of the International Atomic Energy Agency (IAEA)

“Utilization of the Network of Small Magnetic Confinement Fusion Devices for Main Stream Fusion Research”, some research activities on plasma startup by high frequency ECWs/EBWs and low frequency Alfven waves are performed. Main works includes: (1) to setup the experimental system using the new ECW source with 5GHz, 20ms, 100 KW; to perform the ECW experiment to explore high efficient ECW startup by adjusting the gas pressure, toroidal field, vertical field, their injection time and the insulation between two parts of vacuum vessel of the SUNIST, to improve the modeling of ECW startup based on the experiments; (2) to explore EBW startup by oblique injection of ECW; to preliminarily understand the key elements in EBW startup and ramp-up; to understand the physics based on experimental results as well as theory and modeling efforts; (3) to explore AW startup by using the existed RF sources with high power (with only few frequency points and working modes and a proposed new source with flexible frequency and middle power, respectively; to diagnose the electric and magnetic field formation with RF application; to investigate the wave coupling, propagation and resonance after the formation of toroidal plasma equilibrium. In this report, we will summary the progress on the SUNIST during the fulfilment of the 4-year activity.

2. ECW STARTUP EXPERMENTS, MODELING AND ENGINEERING EFFORTS

2.1 Experimental setup

The experimental setup of ECW startup on SUNIST is shown in Figure 1. The vacuum vessel of SUNIST consists of an inner cylinder and two semi spheres, which are electrically insulated from each other. The central solenoid is left open in order to avoid choking the toroidal plasma current. A microwave with 2.45 GHz, 40 kW, 10 ms is injected from the equatorial plane in the normal direction to the toroidal field with E field polarization parallel to toroidal field. The working gas, $H2$, is puffed into the vessel through a piezo-valve installed on the top of vacuum chamber with the pressure of 10^{-3}~10^{-2} pa. Three pairs of vertical field (B_V) coils are connected in series thus the decay index of B_V is unchangeable. In our experiments, it is fixed to a quite small value (n~ -0.1 at R=50 cm). Main diagnostics in these experiments include one chord of 46 GHz (8 mm) microwave interferometer, 10 kfps fast visible light camera with the visual angle marked by dashed line in Figure 1b, and a photodiode to pick up the overall light emission. The positions of electron cyclotron resonance (ECR) layers are varied in the dashed region as shown in Figure 1b.

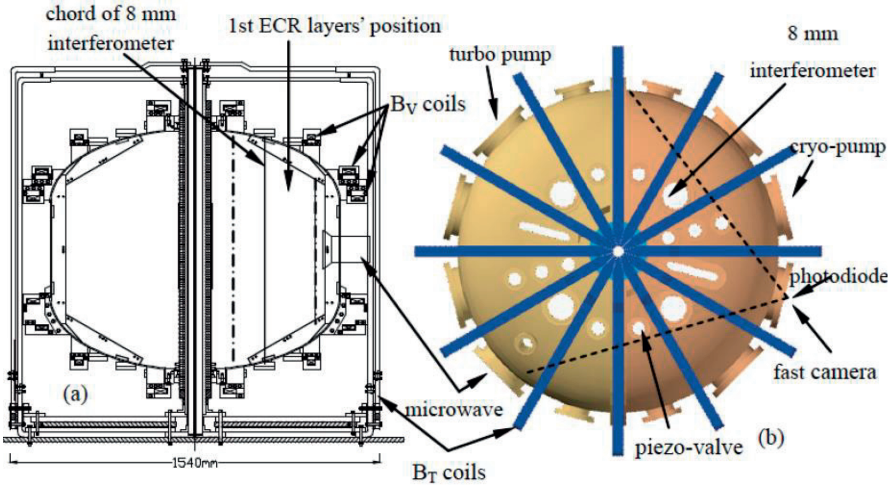

a) b)

FIG. 1. The experimental setup for ECW startup experiments on SUNIST: (a) Side view illustrating the radial positions of electron cyclotron resonance layers and the interferometer chord; (b) Top view showing the toroidal positions of main equipments and diagnostics.

2.2. ECW startup experimental results with 2.45 GHz/10 ms source and modeling

In the SUNIST spherical tokamak, ECW plasma startup with a 2.45 GHz/40 kW/10 ms microwave source was analysed deeply. A plasma current of about 2 kA was obtained with a steadily applied vertical field of 12 Gauss, which is shown in Figure 2.

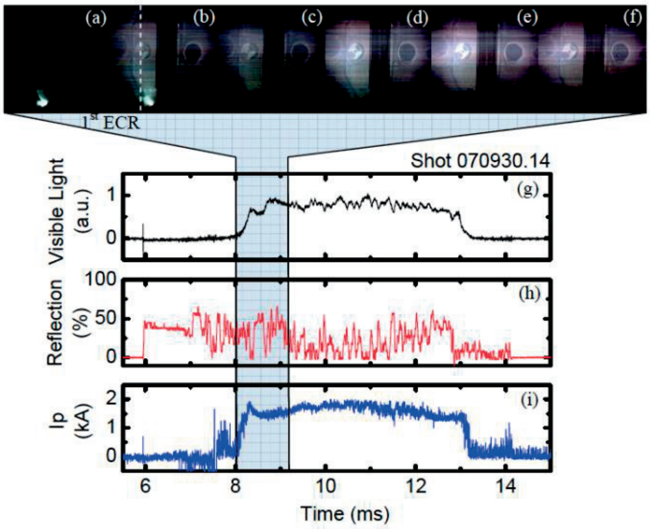

FIG. 2. Pictures of visible light (a) ~ (f) and dependence of overall visible light emission (g), microwave reflection (h) and plasma current (i) on time in a typical discharge with filling pressure PH2 ~ 10^{-3} Pa, vertical field BV ~ 12 Gauss and microwave power ~ 40 kW. The pictures are taken with intervals of 0.2 ms.

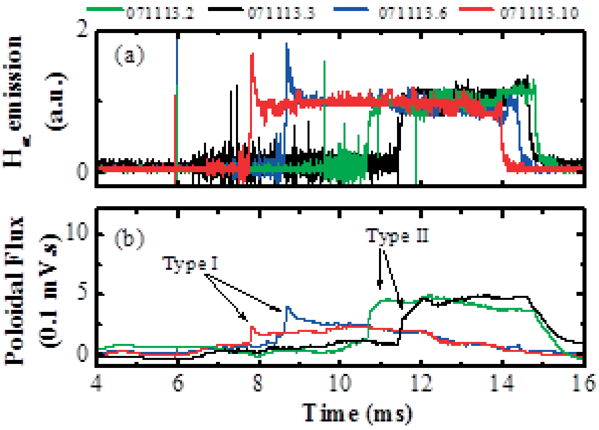

FIG. 3. Two types of ECW startup discharges.

This stable current of 2 kA was obtained in rather low filling gas pressure (~10^{-3} Pa). The discharges with relatively higher filling pressure (~5 10^{-3} Pa) were typically unstable. We may categorize them two types of discharges, with quite different transient characteristics, shown in Figure 3. The unstable (in other words, oscillating) discharge often had such a process: under high filling pressure, the ionization of microwave is effective; then the plasma density rises up rapidly and easily exceeds the cutoff density (attenuated microwave can still reach the ECR layer since the wavelength is more than half of the minor radius in SUNIST); over dense plasmas drift outward and block the antenna; microwave reflection increases; microwave can not reach the ECR layer anymore, then the plasma density drops; then another cycle starts.

The transient processes of discharges were experimentally investigated by scanning the radial position of the ECR layer, the vertical magnetic field and the microwave power, shown in Figure 4. Time domain analysis of microwave reflections and H_α emissions revealed a process dominated by the combination of ionization, loss along the open field lines and the gradient B drift.

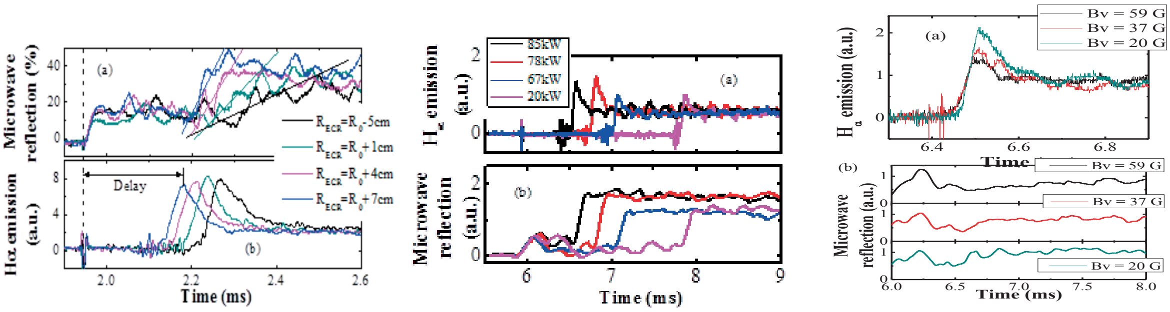

FIG. 4. Time revolution of microwave reflections and H_α emissions by scanning the radial position of the ECR layer (left), the microwave power (middle) and the vertical magnetic field (right).

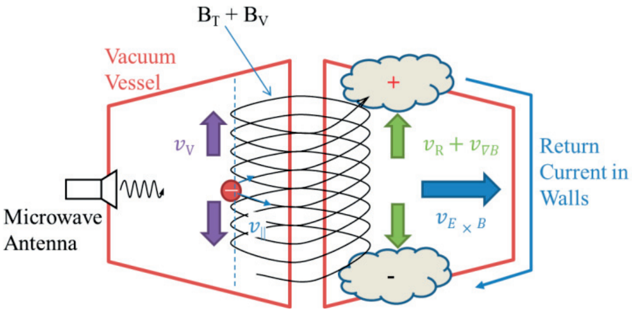

FIG. 5. A simulating model of ECW startup.

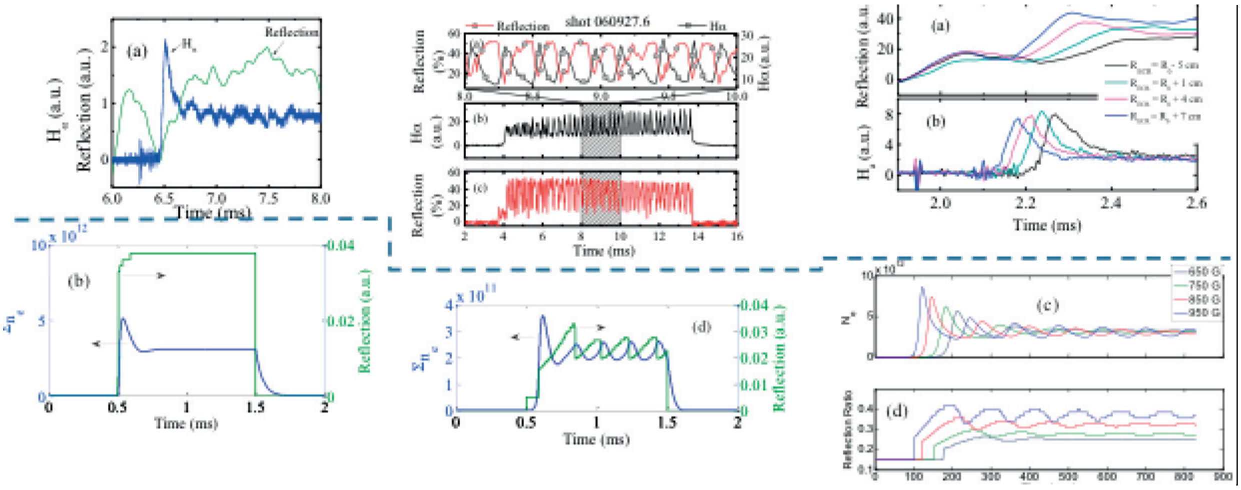

FIG. 6. Comparison between the modelling results (bottom) and experimental results (up) for one spike discharge (left), oscillating discharge (middle) and the case of scanning toroidal fields.

The process was modelled as well. The model assumes the microwave optical launch and receive, but includes such main process as ionization by microwaves, motion of particles and reflection of microwaves with the coefficients estimated from experiments. A schetch drawing of the model is given in Figure 5. The simulation results of this model qualitatively agreed with experimental observations and support the physical images discussed above, which is shown in Figure 6.

2.3. Engineering efforts for building a new 5GHz/20ms source

It is noted that, although the plasma current startup has been already the pressure driven current, which can be identified the formation of close flux surface and the proportional property of current inversely proportional to the vertical field, the current cannot ramped up, that is, continued with the normal high-density discharge. Also, no mode conversion to EBW was observed. To increase the startup plasma density, a microwave source with higher frequency is planned. Moreover, a high toroidal field will benefit the particle confinement and then the startup efficiency (see Figure 7).

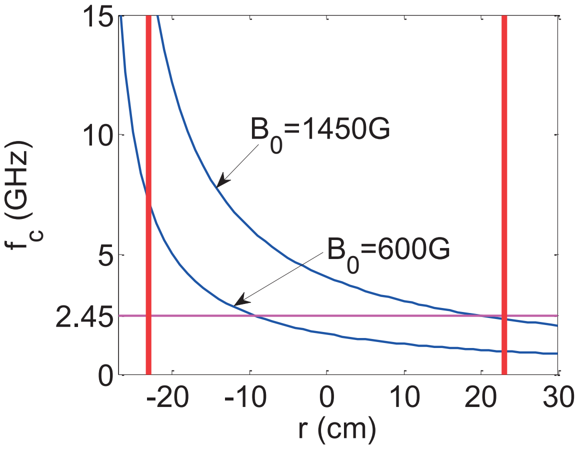

FIG. 7. The range of resonant position in SUNIST.

A new microwave source (5 GHz/200 kW/50 ms) is being tested. The microwave source mainly consists of a klystron, a high voltage power supply and an adjustable horn antenna. The klystron is made by Institute of Electronics, Chinese Academy of Sciences. This klystron has been tested under full power but short pulse (200 kW/1 ms) in the factory. A PSM high voltage (42 kV/20 A/100 ms) power supply is being tested now. The microwave will be injected into the vacuum vessel from a horn antenna, which is being manufactured by a local company. The launching angle of the antenna is adjustable.

FIG. 8. The klystron (left) and 20 modules of the PSM power supply (right) under test.

3. THEORETICAL RESEARCH ON ECW/EBW MODE CONVERSION

The mode conversion from ECW to EBW has been studied theoretically although the new ECR source is not ready. Firstly, a one dimensional ordinary-extraordinary mode conversion process in the electron cyclotron frequency range is investigated analytically and numerically. An inhomogeneous plane slab model of the plasma with density gradient, magnetic field gradient and magnetic shear is considered. A formula for the conversion coefficient is derived analytically as follows,

$$T=\exp\left[-\pi k_0 L_n\sqrt{\frac{Y}{2}}\,\frac{2\left(1+Y\right)\left(n_z-n_{zc}-rn_yn_{zc}^2/2\right)^2+n_y^2\left(1-bn_{zc}^2-r^2Yn_{zc}^2/2\right)}{\left(1-bn_{zc}^2-r^2Yn_{zc}^2/2\right)^{\frac{3}{2}}}\right] \tag{1}$$

where the dimensionless parameters are defined as follows, $b=L_n/L_B$, $r=L_n/L_\theta$, $Y=\omega_{c0}/\omega$, $n_{zc}=\sqrt{Y/(1+Y)}$. Using the following parameters, $k_0L_n=40\pi$, $k_0L_B=200\pi$, $k_0L_\theta=200\pi$, $Y=0.9$, $n_y=0$, the effects of density gradient, magnetic field gradient and magnetic shear are shown in Figure 9. It is noted that, for steep profiles, the full-wave calculation is needed rather than the analytical formula. Also, a comparison with previous theories was also performed, which is shown in Figure 10. It is noted that sometimes too much/unreasonable assumptions were used in preview literatures [6–10] and then induced large gap between from the result of full wave calculation.

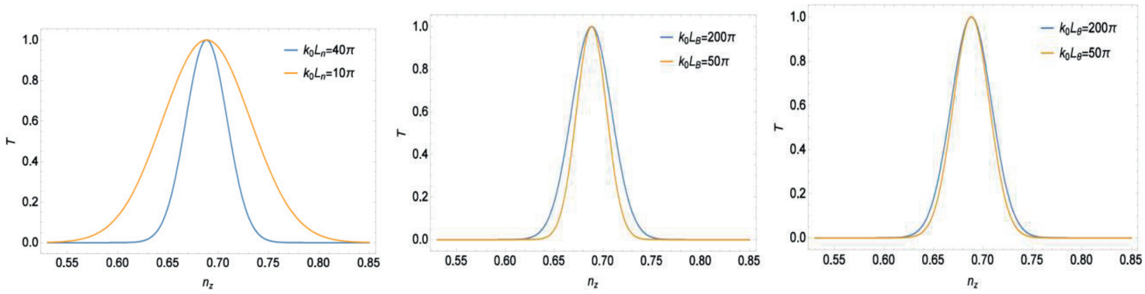

FIG. 9. The O-X conversion efficiency for different density gradient, magnetic field gradient and magnetic shear.

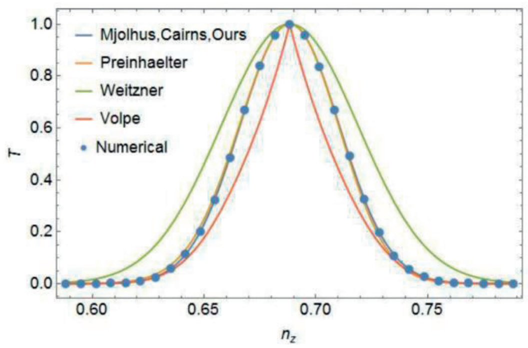

FIG. 10. Comparison among the conversion efficiency from the full-wave calculation and previous theories.

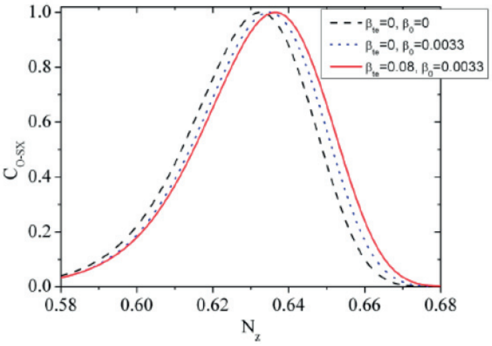

FIG. 11. The change of optimal incident angle due to electron temperature and current.

Secondly, effects of electron flow and finite temperature on the O-X-B mode conversion are investigated [12–14]. For the first step (O-SX), the modified optimal parallel refraction index N_{zc} has been obtained analytically. Finite electron temperature shifts the O-SX conversion layer towards lower plasma density region and therefore the value of N_{zc} increases; while the effect of electron flow depends on its direction. When the electron flow is along the parallel wave vector, the effects of finite temperature and electron flow accumulate and then a more oblique incidence angle is required for efficient O-SX conversion, which is shown in Figure 11. If this effect is not considered, the degeneration of O-X conversion efficiency will be about 10%. However, the full width at half maximum of the conversion window is hardly influenced. On the second step (SX-B), the conversion coefficient essentially depends on the width of evanescent layer, therefore. The conversion efficiency is not 100% as expected. the lost power is carried not only by the tunneled FX-mode on the lower density side, but also by the reflected SX-mode (though on a small scale) and the reflected-converted O-mode (for large Nz) on the incident side. Flow effect influences the efficiency by varying the width and the location of the evanescent layer.

4. ALFVEN WAVE EXPERIMENTS AND ENGINEERING EFFORTS

4.1. Experimental setup

The experimental setup of Alfven wave on SUNIST is shown in Figure 12. An antenna system was designed and installed, which consists of four modules in toroidal direction and two antenna straps in poloidal direction for each module. [15]. the first RF generator was referenced to the design for the TCABR by Ruchko [16]. A four phase oscillator is designed, where each can deliver a 90 degree phase shift from its neighboring module and this phase shift between outputs does not depend on the variation of the antenna impedance. Therefore, the RF generator can deliver two possible phase shift, 90 degree or 180 degree, to nearby straps in either toroidal or poloidal direction. For experiments at the SUNIST, a RF generator with the power of 4x100kW and the working frequency of 0.4~1MHz has been manufactured.

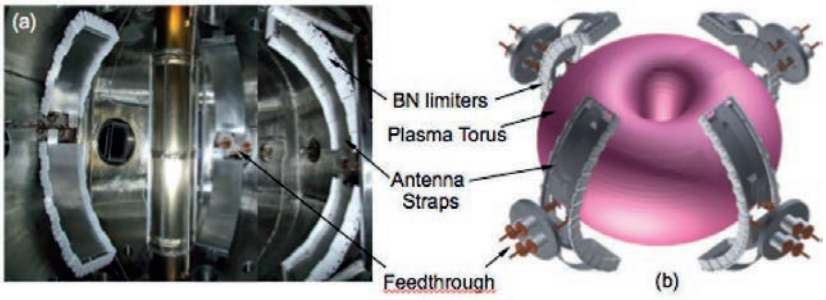

FIG. 12. Alfven wave antenna system on the SUNIST.

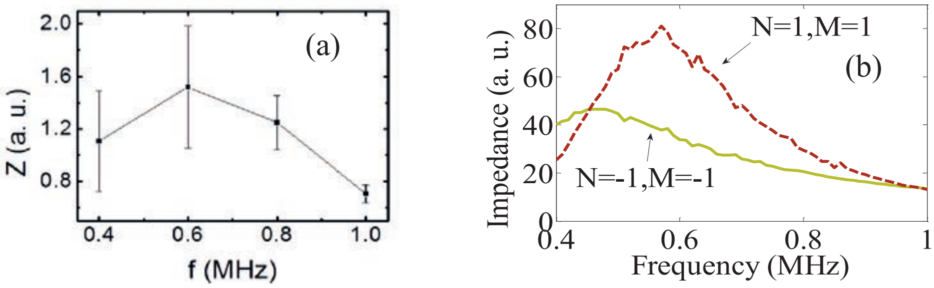

FIG. 13. The experimentally measured p phasing antenna impedance as a function of frequency (left) and the 1-d MHD calculated impedance spectrum (right).

4.2. Preliminary Experimental Results with two antenna straps without limiters

In the discharge before 2013, since four phases of the output cannot be stably provided from the RF source, only two antenna legs were used and, also no antenna limiter or shielding box was installed. Preliminary experiment was performed. When the RF was injected, the Fe and C lines were intensified, and the antenna impedance changed clearly. The measured impedance spectrum has similar trends with 1-D MHD calculation (Figure 13).

Possibly due to the inflexibility of present RF source and also the absence of antenna shielding, no obvious effect was find in typical discharges, but it was showed the trend to enhance the runaway discharge at low density. The physics needs to be explored.

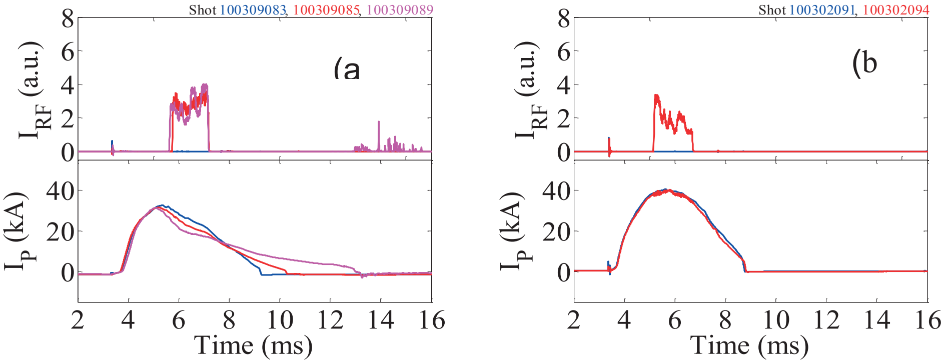

FIG. 14. Discharge at relatively low electron density (left: $n_e < 0.8\times10^{19}$ m^{-3}) and at relatively high electron density (right: $n_e < 0.8\times10^{19}$ m^{-3}).

4.3. Further experiments after some engineering improvements

The antenna configuration for AW experiments has been optimized (Figure 15). Since the RF generator has only two out phase outputs, previously only two of four antennas were utilized. Recently, wwo nearby antennas are now connected in series. Because the frequency of AW in SUNIST is rather low (0.4 ~ 1 MHz), the corresponding wavelength is quite long (~ 300 m). The phase shift between two antennas connected by one meter long cables is less than 1 degree. Therefore, the two antennas can be used as in phase or out phase depends on the connection. This configuration enables a higher efficiency in power delivering and also a more pure wave spectrum.

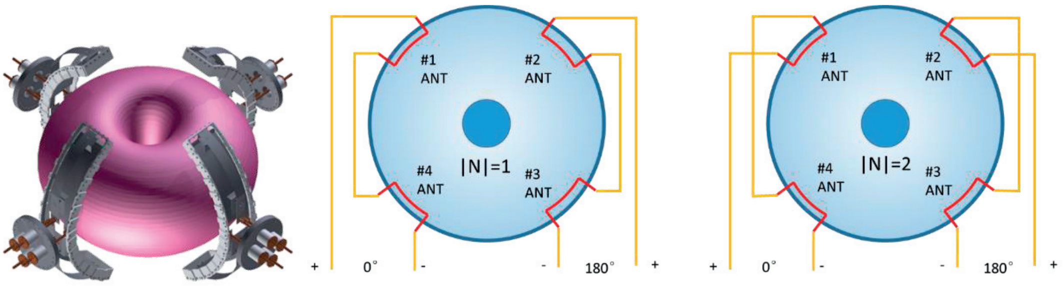

FIG. 15. The antennas used for AW experiments (left) and the optimized configuration for |N|=1 modes (center) and |N|=2 modes (right).

The character of optimized antennas has been investigated. The impedance of antennas has been evaluated. During an ohmic plasma discharge, it was found that the impedance of the antenna is smaller than the vacuum impedance. As long as the plasma column shrank inward, the impedance increased. This prompts a short circuit of two nearby antennas by plasmas during discharge. A shielding system is required to avoid short circuits.

As we know, side limiters made by boron-nitride plates have been proven to be effective in Phaedrus-T [17], limiters made by boron nitride plates (loan from PPPL) have been assembled and two limiters have been installed now. With the limiters, the discharge becomes stable, as well as the measured antenna current and velotages. Figure 16 shows the coupling impedance at $I_P \sim 50$ kA, $n_eL \sim 10^{19}$ m^{-2} with antenna limiters. It shows that the dependence of the impedance of antennas with BN limiters on toroidal field is much weaker than those without BN limiters. This may suggestsan over protection by the BN limiters. A compromise between the protection and the coupling should be found.

A new four phase RF generator has been installed on SUNIST with 0.56 ~ 1.6 MHz / 4 *25 kW. The output phase of this source can be arbitrary adjusted. However, till now, no significant observation observed. Also, a low power frequency-sweeping source was employed, but no resonant phenomena were observed.

The idea of AW startup by using the electric field in large spatial scale is also suggested. Since the mechanism of the generation of plasmas in AW startup is quite different from ECW startup, AW startup may have totally different phenomena and physical properties. Further experiments with limiters will be started within two months. Plasma startup by low frequency waves has been tried using RF waves up to 30 kW/500 kHz. But no breakdown happens. The experiments are ongoing.

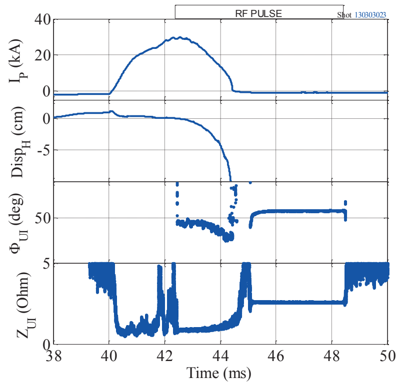

FIG. 16. The impedance of optimized antenna configuration during a shrinking ohmic discharge.

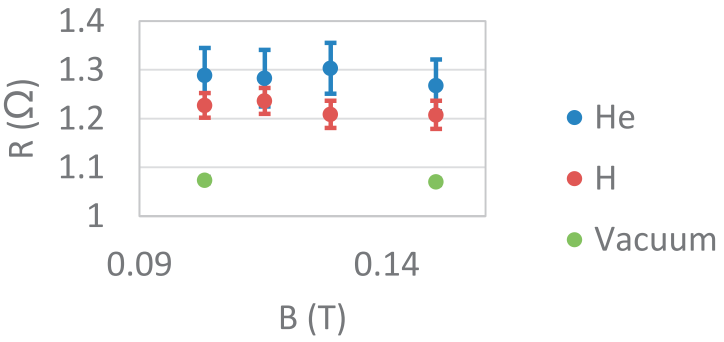

FIG. 17. The experimentally measured p phasing antenna impedance with BN limiters as a function of toroidal field. The frequency is fixed at 0.8 MHz.

5. OTHER RELATED RESEARCH TOPICS IN THE SUNIST AND GRADUATE STUDENT TRAINNING

In the SUNIST, other related research topics are performed, including the experimental studies of MHDs during current ramp-up and step-down, eddy current identification and its effect on equilibriums and MHD, Interaction of turbulence and MHDs, as well as the theoretical studied on parametric decay instability during RF injection, plasma rotation due to RF . During these four years, seven graduate students have obtained their Ph.D. degree, and there are other few students were on the road. Most of them are involved the researcher realted with the RF physics in spherical tokamaks.

6. SUMMARY

The SUNIST group has performed some related research activities on RF startup, including the ECW stratup experiments and modelling, Alfven wave experiments and related theoretical studies. Results are presented in this report, but more works on hardware, experiments, physical understanding, theory and modelling are needed by the world wide efforts.

ACKNOWLEDGEMENT

This research has been supported in the framework of in the framework of the Co-ordinated Research Project (CRP) of the International Atomic Energy Agency (IAEA) “Utilization of the Network of Small Magnetic Confinement Fusion Devices for Main Stream Fusion Research”, ad mostly by National Natural Science Foundation of China under Grant Nos. 11325524, and 11261140327; the Ministry of Science and Technology of China under Contract Nos. 2013GB112001 and 2013GB107001.

REFERENCES

[1] FOREST, C.B., et al., Phys. Rev. Lett. **68** (1992) 3559.
[2] EJIRI, A., et al., Nucl. Fusion **46** (2006) 709.
[3] TAKASE, Y., et al., Nucl. Fusion **41** (2001) 1543.
[4] MAEKAWA, T., et al., Plasma Sci. Technol. **8** (2006) 95.
[5] HE, Y., et al., Plasma Sci. Technol., **8** (2006) 84.
[6] PREINHAELTER, J. and KOPECKY, V., J. Plasma Phys. **10** (1973) 1.
[7] PREINHAELTER, J., Czech. J. Phys. B **25** (1975) 39

[8] WEITZNER, H. and BATCHELOR, D. B., Phys. Fluids **22** (1979).
[9] MJØLHUS, E., J. Plasma Phys. **31** (1984) 7.
[10] CAIRNS, R. A. and LASHMORE-DAVIES, C. N., Phys. Plasmas **7** (2000).
[11] VOLPE, F., Phys. Lett. A **374** (2010) 1737.
[12] JIA, G. Z, and GAO, Z., One dimensional full wave analysis of slow-to-fast mode conversion in lower hybrid frequencies, Phys. Plasmas **21** (2014).
[13] JIA, G. Z, GAO, Z., and ZHAO, A., Effects of electron temperature and electron flow on O-X conversion, Phys. Plasmas **20** (2013).
[14] JIA, G. Z., Ph. D. Dissertation, University of Chinese Academics of Science (2013)
[15] TAN, Y., GAO, Z., and HE, Y. X., Fusion Eng. Design **84** (2009) 2064
[16] RUCHKO, L.F., et al., Fusion Eng. Des. **43** (1998) 15.
[17] SORENSEN, J., et al., Nucl. Fusion, **36** (1996) 173.

EDGE PLASMA STUDIES ON THE COMPASS TOKAMAK

J. STOCKEL*, J ADAMEK*, P BILKOVA*, R DEJARNAC*, M. DIMITROVA*, J GUNN**, J HAVLÍČEK*, J HORÁČEK*, M KOMM*, K. KOVARIK*, T MARKOVIC*, A MELNIKOV++, J LOUREIRO+++, R PANEK*, M PETERKA*, TSV POPOV+, J. SEIDL*, C SILVA+++, M SPOLAORE***

* Institute of Plasma Physics, AS CR v.v.i., Prague, Czech Republic
**CEA, IRFM, F-13108 Saint Paul Lez Durance, France.
***Consorzio RFX Padova, Italy
\+ Sofia University, Bulgaria
\++ National Research Centre ‘Kurchatov Institute’, Moscow, Russia
\+++Instituto de Plasmas e Fusão Nuclear, Instituto Superior Técnico, Universidade de Lisboa, Portugal

Abstract
The proposed project is focused on developments and exploitation of electric and magnetic probes in the COMPASS tokamak. The main aim is better understanding of phenomena, which take place at the edge of tokamak plasmas, such as turbulent transport in the scrape of layer, features in the pedestal region, edge localized modes e.t.c. Probe measurements are compared with others non-invasive diagnostics available on the COMPASS tokamak. The research is performed in a broad international collaboration, which is either already established or newly established during execution of this project.

1. INTRODUCTION

Our investigations were performed in the framework of the Co-ordinated Research Project (CRP) of the International Atomic Energy Agency (IAEA) “Utilization of the Network of Small Magnetic Confinement Fusion Devices for Mainstream Fusion Research” during the period 2012–2015. The main goals of the project are detail studies of the edge plasma on the COMPASS tokamak under various discharge regimes. Several advance electric and magnetic probes are developed and exploited for measurement at the plasma edge with a high spatial and temporal resolution. Main achievements were published in refereed journals and presented at international conferences. This report summarizes main experimental results achieved in the frame in the CRP project.

2. EQUIPMENT AND DIAGNOSTIC TOOLS

2.1. The COMPASS tokamak

Figure 1 shows current view of the COMPASS tokamak installed in IPP Prague in the years 2006-2008 [1].

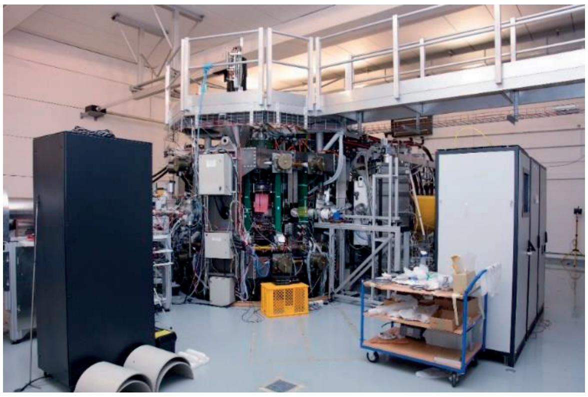

FIG. 1. Picture of the COMPASS tokamak.

Full scientific exploitation has begun in 2012, when the H mode regime was achieved. The device is characterized in the Table 1.

TABLE 1. MAIN PARAMETERS OF THE COMPASS TOKAMAK

Major radius	0.56 m
Minor radius	0.2 m
Toroidal Magnetic field	1.15 T
Working gas	Deuterium, Hydrogen
Elongation	1.8
Triangularity	0.4
Discharge duration	< 0.5 sec

The system of poloidal field coils and corresponding power supplies allows operating COMPASS with several plasma shapes such as circle, ellipse and divertor D-shape with different triangularity.

Additional plasma heating is performed by two Neutral Beam Injectors (NBI) which deliver beams of Deuterium or Hydrogen atoms to plasma. The energy of beam is 40 keV and the beam power at the output of NBI is up to 320 kW. The neutral beams are injected tangentially to the vacuum vessel. All experiments are performed with co-injection, i.e. neutral beams are oriented in the same direction as the plasma current. In principle, balance injection is also possible by moving one NBI toroidally by 180°.

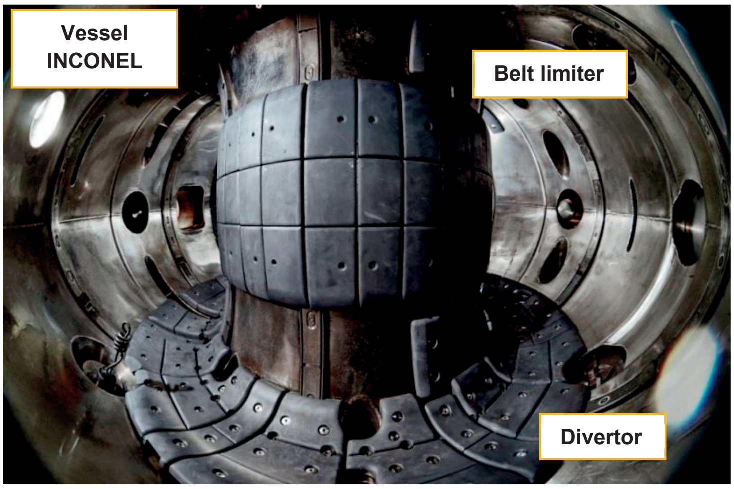

FIG. 2. Picture of the vessel. The divertor and belt limiter, made of graphite tiles, are cooled inertially between the discharges. There are also protecting limiters at the low field side of the vessel, protruding by 18 mm from the vessel wall (not seen in the picture). The vessel is equipped by 64 ports, used mostly for plasma diagnostics (1 port for vacuum pumping, 3 ports for NBIs). Glow discharge cleaning is used in between every discharge.

The typical poloidal cross section of the plasma column is of D shape, with the elongation 1.8 and triangularity ~0.4. In this magnetic configuration, the typical central electron temperature is 0.8 – 1 keV, the central ion temperature is 0.3–0.4 keV, and the central electron density up to 1 10^{20} m^{-3}. For plasma current > 0.25 MA, and the line average densities n > 0.4 10^{20} m^{-3}, the transition to H mode occurs. Two types of H-modes are achieved:

- Ohmic H-mode
- NBI assisted H-mode (available power approx. 3 x P_{LH}).

The H mode is characterized by three types of regimes:

- ELM-free H-mode
- Type-III ELMs (f = 300 – 1000 Hz)
- Type-I ELMs (f = 80 – 200 Hz)

The global energy confinement time, typically t_E ~ 10 ms in the L mode, increases by a factor of 2 in the H mode phase of the discharges. An example of discharge evolution is shown in Figure 3.

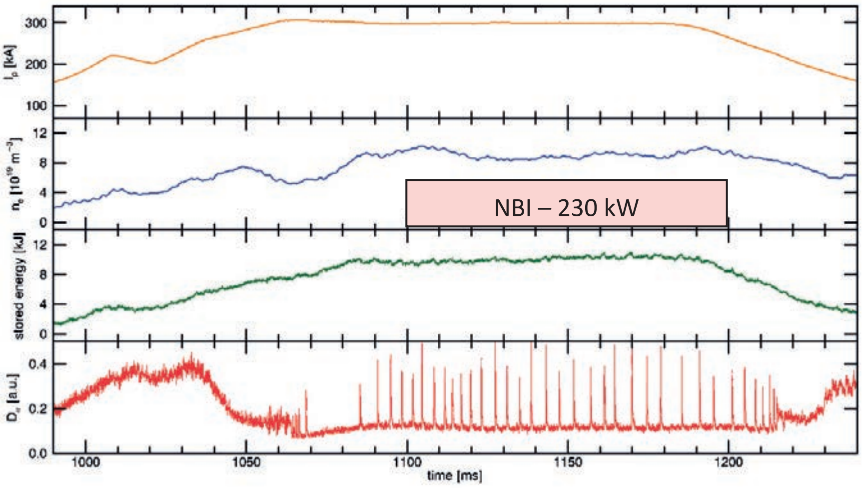

FIG. 3. Evolution of the discharge # 9339 – Ohmic plasma with transition to H mode at t = 1067 ms. From top to bottom – plasma current, line-average density, stored energy and D_α signal. NBI heating is pulse switched on at t = 1100 ms.

It is seen in the figure that the LH transition is followed by a short ELM-free period for ~ 15 ms, and subsequent "train" of ELMs. Note that the ELMy phase of the discharge is quasistationary, as seen from the evolution of the plasma density and the stored energy for more than 100 ms.

2.2. Plasma diagnostics

Scientific programme of the COMPASS tokamak is focused to study physics of the plasma boundary. Therefore, the plasma diagnostics focused on the edge, SOL and divertor plasmas. In addition, COMPASS is equipped with a set of following tools described in detail in Ref. [2]:

1. Magnetic diagnostics (400 coils)
2. Microwave diagnostics (2-mm interferometer, microwave reflectometer (K & K_α bands) ECE / EBW radiometer
3. Spectroscopic diagnostics HR Thomson scattering, fast VIS cameras, AXUV-based fast bolometers and SXR detectors, IR cameras, photomultipliers (VIS, D_α, CIII + continuum for Z_{eff})
4. Beam & particle diagnostics neutron scintillation detector, diagnostics using Li-beam (BES, ABP) Neutral Particle Analyzers detection of fusion products

Edge plasma plays a decisive role in global plasma confinement in tokamaks. It is evident that understanding of underlying physics in the edge plasma requires simultaneous measurements of plasma parameters such as the plasma density, temperatures, potential with a good spatial and temporal resolution (turbulence, ..), and plasma flows in poloidal (and toroidal) direction.

Practical solution used almost in all tokamaks is exploitation of electric (Langmuir) probes, which are almost ideal tool to diagnose the edge plasma with sufficient spatial (up to ~1-2 mm) and temporal resolution (< 1 ms). Magnetic probes should sometime accompany electric probes to study electromagnetic features (turbulence, quasi-coherent modes, etc.).

It has to be noted that electric probes always perturb plasma, therefore non perturbing diagnostics also exploited in tokamaks, and eventually used for benchmarking of probe results such as fast cameras to visualize the density fluctuations , the beam emission spectroscopy, the microwave reflectometry, the gas puff imaging, the edge Thomson scattering and others. Some of them provide information in 2D, however usually just for a selected plasma parameter.

Here, we describe the complex of electric (and selected magnetic) probes which is operational on the COMPASS tokamak in more detail. Localization of electric probes in the poloidal cross section of the COMPASS tokamak is schematically depicted in Figure 4.

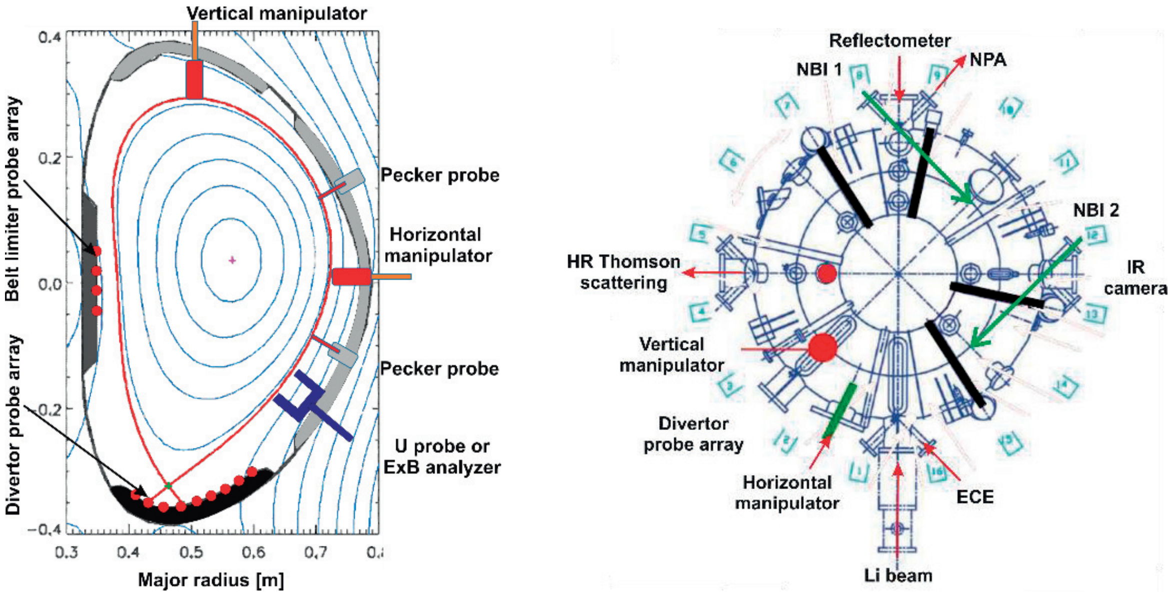

FIG. 4. Left - Location of various electric probes in the poloidal cross section of COMPASS. The magnetic surfaces are derived by EFIT reconstruction. The separatrix is marked by the red line. Right – View of the COMPASS vessel from the top, showing toroidal distribution of probes as well as selected diagnostics used for benchmarking probe data. Black lines crossing the vessel are four poloidal arrays of magnetic probes.

Several probe systems are fixed (probe arrays embedded in divertor/limiter tiles, and the U probe). Remaining probe heads are fixed on reciprocating manipulators. There are two kinds of reciprocating manipulators differing in the drive system.

- Pneumatic drive (just one or two reciprocations during the discharge only) are used for horizontal and vertical manipulators.
- Electromagnetic drive is used for the pecker probes.

3. MAIN EXPERIMENTAL RESULTS

3.1. Edge plasma diagnostics

3.1.1. *Probe heads installed on reciprocating manipulators*

Special measures have to be taken, if the probe head is used to measure plasma parameters in proximity or even inside the separatrix. As already mentioned, the probe head must stay in plasma as short as possible, i.e. it must be fixed to a reciprocating manipulator to stay in plasma for a short time (<150 ms). Furthermore, the probe head must be sufficiently robust to survive high heat loads. Figure 5 presents three examples of the probe heads used on COMPASS.

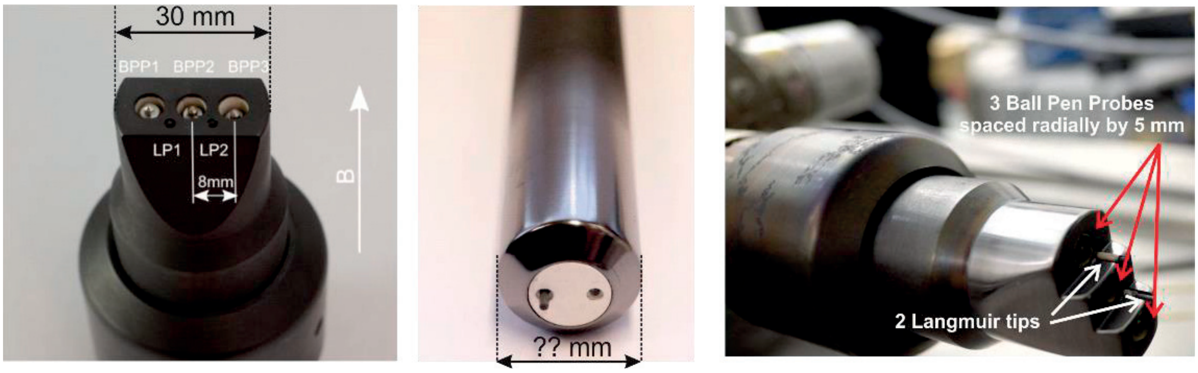

FIG. 5. Three examples of the probe heads used on reciprocating manipulators. Left: The probe head at the horizontal manipulator equipped by thee Ball Pen Probes and two Langmuir tips. Middle: probe head of the vertical manipulator with one Ball Pen Probe and a single Langmuir tip (15 mm). Left: The rake of three Ball Pen Probes and two Langmuir tips spaced radially by 5 mm.

It is seen that all probe heads contain the Ball Pen Probe (BPP), which was originally invented on the CASTOR tokamak [3], and it is now widely used on to measure directly the plasma potential U_{pl} in magnetized plasmas. This novel concept is based on different Larmor radii of electrons and ions. In this case, the hidden floating electrode of BPP collects almost the same ion and electron currents, and consequently, the dependence on the electron temperature in the expression for the floating potential V_{fl} vanishes. It has to be emphasized that three essential conditions have to be fulfilled to assure proper performance of BPP.

- The diameter of the cylinder should be in the range of the ion Larmor radius
- The collector has to be hidden in an insulating cylinder (usually made of Boron Nitride).
- The measuring circuit must obey to a high impedance (~ 4 MΩ), if fast measurements of the plasma potential are required.

Although the physics of BPP is not yet fully understood, its reasonable performance was benchmarked by comparative measurements with the emissive probe [4], and with determination of the plasma potential by using the First Derivative Probe Technique (FDPT) from the IV characteristics of the Langmuir probe [5].
Figure 6 shows a comparison of the radial distribution of the plasma potential measured by BPP and evaluated by FDPT from Langmuir Probe.

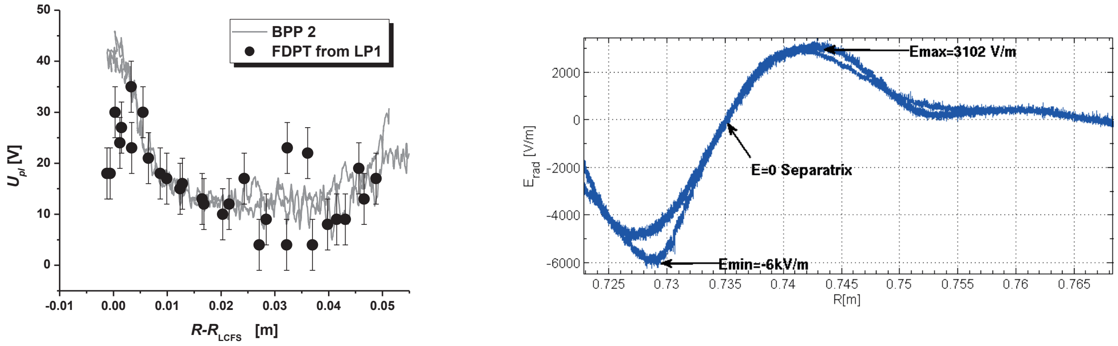

FIG.6. Left - Comparison of the plasma potential measured by BPP (solid line) and by FDPT. Right - Radial profile of the radial electric field measured by BPP.

A good agreement can be seen between the values measured in the SOL. The difference in the results in the confined plasma can be explained by the above-mentioned rapid drop of the floating potential in a radial direction and the different positions of the ball-pen and Langmuir probes. The radial profile of the radial electric field $E_{rad} = -dU_{pl}/dR$ is plotted in the right panel of Figure 6. Position of the velocity shear layer of $E_{rad} = 0$ is usually identical with the separatrix position. It is seen that the probe head survives insertion up to 20 mm inside the separatrix.

Another, quite attractive, possibility is to exploit simultaneously the floating Langmuir probe and the Ball Pen Probe located at the same magnetic flux surface. This combination makes possible to measure the electron temperature with a high temporal resolution, by using the expression

$$V_{fl} = \Phi - \alpha T_e \qquad (1)$$

The floating potential is measured by the Langmuir tip and the plasma potential by the BPP. Consequently, the electron temperature is proportional to their difference

$$T_e = (\Phi - V_{fl})/\alpha \qquad (2)$$

By comparing the resulting electron temperature with that measured by the Thomson scattering (TS), the coefficient $\alpha = 2.2$ for Deuterium plasmas, which is close to theoretical value. An example of comparative measurements is shown in Figure 7.

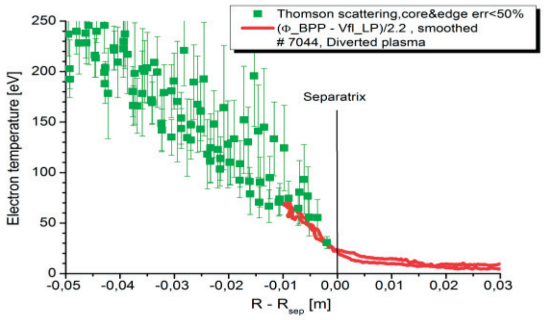

FIG. 7. Comparative measurement of the electron temperature by combined BPP +LP probe and the Thomson scattering.

Such comparison with TS has been done also on the ASDEX Upgrade tokamak [6].

A specific feature of the COMPASS probe heads design has to be emphasized. The interface of the above mentioned probe head is compatible with reciprocating manipulator of the ASDEX U tokamak. This extremely simplifies international collaboration.

Simultaneous measurements with the vertical and horizontal probes reveal coherent fluctuations at frequency range of ~25–35 kHz [7]. They are interpreted as Geodetic Acoustic Modes (GAMs). Figure 8 shows an example of such measurements.

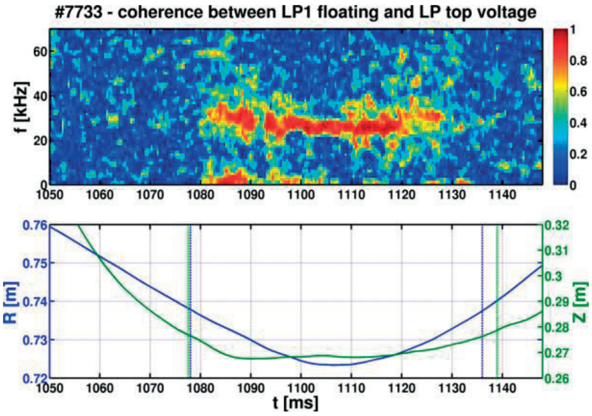

FIG. 8. Top panel - Coherence between horizontal and vertical probes, which measure the floating potential; Bottom panel - Evolution of the positions of the horizontal (blue line) and vertical (green line) probe. The vertical lines mark the time interval, when the probes are inside the separatrix (velocity shear layer).

A strong long range correlation (observed both in the floating and the plasma potential) is evident, if probes are localized inside the separatrix. Moreover, a strong magnetic component is identified in D shape plasmas with n ~0 and m ≠ 2 mode, which doesn't rotate. Probe measurements appear to be useful to identify location of high frequency fluctuations measured by magnetic sensors, as seen in Figure 9.

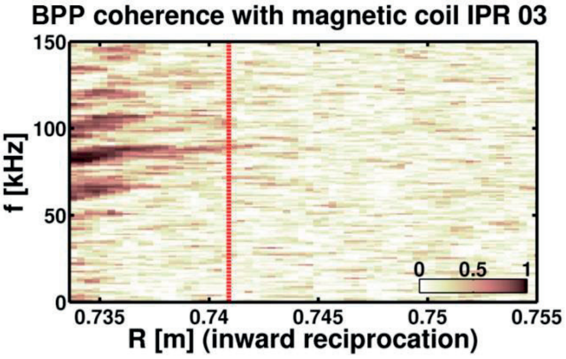

FIG. 9. Coherence between horizontal BPP and magnetic probe located above the midplane. The horizontal red line is position of the velocity shear layer (separatrix).

A strong coherence (~1) is recorded when the electrostatic probe is located inside the velocity shear layer at frequency range 60 – 100 kHz. These modes are interpreted as the Ballooning Alfven Eigenmodes [7]. The parallel heat flux and its radial decay length is also measured by the combined probe head depicted in the left panel of Figure 5 by using expression

$$q_{,,} = \gamma T_e I_{sat}/S_{LP} \qquad [\mathrm{MW, eV, A, mm^2}], \qquad (3)$$

where we use $\gamma = 7$ and $S_{LP} = 30\ \mathrm{mm}^2$ is the total exposed surface of the Langmuir probe.

The radial profile of this quantity in the SOL region is exponential $q_{||} \sim \exp(-r/\lambda_q)$. The decay length λ_q of this radial profile is then determined [8]. Furthermore, the cross correlation between signals of two BPPs allows calculating the time lag between these two signals and thereby to determine the position of velocity shear layer (separatrix). The result of such measurements is shown in Figure 10.

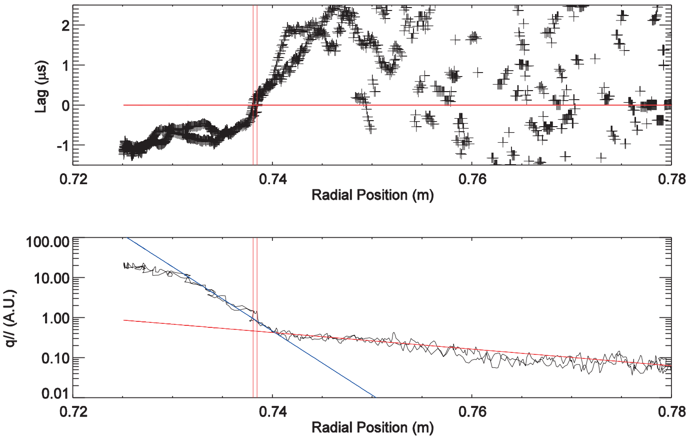

FIG. 10. Radial profiles of the time lag and parallel heat flux for #6024. The position of zero time lag clearly marked by double red vertical line corresponds to the separation between the two different exponential regimes.

Pecker probe

One of important parameters to be measured at the plasma edge is the ion flow velocity. Recently, such diagnostic was designed and manufactured at IPP Prague in collaboration with CEA Cadarache [9,10], as shown in Figure 11.

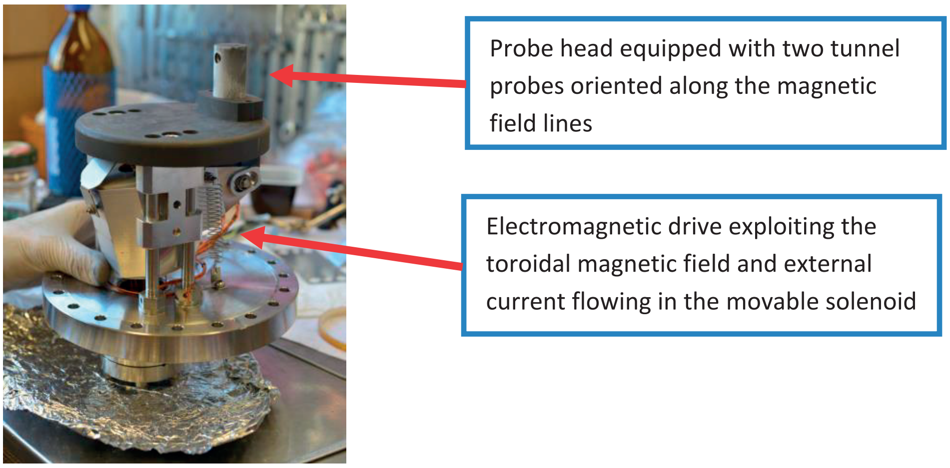
Probe head equipped with two tunnel probes oriented along the magnetic field lines

Electromagnetic drive exploiting the toroidal magnetic field and external current flowing in the movable solenoid

FIG. 11. Picture of the Pecker probe.

The probe head id equipped by two tunnel probes oriented along the toroidal magnetic field lines. The tunnel probe is a concave Langmuir probe designed to operate in strongly magnetized plasma, schematically shown in Figure 12.

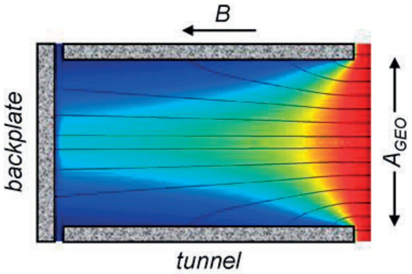

FIG. 12. Section of TP along cylindrical axis. Colour indicates ion density (red is denser than blue). Streamlines of the ion flow are indicated by the black curves in the axial-radial plane. The effective collecting area of the probe is equal to the geometrical projection A_{GEO} of its opening along B.

A two-dimensional, self-consistent kinetic model is employed to model the flow of charges within the cavity of the tunnel probe. The calculation predicts that the distribution of ion flux onto the inner conductors depends on the electric field inside the tunnel, which in turn depends on the electron temperature. Therefore, if the tunnel is divided into two negatively biased collectors, it is possible to use the simulation results to determine the electron temperature from the measured ion current ratio. This means that a DC-biased tunnel probe can be used to provide fast, simultaneous measurements of parallel ion current density and electron temperature without collecting a single electron [11]. Measurements in the CASTOR and Tore Supra tokamaks agree well with the numerical simulations.

The Pecker probes are still commissioned on COMPASS [10]. They will be exploited for fast measurements of T_e, J_{sat} and, in particular for measurements of the parallel Mach number at two poloidal angles (as seen in Figure 4).

Electric probes embedded in the divertor/limiter tiles

The COMPASS tokamak is equipped by several arrays embedded in the divertor/limiter tiles. The array of 39 Langmuir probes in divertor is routinely used to determine distribution of plasma parameters in the divertor region, such as T_e, I_{sat}, the electron energy distribution function and the parallel heat flux [12].

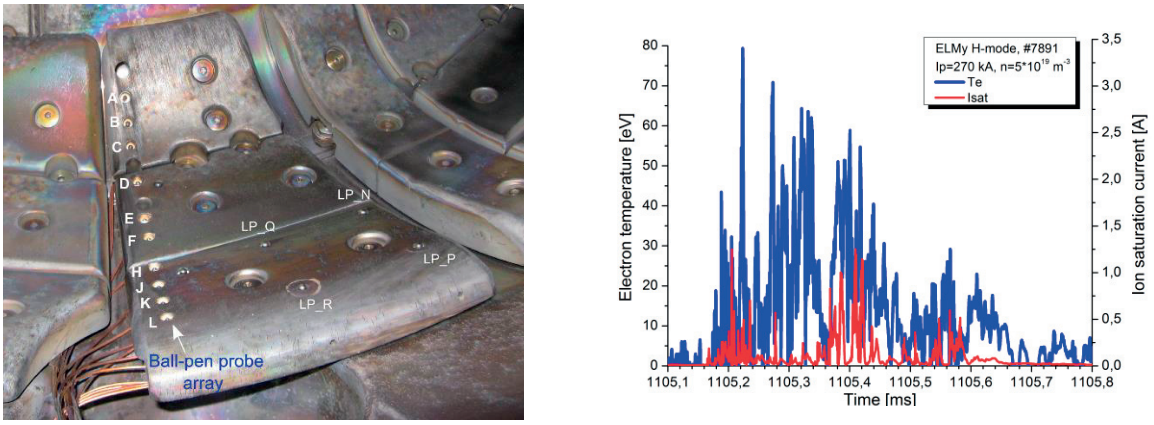

FIG. 13. Left - Picture of the array of 10 BPPs and four Langmuir pins embedded in a divertor tile. Right –Evolution of the electron temperature and the ion saturation current at divertor during a single ELM.

Our experience with the combined BPP and Langmuir probe encourage us to design and manufacture the array of that combined probes in a divertor tile, see Figure 13.

The right panel shows the temporal evolution of T_e and I_{sat} during a single ELM [13, 14]. This diagnostic tool provides a sub-microsecond temporal resolution, and filamentary structure of the ELM is evident. A new array with two toroidally separated arrays of 55 Ball Pen Probes and two toroidally separated arrays of 55 Langmuir probes. The spatial resolution 3 mm will be achieved.

3.1.2. U probe

ELMs are characterized by a complex electromagnetic filamentary structure. Combined local measurements of electric and magnetic properties of turbulent structures in the edge plasma are important tools to improve our understanding of the filaments. Therefore, the U-Probe has been designed and manufactured in collaboration with RFX Padova [15]. As it is seen in Figure 14, the probe head consists of two identical towers, made of Boron Nitride, which are spaced poloidally by 40 mm.

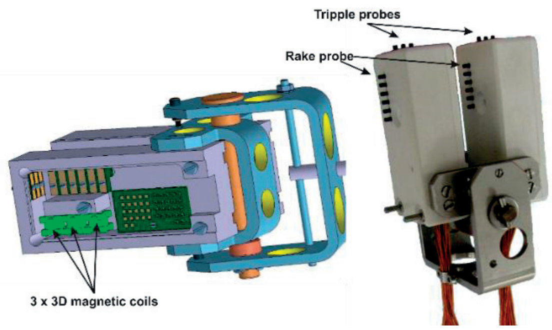

FIG. 14. Design (left) and picture of the U probe (right).

Each tower is equipped by the rake of six Langmuir tips to measure radial profiles either of the floating potential or the ion saturation current. The triple probe at the top of the tower measures the electron temperature with a sufficiently high temporal resolution. Each tower contains the radial array of three magnetic probes spaced radially, which measure poloidal, radial and toroidal components at three radii. The U probe is installed in the port below midplane and movable on shot to shot basis. An example of measurements of electromagnetic structure of an ELM event is shown in Figure 15.

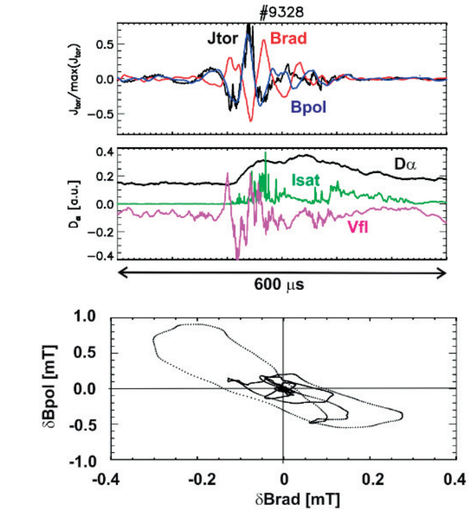

FIG. 15. Structure of a single ELM as measured by the U probe.

Several conclusions can be drawn from these experimental results:

- Filament fragmentations and their radial propagation are observed in $I_{sat}(r,t)$
- Main I_{sat} peak corresponds to a potential valley
- Positive peak of parallel current density, J_{tor} is accompanied by negative secondary Jtor peaks => a nearly zero time integral of the J_{tor} is associated to the current filament
- Filamentary feature is confirmed by the closed patterns of δB_{pol} and δB_{rad} fluctuations in the cross-field plane.

Further experiments on COMPASS with the U probe are in progress.

3.1.3. ExB analyzer

Existing measurements show that the ion temperature in SOL is 2x – 10x higher than the electron temperature [16]. However, T_i is rarely measured at high temporal resolution, in spite of the fact that ions transport majority of heat flux. Therefore, we are attempted to develop diagnostics for fast measurements of T_i with temporal resolution better than 10 μs (with the sampling rate >= 100 kHz). The goal of this diagnostics is to measure evolution of the ion temperature evolution during ELMs, and at T_i fluctuations in SOL in L-mode.

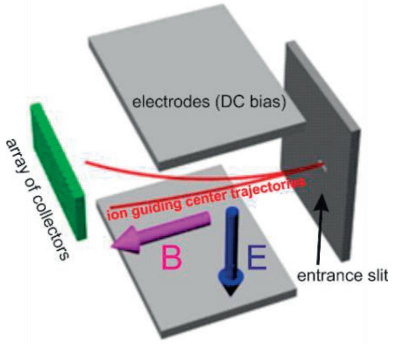

FIG. 16. Scheme of the ExB analyzer.

As shown in Figure 16, the ExB analyzer consists of a negatively biased slit plate which reflects electrons back to the plasma and admits a fraction of the incident ion flux inside the analyzer. Inside the analyzer, two planar electrodes, biased to different constant voltages, create an electric E perpendicular to B, which leads to the dispersion of transmitted ions due to the ExB drift. The ions, displaced from the slit axis by the distance Δ_x, which is inversely proportional to the parallel ion velocity. Since all bias voltages are kept constant, the parallel ion distribution function $f(v_{II})$ can thus be measured at high acquisition frequencies (2 MHz in present experiment) from the currents to the array of collectors. Figure 17 shows first results with the analyzer presented in Ref. [17].

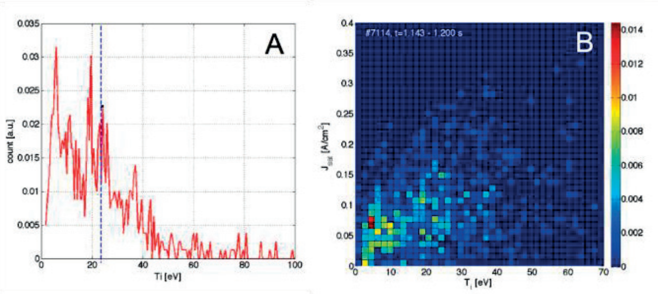

FIG. 17. Distribution of the ion temperature fluctuations.

Results indicate that two ion populations in SOL with different temperatures are present in SOL. The ratio of the populations depends on the plasma density. Speculations - low ions (T_i

< 15 eV) can result from recycling/fueling, while the high ions (T_i >15 eV) are transported from the confinement region i.e. their origin is inside the last closed flux surface. However, measurements with the ExB analyzer need more experimental verification on the COMPASS tokamak.

4. CONCLUSIONS

Edge plasma is an important region in tokamaks for several phenomena such as confinement, transport barriers, turbulence, quasi-coherent modes, transient phenomena. Edge plasma diagnostics with a good spatial and temporal resolution are required to understand the underlying physics. Electric probes (arrays) accompanied by magnetic sensors are extremely useful tools for that purpose. The COMPASS tokamak is now well equipped with several probe systems, and interesting results are achieved.

ACKNOWLEDGEMENT

This work was funded by the project MSMT LM2011021, projects of the Grant Agency of the Czech Republic GA15-10723S, GA14-35260S, Eurofusion projects WP12-FRF-IPP.CR, WP12-GOT-GOT4TSI, and GAP205/11/2341.

It has to be also emphasized that presented results were achieved in close international collaboration with Kurchatov Institute (AEM), RFX Padova (U probe, filaments), Sofia University (Langmuir probes), ASDEX Upgrade team (Ball Pen Probe, ExB analyzer), CEA Cadarache (Pecker probe, tunnel probe), IST Lisabon (probe measurements).

REFERENCES

[1] PÁNEK, R., ADÁMEK, J., AFTANAS, M., BÍLKOVÁ, P., BÖHM, P., BROCHARD, F., CAHYNA, P., CAVALIER, J., DEJARNAC, R., DIMITROVA, M., GROVER, O., HARRISON, J., HÁČEK, P., HAVLÍČEK, J., HAVRÁNEK, A., HORÁČEK, J., HRON, M., IMRÍŠEK, M., JANKY, F., KIRK, A., KOMM, M., KOVAŘÍK, K., KRBEC, J., KRIPNER, L., MARKOVIČ, T., MITOŠINKOVÁ, K., MLYNÁŘ, J., NAYDENKOVA, D., PETERKA, M., SEIDL, J., STÖCKEL, J., ŠTEFÁNIKOVÁ, E., TOMEŠ, M., URBAN, J., VONDRÁČEK, P., VARAVIN, M., VARJU, J., WEINZETTL, V., ZAJAC J., and the COMPASS TEAM, Status of the compass tokamak and characterization of the first h-mode, Plasma Phys. Control. Fusion **86** (2016) 9.

[2] WEINZETTL, V., PANEK, R., HRON, M., STOCKEL, J., ZACEK, F., HAVLICEK, J., BILKOVAA, P., NAYDENKOVA, D.I., HACEK, P., ZAJAC, J., DEJARNAC, R., HORACEK, J., ADAMEK, J., MLYNAR, J., JANKY, F., AFTANAS, M., BOHM, P., BROTANKOVA, J., SESTAK, D., DURANA I., MELICH, R., JARES, D., GHOSH, J., ANDA, G., VERES, G., SZAPPANOS, A., ZOLETNIK, S., BERTA, M., SHEVCHENKO, V.F., SCANNELL, R., WALSH, M., MULLER, H.W., IGOCHINE, V., SILVA, A., MANSO, M., GOMES, R., POPOV, TSV., SARYCHEV, D., KISELOV, V.K., NANOBASHVILI, S., Overview of the compass diagnostics, Fus. Eng. Des. **86** (2011) 1227-1231.

[3] ADAMEK, J., STOCKEL, J., HRON, M., RYSZAVY, J., TICHY, M., SCHRITTWIESER, R., IONITA, C., BALAN, P., MARTINES, E., VAN OOST, G., A novel approach to direct measurement of plasma potential, Czech. J. Phys. **54** (2004), C95.

[4] ADÁMEK, J., STÖCKEL, J., ĎURAN, I., HRON, M., PÁNEK, R., TICHÝ, M., SCHRITTWIESER, R., IONITA, C., BALAN, P., MARTINES, E., VAN OOST, G., Comparative measurements of the plasma potential with the ball-pen and emissive probes on the castor tokamak, Czech. J. Phys. **55** 3 (2005) 235–242.

[5] POPOV, TSVIATKO, DIMITROVA, MIGLENA, IVANOVA, PAVLINA, KOVAČIČ, JERNEJ, GYERGYEK, TOMAZ, DEJARNAC, RENAUD, STOCKEL, JAN, PEDROSA, LOPEZ-BRUNA, DANIEL, HIDALGO, CARLOS, Advances in langmuir probe diagnostics of the plasma potential and electron energy distribution function in magnetized plasma, Plasma Sources Sci. Technol., **25** (2016) 033001

[6] ADAMEK, J., HORACEK, J., MULLER, H.W., ROHDE, V., IONITA, C., SCHRITTWIESER, R., MEHLMANN, F., KURZAN, B., STOCKEL, J., DEJARNAC, R., WEINZETTL, V., SEIDL, J., PETERKA, M., and the ASDEX UPGRADE TEAM, Ball-pen probe measurements in l-mode and h-mode on asdex upgrade, Contrib. Plasma Phys. **50** 9 (2010) 854 – 859.

[7] SEIDL, J., HRON, M., ADAMEK, J., VONDRACEK, P., HORACEK, J., HIDALGO, C., MELNIKOV, A., ELISEEV, L., MARKOVIC, T., STÖCKEL, J., BASU, D., HACEK, P., HAVLICEK, J., KOVARIK, K., IMRÍŠEK, M., PANEK R., and COMPASS TEAM, Observation of geodesic acoustic mode-like oscillations on compass, 42nd EPS Conference on Plasma Physics, Lisbon, Portugal, 22nd—26th June 2015, P 4.103.

[8] LOUREIRO, J., SILVA, C., HORACEK, J., ADAMEK, J., STOCKEL, J., Scrape-off layer width of parallel heat flux on tokamak compass, Plasma Phy. Tech. **1**, 3 (2014) 121–123.

[9] MELNIKOV, A. V., MARKOVIC, T., ELISEEV, L.G., ADÁMEK, J., AFTANAS, M., BILKOVA, P., BOEHM, P., GRYAZNEVICH, M., IMRISEK, M., LYSENKO, S.E., MEDVEDEV S. YU., PANEK, R., PETERKA, M., SEIDL, J., STEFANIKOVA, E., STOCKEL, J., WEINZETTL, V., and the COMPASS TEAM, Quasicoherent modes on the compass tokamak, Plasma Phys. Control. Fusion **57** (2015) 13.

[10] DEJARNAC, R., GUNN, J. P., DIMITROVA, M., HRON, M., PANEK, R., PASCAL, J-Y., SARAGOSTI-CHAUSY, C., TAMAIN P. and the COMPASS TEAM, Simultaneous poloidal measurements using new magnetically driven reciprocating probes in compass, International workshop on electric probes, Sozopol, Bulgaria, 2015, J. Phys., Conference Series (2016).

[11] GUNN, J.P., DEJARNAC, R., STÖCKEL, J., Simultaneous DC measurements of ion current density and electron temperature using a tunnel probe, International workshop on electric probes, Sozopol, Bulgaria, 2015, J. Phys., Conference Series (2016).

[12] GUNN, P., DEVYNCK, P., PASCAL, J.Y., ADAMEK, J., DURAN, I., HRON, M., STOCKEL, J., ZACEK, F., BARINA, O., HRACH, R., VICHER, M., VAN OOST, G., A DC probe diagnostics for fast electron temperature measurements in tokamak edge plasmas, Czech J. Phys. **52** (2002) 1107 .

[13] DIMITROVA, M., IVANOVA, P., KOTSEVA, I., POPOV, TSV. K., BENOVA, E., BOGDANOV, T., STÖCKEL J. AND DEJARNAC, R., Evaluation of the plasma parameters in compass tokamak divertor area, J. Phys., Conference Series **356** (2012).

[14] ADAMEK, J., SEIDL, J., PANEK, R., KOMM, M., VONDRACEK, P., STÖCKEL J., and the COMPASS TEAM, Fast measurements of heat flux in elm filaments in sol and divertor region on the compass tokamak, 15th EPS international workshop on h-mode physics and transport barriers, Garching, Germany, October 19 – 21, 2015, Nucl. Fusion (2015).

[15] ADAMEK, J., et al, Fast measurements of the electron temperature in divertor region of the compass tokamak using ball-pen probe, 42nd EPS conference on plasma physics, Lisbon, Portugal, 22nd — 26th June 2015.

[16] SPOLAORE, M., et al, Elm and inter-elm electromagnetic filaments in the compass scrape off layer, 42nd EPS conference on plasma physics, Lisbon, Portugal, 22nd — 26th June 2015.

[17] KOCAN, M., et al, Measurements of ion energies in the tokamak plasma boundary, J. Nucl. Mater **415** (2011).

[18] KOMM, M., KOCAN, M., CARRALERO, D., MÜLLER, H.W., STÖCKEL, J., REA, C., COMPASS team and the ASDEX Upgrade Team, Fast measurements of ion temperature fluctuations in compass and aug scrape-off layer, EPS (2014).

[19] MARKOVIC, T., et al, Alfven-wave character oscillations in tokamak compass plasma, 42nd EPS conference on plasma physics, Lisbon, Portugal, 22nd — 26th June 2015.

[20] ADAMEK, J., et al, Fast measurements of the electron temperature in divertor region of the compass tokamak using ball-pen probe, 42nd EPS conference on plasma physics, Lisbon, Portugal, 22nd — 26th June 2015.

USE OF SMALL TOKAMAK GOLEM AS A TEST BED FOR APPLICATION OF HIGH TEMPERATURE SUPERCONDUCTORS IN FUSION DEVICES

V. SVOBODA*, J.STOCKEL***, M. GRYAZNEVICH**, G. VOROBLEV****, O. GROVER*

*Faculty of nuclear sciences and physical engineering, Czech technical university in prague, cr.
**Tokamak energy, tokamak solutions, oxford instruments, gb (st 25, st 25 hts)
***Institute of plasma physics, Czech academy of sciences, cr (compass)
****Saint Peterburg university, rf.

Abstract
The tokamak GOLEM contribution to the IAEA coordinated research activity is developd in these tasks: i) investigation of performance of hts magnets during tokamak operations. ii) providing experimental data for the development of new concept of advanced magnets in fusion devices, based on high temperature superconductors. iii) studies of properties of hts in tokamak environment: critical current dependence on magnetic field, temperature, stresses, etc. iv) mw driven pre-ionization - reduction in the loop voltage achieved for the plasma breakdown with respect to electron gun pre-ionization. v) probe measurements performed in two different - tokamak and microwave – plasmas.

1. INTRODUCTION

The GOLEM tokamak is operational at the Faculty of Nuclear Physics and Physical Engineering (FNPPE), Czech Technical University in Prague [1]. GOLEM is a small tokamak which was constructed at the end of 1950's at the Kurchatov Institute, Moscow as TM-1. The tokamak was moved to the Institute of Plasma Physics in Prague in 1977 and re-named CASTOR. After 30 years of operation, the tokamak was given to the FNPPE for education of students and renamed GOLEM.

FIG. 1. Tokamak GOLEM equipped with cryostat and MW launcher.

The GOLEM tokamak has a circular cross section. The major and minor radii of the tokamak vessel are R_0=0.4 m and b=0.1 m respectivelly. The stainless steel vessel is equipped with a poloidal limiter (made of Molybdenum) of radius a=0.085 m. The power supplies of individual windings are based on several condenser banks. The tokamak is equipped by a set of simple diagnostics, which measure the loop voltage, plasma current, toroidal magnetic field, and visible emission. GOLEM is also equipped with interferometer, Mirnov coils, a visible spectrometer, an array of bolometers, a fast camera for time resolved pictures, etc.

Engineering and plasma parameters, which can be achieved on GOLEM are quite modest. The tokamak operates at maximum toroidal magnetic field of up to 0.5 T. The central electron temperature is less than 100 eV, the maximum line average density ~ 10^{19} m^3, the maximum pulse length is around 18 ms. An unique feature of this experimental arrangement is the possibility of a complete remote handling operation via Internet access. From the client side the tokamak is operated through a HTTP or SSH connection, whereby a remote operator can set all the discharge parameters and submit them into a queue and then special software performs the queued discharges according to the submitted requests. Consequently all data in graphical/raw form are accessible on a special discharge web page. More than 2000 discharges were performed remotely across the borders of the Czech Republic as a part of a remote laboratory practice or a tokamak performance presentation for foreign students in various plasma schools, workshops, lectures and training courses.

2. TESTING OF THE HIGH TEMPERATURE SUPERCONDUCTORS (HTS) IN THE TOKAMAK ENVIRONMENT

Two poloidal field coils made of the HTS were installed on the GOLEM tokamak. The HTS tape (50 m) was provided by the company "Tokamak Solutions, Culham, UK". For their installation on the GOLEM tokamak, two cryostats, made of polystyrene, were designed and manufactured at the Faculty of Nuclear Physics and Physical Engineering, Czech Technical University (CTU) in Prague. The HTS tapes are cooled by liquid nitrogen to temperature around 70 K with the cooling system developed at the CTU as well. Series of successful tests were performed in a broad international collaboration (Tokamak Solutions, CCFE, Fusion Association, Culham, UK) and also with participation of the Institute of Plasma Physics, Academy of Sciences of the Czech Republic. The achieved results were published in the journal Fusion Engineering and Design [1].

2.1. Experimental setup

It has long been known that high temperature superconductors (HTS) could have an important role to play in the future of the tokamak fusion research [1, 2]. First results of the use of HTS in a tokamak magnet are presented. In the experiment, the two copper poloidal field coils of the small tokamak GOLEM in Prague [3] were replaced by two coils with 6 turns of the 2nd generation HTS (Re)BCO tape SCS12050-AP supplied by “SuperPower Inc.”, US. The coils were wound in-situ by hand to avoid the need to disassemble the tokamak. The dimensions of the tape are approximately 0.1x12 mm, HTS thickness ~1 μm, with two 20 μm Cu stabilising layers on the 50 μm Hastelloy substrate and the maximum claimed current capacity at liquid nitrogen (77K) temperature of ~ 320 Amps. Two simple liquid nitrogen (LN) cryostats made by “Forma Machinery Ltd” in Latvia, were assembled and filled with LN to cool the HTS tape to below the critical temperature at which it becomes superconducting. Plasma pulses were then fired in a normal way with HTS coils providing the vertical field and the tokamak operated exactly as expected. There had been concerns that the plasma pulses might cause a “quench”, i.e. cause a sudden and potentially damaging transition from superconductor to normal conductor. However, many plasma pulses were achieved without any quenches. In addition, experiments without plasma have been performed to study properties of the HTS in a tokamak environment, i.e. critical current and its dependence on magnetic and electrical fields generated in a tokamak both in DC and AC operations, maximum current ramp-up speed, performance of the HTS tape after number of artificially induced quenches etc. Considerable experience has been gained during design and fabrication of the cryostat, coils, isolation and insulation, feeds and cryosystems. Figure 2 shows the GOLEM tokamak with two HTS vertical field coils. The plasma is seen through the midplane port. The cryostat, feeds and coil designs have evolved and the final version of the cryostat has improved insulation, so the ice seen in Figure 2 on the coils has been avoided. The typical time of cooling to superconducting conditions has decreased from the initial value of 90 min to 15 min. The final design of feeds avoids the local overheating observed in earlier designs. It was also found that circulation of LN in the cryostat resulted in ~15% increase in the critical current.

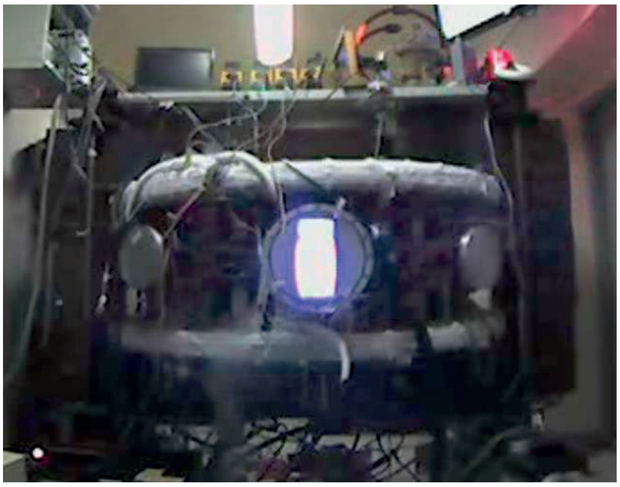

FIG.2. Plasma pulse in the GOLEM tokamak with HTS poloidal field coils.

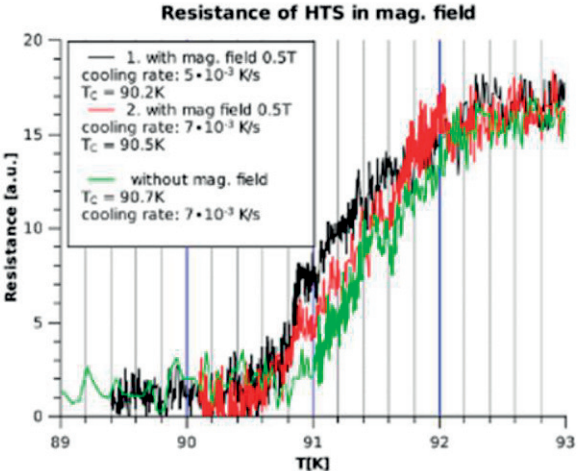

FIG.3. Dependence of the critical temperature for achievement of superconductivity in the HTS coil without and with 0.5 T on GOLEM.

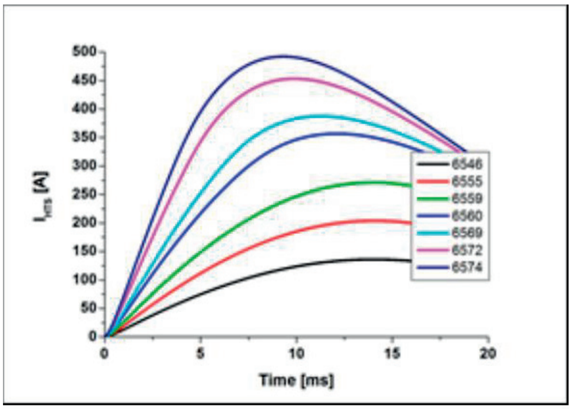

FIG. 4. Evolution of the inductively induced current in the HTS coil in different pulses.

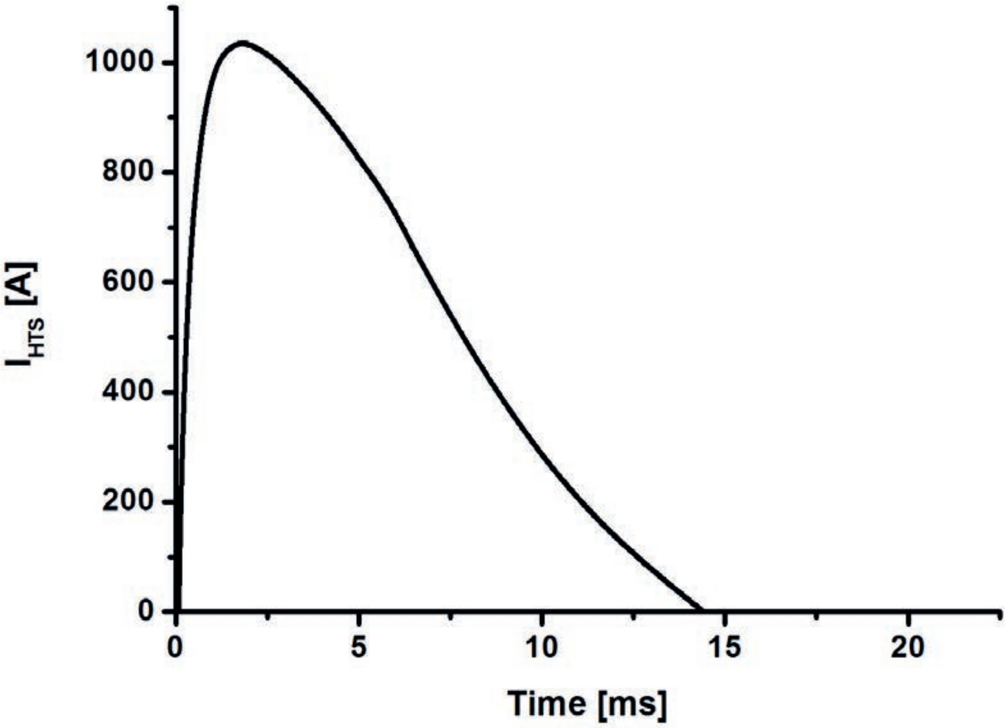

FIG.5. Evolution of the inductively induced current in record pulse 6975.

2.2. Basic HTS experiments in real tokamak operation

Although it is known that the critical current in HTS strongly depends on magnetic field, for the GOLEM conditions, where magnetic fields at the coil position do not exceed 0.5 T, little effect has been observed for perpendicular field up to 0.5 T and superconductivity has been achieved at ~90.50 K, Figure 3. No quench has been observed at DC currents up to 250 A (the limit of the available power supply) during bench tests of the tape. The HTS was kept on the full current for tens of minutes with no observed changes in resistivity. In the AC tests, current up to 1 kA through the tape (6 kA-turns through the coil) has been achieved with no degradation of the HTS performance afterwards, although in such short pulse the current was probably distributed between the HTS and other components of the tape. Figure 4 shows time evolution of the inductively induced current in the HTS coil demonstrating the current ramp-up speed of up to 90 kA/s, however, the highest rate of ~0.6 MA/s has been achieved in pulse #6975, Figure 5, where current through the tape has reached 1 kA.

In typical plasma pulses such a high level of current in equilibrium field coils is not needed and plasma operations have been performed with moderate I_{HTS} ~ 50–100 A current in the tape. This probably explains the absence of quenches during plasma pulses as the current was much below the critical value. However in some cases plasma disruptions occurred with corresponding induced electrical fields, and they also did not cause quenches. In future experiments, increases in both the plasma current and pulse duration are planned. To study quenches in DC operations, the current was increased and quenches have been observed at I_{HTS} ~ 150 A when operating together with other tokamak magnets but without plasma. When “up-to-destruction” tests have been performed, a quench caused an arc in the inter-turn isolation in one coil. There was no surprise that the location of the quench was under the limb of the iron transformer, where the highest leakage magnetic field has been measured. The damaged pieces of the tape have been cut out, the ends re-soldered and the coil has shown the same performance as before the accident, i.e. the local quench has not affected the performance of the rest of the coil. Over 25 quenches have been performed and a whole series of further experiments is now planned. The internal structure of the damage caused by the quench that caused arcing is under investigation.

2.3. Plasma position stabilization with HTS poloidal field coils

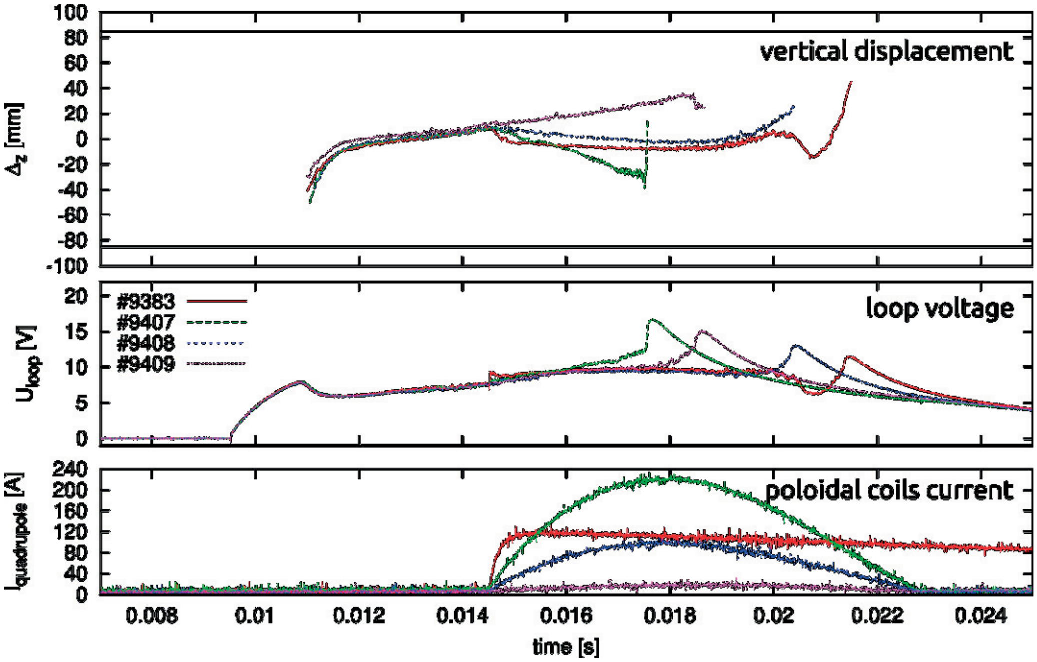

FIG. 6. Plasma displacement using the HTS coils. In discharges #9407 and #9408 the HTS coils were in a superconductive state and the capacitor bank charging voltage was only 70 V and 20 V whereas it was 400 V in discharge #9383 where the coils were in a non-superconductive state and the coil current was similar. Discharge #9409 is a reference discharge with no radial stabilizing field.

As can be seen in Figure 6, an appropriate radial magnetic field can prolong the plasma pulse by compensating the tendency of the plasma column to go upwards. With HTS coils in a superconductive state the coils target current can be reached with a much lower capacitor bank charging voltage than with the coils in a non-superconductive state. However, due to the low resistance the characteristic time constant of the circuit changed and the stabilization pulse was much shorter, making it ideal for fast feedback systems

3. OPTIMIZATION OF THE PLASMA PERFORMANCE ON THE GOLEM TOKAMAK

Experiments with the HTS coils have shown that upgrading of several key elements of the GOLEM tokamak are required to improve tokamak performance. In particular, optimization of plasma breakdown and installation of feedback system for the plasma position control appeared to be necessary.

New systems for pre-ionization of the working gas have been installed and tested on the GOLEM tokamak. The microwave power source has been developed and manufactured in collaboration with experts from the St Petersburg State University, Russian Federation. This microwave source provides the electromagnetic wave at 2.45 GHz either DC or in pulse operation. The power is in the range of 1 kW. It has been demonstrated that the breakdown voltage is significantly reduced by 2–3 V with respect to the standard pre-ionization by means of the electron gun. Furthermore, pure microwave plasma was generated at low toroidal magnetic field, when the electron cyclotron resonance is present in the tokamak vessel. Picture of the apparatus and the electrical scheme of power supplies are shown in Figure 1 and Figure 7.

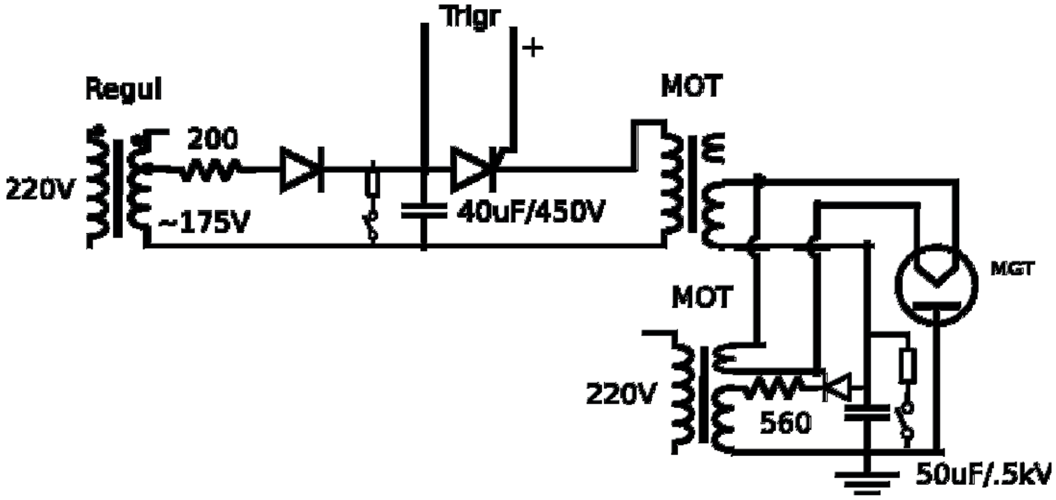

FIG. 7. The electrical scheme of the MW pre-ionization at the GOLEM tokamak.

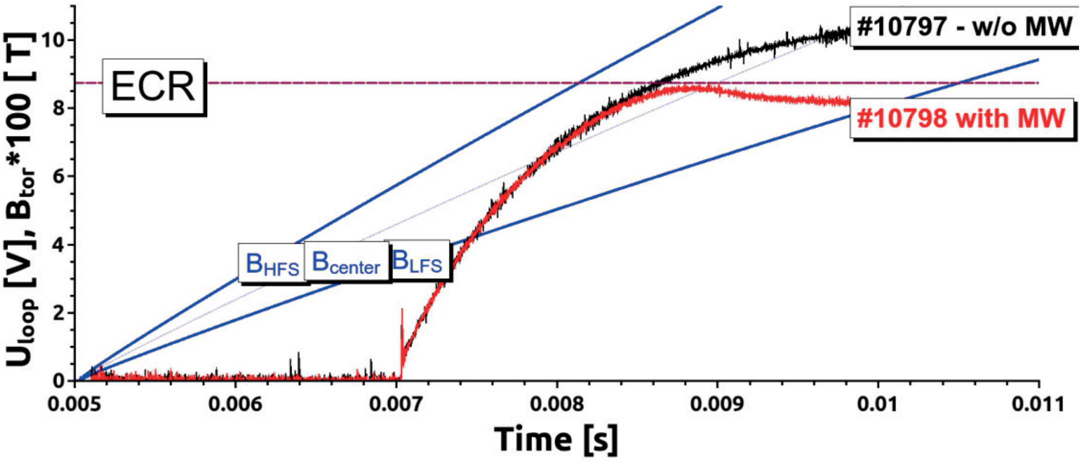

FIG. 8. Loop voltage characteristics of vacuum shot (black) and plasma discharge performed by means of microwave (red) - breakdown occurs when ECR layer is in the center of the vessel.

Figure 8 demonstrates that the microwave breakdown is effectively achieved with this apparatus. The RF power was injected in a short (<10 ms) pulse during the ramp-up of the toroidal magnetic field B_t and the breakdown occurs at $B_t = 0.0875$ T, which corresponds to localization of the Electron Cyclotron Resonance layer (for f = 2.45 GHz) inside the tokamak vessel. A series of discharges, where the breakdown was achieved either by electron gun or microwave pre-ionization was performed. Results are compared in Figure 9. It has been proven that the MW pre-ionization is more efficient when the EC resonance layer is inside the tokamak vessel, while the electron gun pre-ionization acts better at low magnetic fields.

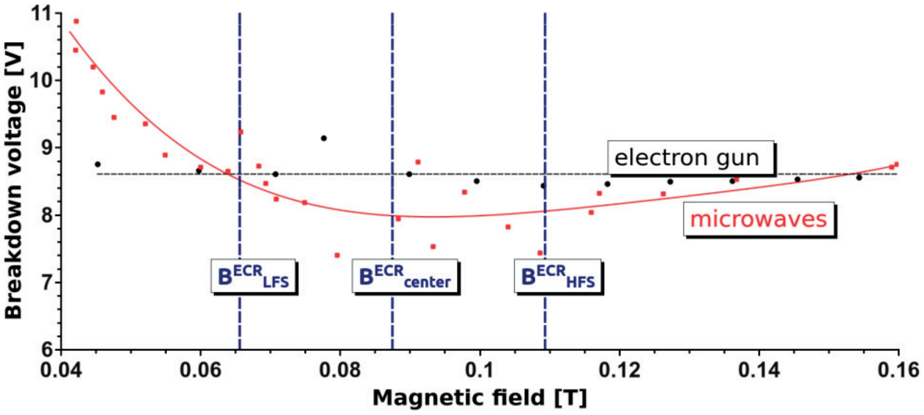

FIG. 9. Loop voltage at breakdown versus the toroidal magnetic field. Comparison of the microwave pre-ionization (red symbols) and the electron gun pre-ionization (black symbols) at the pressure of the working gas 10 mPa.

4. DEVELOPMENT AND TESTING OF NOVEL DIAGNOSTICS

To improve plasma diagnostic capabilities of GOLEM, several diagnostic tools are designed. In particular, The linear array of Langmuir probes for measurements of radial profiles and plasma fluctuations, The poloidal ring of 32 Mach probes to measure the poloidal distribution of flows in the edge plasma, 2 poloidal rings of 16 Mirnov coil probes to measure poloidal and toroidal magnetohydrodynamic activity in the edge plasma.

4.1. Probe measurements in the microwave plasma

Preionization of GOLEM discharges is performed by a microwave generator at f = 2.45 GHz. The resulting MW plasma is studied by means of the planar Langmuir probe located at the radius r/a = 0.8 (effective collecting area is 50 mm^2), and oriented perpendicularly to the magnetic field lines (see Figure 10). Thanks to good reproducibility, the IV characteristics are measured on a shot to shot basis in 18 discharges (#18480 – #18497). The typical IV characteristic constructed at t = 12 ms is shown in the right panel in Figure 11, it is also shown that the saturation currents (I_{+sat} and I_{-sat}) are not constant. Increase of I_{+sat} is a consequence of the probe sheath expansion, however the decrease of I-sat with the probe voltage is not yet understood. The fitting function was used to calculate plasma parameters by using the technique proposed by Popov.

The resulting evolutions of the electron temperature and the ion saturation current are plotted in the central panel of Figure 11. It is evident that plasma is confined in the vessel after switching of the MW power at t = 10.8 ms. Since that time, the ion saturation current, and electron density decay exponentially, with a time constant ~ 1.4 ms. Such a relatively long confinement of plasma is possible due to the low electron temperature, which remains constant at T_e = 0.6–0.8 eV. Consequently, the centrifugal and ExB drift velocities are small.

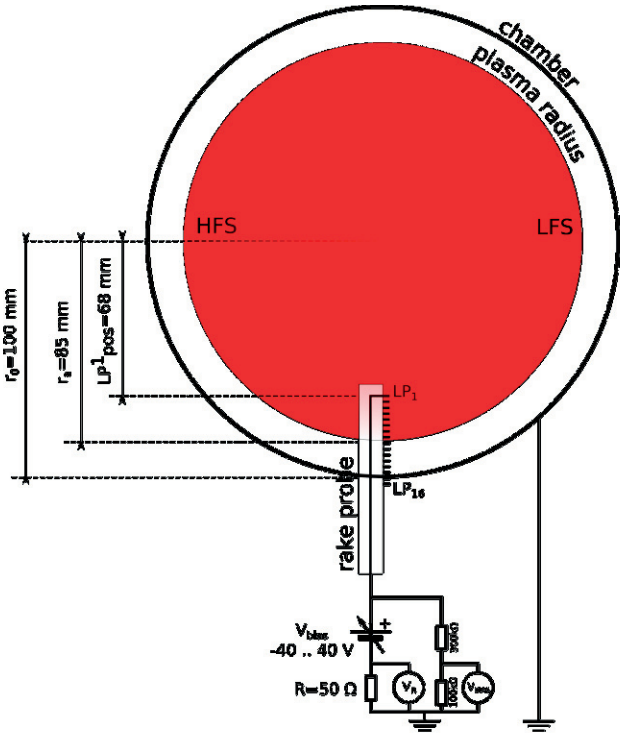

FIG. 10. Experimental setup.

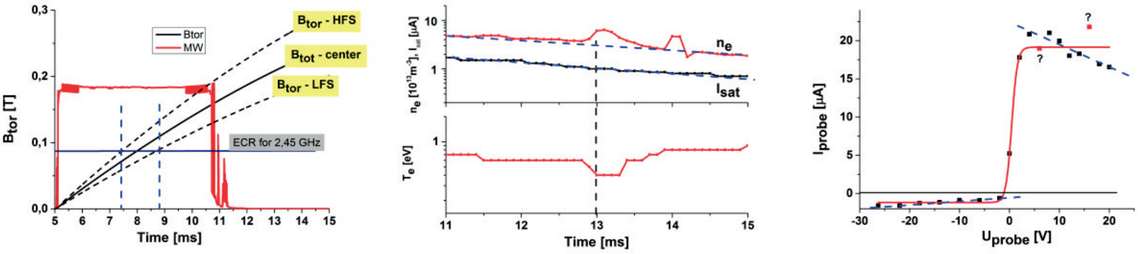

FIG. 11. Left - Temporal evolution of the toroidal magnetic field and the microwave power (the ECR resonance indicated); *Center - Temporal evolution of selected plasma parameters after the MW power was switched off*; *Right* - a *selected IV characteristics (t = 12 ms, B_t = 0.188 T).*

5. EDUCATION AND TRAINING OF STUDENTS

The GOLEM tokamak is a university-type of an experimental facility, which is exploited for practical training of students. Students are acquainted with basics of tokamak operation, data processing and evaluation of some plasma parameters. Repetition rate of plasma discharges is quite high (one shot in ~ 2–3 minutes), therefore scans of discharge parameters can be easily performed in a couple of teaching hours. The unique feature of the GOLEM tokamak is its capability to be handled remotely via standard Internet. Several remote courses have been organized annually:

- French fusion master course together with Erasmus Mundus at CEA Cadarache, France
- GOMTRAIC – GOLEM Remote training course, education and training course oriented on basic understanding of experimental tokamak physics and control.

It is meant for undergraduate and postgraduate students who want to get experience with operating of a fusion device. Prague, Czech Republic

- SUMTRAIC – Summer training course, Prague, Czech Republic
- EMTRAIC – Erasmus Mundus Training Course, Prague, Czech Republic
- SCIWEEK – Science week for high school students from Czech Republic. 4 groups of students making more then 100 on-site discharges performing spectroscopic studies, plasma position studies using fast camera, vertical plasma position studies using Mirnov coils and HXR studies at the tokamak GOLEM.
- Remote laboratory practice for students from Budapest University, Hungary.
- Tokamak GOLEM has also contributed to the Prague Museum Night and Nights of Scientists – excursions for more then 100 visitors during the night.

Tokamak GOLEM has contributed to the programme of numerous lectures, demonstrations, workshops, plasma physics courses, etc. such as for: Ghent University 2009, TU Eindhoven 2011,2015,2016, Bochum University 2013, Garching 2013, Lemvig High School 2014, TU Kobehaven, TU Denmark 2015,2016, University of Belgrade 2015, BUTE Budapest 2010,2012–2014, Instituto Tecnologico Costa Rica 2010, University of Padova 2014, Workshops in Kiten 2014, Observatorium Valasske Mezirici 2014, Islamabad 2014, Global Tokamak Experiment 2010, Plasma physics course in Trieste, Italy, etc.

6. CONCLUSION

The HTS coils have been routinely and successfully used at the GOLEM tokamak both for plasma generation and stabilization. Provided the LN cooling was sufficient and sustained, the HTS coils are reliable and can greatly reduce the necessary capacitor bank charging voltage, thus lowering the energy demands for plasma position. The coil currents in fast ramp-up pulse operation exceeded those in the tape specification by almost 50 %. Other relevant results are presented in the Fusion Engineering and Design journal, see [1].

Regarding MW pre-ionization, it is more efficient when the EC resonance layer is inside the tokamak vessel, while the electron gun pre-ionization acts better at low magnetic fields.

Tokamak GOLEM contributed to a numerous educational events and activities with the help of its unique capability to be operated remotely. More than 2000 discharges were performed remotely across the borders of the Czech Republic as a part of a remote laboratory practice or a tokamak performance presentation for foreign students in various plasma schools, workshops, lectures and training courses.

ACKNOWLEDGEMENT

This work was partially supported by the project RVO: 68407700 of the Czech Technical University in Prague. Additional support has been granted from IAEA technical contract CRP F1.30.14 on “Utilization of the Network of Small Magnetic Confinement Fusion Devices for Mainstream Fusion Research”. The opinions expressed by authors do not necessarily represent the positions of the European Commission neither IAEA.

REFERENCES

[1] GRYAZNEVICH, M., SVOBODA, V., STOCKEL, J., SYKES, A., SYKES, N., KINGHAM, D., HAMMOND, G., APTE, P., TODD, T.N., BALL, S., CHAPPELL, S., MELHEM, Z.,

ĎURAN, I., KOVARIK, K., GROVER, O., MARKOVIC, T., ODSTRCIL, M., ODSTRCIL, T., SINDLERY, A., VONDRASEK, G., KOCMAN, J., LILLEY, M.K., DE GROUCHY, P., KIM, H.-T., Progress in application of high temperature superconductor in tokamak magnets, Fus. Eng. Des. **88** (2013) 1593 – 1596.

[2] MIKHAIL GRYAZNEVICH et al., Contribution to fusion research from iaea coordinated research projects and joint experiments, Nucl. Fusion **55** (2015).

[3] SVOBODA, V., KOCMAN, J., GROVER, O., KRBEC, J., STÖCKEL, J., Remote operation of the vertical plasma stabilization at the GOLEM tokamak for the plasma physics education, Fus. Eng. Des. **96–97** (2015) 974–979.

IMPROVEMENT OF HEAVY ION BEAM DIAGNOSTIC TOWARDS A REAL-TIME CAPABLE DIAGNOSTIC AND ITS USE FOR MHD ACTIVITY DETECTION

H. FERNANDES, A. MALAQUIAS, R.B. HENRIQUES, S. NEDZELSKIY, B.B.CARVALHO, A. S. DUARTE, C. SILVA

Instituto de Plasmas e Fusão Nuclear, Instituto Superior Técnico, Universidade de Lisboa, Portugal

Abstract

The Heavy Ion Beam Diagnostic (HIBD) on the tokamak ISTTOK has been modified, in terms of signal conditioning, to measure the local fluctuations of the $n_e\hat{\sigma}_{1,2}(T_e)$ product (plasma density times the effective ionization cross section) along the tokamak minor diameter, in 12 vertically distributed sample volumes in the range of $-0.7a < r < 0.7a<r<0.7a$, with a maximum delay time of 1μs. The corresponding signals show high correlation with the magnetic Mirnov coils in the characteristic MHD frequency range of ISTTOK plasmas and enable the identification of tearing modes. A further improvement on the ion beam modulation frequency, up to 150 kHz, has allowed the measurement of fast $n_e\hat{\sigma}_{1,2}(T_e)$ profiles (more than 10 profiles in one ISTTOK real-time cycle). The HIBD has demonstrated promising results of off-line plasma vertical position measurements. These two characteristics/results make the HIBD a promising diagnostic for the plasma vertical position measurements and feedback control using magnetic actuators. This document describes: (i) the HIBD signal conditioning system and presents a preliminary analysis of the radial profile measurements of local $n_e\hat{\sigma}_{1,2}(T_e)$ fluctuations and (ii) the description of the HIBD data integration for real-time plasma position measurement and control.

1. INTRODUCTION

The research work provided in the framework of the current Co-ordinated Research Project (CRP) of the International Atomic Energy Agency (IAEA) "Utilization of a Network of Small Magnetic Confinement Fusion Devices for Mainstream Fusion Research" during the fulfilment of the 4-year activity made by Instituto Superior Técnico through Instituto de Plasmas e Fusão Nuclear were focused on tokamak diagnostics, plasma control and data analysis. Contributions were made as well in other fields, in particular during the Joint Experiments in Prague and Saskatoon.

The project was focused on the development and improvement of (i) the Heavy Ion Beam Diagnostic (HIBD), (ii) the amelioration of the tomography camera system to allow its work in real time and control, (iii) the upgrade of the MARTe towards a Multi-input multiple-output control real-time plasma control allowing a more proficient plasma control improving even more the reliability for producing optimized AC discharges and (iv) the throughput of the data analysis by using GPUs.

In this report we will focused on the HIBD as other works, namely electrostatic probe measurements and development were carried out within other partners and cited elsewhere in this tecdoc.

2. ISTTOK TOKAMAK

2.1. Machine status

ISTTOK is the only fusion device in Portugal being a tokamak with a circular cross section, a poloidal graphite limiter and an iron core transformer. It is the only European tokamak allowing regular use of alternate discharges (AC) with a time span of more than 1s. Presently ISTTOK servers as a research infrastructure enrich by several Ph.D. and master projects developed around it. As in the past it is being used for diagnostics and data acquisition systems developments and for physics studies but due to the long discharges for such a small machine. It is foreseen to increase in the near future its contribution for the studies of fusion-devices compatible materials. ISTTOK is equipped with an ATCA data acquisition system running MARTe [6] as a plasma controller framework, leading to implement very flexible control strategies.

2.2. Deuterium retention in liquid metals

Presently deuterium retention in liquid metals studies are being pursuit. As a matter of fact the use of liquid metals as plasma-facing material has been pointed out as possible alternative to the solid walls to cope with the high power loads impinging on the first wall of fusion reactors. Materials such as tin and an alloy of tin and lithium (particularly Sn with 20–30% Li) have been exposed in ISTTOK to access the discharge performance degradation induced by the enhanced impurity contamination and on their affinity to retain hydrogenic isotopes. The high Z of tin is seen as a disadvantage however the addition of lithium into a lithium-tin alloy displays beneficial properties particularly an evaporation rate of at least three orders of magnitude lower than that of pure lithium while keeping an effective Z similar to lithium. An experimental setup has been developed to produce and expose LM samples in both liquid and solid states to ISTTOK plasmas. Specimens of pure Sn and Li-Sn alloy were exposed in the ISTTOK edge plasma (r/a~0.8) for several alternating current discharges with a total duration of 250 ms. At this position the typical plasma parameters are Te~30 eV and n~1x1018 m^{-3}. Post-mortem analysis of the samples was performed by means of ion beam diagnostics. Nuclear reaction analysis (NRA) technique was applied using the D(3He,p)4He reaction to quantify the fuel retention on the samples. Deuterium retention was compared between pure Sn sample (in liquid state) and Li-Sn alloy samples (in both states). All the samples were found to have retention smaller than 0.1 %.

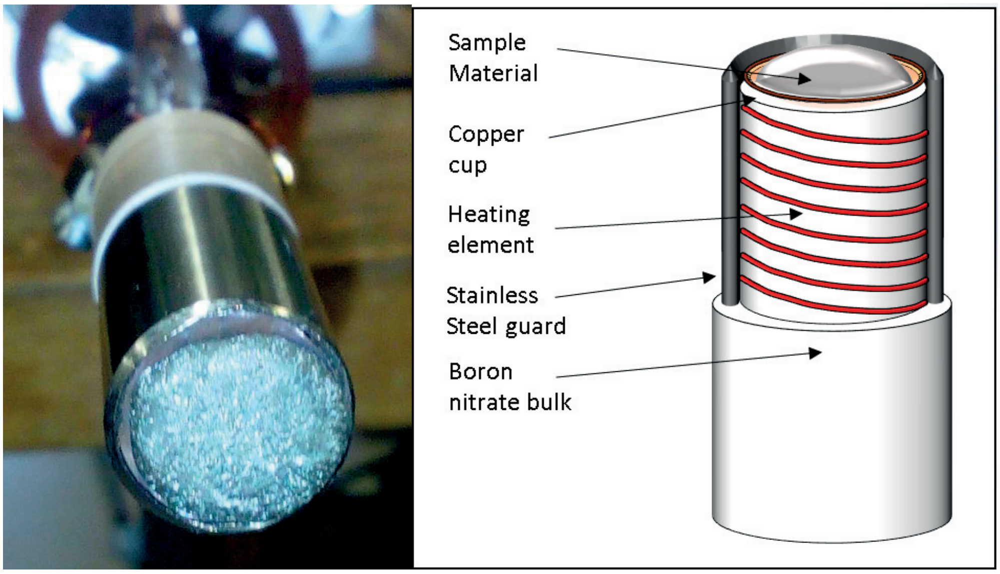

FIG. 1. Built sample holder at ISTTOK with heating capabilities.

2.3. Machine control and operation

The ISTTOK tokamak was upgraded with a plasma control system based on the Advanced Telecommunications Computing Architecture (ATCA) standard. This control system was designed to improve the discharge stability and to extend the operational space to the alternate plasma current (AC) discharges as part of the ISTTOK scientific program. In order to accomplish these objectives all ISTTOK diagnostics and actuators relevant for real-time operation were integrated in the control system.

To extend the duration of the AC discharges and the plasma stability a new magnetising field power supply was commissioned and the horizontal and vertical field power supplies were also upgraded.

The control system software was developed in C++ on top of a Linux system with the Multi-threaded Application Real-Time executor (MARTe) Framework to synchronize the real-time code execution under a 100 μs control cycle. In addition, to simplify the discharge programming, a visual Human–Machine Interface (HMI) was also developed using the BaseLib2 libraries included in the MARTe Framework.

These optimizations extended the AC current discharges duration to more than 1 s, corresponding to 40 semi-cycles without apparent degradation of the plasma parameters. This upgrade allows ISTTOK to be used as a low-cost material testing facility with long time exposures to nuclear fusion relevant plasmas, comparable (in duration) with medium size tokamaks.

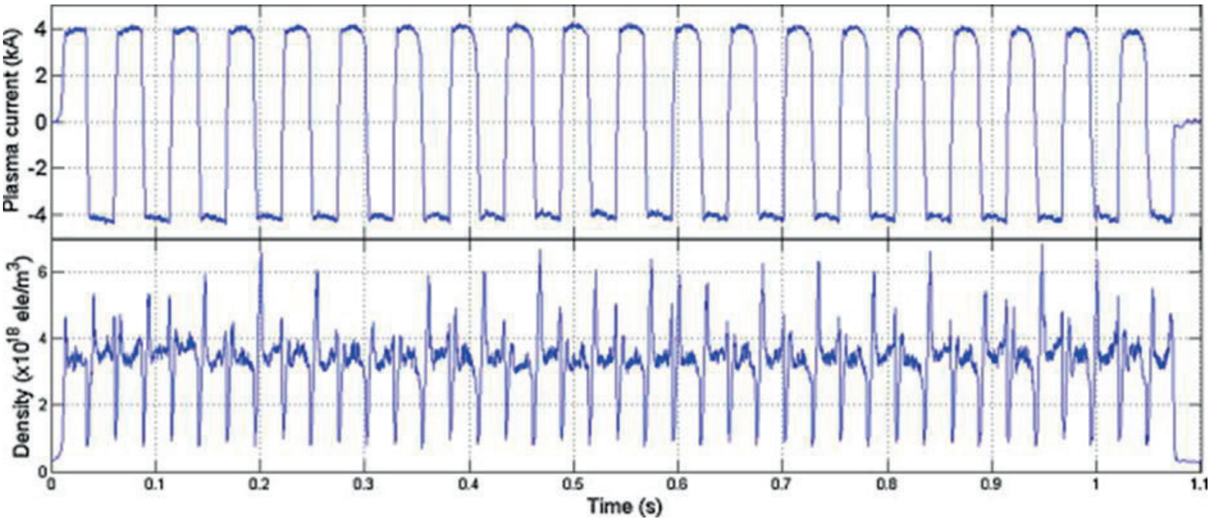

FIG. 2. Pulse #34332. Discharge with 40 AC cycles (1.07 s) using gas puffing feedback with H-alpha radiation, pre-programmed breakdown, preprogrammed AC inversions, radial/vertical position feedbacks.

3. THE HEAVY ION BEAM

3.1. Introduction

Fluctuation studies are important to understand and improve the plasma confinement and performance. Plasma density, temperature and electric potential turbulent fluctuations are associated with the anomalous transport, while the Magnetohydrodynamic (MHD) activity may impact strongly on the plasma stability and the equilibrium, for instance, through large fluctuations and/or reorganization of the plasma pressure and current, limiting the performance of fusion devices.

The Heavy Ion Beam Diagnostic (HIBD), operated with a Xe^+ ion beam on the tokamak ISTTOK, allows for the local measurements of the $n_e\hat{\sigma}_{1,2}(T_e)$ product (plasma density, n_e, times the effective ionization cross section of Xe^+ to Xe^{2+}, $\sigma_{1,2}(T_e)$, which depends on the plasma electron temperature distribution and the Xe^+ ion velocity) with an improved Multiple Cell Array Detector (MCAD)[1]. The HIBD signal conditioning system has been redesigned for low noise and wide bandwidth measurements. We shall demonstrate that the introduced improvements and modifications allow to measure and investigate the radial profile of $n_e\hat{\sigma}_{1,2}(T_e)$ fluctuations.

3.2. The ISTTOK HIBD

The HIBD on the tokamak ISTTOK (a=8.5 cm, R=46 cm, B_t=0.5 T, I_p=5 kA, $q(a)$=7.9, $<n_e>=5\times10^{18}\ m^{-3}$, $T_e(0)$~120-150 $\mathrm{eVa} = 8.5\mathrm{cm}, \mathrm{R} = 46\mathrm{cm}, \mathrm{B_T} = 0.5\mathrm{T}$) consists of an ion beam injector and detectors (primary and secondary). The injector is constituted by a plasma ion source (currently Xe^+ for the primary beam), an accelerator (up to 25keV), a beam focusing system and a steering/modulation plate system. The typical characteristics of the primary beam at the injector output are 2 μA of Xe^+ current and 3 mm of FWHM. The primary beam can be electrostatically modulated across a slit in the injector part to discriminate the plasma background signal on the detector cells. The secondary detector consists of a MCAD which collects the secondary (Xe^{2+}) ions from 12 sample volumes inside the plasma, as shown in Figure 3a and Figure 3b. Figure 1a and Figure 1b present wider beams and sample volumes for better visual perception. Experimentally, the obtained primary beam FWHM value inside the plasma is ~5.3 mm. The longest of the combined primary plus secondary ions flight time, across the plasma toward the MCAD, is ~2μs with a maximum relative time delay of ~0.5μs from the first to the last detector cells. Therefore, the measurements are considered to be instantaneous from all the detector cells within the frequencies of interest (<200 kHz). The current collected by each cell is amplified and converted to voltage by the signal conditioning system and stored by the ISTTOK data acquisition system at a rate of 2Msp/s.

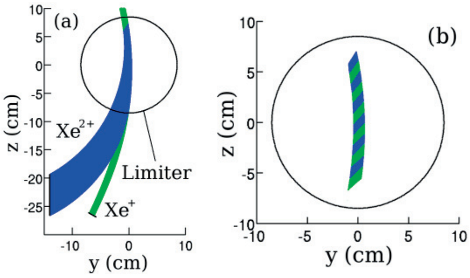

FIG. 3. (a) – Primary Xe^+ and secondary Xe^{2+} ion trajectories; (b) – sample volumes location inside the plasma.

The secondary ion current, detected on any detector cell is given by:

$$I^{2+}_{j(det)} = 2I^{+}_{0}AB\,n_e\hat{\sigma}_{1,2}(T_e)(r_j)\sigma_{1,2}(T_e(r_j))ds_{1j} \quad (1)$$

where $I^{2+}_{j(det)}$ is the secondary ion current measured at cell index j, I^{+}_{0} is the primary ion current intensity at the plasma entrance, $A = exp(-\int(n_e\hat{\sigma}_{1,2}(T_e)(s_1)\sigma_{1,2} + n_e\hat{\sigma}_{1,2}(T_e)(s_1)\sigma_{1,3})ds_1)$ and $B = exp(-\int(n_e\hat{\sigma}_{1,2}(T_e)(s_2)\sigma_{2,3})ds_2)$ are the primary and secondary beam attenuation factors along the respective trajectories, $n_e\hat{\sigma}_{1,2}(T_e)(r_j)$ is the plasma density in the sample volume at position r_j, $\sigma_{1,2}(T_e(r_j))$ is the effective ionization cross section for $Xe^++e^-\rightarrow Xe^{2+}+2e^-$, which depends on the electron temperature – $T_e(r_j)$, and ds_{1j} is the length of the sample volume j along the primary beam trajectory.

For T_e>100 eV, the effective cross section $n_e\widehat{\sigma}_{1,2}(T_e)$ is weakly sensitive to variations of T_e, while for T_e < 100 eV, the generation factor $n_e\widehat{\sigma}_{1,2}(T_e)n_e\widehat{\sigma}_{1,2}(T_e)$ depends on both n_e and T_e. Therefore, fluctuations on $n_e\widehat{\sigma}_{1,2}(T_e)n_e\widehat{\sigma}_{1,2}(T_e)$ can be attributed to either n_e and/or T_e fluctuations and the $n_e\widehat{\sigma}_{1,2}(T_e)$ profile can roughly be interpreted as a proxy for the pressure profile.

3.3. Signal conditioning system

The HIBD signal conditioning system was improved to allow a low noise/wide bandwidth simultaneous amplification of all the signals coming from the detectors. The whole amplification system consists of two PCBs (Printed Circuit Boards) which hold and feed (power and signals) up to 50 amplifier modules connected side by side in several layers, Figure 4a. The passive PCB (front PCB in Figure 4a) connects directly to the tokamak flange with two D25 connectors and brings the input signal and reference (ground – GND) to the amplifier modules. The input GND reference is designed in a star connection to avoid induced currents and consequently undesired noise in the reference signal ground. The active PCB (back PCB in Figure 2a) feed the amplifiers and brings the output signals to the ISTTOK data acquisition system. The amplification system, powered by batteries to reduce noise in the power lines, is shielded by a Mu-metal box directly connected to the tokamak flange (Figure 2b) in order to reduce the electromagnetic induced noise.

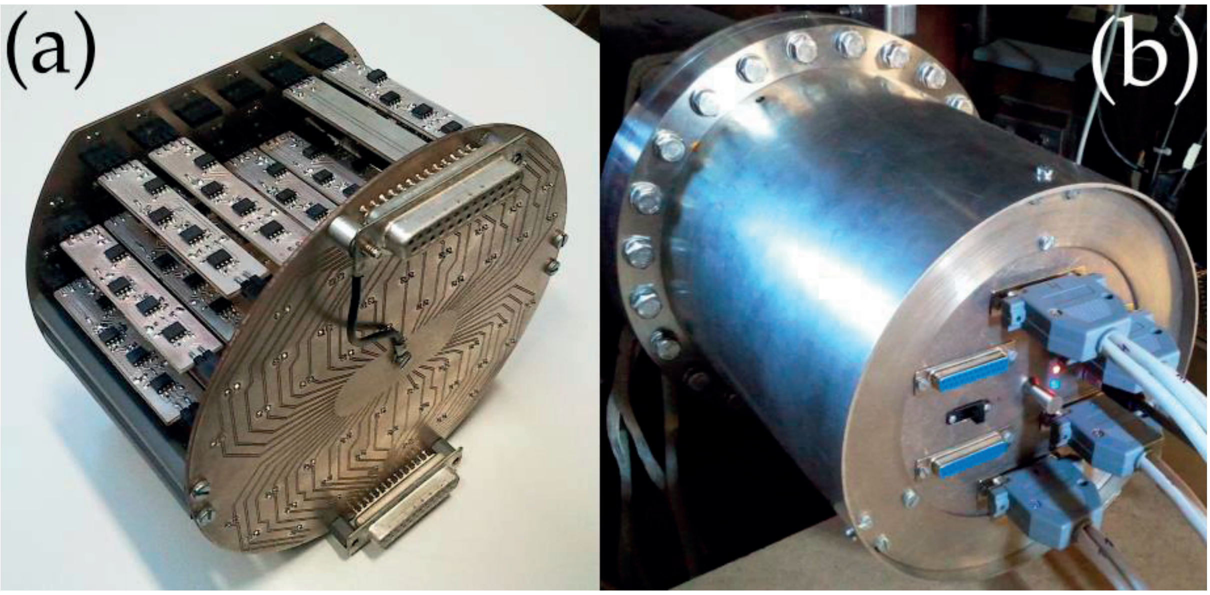

FIG. 4. (a) – Whole amplification system currently with 29 amplifier modules. (b) – Arrangement on the tokamak diagnostic port.

The prototype of a trans-impedance amplifier module has been described previously [1], and its final version is shown in Figure 5. Every secondary current amplifier module is characterized by a gain of 20MV/A, a bandwidth of 0–400kHz and an equivalent input noise current of 0.4nA$_{rms}$. The typical secondary detected currents are in the range of 10 to 100 nA. The signal-to-noise ratio of fluctuations (given by the ratio of the variances) ranges from 1.5 to 1300 depending on the detector cell no. and on the applied biasing voltage [1].

3.4. Results and analysis

3.4.1. $n_e\hat{\sigma}_{1,2}(T_e)$ *profile during a MHD event*

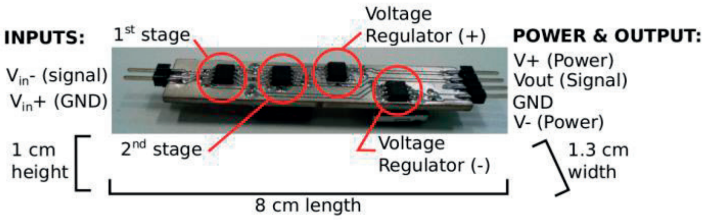

FIG. 5. Trans-impedance amplifier module.

The results presented in this subsection were obtained in the ISTTOK discharge # 36133, with B_t=0.49T, I_p=-6kA and $<n_e>=4x10^{18}m^{-3}$, characterized by repetitive bursts of MHD activity and density drops, as shown in Figure 6. Figure 7 presents the reconstructed $n_e\hat{\sigma}_{1,2}(T_e)$ radial profile retrieved with an algorithm[3] which takes into account the primary beam attenuation (enough to reconstructs accurately the normalized profile). The profile is presented during the time window of 112.8–113.2 ms where a growing global fluctuation and sudden "crash", can be observed. During this event, the transition from a peaked to flat $n_e\sigma_{1,2}(T_e)$ profile takes place. However, the integrated value of $n_e\hat{\sigma}_{1,2}(T_e)$ remains the same (variation < 2%) before and after the crash, while the line integrated density signal drops off 40%. The observed property can more probably be due to a combined response of the $n_e\sigma_{1,2}(T)$ product on variations in n_e and T_e as mentioned in Section II. In that instance a flattening of the $n_e\sigma_{1,2}(T_e)$ profile could suggest a major change of the plasma current profile (pressure dependent) without major loss (total current variation of only ~ 5% was observed during crash).

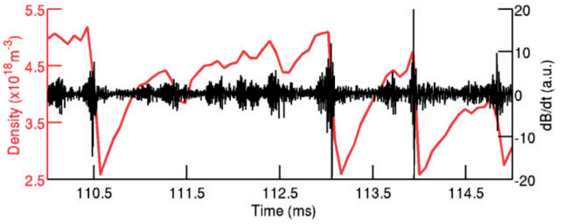

FIG. 6. Line integrated density (r=0) from interferometer and Mirnov coil signal for the discharge #36133.

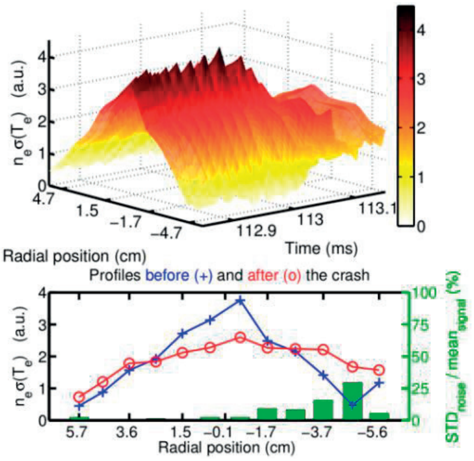

FIG. 7. (top) – $n_e\hat{\sigma}_{1,2}(T_e)$ *profile; (bottom) –* $n_e\sigma_{1,2}(T_e)$ *profile averaged over time before (112.85-113.03ms) and after the crash (113.09-113.15ms). Radial position:* $r=(z/|z|)(y^2+z^2)^{1/2}$*. The bars indicate the typical errors (due to the background noise) in the measurements.*

In order to assess the origin of the $n_e\widehat{\sigma}_{1,2}(T_e)$ profile behavior in more detail and to interpret/validate the HIBD results Figure 6 shows the combined view of the $n_e\widehat{\sigma}_{1,2}(T_e)$ profile, the signals from the Mirnov coil and the line integrated density during the MHD event. The Mirnov coil signal indicates a violent and unstable growing before the crash. The $n_e\widehat{\sigma}_{1,2}(T_e)$ profile starts to fluctuate mainly in the plasma core with growing amplitude up to 30% of the absolute value. As illustrated, the fluctuations of $n_e\widehat{\sigma}_{1,2}(T_e)$ profile are well correlated with the MHD fluctuations. After the crash (from 113.08 ms) the MHD activity and fluctuations in the $n_e\widehat{\sigma}_{1,2}(T_e)$ profile are significantly reduced and the plasma remains in a "quiescent" state during some time. The properties of the observed event are quite similar with the plasma relaxation events due to stochastic perturbations of the magnetic field lines [4]. These results demonstrate that the $n_e\widehat{\sigma}_{1,2}(T_e)$ profile is strongly linked with the MHD activity.

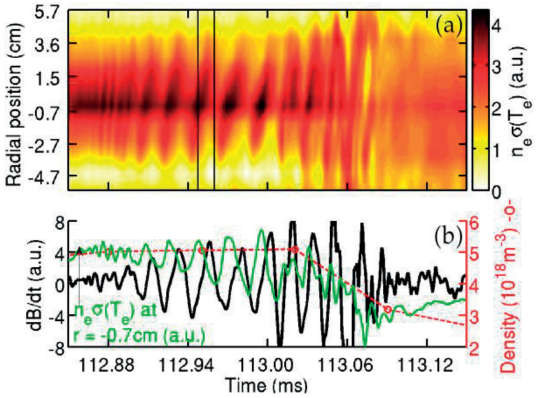

FIG. 8. (a) – $n_e\widehat{\sigma}_{1,2}(T_e)$ profile; (b) – Mirnov coil no. 12 signal, density from interferometer diagnostic and $n_e\widehat{\sigma}_{1,2}(T_e)$ at r=-0.7cm (normalized to interferometer density at 112.88 ms).

The poloidal mode number *m* of the dominant MHD mode fluctuation has been derived, by cross correlating a HIBD signal with all the magnetic signals from Mirnov coils (poloidal array of 12 coils equally spaced), and is shown in Figure 9 for the signal of cell no. 4 and a time window of 2 ms. A well-defined pattern, resulting from the high correlation with each Mirnov coil, is clearly observed with a period of ~16 μs. This period corresponds to the dominant frequency of ~63 kHz and is identified as an *m*=2 mode. For fluctuations with an even mode number, two radially symmetric (with the plasma center) maximums/minimums should be observed in Figure 8a at any time. Instead, only one maximum/minimum is observed (as indicated by the vertical lines at t~112.95 ms), that is apparently moving in time from the bottom to the top of the plasma. This behavior may be explained by a shift in the primary beam trajectory with respect to the mode rotation axis. In this case the observed slope of the maximum/minimum along time would result from the rotation of the mode.

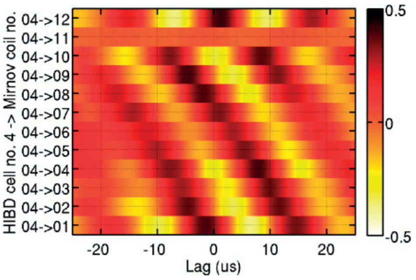

FIG. 9. Cross correlations between the secondary HIBD cell no. 4 and all the Mirnov coils (coil no. 11 has no signal).

3.4.2. Tearing mode signature

A tearing mode (TM) is usually associated to a local flattening of the pressure profile driven primarily by fast parallel heat transport inside the magnetic island although plasma density is also flattened on longer time scales. In the discharge #36540, configured to study the evolution of MHD modes with slow ramp-up plasma current (from 4 to 7 kA in 18 ms), a strong indication of spatial and temporal TM signature has been identified by filtering the HIBD signals at the dominant MHD frequency, determined from the Mirnov coil signals. The TM like signature was identified when I_p=6 kA. Figure 10 presents the filtered HIBD signals ($\mathrm{n_e}\widehat{\sigma}_{1,2}(\mathrm{T_e})$ fluctuations). A clear phase reversal between two successive cells (marked by dashed line rectangles) is observed. The TM spatial structure indicates that it has an even m mode number with the rational flux surfaces located roughly at r ~ +2 cm and r ~ -1.5 cm. From the Mirnov coil signals, the observed TM appears to be an m=4 mode. The asymmetry on the radial TM location indicates that plasma current centroid is slightly shifted upward, which is in agreement with the ISTTOK plasma position measurement [5]. The lower fluctuation amplitude for the central secondary cells no. 5, 6 and 7 can be explained by the nature of the measurement, due to the $\sigma_{1,2}(T_e)$ flattening above 100 eV, as mentioned previously. The lower fluctuation amplitude observed for the first and last cells (1 and 12) is simply due to the lower average value of n_e and T_e observed in the outer region of the plasma and the larger distance from the TM location.

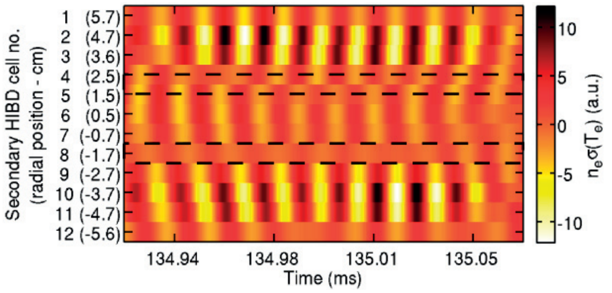

FIG. 10. HIBD signals filtered with a 20 kHz bandwidth filter centred at 65 kHz. Dashed line rectangles indicate the location of the phase reversal.

3.4.3 Real-time control

The HIBD is usually operated with the ion beam modulated in order to discriminate and remove the background noise from the collected signals. A fast beam modulation is essential to remove fast background noise variations. In this way, the HIBD was upgraded to allow the fast beam modulation up to 150 kHz. With such modulation frequency it is possible to obtain up to 15 $\mathrm{n_e}\sigma(\mathrm{T_e})$ profiles in one ISTTOK real-time cycle (100 μs). The beam is square modulated (in half of the period the beam is ON and the other half is OFF). In order to provide a single profile in real-time, it is necessary first to detect the time interval when the beam is ON. Then, perform a signal average in each time zone (ON and OFF) and the difference between these two mean amplitudes is the real ion beam current collected on the detector cell. Since an average should be performed to remove the background noise of the HIBD signals below 100 μs latency, the processing must necessarily be performed at the hardware acquisition stage (FPGA - Field Programmable Gate Array) before reaching the real-time software framework (MARTe - Multi-threaded Application Real-Time executor). ISTTOK data acquisition [6, 7] consists of ATCA boards with an incorporated FPGA. The raw data acquisition is performed at 2Msps. The fast processing for removing the background noise in the HIBD signals is performed in the FPGA. In this way, the FPGA provides directly the processed ion beam current signal to MARTe in a much faster time scale than the

ISTTOK MARTe real-time cycle. Finally, MARTe grabs the input data, performs the calculations of the vertical plasma position and sends the results to the horizontal field power supply. Figure 11 shows a simplified diagram of the complete setup.

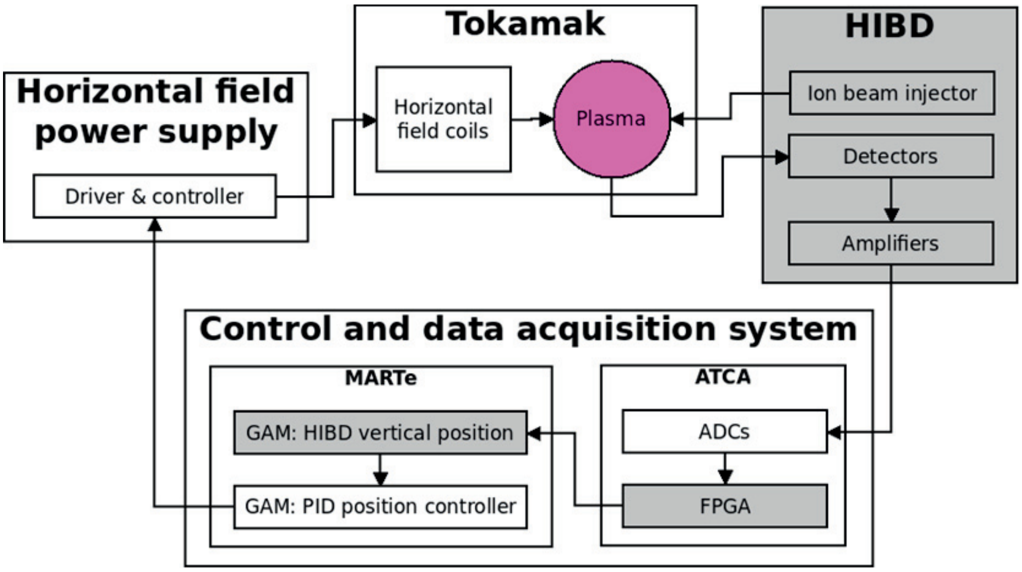

FIG. 11. Simplified diagram of the HIBD closed loop integration for plasma vertical position measurement and control. GAM stands for Generic Application Module. The grey boxes represent the performed changes and additions related to the ISTTOK control and feedback system.

For validation and calibration purposes, off-line HIBD results for the plasma position have been obtained and compared with the ones from the Langmuir Probes (LP). Figure 12 shows the over-plot of the vertical plasma position from the HIBD and LP diagnostics in three different cycles: 1st cycle ended in a disruption, 2nd cycle with edge biasing polarization and the 3rd cycle is a normal cycle. The plasma position from the HIBD signals is calculated with the centre of mass of the $n_e\sigma(T_e)$ profile. Therefore any change in the vertical position represents a change in the whole plasma column as in opposite to the vertical position given by LPs which is obtained from two radially opposite local measurements in the plasma periphery. Despite the big differences in the nature of the measurement, a qualitative agreement between both diagnostics is observed at the beginning of the discharge. On the other hand, in the disruption cycle a clear disagreement between the diagnostics is observed in the last 5ms. In the biasing cycle, the LPs indicate a fast change in the plasma position (goes to near 0) which cannot happen in such time scale. In the normal cycle a small discrepancy is observed from the half until the end of the cycle.

The FPGA firmware, further than acquiring ADC data, is programed with an algorithm to remove the background noise from the HIBD raw data signals. The algorithm detects the transitions between beam ON and OFF and vice-versa and performs the sum of a predefined number of samples (depending on the modulation frequency) after each transition. After each control cycle, the FPGA returns the last obtained difference between the ON and OFF phase sums (corresponding to the real ion beam current multiplied by the number of predefined samples). Figure 13 shows a visual description on how the algorithm works in the FPGA.

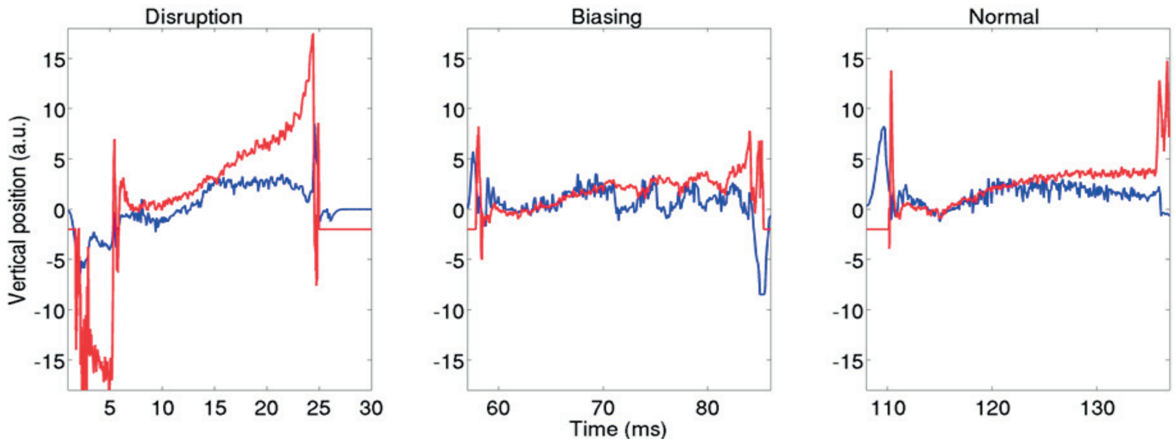

FIG. 12. Plasma vertical position (HIBD in red and LPs in blue) in three different positive cycles of one AC discharge: disruptive, biasing and normal. The signals were normalized and offset in order to have a better visual comparison.

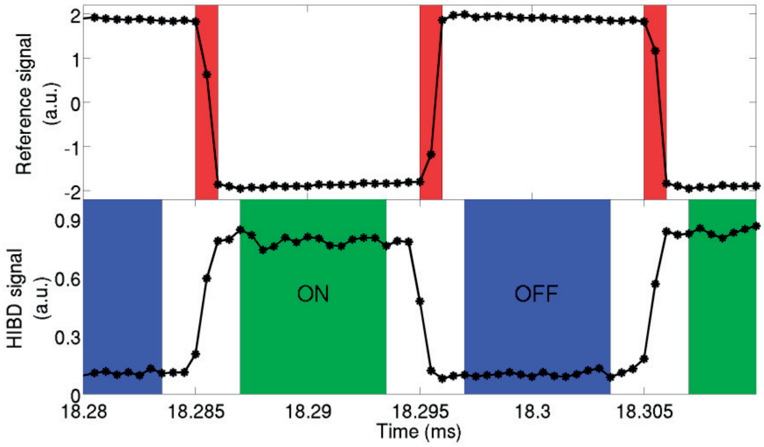

FIG. 13. Red time slices (top plot) correspond to the transition detections while green and blue time slices to the ON and OFF sums of the predefined number of samples (bottom plot).

4. SUMMARY

The ISTTOK HIBD signal conditioning system has been upgraded for the radial profile measurements of $n_e\hat{\sigma}_{1,2}(T_e)$ fluctuations. The first HIBD results show that MHD activity has a global structure affecting the entire $n_e\hat{\sigma}_{1,2}(T_e)$ profile. The spatial structure of a TM (identified as *m*=4 mode) was clearly observed. These results demonstrate the capabilities of the HIBD for measuring the radial distribution of MHD fluctuations. Currently, the HIBD has been used for the plasma core fluctuation studies (mainly MHD) but future works related with turbulent fluctuation measurement on the SOL are planned as well.

An overview of the HIBD real-time control integration was presented as well. The current development status is at the FPGA coding stage. Real-time processed data from the FPGA was compared with post-processed data showing a very good agreement between both results and demonstrating the correct performed calculations in the FPGA. The remaining steps to finalize the integration will be MARTe programming and control tests on the tokamak ISTTOK.

ACKNOWLEDGEMENT

This research work was supported by EURATOM and carried out within the framework of the European Fusion Development Agreement. It has also benefited from support from the IAEA through Research Agreement POR 17003 within the Coordinated Research Project F1.30.14 on “Utilization of the Network of Small Magnetic Confinement Fusion Devices for Mainstream Fusion Research”. IST activities also received financial support from “Fundação para a Ciência e Tecnologia” through project Pest-OE/SADG/LA0010/2013. The views and opinions expressed herein do not necessarily reflect those of the European Commission.

REFERENCES

[1] HENRIQUES, R.B., NEDZELSKIY, I.S., MALAQUIAS, A. and FERNANDES, H., New detection system and signal processing for the tokamak isttok heavy ion beam diagnostic, Rev. Sci. Instrum. **83** (2012) D705.

[2] CABRAL, J. A. C. et al, Improved 20 keV injection system for the heavy-ion-beam diagnostic of the tokamak ISTTOK, Rev. Sci. Instrum. **74** (2003) 1853.

[3] MALAQUIAS, A., NEDZELSKIY, I.S., VARANDAS, C.A.F., and CABRAL, J.A.C., Evolution of the tokamak isttok plasma density and electron temperature radial profiles determined by heavy ion beam probin, Rev. Sci. Instrum. **70** (1999) 947.

[4] ERZHONG, L., LIQUN, H., IGOCHINE, V., DUMBRAJS, O., and KAIYUN, C., Understanding complex magnetohydrodynamic activities associated with a relaxation in the ht-7 tokamak, Plasma Phys. Control Fusion **53** (2011).

[5] CARVALHO, I.S., FERNANDES, H., DUARTE, P., SILVA, C., FIGUEIREDO, H.F.C., HEKKERT, T., Isttok real-time control assisted by electric probes, IOP J. Phys. Conference Series **591** (2015) 012008

[6] NETO, A.C., SARTORI, F., PICCOLO, F., VITELLI, R., DE TOMMASI, G., ZABEO, L. et al., Maerte: a multiplatform real-time framework, IEEE transactions on Nucl. Sci. **57** 2, 479–486.

[7] CABRAL, JAC, FERNANDES, H, FIGUEIREDO, H., VARANDAS, CAF, Operation of the tokamak istokk in a multicycle alternating flat-top plasma current regime, Nucl. Fusion **37** 11, 1575

OPERATIONS OF KTM FOR PLASMA FORMATION AND START-UP STUDIES

B.J. CHEKTYBAEV*, G.V. SHAPOVALOV*, A.D. SADYKOV*, E.B. KUPISHEV*

*Institute of Atomic Energy of NNC RK, Kurchatov, Kazakhstan

Abstract

KTM tokamak is in preparation for the start-up, so the work carried out to study the processes starting current plasma and diagnostics of the first stage testing. Two schemes were used to start-up the plasma current with a positive and negative derivation of the magnetic flux in the central solenoid. Power supply poloidal coils were high voltage capacitor banks, preionization system based on the microwave magnetron with a frequency of 2.45 GHz radiation. Measurements were made of the toroidal magnetic field in the vertical and radial directions to verify accordance with the specified characteristics of the field, the level of the ripple of the toroidal magnetic field using Hall sensors.

1. INTRODUCTION

Our investigations provided in the framework of the Coordinated Research Project (CRP) of the International Atomic Energy Agency (IAEA) “Utilization of the Network of Small Magnetic Confinement Fusion Devices for Mainstream Fusion Research” during the fulfillment of the 3-year activity.

2. OPERATIONS OF KTM FOR PLASMA FORMATION AND START-UP STUDIES BY THE KTM TOKAMAK TEAM

2.1. Breakdown study with positive derivation of magnetic flux in central solenoid

2.1.1. Equipment used and scheme of the experiment

Several systems have been used to study the breakdown of the positive derivation of the magnetic flux in the CS coil: three high-voltage capacitor batteries, a preionization system based on magnetron radiation of 2.45 GHz, the vacuum chamber (VC), poloidal and toroidal coils of the KTM tokamak [1], not staffing system of the parameters registration, the diagnostics of the first stage (sensors loop voltage, video, Rogowski coil inside VC, diagnostics H_α-D_α), the MMF computer code, developed in NIIEFA name Efremov, Russia. The scheme of the experiment is presented in Figs 1 and 2. Figure 3 shows the configuration of magnetic fields with null field in the poloidal cross section VC of the KTM tokamak obtained in the experiment. Figure 4 shows a diagram of the current in the coil circuits CS, PF2, PF5, PF1, PF4 and PF3, PF6.

2.1.2. Methods and experimental results

The breakdown has been realized on the increasing of CS current in the time interval 0 – 0.02 s at a distance of 0.3 m from the inside wall of the VC, where there are the electron cyclotron resonance layer and the center of the null field. The toroidal electric field E_t in the center of the null field is equal to 1.82 V/m. It is known that the breakdown can be achieved in the absence of a proper null in case where the ionization avalanche dominates over the losses [2, 3, 4 and 5].

$$E_t \cdot B_t / B_{pol} \geq 10^3 Vm^{-1} , \qquad (1)$$

where B_t – the magnitude of the toroidal magnetic field at the major radius of null region, B_{pol} – the magnitude of the poloidal stray field at the null region boundary.

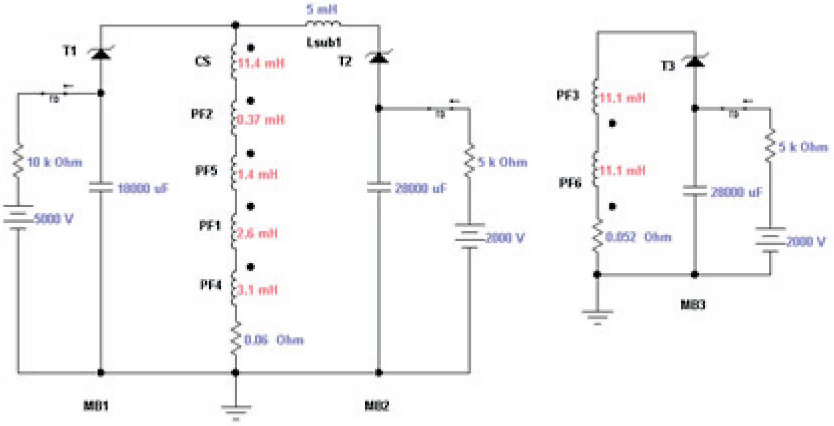

FIG. 1. The scheme of connection of poloidal coils of KTM to capacitor powersupplies (the point corresponds to the coil beginning).

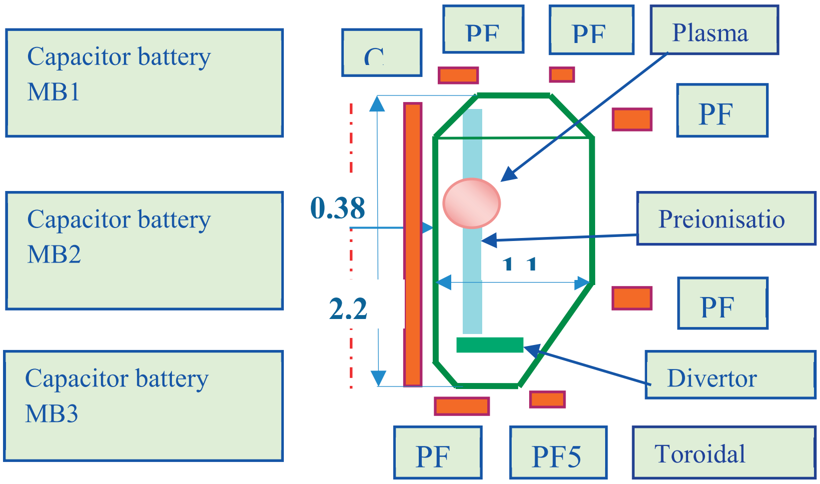

FIG. 2. The scheme of experiments to obtain the breakdown in the vacuum chamber of KTM tokamak.

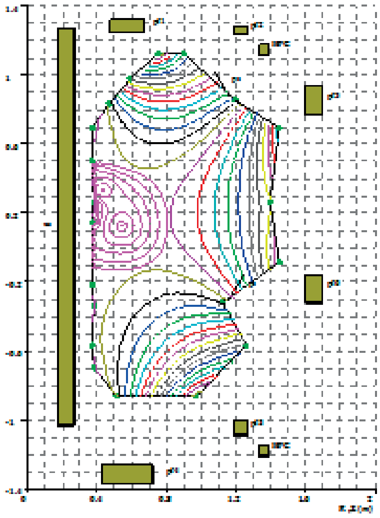

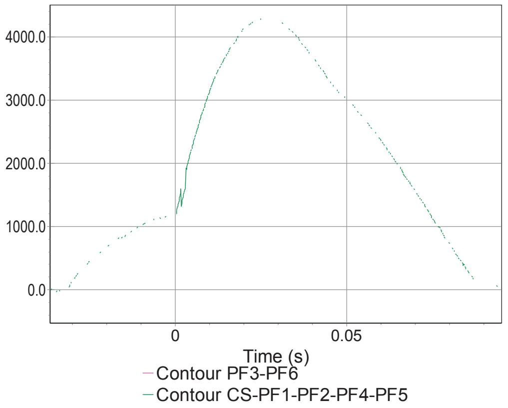

FIG. 3. Configuration of the magnetic field, obtained in the experiment (violet -module, rest- flux).

FIG. 4. Currents in the contours of the poloidal coils, obtained in the experiment.

Since according to (1) the toroidal electric field E_t was insufficient for the breakdown, electron cyclotron preionization with microwave radiation frequency of 2.45 GHz and a power of 2 kW was used.At about the same parameters of the breakdown was obtained preionization at the START tokamak. In Figs 5 and 6 results of receiving breakdown on KTM tokamak for a case with positive change of a magnetic flux in the CS coil are shown. Plasma current – about 0.5 kA near to internal round, registered by Rogovsky coil, internal for a vacuum chamber, as pulse excess over the eddy current induced on a divertor is received. It is not possible to separate these currents as the mesuraments of the current of the divertor is not provided on the tokamak KTM. However, the bright glow of the plasma on the video frame in Figure 6 shows the obtained initial phase of the breakdown.

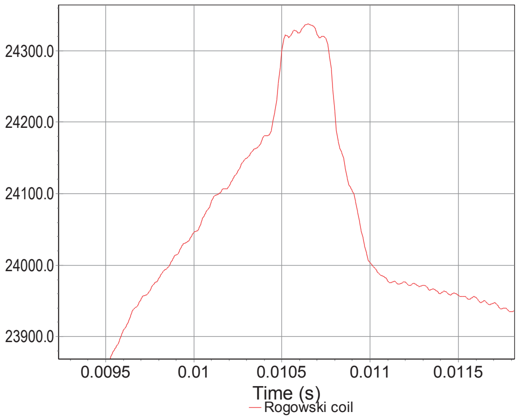

FIG. 5. Current obtained at the breakdown.

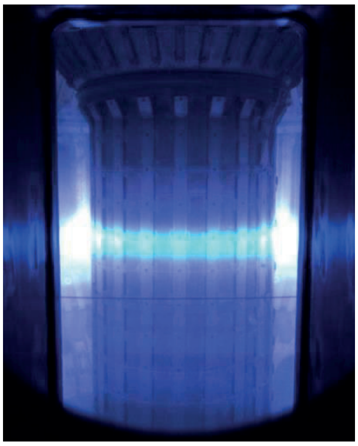

FIG. 6. Video frame of the plasma discharge at the breakdown.

2.2. Research of breakdown with negative derivation of magnetic flux in central solenoid

2.2.1. Equipment used and scheme of the experiment

To study the breakdown of the negative derivation of the magnetic flux in the CS coil four high-voltage capacitor batteries, system preionization based magnetron radiation of 2.45 GHz, the vacuum chamber (VC), poloidal and toroidal coils of the KTM tokamak, staffing system of the parameters registration, the diagnostics of the first stage (sensors loop voltage, advanced video system, Rogowski coil inside VC, AXUV diagnostics, review bolometer), the MMF computer code, developed in NIIEFA name Efremov [6], Russia, working gas - argon have been used. Figure 7 shows the scheme of the experiment. Figure 8 shows photos of the switch current of the CS coil.

2.2.2. Methods and experimental results

The breakdown was realized in the decrease of the CS current at time interval 0.03–0.05 s at a distance of 0.2–0.3 m from the inner wall of the VC. The toroidal electric field Et in the center of the null field is 1.3 – 1.1 V/m. Since according to the estimate of equation (1) the toroidal electric field was insufficient for the breakdown, the electron-cyclotron preionization with a microwave radiation frequency of 2.45 GHz and power of 2 kW was used.

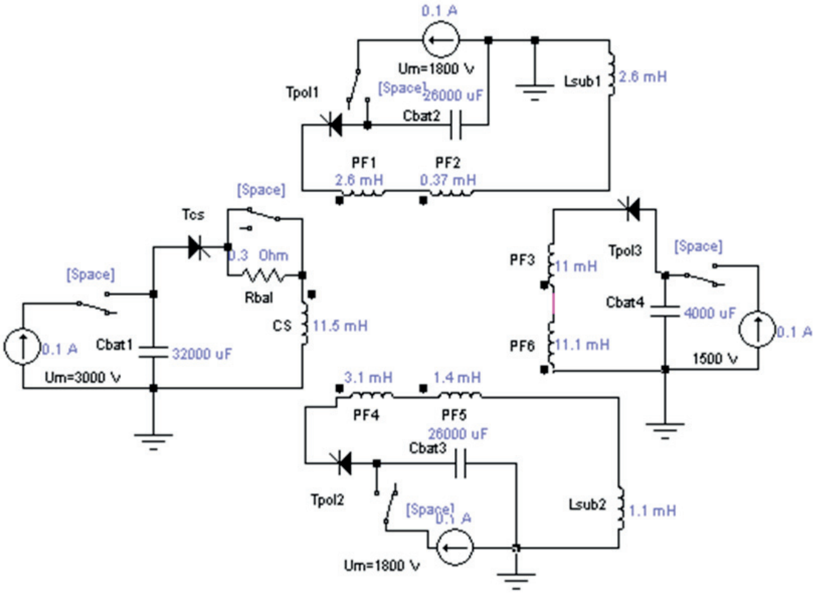

FIG. 7. The power supply circuit of the poloidal field coils of KTM tokamak for experiments.

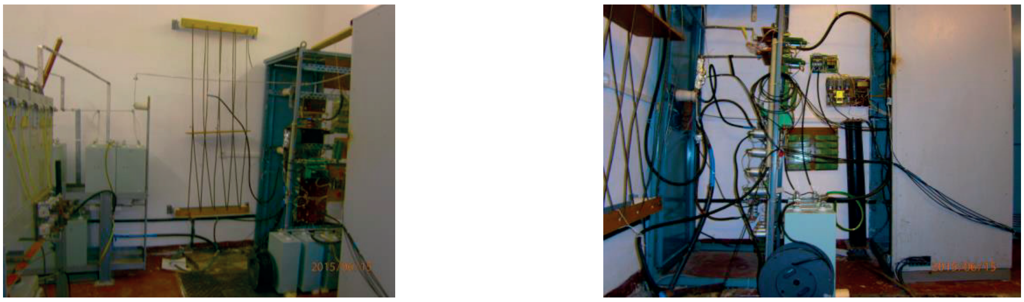

a) b)

FIG. 8. High-voltage CS current switcher: a) at the left - capacitor bank, in the center - ballast resister; b) assembly of load-bearing elements of a current switcher.

Figure 9 shows currents in the poloidal coils measured in the experiment. Figure 10 shows measured signals of voltage loops, located near the expected breakdown. Figure 11 shows the results of reconstruction of module of magnetic field in the vacuum chamber of KTM obtained by the scenario of currents in the poloidal field coils shown in Figure 9. Figs 12, 13, and 14 show diagnostics used in experiments, their placements and angles of view.

Figs 15 and 16 show the signal diagnostics (AXUV bolometer and review) on the experiment. Figure 17 shows two video frames (at 37 and 45 ms) of a plasma discharge in a vacuum chamber for the experiment. At 37 ms it shows that the plasma fills the half of the vacuum chamber, indicating the preionization and the initial formation of the plasma column. At 45 ms it shows the formation of the plasma column as a result of the breakdown and initial plasma current. At the same time, there are pulse signals AXUV diagnostics and angle of view of bolometer are shown in Figs 15 and 16.

Thus, the obtained modes of the currents in the poloidal coils are formed in order to null the magnetic field in the middle part of the vacuum chamber at the time points with a negative change of magnetic flux in the CS coil. In the experiment observed the preionization of the working gas around the inner bypass through radiation in the vacuum chamber of the microwave wave with a frequency of 2.45 GHz and a few milliseconds was observed the formation of a plasma filament in place of null magnetic field. These results can be considered the completion of the initial phase of breakdown to obtain the plasma column.

2.3. Toroidal field configuration measurements

Toroidal field (TF) plays an important role in plasma creation and confinement in tokamak device. The main requirements for TF are isotropy and absence of error fields which can be due to inaccuracy of assembly. In all tokamak devices, the finite number and toroidal extension of the toroidal field coils causes a periodic variation of the toroidal field from its nominal value, called toroidal field ripple. TF ripple breaks the axisymmetry of the magnetic field and enhances particle losses, in particular energetic ions. In association with all above saying on the start up operations of KTM it will actually make measurements of real characteristic of toroidal magnetic field. For TF coils three parameters are measured, the first one is the B_t value, the second is the ripple and the third is the error field in the R and Z directions.

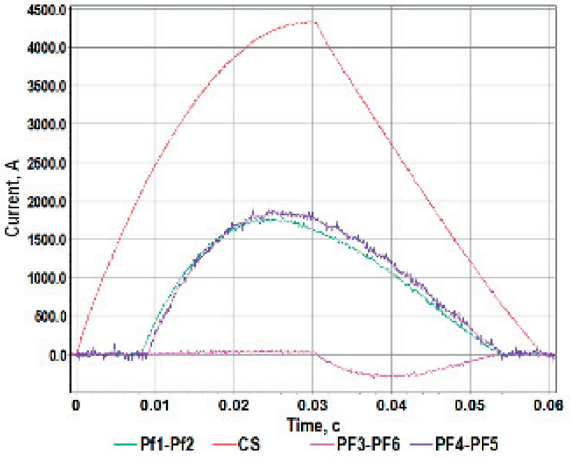

FIG. 9. *Currents in the poloidal field coils on the experiment.*

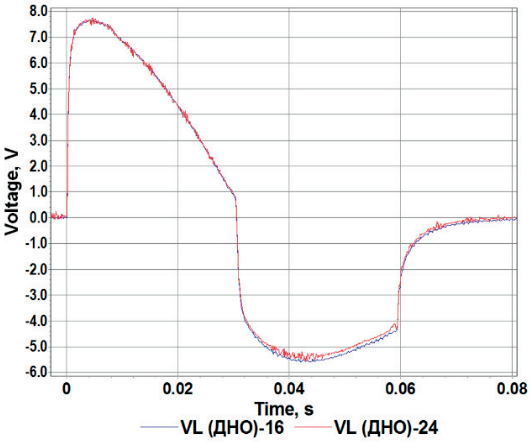

FIG. 10. *Voltage loops around the inner cylinder of the vacuum chamber.*

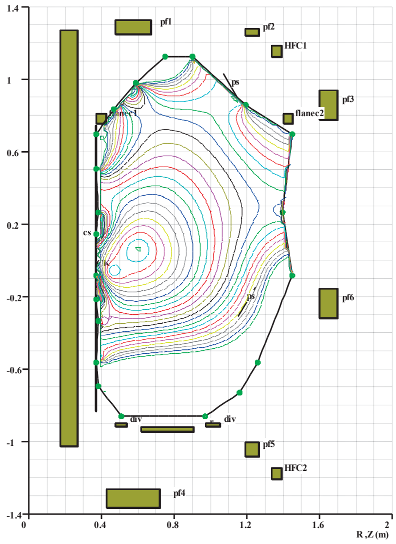

FIG. 11. *Isolines of magnetic field module (Gs) in the poloidal cross section of vacuum chamber of the KTM tokamak.*

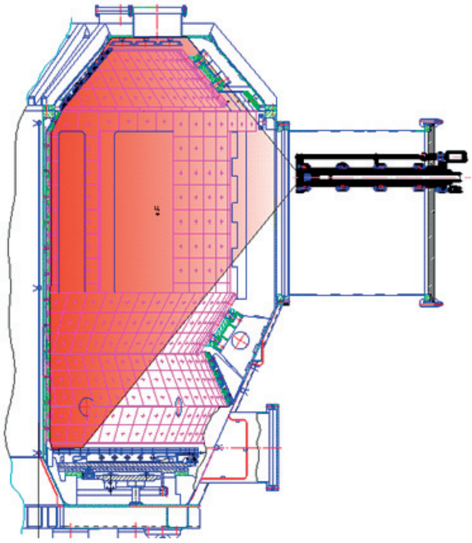

FIG. 12. *Angle of view of imaging system.*

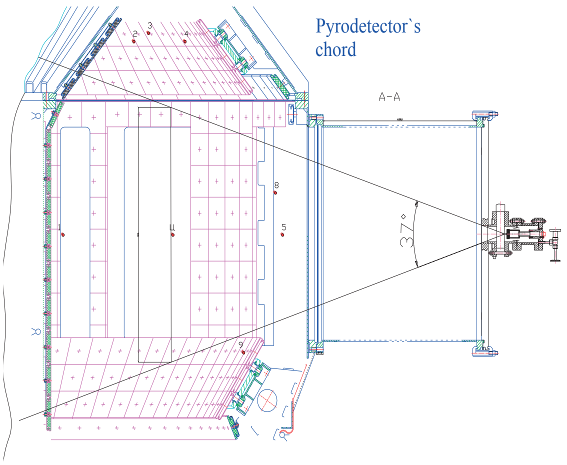

FIG. 13. *Angle of view of bolometer.*

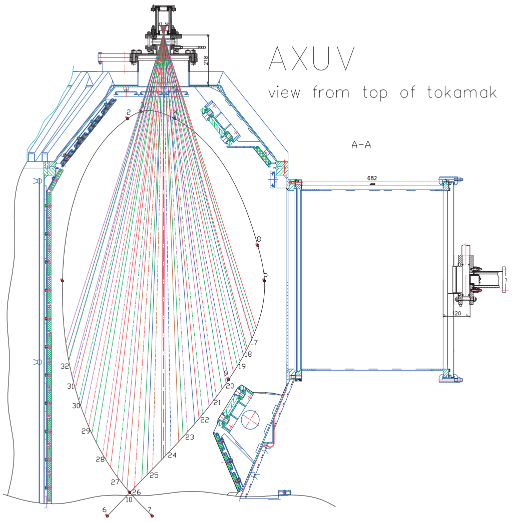

FIG. 14. *Vertical viewing chords of the AXUV.*

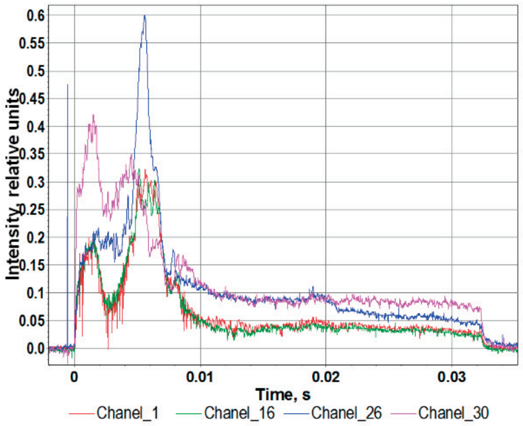

FIG. 15. *Signals from AXUV diagnostics along the chords (channels) at the discharge.*

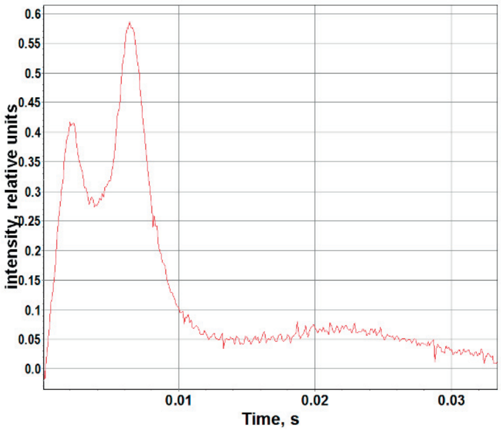

FIG. 16. *Signal from bolometer.*

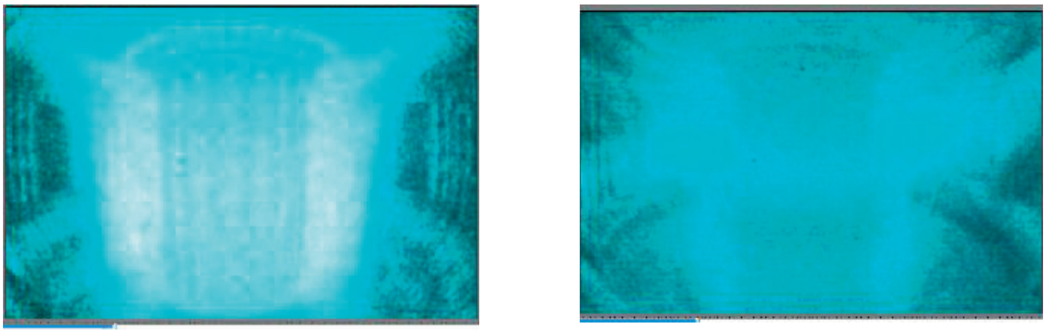

37 ms

45 ms

FIG. 17. *Video frames captured by fast camera of imaging system at the discharge.*

2.3.1. Construction of KTM toroidal coil

The toroidal field coil (TFC) system of KTM tokamak is designed to create magnetic field B_θ = 1 T on major radius R = 0.9 m. Cross section of the TFC is shown in Figure 18. TFC consists of 20 toroidal coils arranged symmetrically the angle between the coils is 18 degrees. General view of the KTM tokamak is shown in Figure 19. Each toroidal coil contains of 4 turns. TFC is «warm» coil cooling by water through special technological holes inside coils.

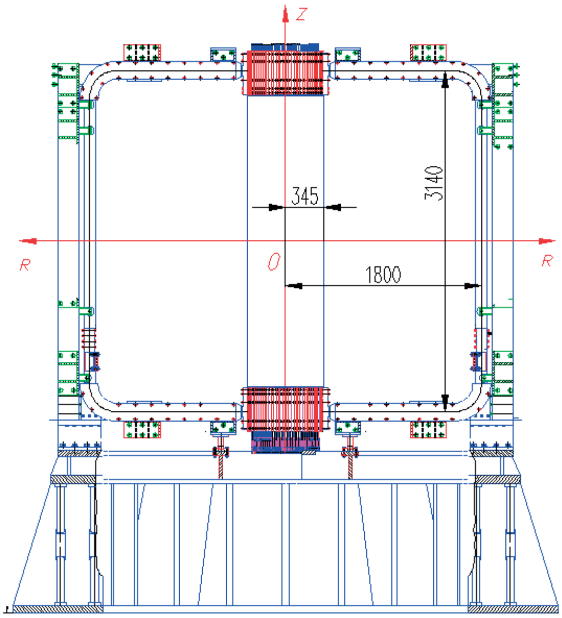

FIG. 18. Cross section of KTM toroidal coil.

FIG. 19. Overall view of KTM.

2.3.2. Features of Hall sensors for KTM

Hall sensors were chosen for measurements of toroidal magnetic field because of their advantages (small size, the point field measurements, accuracy, wide measuring range, high frequency, measure constant field) compared to other inverters.

On Figure 4 is shown Hall sensor model A1321LUA of Allegro Microsystems which were used for measurements. Main characteristics of Hall sensors are given in Table 1.

TABLE 1. A1321LUA HALL SENSOR SPECIFICATIONS

Parameters	Value
Maximum measured magnetic field	440 Gs
Output voltage without magnetic field	2,5 V
Supply Voltage	5,0 V
Sensitivity	5 mV/Gs
Output Bandwidth	30 кHz
Dimensions (LxWxH)	4x3x1,5 mm

2.3.3. Experimental measurement of toroidal magnetic field of KTM tokamak

Measurement scheme of the toroidal field in the VC is shown in Figs 20 and 21. For TF magnetic measurements was developed a special crossbar which allows placing 30 Hall sensors.

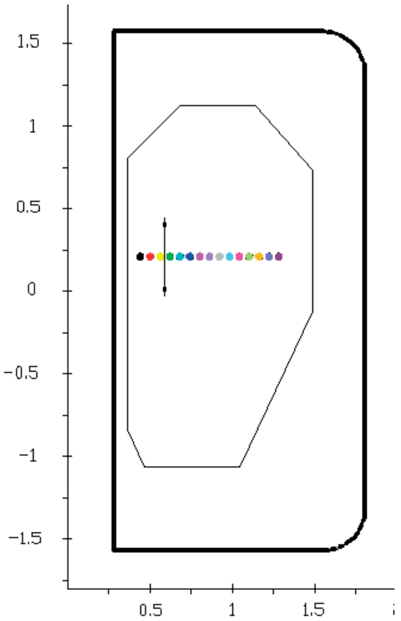

FIG. 20. The measurement system of $B_t \propto 1/R$.

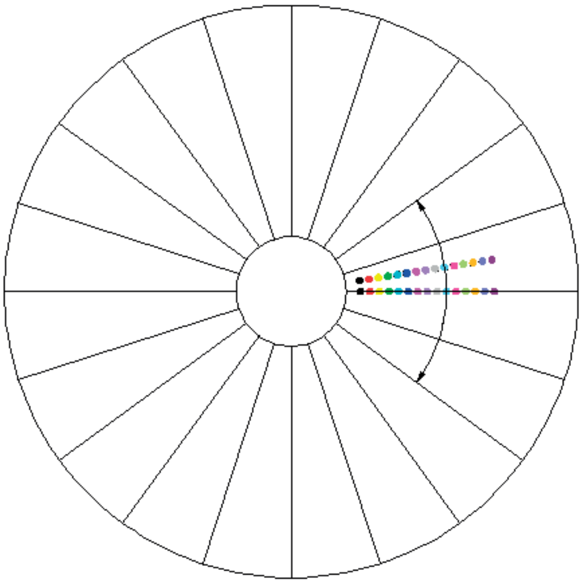

FIG. 21. The measurement system of TF error field and ripple.

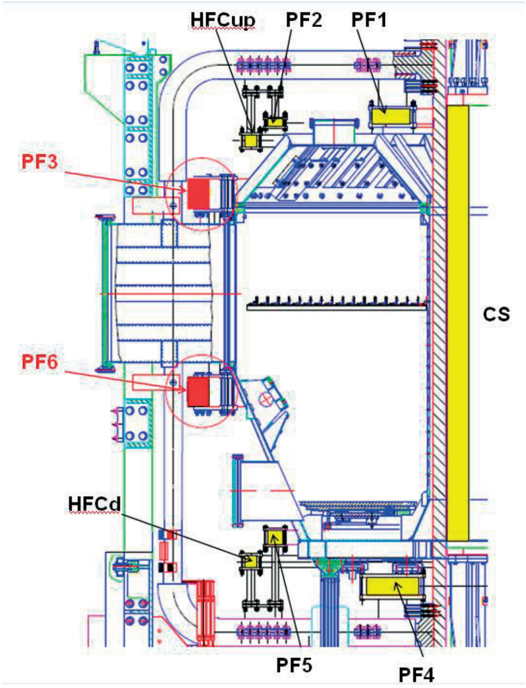

FIG. 22. Location of Hall sensors array in VC.

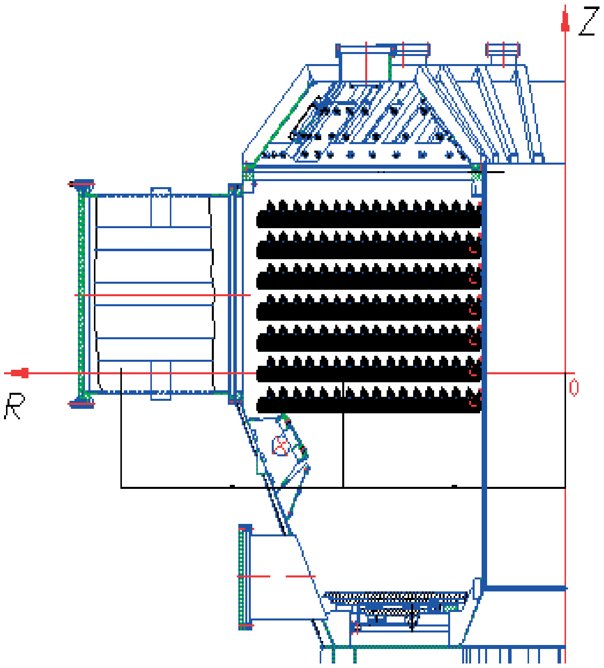

FIG. 23. Positions of Hall sensors array in VC during measurements of distribution TF magnetic field in Z direction.

The design provides placing 15 Hall sensors for measurement of the vertical component of the magnetic field and 15 Hall sensors for measurement the radial component of the magnetic field. Figure 22 shows placement of HS's array in VC. To measure distribution of toroidal field in vertical direction array of HS's is placed as shown in Figure 23.

Measurement results are shown in Figure 24. A difference above 2 G between values of magnetic field in plane of section and values of magnetic field between sections of toroidal coils is oserved.

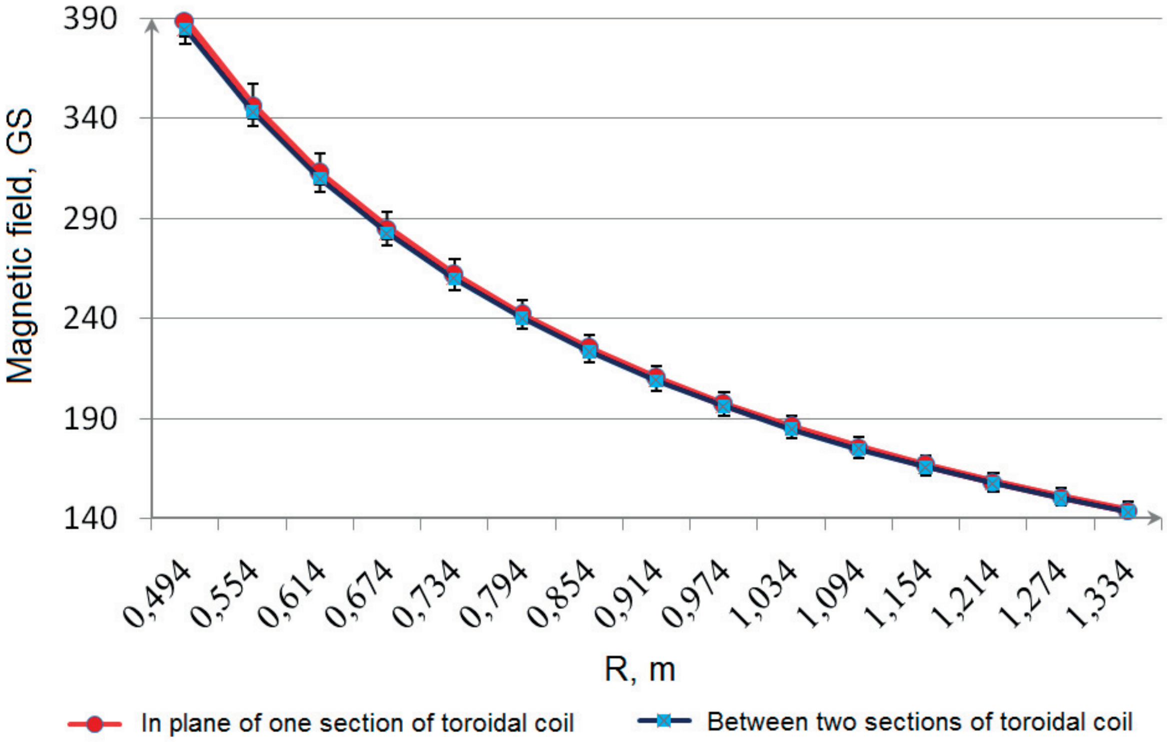

FIG. 24. Magnetic field in plane of section and between of sections of toroidal coils.

More accurate measured values of toroidal magnetic field are given in Table 3, where magnetic field in plane of coil on the grey background and field between coils on white background. It can be seen that the value of magnetic field in Z direction doesn't change B_z~const in the range of HSs accuracy.

Relationship between the B_t and R has very near hyperbolic dependence. Deviation from calculation value is not above 1% that lies in the range of error measurements.

It is also noted that the difference between the values of the field in the cross section of the toroidal coil and between the coils practically no or is in the range of measurement error.

Thus, we can say that in this range of measurement ripple is less than 1%. It is known that estimated value of ripple of KTM TFC is 0.56% and can be argued that the measured value of the same order.

TABLE 2. MEASUREMENT RESULTS OF TOROIDAL FIELD

R, mm Z, mm	620	500	380	260	140	20	-100
1	2	3	4	5	6	7	8
494	374,5	372,3	374,0	372,5	373,4	372,1	372,1
	373,7	373,4	375,7	373,5	375,1	375,1	374,9
554	334,9	332,9	334,2	332,9	335,0	332,8	334,8
	333,9	332,2	332,6	333,0	335,3	334,0	336,5
614	306,0	304,6	306,9	304,0	306,8	304,6	304,6
	307,6	304,3	303,9	305,6	307,6	305,6	307,2
674	274,8	273,4	275,5	272,8	275,3	273,6	274,6
	276,9	273,0	273,0	274,1	275,1	274,6	276,9
734	256,6	256,8	258,2	255,1	257,2	255,8	257,6
	258,7	255,2	254,5	255,1	256,2	254,9	258,7
794	236,1	236,2	237,3	235,1	237,5	235,9	236,5
	236,9	234,0	234,3	236,6	237,4	235,7	238,2
854	221,1	222,6	223,3	220,0	221,8	221,0	220,0
	222,2	219,8	220,4	220,4	220,8	220,9	222,7
914	203,7	203,5	204,2	202,6	204,6	203,8	202,6
	204,4	202,5	202,8	204,1	206,2	204,5	205,1
974	191,8	191,5	192,1	191,0	192,0	191,7	191,8
	192,8	190,7	190,0	190,6	190,4	187,6	191,2
1034	181,3	182,4	182,6	181,2	183,1	181,9	182,0
	181,6	180,4	180,7	180,3	183,1	181,0	182,2
1094	171,6	171,5	172,0	170,8	172,1	171,4	170,8
	171,9	170,7	170,7	170,4	169,6	169,8	172,9
1154	162,5	162,6	162,7	161,4	163,1	162,7	162,9
	163,3	161,3	161,1	161,7	163,8	162,3	163,9
1214	155,8	156,0	155,7	154,9	156,7	155,5	155,3
	155,1	154,7	154,6	154,7	155,5	155,8	155,3
1274	147,8	148,6	148,4	145,5	149,1	148,4	149,2
	148,0	146,9	146,4	147,7	148,7	147,6	149,1
1334	141,2	141,2	141,6	141,3	142,3	142,6	144,3
	142,9	141,2	139,3	141,2	141,0	141,5	142,9

2.4. Measurements of magnetic field null of matrix of Hall sensors

2.4.1. Hall sensor matrix design

A large number of shots (discharges) with different position of the sensors in the vertical direction are required in order to measure configuration of null field region using linear array Hall sensors. This leads to methodological errors due to the difficulty of putting a sufficiently precise coordinates of the Hall sensors. In this work disadvantage of previous measuring method is canceled by using a specially designed matrix of Hall sensors.

The Allegro Microsystems A1301KUAT Hall sensors [3] (small-sized 3x4x1.5 mm) was used to verify the reliability of the calculation results obtained (previously we'd used A1321LUA Hall sensors with a twice smaller measuring range and a lower signal/noise ratio). Table 1 provides the main specifications of applied Hall sensors.

TABLE 3. A1301KUAT HALL SENSOR SPECIFICATIONS

Characteristic	Value	Unit
Maximum magnitude of measured magnetic field	880	G
Quiescent Output Voltage (B = 0 G; T = 25°C)	2.5	V
Supply Voltage	5	V
Sensitivity	2.5	mV/G
Output Bandwidth	20	kHz
Wide Band Output Noise, rms	150	µV

Figure 25 shows the results of magnetic field reconstruction (magnetic field and magnetic flux) in one of the considered time point. Figure 26 shows design of HSs measurement matrix. Measurement matrix has 450x450 mm outer dimensions. HS inside the matrix create mesh 6x6 with 70 mm step between the sensors. There are six supporting strips with six HSs on each strip in the matrix. Figure 27 shows a ready-assembled measurement system in the VC during measurements.

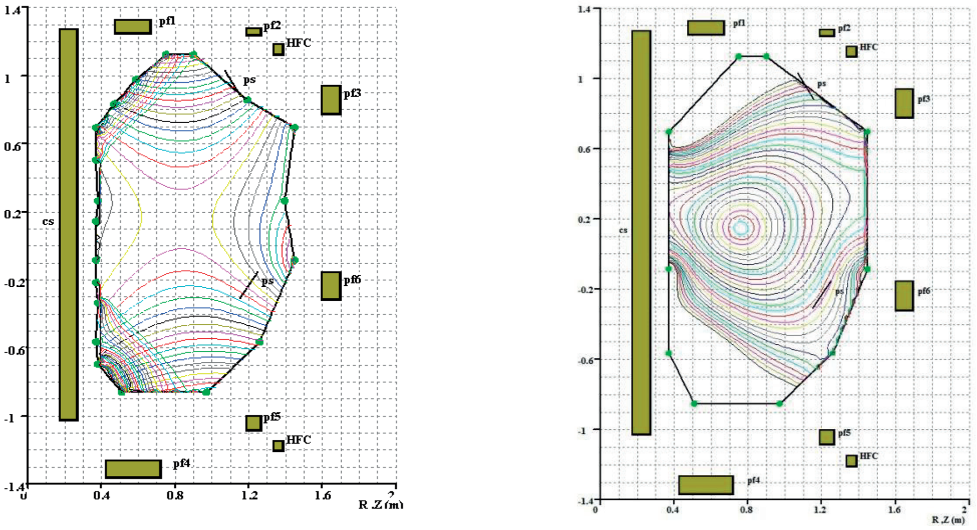

a) Level lines of magnetic flux *b) Lines of module-level magnetic field*

FIG. 25. Chart of magnetic fields calculated by MMF for considered time point.

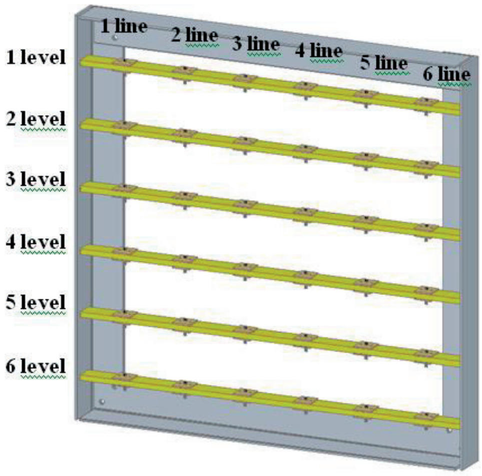

FIG. 26. Hall sensor matrix design. *FIG. 27. Matrix of HS inside of VC.*

2.4.2. Measurement results

Measurement results compared with reconstruction by the code are shown in Figs 28, 29 and 30. Magnetic fields measurements at the KTM tokamak by Hall sensors matrix produce results at the determination of position of null of the field, close to the calculated by the code, but significantly different from the calculated by values of the magnetic field and its gradients in null area of field. It is possible assume that error in the calculation of the code associated with an insufficient number of loop voltage sensors (VLS), being that the accuracy of the restoration of magnetic fields by the code is largely dependent on the accuracy of the approximation of the poloidal magnetic flux by passing VC of tokamak. We are seeing confirmation of this assumption by comparing the experimental results with calculations based on the 12 and 24 VLS.

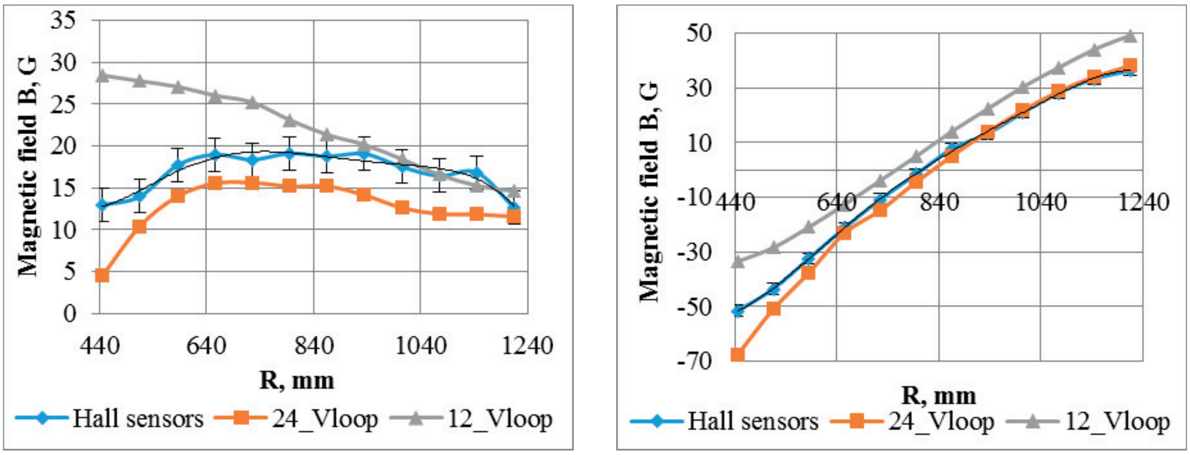

a) Horizontal component of Br magnetic field. *b) Vertical component of Bz magnetic field.*

FIG. 28. Results of identification of the magnetic field using Hall sensors and calculation code (2nd level).

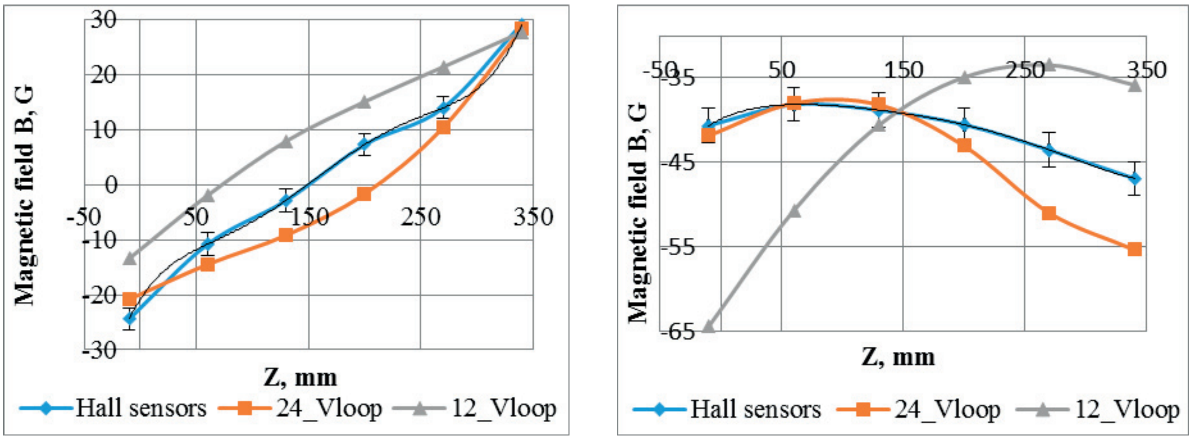

a) Horizontal component of Br magnetic field. *b) Vertical component of Bz magnetic field.*

FIG. 29. Measured results of magnetic field using Hall sensors and calculation code (2nd line).

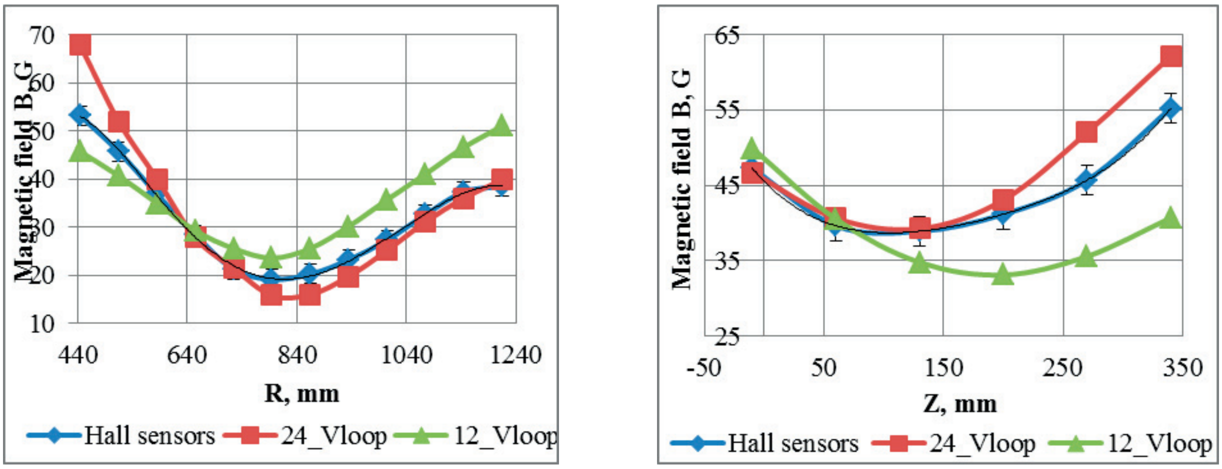

a) 2nd level *b) 2nd line*

FIG. 30. Module of the field according to measured result and calculated by the code.

2.5. Development and testing of a new plasma visualization system of KTM

Plasma imaging systems are an integral part of the diagnostic complex of the facilities type of tokamak. These systems are among the first to the introduction and the main as during of start-up of tokamak and at next facility operation. Plasma imaging systems include at least two cameras, one of which is high-speed camera, and the other slow - high resolution. The first camera allows performing researches of fast processes, and the second have a clear color image of the plasma and the first wall, to carry out a comparative analysis with a fast camera and other diagnostics, as well as to observe the plasma in real time.

System requirements for imaging associated with the presence of relatively long equatorial branch tubes of the vacuum chamber of the tokamak KTM restricting implementation of visual observations of the plasma and the processes in the plasma. Figure 31 shows the half-section of the vacuum chamber of the tokamak KTM with equatorial port. Figure 32 shows an image obtained at placement of the video camera directly at the viewing window located in the plug socket of the equatorial port. As seen in Figure 31 equatorial port is severely restrict of the viewing angle - visible only the central cylinder of the vacuum chamber and the small splits on the peripheries of it.

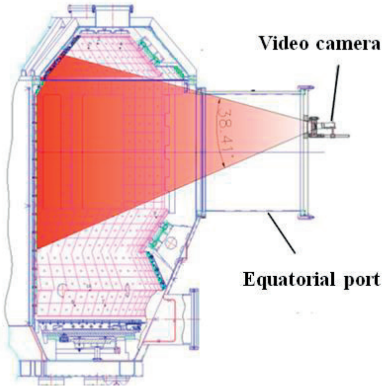

FIG. 31. The section of the vacuum chamber.

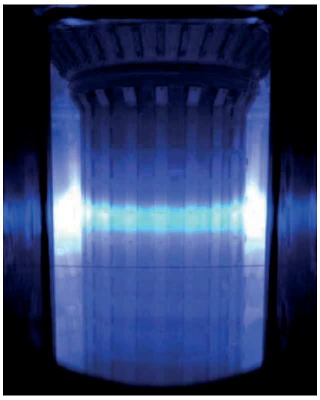

FIG. 32. The image obtained at the camera installation on the plug socket of equatorial branch tube.

Figure 33 shows a principle optical diagram of the imaging system of the plasma column. As seen in Figure 33, the image from output of the image fiber bundle by means of a special lens that transmits an image without increasing after get through a beamsplitter, projected on the matrix of the slow camera and image intensifier. From the output of the image intensifier the thickened image will be transferred to the matrix of the fast camera using Relay lens. It should be noted that the use of image intensifier is the need to increase of the brightness gain of the image to get a hard and sharp image from the fast camera.

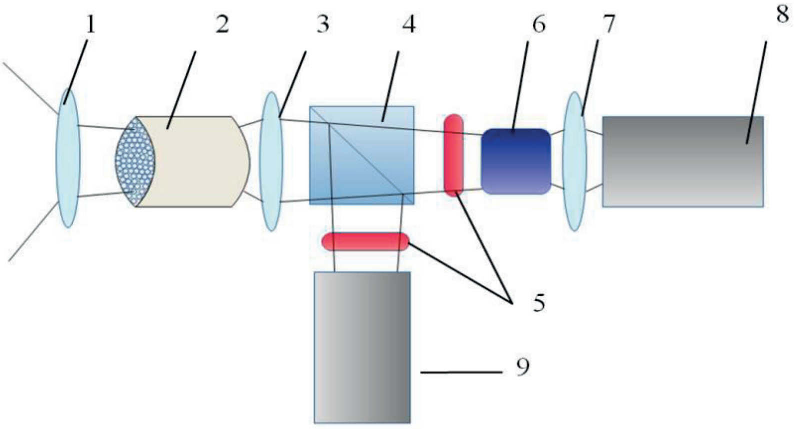

FIG. 33. Principle optical diagram of the imaging system of the plasma column.
1 – output object lens; 2 – fiber-optic light-pipe; 3 – projection lens;4 – optical divider; 5 – filters; 6 – image intensifier; 7 – erector lens; 8 – speed camera;9 – slow camera.

Figure 34 shows the arrangement of optical elements of the plasma imaging system. Figure 35 shows sketch of placement of imaging system on the VC of KTM. Figure 36 shows vacuum nipple with viewport for installation of imaging system. Figure 37 shows imaging system installed on working place at KTM. Figure 38 shows some examples of images during glowing of working gas under influence of radiation of the preionization system.

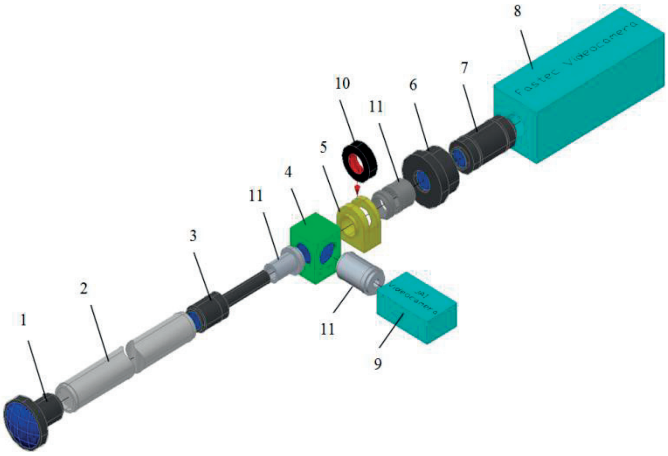

FIG. 34. The layout of the optical elements of the KTM imaging system. 1 – input object lens ; 2 – image fiber bundle ;3 – projection lens (1:1); 4 – beamsplitter ; 5 – optic cell; 6 – image intensifier; 7 – relay lens (1:1); 8 – high speed video camera; 9 – slow video camera ; 10 – filter holder; 11 – optical connecting tubes.

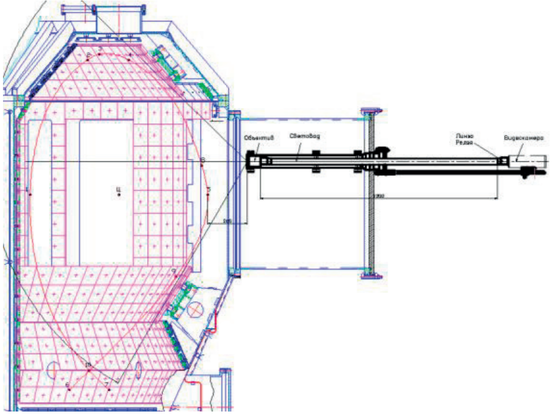

FIG. 35. Sketch of placement of imaging system on the VC of KTM.

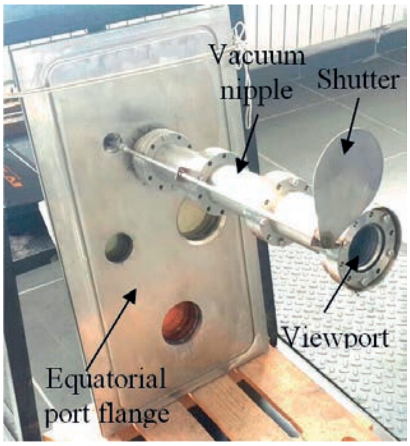

FIG. 36. Vacuum nipple with viewport for installation of imaging system.

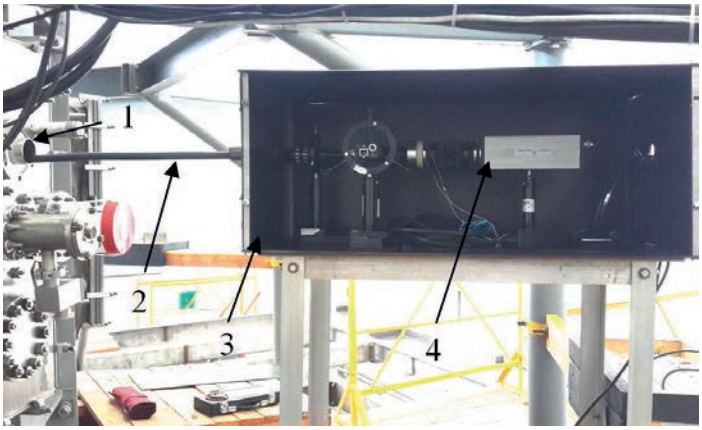

FIG. 37. Imaging system installed on working place at KTM. 1 - entrance into the vacuum nipple; 2-image fiber bundle; 3-magnetic shield; 4- receiving part of the system.

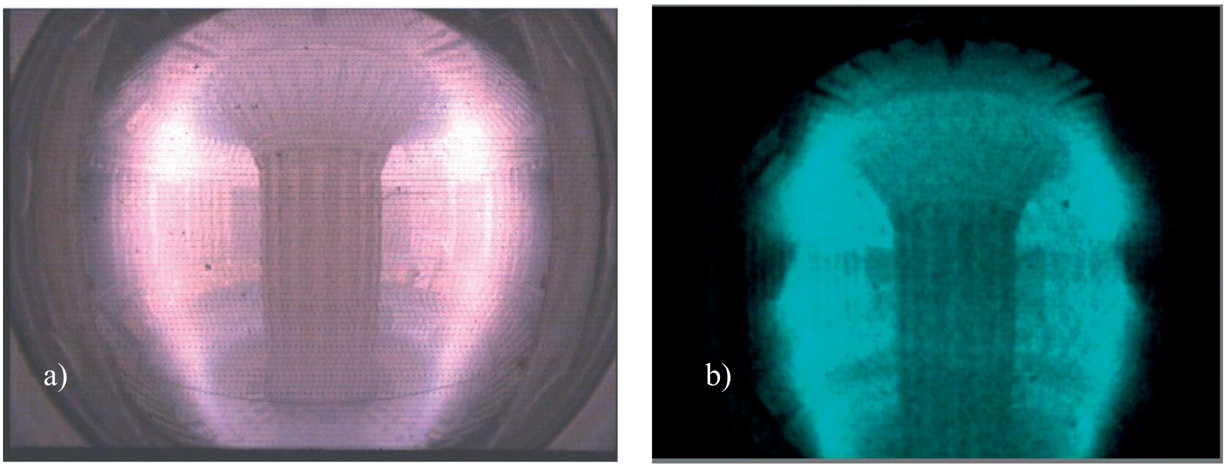

FIG. 38. Images of gas glowing inside of KTM's vacuum chamber taken by imaging system during pre-ionization system working. (a) frame recorded by the slow camera at 30 fps and (b) frame recorded by the fast camera at 250 fps.

In general, based on first results of imaging system, it is arguable that the obtained image has suitable quality. The image shows the whole process that take place in a vacuum chamber. The requirements specified to imaging system have been completed [7].

ACKNOWLEDGEMENT

This research has been supported by the research program «Scientific and technical support of manufacturing and operation of the Kazakhstan thermonuclear material tokamak reactor» of the budget programme 029 «Applied research of technological nature» of the Ministry of Energy of the Republic of Kazakhstan.

REFERENCES

[1] AZIZOV, E.A., et al., Kazakhstan tokamak material testing (KTM), Problems of atomic science and technology, Series TermoNucl. Fusion **4** (2005) 13-18

[2] GRYAZNEVICH, M., et al., Plasma formation in start and mast spherical tokamaks, Nucl. Fusion **46** (2006) S573-S583

[3] JAYHYUN, K. et al., Time-dependent optimization of initiation phase of the outer pf coil-only inductive start-up of nstx plasmas, Plasma Phys. Control. Fusion **46** (2004) 1647–1657.

[4] OSAMU, M., Inductive plasma current start-up by the outer vertical field coil in a spherical tokamak, Plasma Phys. Control. Fusion **41** (1999) 1469–1483.

[5] Operations of KTM for Plasma Formation and Start-up Studies, final report, IAEA Research Contract No: 17111/R0, 2013.

[6] KAVIN, A.A, LOBANOV, K.M., Manual of how to use a calculation code to restore magnetic field map inside of the ktm vacuum chamber by magnetic measurements and currents in poloidal coils, NIIEFA (2009).

[7] CHEKTYBAYEV, B., SHAPOVALOV, G. and KOLODESHNIKOV, A., Visible wide angle view imaging system of ktm tokamak based on multielement image fiber bundle, Rev. Sci. Instrum. **86** (2015) 5.

POLOIDAL FIELD COILS SYSTEMS OF GLAST-III

Z. AHMAD, S. AHMAD, F. DEEBA, S. HUSSAIN

National Tokamak Fusion Program, Islamabad, 4400, Pakistan

Abstract

Poloidal field coils system of GLAST Tokamak is studied both theoretically and experimentally. Poloidal field coils numbers are optimized to 6 coils. A comparison of coil current model for fast and slow capacitor bank to energize PF coils is made with the experimental measurements which are in good agreement. Further magnetic field produced from PF coils is theoretically calculated using vector potential and grreen's function and compared with experimental measurements. In the last magnetic field produced by central solenoid is compared with theoretically calculated profile. Our results show that both experimental and theoretical measurements are in good agreement. Further HTS PF coils for GLAST are fabricated and tested successfully.

1. INTRODUCTION

In recent years spherical tokamaks are getting more and more attraction [1]. GLAST-III is a fully glass spherical tokamak with major radius R=20 cm, minor radius a=10cm and B_t=0.1 T. It is the successor of GLAST-II tokamak which is operational in Pakistan [2,3]. A 2.45 GHz preionization RF source is used along with the toroidal field to assist the plasma discharge. One of the advantages of dielectric vacuum vessel is that the field penetration is faster as compared with the metallic vessel. Figure 1 shows the photograph of GLAST-III, its coils and some diagnostics systems. Figure 2 shows the plasma current discharge of GLAST-III.

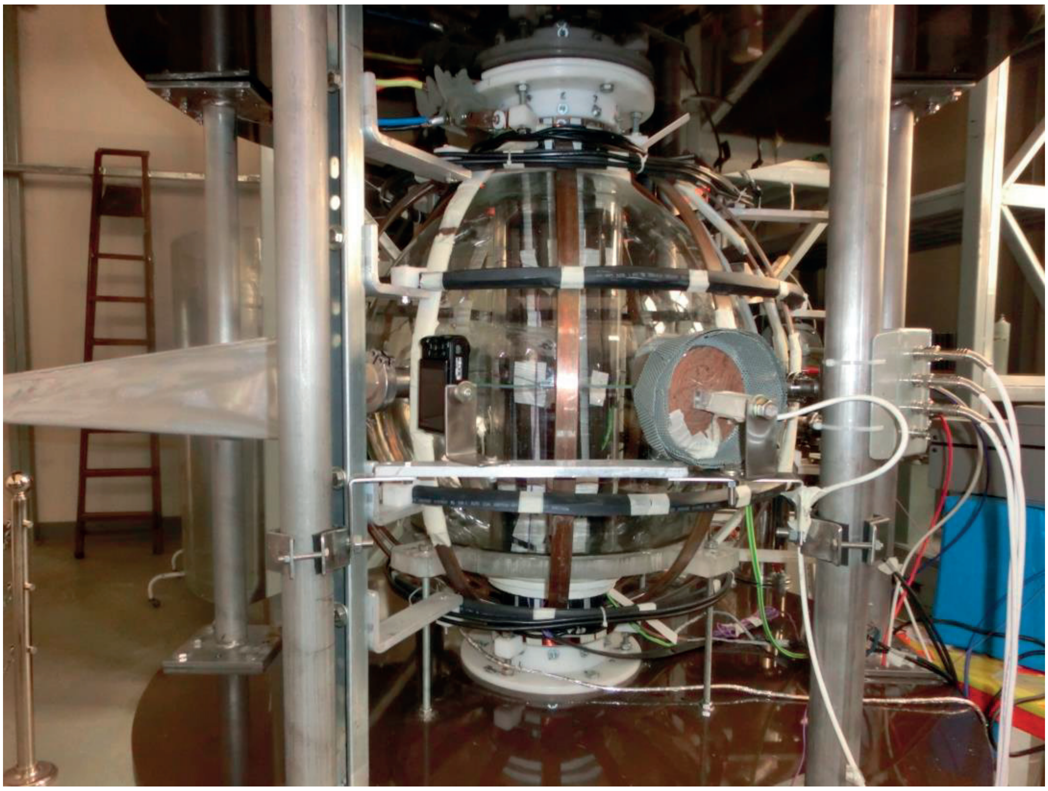

FIG.1. Photograph of GLAST-III.

FIG. 2. Photograph of GLAST-III typical discharge of plasma current.

2. PF COILS SYSTEMS OF GLAST-III

The magnetic system of a tokamak consists of Toroidal magnetic field (TF) and Poloidal Field (PF) system. Poloidal field coils system is further sub-divided into central solenoid and poloidal (vertical/equilibrium/elongation) field coils. The main goal of PF coils is to keep the plasma in desired MHD equilibrium generating an additional equilibrium magnetic field in (R, Z) plane. Working principle of equilibrium field coils is shown in the Figure 2a [4]. Similarly working principle of elongation coils is shown in Figure 2b.

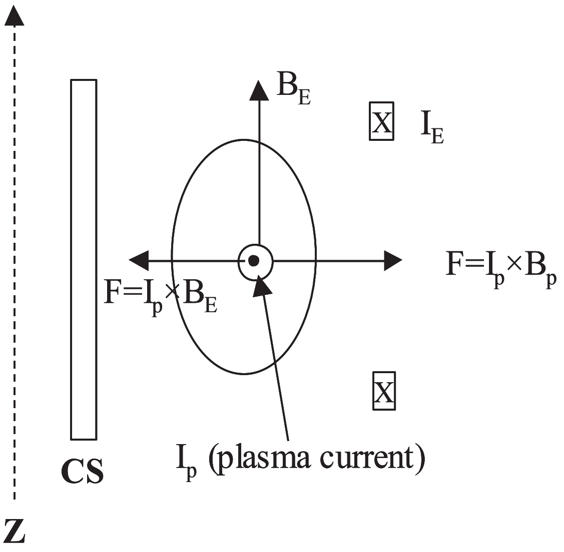

FIG. 2. (a): Inward force produced by the Equilibrium field coils to balance the outward force due to plasma current and poloidal magnetic field.

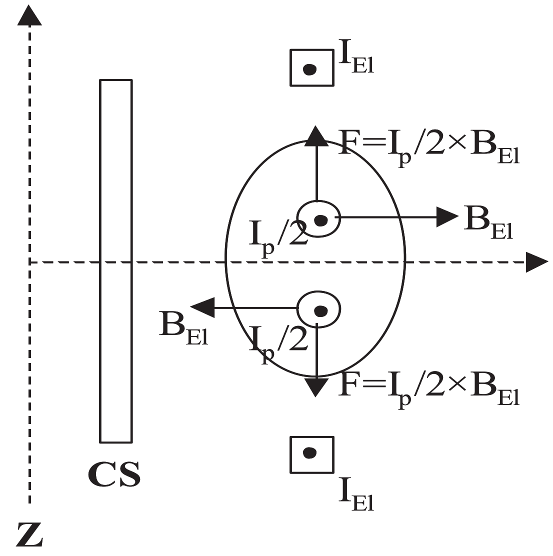

FIG. 2. (b). Elongation coils stretch the plasma in upward and down direction making an elongated plasma.

Equilibrium field coils provide the radial inward force to balance the outward force generated by the self magnetic field of plasma. Purpose of elongation filed coils is to elongate the plasma in the vertical direction as it has direct impact on the q value, beta value. It is the characteristic of spherical tokamak that it has natural elongation. To have control at n points we need n-1 coils in poloidal coils system. Therefore larger number of coils would be better and are justified.

In an earlier work on Poloidal field coils of GLAST-I and GLAST-II use of TOKAMEQ was made to find the equilibrium. A typical scenario is shown in Figure 3 and the coil parameters are shown below in Table 1

TABLE 1. PARAMETERS OF PF COILS

Coil	Position (r) cm	Position (z) cm	No. of Turns	Inductance (mH)	Resistance Ω
CS	4.1	0	240	435.63	0.19
CC1	9	-35	5	26.13	0.03
CC2	22	-23	1		
CC3	22	23	1		
CC4	9	35	5		
PF1	8	35	30	7050	2.07
PF2	21	23	30		
PF3	29	8	30		
PF4	29	-8	30		
PF5	21	-23	30		
PF6	8	-35	30		

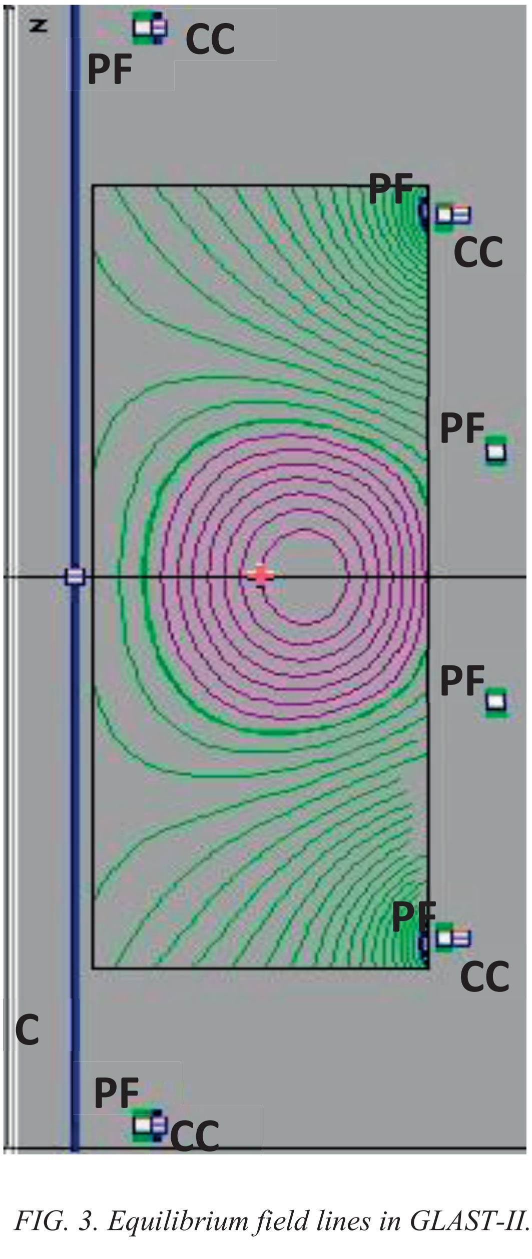

FIG. 3. Equilibrium field lines in GLAST-II.

To locate the position (R, Z) of the coils, for upper half ($0–90^0$) of GLAST-III we divided it in to three equal parts and then in the middle of each part i.e. 15^0, 45^0 and 75^0 R and Z are calculated from $r = r_0 \cos \theta$ and $z = r_0 \sin \theta$. Parameters of PF coils are given in the Table 2. This design has up-down symmetry of poloidal coils.

TABLE 2. PARAMETERS OF PF COILS

Coil	No. of Turns	Position (r) cm	Position (z) cm	Resistance Ω	Inductance mH
E1	30	10.0	37.0	0.21	0.341
E2	30	26.0	27.5	0.45	1.1
E3	30	35.0	12.0	0.58	1.7
E4	30	35.0	-12.0	0.57	1.7
E5	30	26.0	-27.5	0.41	1.1
E6	30	10.0	-37.0	0.22	0.334

The following studies on these poloidal coils have been performed numerically and experimentally.

2.1. Study of Current through the Poloidal Field (PF) Coils:

Current wave form RLC series circuit can be estimated using the following equation:

$$\frac{d^2I}{dt^2} + \frac{L}{R}\frac{dI}{dt} + \frac{I}{LC} = 0 \qquad (1)$$

where R, L, and C are resistance, inductance and capacitance respectively. To solve this equation numerically the following two initial conditions are applied at t=0:

$$\frac{dI}{dt} = -\frac{1}{L}(RI_0 + V_0), \qquad (2)$$

and

$$I = 0 \qquad (3)$$

For our system of PF coils we have solved the above equation for the following circuit parameters V_0=250 and C=3 mF, and t=20 ms. The resulting wave form of Current (A) vs time (sec) is plotted in Figure 4.

The maximum current is 70 A at 5.5 m and then it falls down. In case we want to have constant current in the PF coils we need to fire a second bank in the same coils with higher capacitance and lower voltage at 5.5 m. The equation which deals with the current wave form, when a second bank is fired, is as under [5]

$$\frac{d^2I_1}{dt^2} + \frac{L}{R}\frac{dI_1}{dt} + \frac{I_1}{L(C_1 + C_2)} = 0 \qquad (4)$$

$$I = \frac{C_1 + C_2}{C_1} I_1 \qquad (5)$$

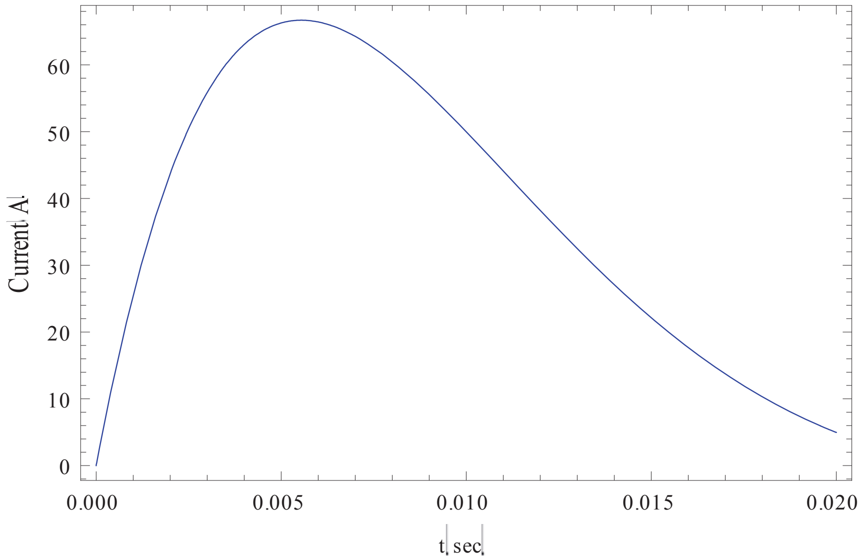

FIG. 4. Calculated current in Poloidal field coils using single capacitor bank.

With the initial conditions

$$I_1(t_0) = \frac{C_1}{C_1 + C_2} \tag{6}$$

$$V_1(t_0) = V_{02} - 2 \tag{7}$$

Here C_1 and C_2 are capacitance of the first and second bank, V_{02} is charging voltage of the second bank.

The above equation is numerically solved for with the circuit parameters like C_1=3mF, C_2= 600 mF, V_0=250, V_{02}=150 and the Current (A) as a function of time is plotted in the Figure 2. Figure 5 shows the resultant current flowing from PF coils.

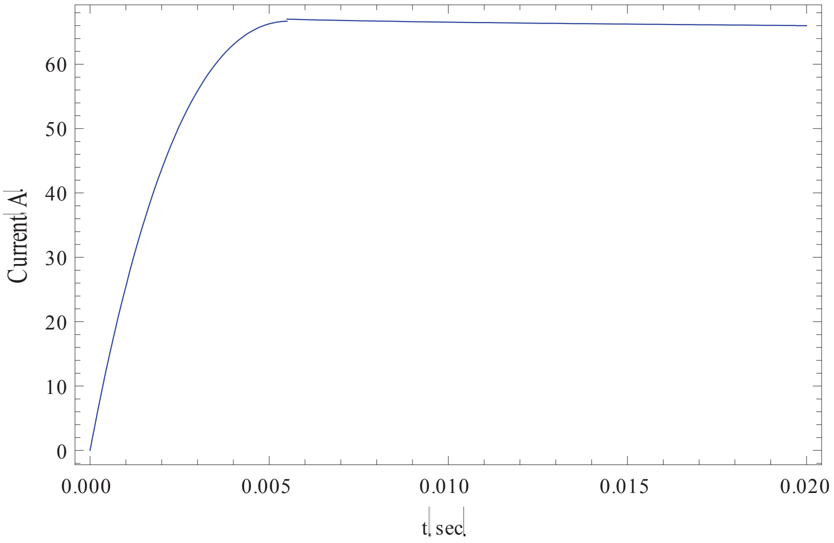

FIG. 5. Calculated current in Poloidal field coils using fast and slow capacitor banks.

With this arrangement (combination of fast and slow banks) we can have flat/constant current in the PF coils. We have implement this fast slow combination of bank for PF coils and the experimental wave form is shown below in Figure 6. It is seen that both theoretical and experimental plots match with each other.

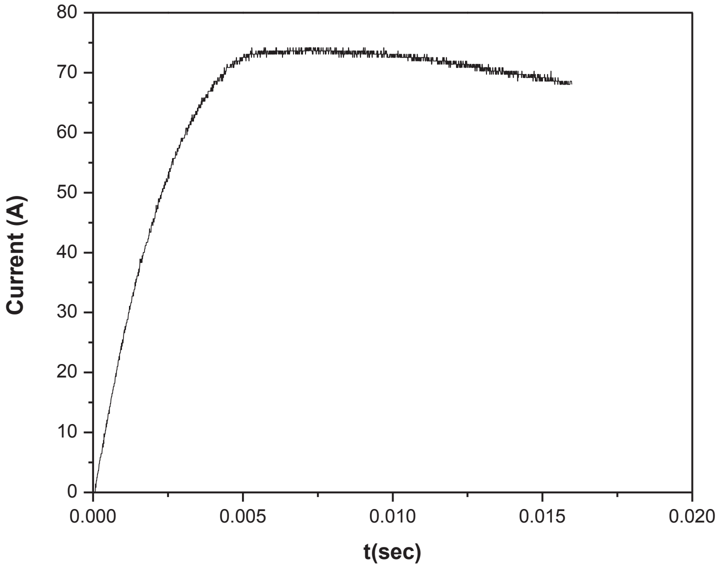

FIG. 6. Measured current in Poloidal field coils using fast and slow capacitor banks.

2.2 Study of vertical field generated from the Poloidal Field (PF) Coils:

According to Ampere law,

$$\mu_o \vec{J} = \nabla \times \vec{\mathrm{B}} \tag{8}$$

B can be written in term of vector potential as,

$$\vec{B} = \nabla \times \vec{A} \tag{9}$$

In cylindrical coordinate (r,θ,z) magnetic field can expressed as,

$$B_r = -\frac{\partial A_\theta}{\partial Z} \tag{10}$$

$$B_z = \frac{1}{r}\frac{\partial}{\partial r}(rA_\theta) \tag{11}$$

Ampere law can be re-written after inserting the value of B

$$\mu_o \vec{J} = \nabla \times \vec{\mathrm{B}} = -\nabla^2 \vec{\mathrm{A}} \tag{12}$$

Writing Vector Potential in terms of Green’s Function

$$A_\theta = \frac{\mu_o I r'^{\frac{1}{2}}}{2\pi r^{\frac{1}{2}}}\left[\left(\frac{2}{k} - k\right)K(k) - \frac{2}{k}E(k)\right] \tag{13}$$

$$k = \sqrt{\frac{4rr'}{z^2 + (r + r')^2}} \tag{14}$$

where *K* and *E* are complete elliptical integrals of 1st and 2nd kind. Radial and axial component of magnetic field can be given as

$$B_r = -\frac{\partial A_\theta}{\partial z} = \frac{\mu_o I k z}{4\pi\sqrt{r' r^3}}\left[-K(k) + \frac{(1 - 0.5k^2)}{(1 - k^2)}E(k)\right] \tag{15}$$

$$B_z = \frac{1}{r}\frac{\partial}{\partial r}(rA_\theta) = \frac{\mu_o I k}{4\pi\sqrt{r'r}}\left[K(k) + \frac{(r'+r)k^2 - 2r}{2r(1-k^2)}E(k)\right] \quad (16)$$

The vertical component of magnetic field generated from the poloidal coils is can be written as [6]:

$$B_z = \frac{\mu_0 NI}{2\pi}\frac{k}{2\sqrt{rr'}}\left[K(k) + \frac{\{r'^2 - r^2 - (z-z')^2\}k^2}{4rr'}E(k)\right] \quad (17)$$

Where N is total number of turns of coil, I is current flowing in coil, E(k) and K(k) are complete elliptical integrals, $k^2 = \frac{4rr'}{[(r+r')^2+(z+z')^2]}$. r' and z' are location of the coils. Using value of maximum current (I=72A) from the six poloidal coils, the contour plot of vertical field is given in Figure 7. Here R is major radius and Z is vertical height.

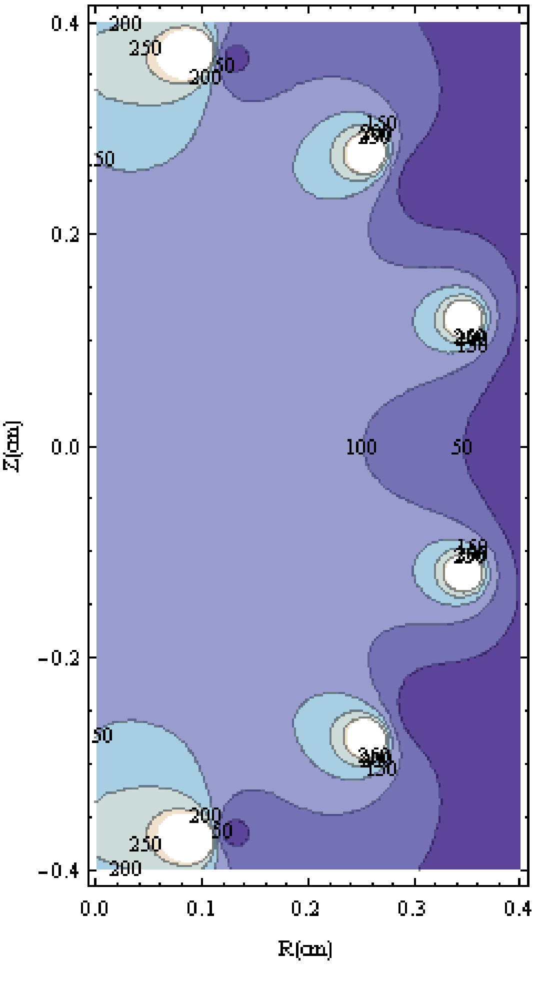

FIG. 7. Contour plot of vertical magnetic field in R, Z plane.

The vertical component at Z=0 plane is plotted in Figure 8.

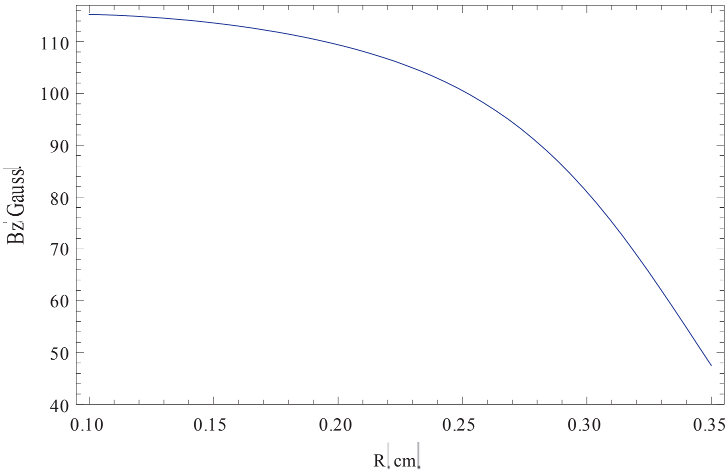

FIG. 8. Calculated vertical magnetic field generated from poloidal coils.

It shows that a magnetic field of 115 gauss will be produced on the inboard side of the GLAST-III. The measured plot of axial/vertical field is shown in Figure 9 which is in agreement with the theoretical/numerical predictions.

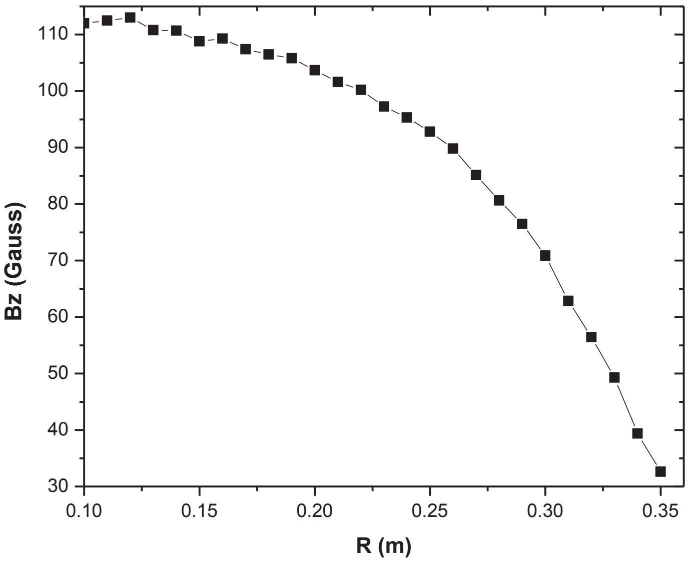

FIG. 9. Measured vertical magnetic field generated from poloidal coils.

3. MAGNETIC FIELD OF A CENTRAL SOLENOID

For a finite length solenoid vector potential takes the form

$$A_{\theta} = \frac{\mu_o\, I\, r'^{\frac{1}{2}}}{2\pi\, L\, r^{\frac{1}{2}}}\left[\zeta k\left(\frac{k^2+h^2-h^2k^2}{h^2k^2}\right)K(k^2)-\frac{1}{k^2}E(k^2)+\frac{h^2-1}{h^2}\Pi(h^2,k^2)\right]_{\zeta-}^{\zeta+} \quad (18)$$

Therefore the radial and axial magnetic field can be written as

$$B_r = -\frac{\partial A_\theta}{\partial z} = \frac{\mu_o\, I\, r'^{\frac{1}{2}}}{4\pi\, L\, r^{\frac{1}{2}}}\left[\frac{k^2-2}{k}K(k^2)+\frac{2}{k}E(k^2)\right]_{\zeta-}^{\zeta+} \tag{19}$$

and

$$B_z = \frac{1}{r}\frac{\partial}{\partial r}(rA_\theta) = \frac{\mu_o I}{4\pi\, L\sqrt{r'r}}\left[\zeta k\left(K(k^2)+\frac{(r'-r)}{(r'+r)}\Pi(h^2,k^2)\right)\right]_{\zeta-}^{\zeta+} \tag{20}$$

Where Π is the elliptical integral of 3rd kind. The other parameters are defined as:

$\zeta\pm = z \mp \frac{L}{2}$, $\zeta = z - z'$ $k = \sqrt{\frac{4rr'}{\zeta^2+(r+r')^2}}$ and $h = \sqrt{\frac{4rr'}{(r+r')^2}}$

The above equation is solved numerically for central solenoid parameters of GLAST-III to calculate the magnetic field profile. Experimental measurements of magnetic field produced from CS is measured using 3-channel Hall probe and gauss meter at different distance from the CS at Z=0 plan. Figure 10 shows comparison of theoretical and experimental results. Both are in good agreement. From the results we conclude that there is a need to install compensation coils to avoid this magnetic from the vacuum vessel area. After this conclusion 4 compensation coils are installed on the GLAST.

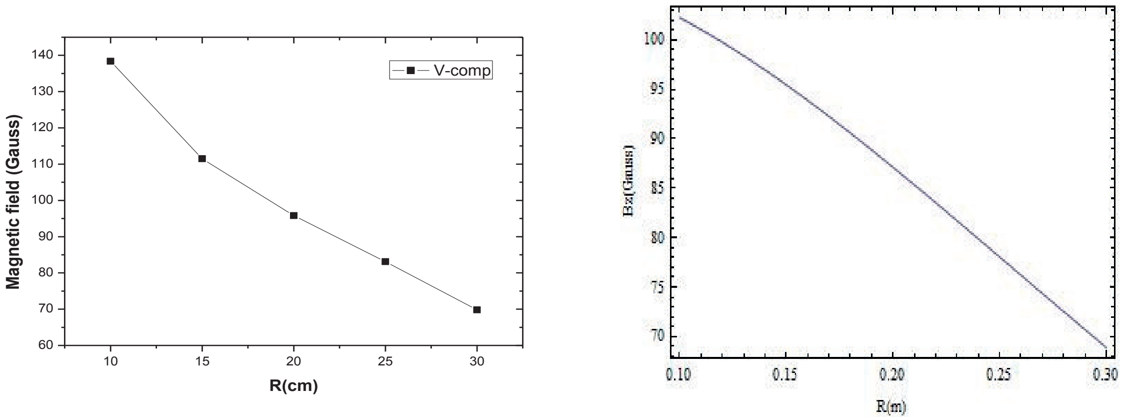

FIG. 10. Comparison of both experimental and theoretical measurements of central solenoid field.

3.1. Force due to two Coaxial Coils

Axial force due to two adjacent compensation coils is calculated as [7]:

$$F_z = \int dF_z = I_2 B_{r1}\int dl_2 = 2\pi a I_2 B_{r1} \tag{21}$$

Where a is the radius of coil, I_2 is the current through the 2nd coil and B_{r1} is the radial magnetic field in coil 1. Using the parameters of GALST compensation coils force between two coils is:

r = 0.27 m,
a = 0.27 m,
Current I= 5kA,
z = 0.27 m
Number of turns N= 2
F = 12 N

4. HTS POLOIDAL FIELD COIL FABRICATION AND TESTING FOR GLAST-III

High Temperature Superconducting (HTS) coils are now in use and have shown good results [7]. We have fabricated HTS Coils for GLAST-III and tested them. Coils testing setup is shown here in the Figure 11. Parameters of the coils are:

No. of coils	2
No. of turns on each coil	4
Radius of coil	30 cm
Distance between coils	60 cm
Thickness of HTS tape	0.1 mm
Width of HTS tape	12 mm
Critical current I_c	446 A

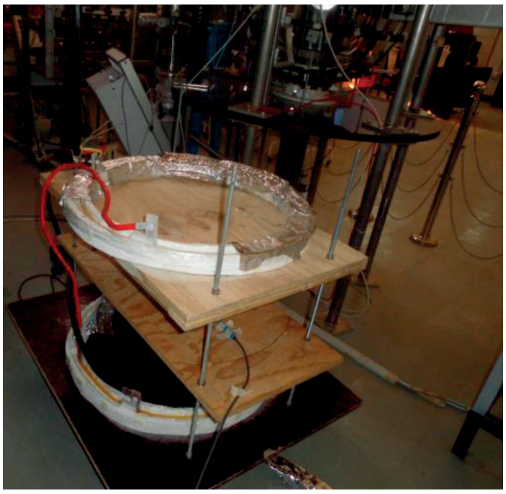

FIG. 11. HTS coils and their testing setup.

The coils housing is made with thermoPor. To stop the leaking of LN2 from housing white glue is used. 10 min before the start of experiment, coils are cooled with LN2. To energize the HTS coils we have used the capacitor charging voltage 20V, with capacitance 600 mF, achieving maximum current of 500 A, where as critical current of HTS tape is 446 A. Current wave form is shown in Figure 12. The rize time of current is 125 kA/s which is an acceptable range for HTS.

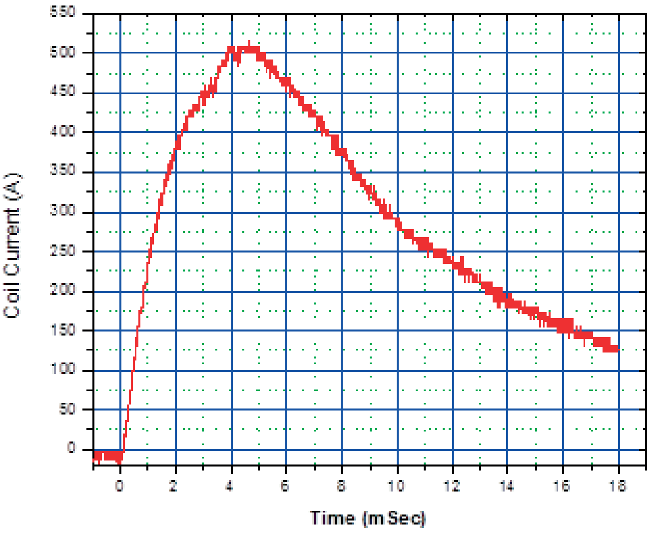

*FIG. 12. Current wave form from HTS coils.*5.

PF coil current and magnetic field produced by them is modeled and the theoretical results are compared with experimental measurements. Also magnetic field produced by central solenoid and calculated and measured as well. Results show good agreement between experimental measurements and theoretical calculations. Also HTS Poloidal coils are fabricated and tested successfully.

ACKNOWLEDGEMENT

The support from IAEA through CRP on “Utilization of the Network of Small Magnetic Confinement Fusion Devices for Mainstream Fusion Research” is highly acknowledged.

REFERENCES

[1] ONO, M. and KAITA, R., Phys. of Plasmas **22** (2015) 040501.

[2] HUSSAIN, S., QAYYUM, A., AHMAD, Z., AHMAD, S., KHAN, R., DEEBA, F., NAVEED, M.A., RAFAQAT ALI, MEHBOOB SADIQ, NAJAM US SAQIB, AHMED, A., NAZIR, M., MAJEED, H.A., BATOOL, S., JAVED, M.A., AHMED, N. and VOROBYOV, G.M., J. Fus. Energy **35** (2016).

[3] QAYYUM, A., AHMAD, N., AHMAD, S., FARAH DEEBA, RAFAQAT ALI, and HUSSAIN, S., Rev. Sci. Instrum. **84** (2013).

[4] THOME, R. J, and TARRH, J. M., Mhd and fusion magnets field and force design concept, John Wiley & Sons (1982) 168.

[5] HE YEXI, LI XIAOYAN and GAO ZHE, Plasma Sci. Technol. **7** (2005) 2624.

[6] LANDAU, L. D. and LIFSHITZ, E.M., Electrodynamics of Continuous Media, Pergamon Press, New York (1966).

[7] DOLAN, T.J., Fusion Research, Principals, Experiments and Technology, Pergamon Press, New York, (2000).

[8] GRYAZNEVICH, M. et al., Fus. Eng. Des **88** (2013) 1593.

DEVELOPMENT OF THE HEAVY ION BEAM PROBE (HIBP) DIAGNOSTICS FOR SMALL FUSION DEVICES (RESEARCH CONTRACT NO. 18033)

A.V. MELNIKOV[*,**], L.G. ELISEEV[*], S.V. LYSENKO[*]

[*] NRC ‘Kurchatov Institute’, Moscow, Russian Federation
[**] National Nuclear Research University (MEPhI) Moscow, Russian Federation

Abstract
Heavy Ion Beam Probing (HIBP) is a unique diagnostics for core plasma potential. Advanced HIBP is operating now in the T-10 tokamak and TJ-II flexible heliac. The fine focused (<1cm) and intense (100 μA) beams provide the measurements in the wide density interval n_e=(0.3–5)x10^{19} m^{-3}, while the advanced control system for primary and secondary beams provides the measurements in the wide range of the plasma current in T-10 and magnetic configurations in TJ-II, including Ohmic, ECR and NBI heated plasmas. The time evolution of the radial profiles and/or local values of plasma parameters from High Field Side (HFS) to Low Field Side (LFS), $-1<\rho<1$, is observed in TJ-II by 125 keV Cs^+ ions in a single shot, while LFS ($+0.2<\rho<1$) profiles are observed in T-10 by 300 keV Tl^+ ions. Multi-slit energy analyzers provide simultaneously the data on plasma potential ρ (by beam extra energy), plasma density n_e (by beam current) and B_{pol} (by beam toroidal shift) in poloidally shifted sample volumes. Thus $E_{pol} = (\psi_1-\psi_2)/x$, $x\sim1$ cm, and the electrostatic turbulent particle flux $\Gamma_{E\times B}(t) = 1/B_t \cdot \tilde{n}_e(t)\tilde{E}_{pol}(t)$ is derived. The density oscillations cross-phase produces the phase velocity of poloidal propagation of perturbation or plasma rotation and the poloidal mode number m. Low noise high gain (10^7 V/A) preamplifiers with 300 kHz bandwidth and 2 MHz sampling allows us to study broadband turbulence and quasi-coherent modes like Geodesic Acoustic Modes, Alfven Eigenmodes, Suprathermal electron induced modes, etc. Finally, HIBP becomes multipurpose diagnostics to study plasma electric potential and turbulence properties in the middle size toroidal devices.

1. INTRODUCTION

Our investigations provided in the framework of the current Co-ordinated Research Project (CRP) of the International Atomic Energy Agency (IAEA) “Utilization of the Network of Small Magnetic Confinement Fusion Devices for Mainstream Fusion Research” during the fulfilment of the activity from November 2013 to February 2016.

HIBP is a unique tool for the direct measurement of the plasma potential in the core plasma of fusion devices. HIBP was first introduced in 1970s; it was recently developed to the multichannel version to study the turbulent particle flux. This TECDOC presents this development and application to the T-10 tokamak (a=0.3 m, R=1.5 m, B_t=1.5–2.4 T, I_p=140–330 kA, P_{ECRH}<1.2 MW) and TJ-II stellarator ($\langle a\rangle$=0.22 m, $\langle R\rangle$=1.5 m, B_t =1 T, P_{ECRH} ≤0.6 MW, P_{NBI} ≤1 MW). It presents the diagnostics capabilities and limitations and also presents the examples of recent measurements of plasma potential and turbulence characteristics.

2. HIBP EQUIPMENT USED IN THE EXPERIMENTS PROVIDED BY THE KURCHATOV TEAM

2.1. Equipment used in the HIBP experiments

2.1.1. The T-10 tokamak and its HIBP

This HIBP device (Figs 1, 2, 3, and 4) was elaborated by Kurchatov Institute. It was modernized during the fulfilment of the current IAEA CRP. General device’s characteristics are presented in the Table 1.

FIG. 1. *HIBP on the diagnostic platform of the T-10 tokamak. Installation phase.*

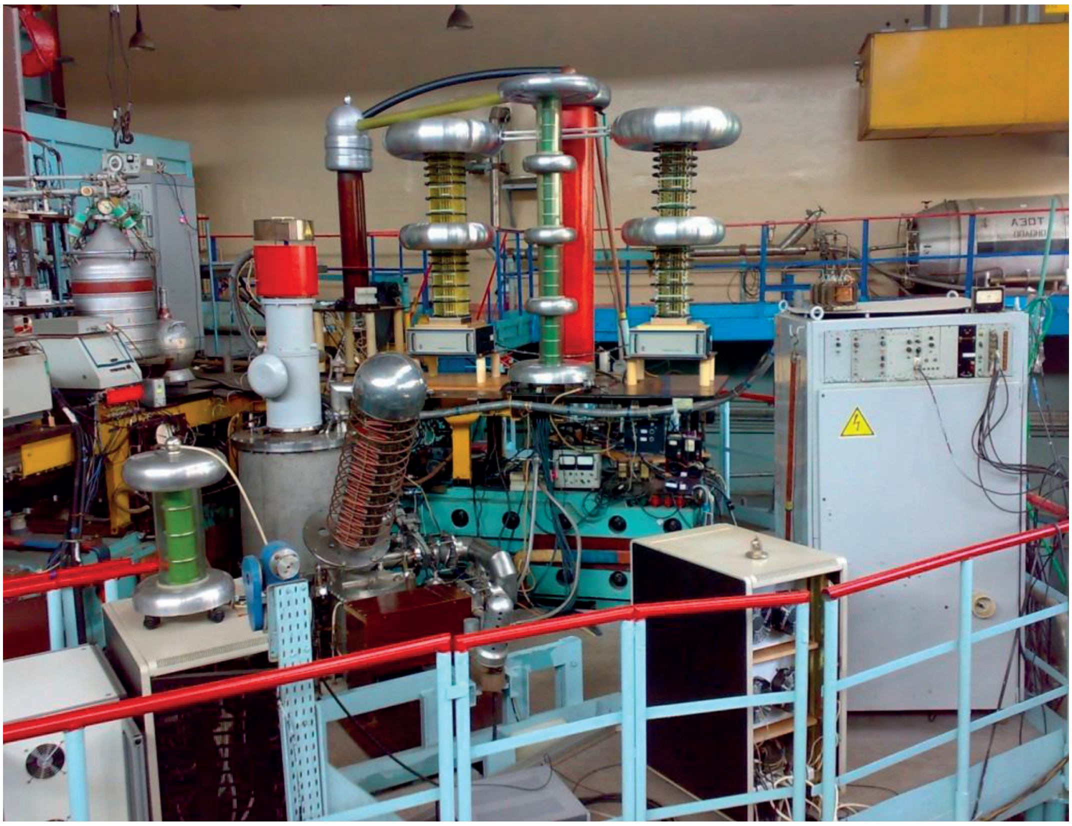

FIG. 2. *HIBP on the diagnostic platform of the T-10 tokamak. Operation phase.*

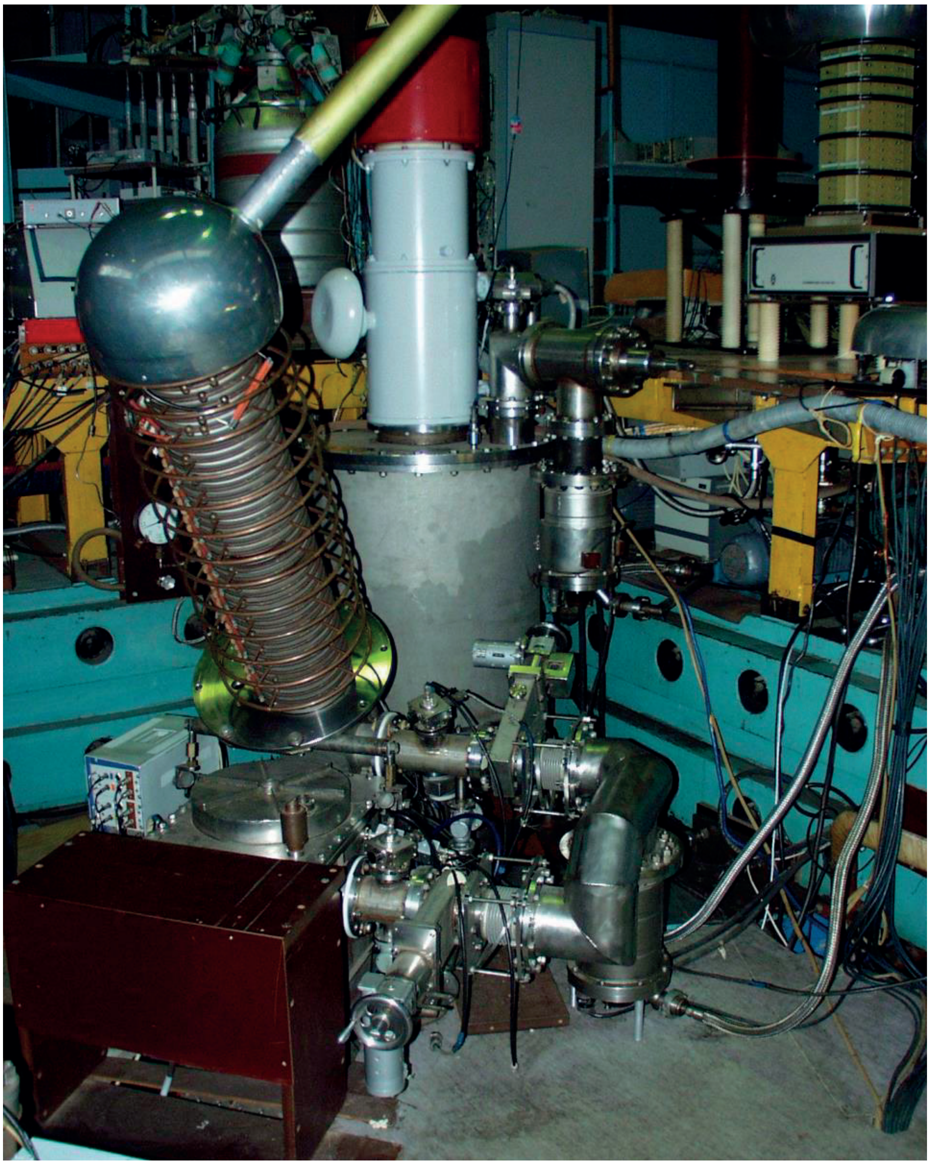

FIG. 3. HIBP accelerator, energy analyzer and pumping system on the T-10 tokamak.

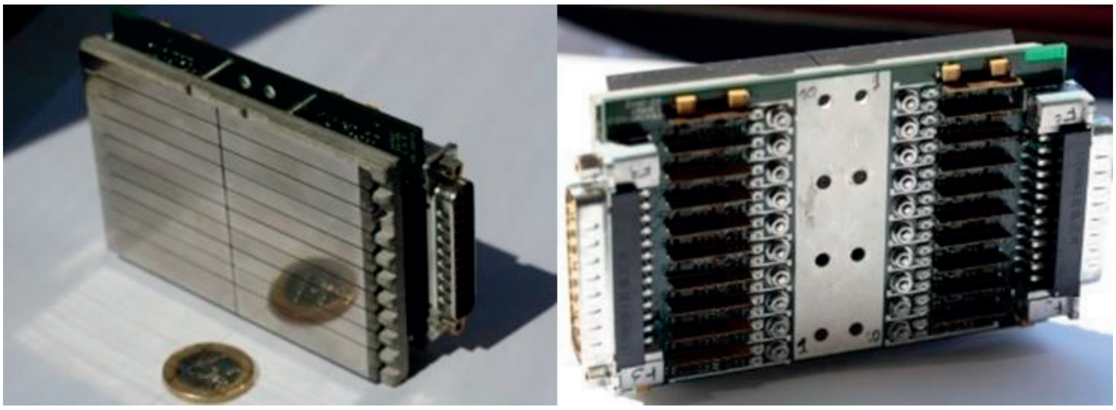

FIG. 4. The 20-channel split plate assembly: left - front view, right - rear view. Twenty screws join both parts and conduct electricity from the sensor to the board.

The works on the 20-channel split plate assembly was carried out by Kurchatov Institute in close collaboration with colleagues from institutes partecipating the CRP (Institute of Plasma Physics NNC KhIPT, Kharkov, Ukraine) and CIEMAT, Madrid, Spain.

TABLE 1. MAIN PARAMETERS OF THE DEVICE

Device parameter	T-10	TJ-II
<R> [m]	1.5	1.5
$<a>_{lim}$ [m]	0.3	0.22
B_t [T]	1.55 - 2.5	1.0
n_e [10^{19} m^{-3}]	1-4	0.3–6
P_{ECRH} [kW]	≤1600	≤600
P_{NBI} [kW]	-	≤900
E_{beam} [keV]	300	125
HIBP ions	Tl+	Cs+
Observation area	$+0.2<\rho<1$	$-0.8<\rho<1$

2.2. Equipment used for the study of plasma mean potential and oscillations in the T-10 tokamak

For the instrumental analysis of the irradiated specimens we have used equipment as follows:

- The hardware of the Heavy Ion Beam Probe Diagnostic on the T-10 tokamak, including electrostatic linear accelerator with multichannel beam detector, beamlines for primary and secondary ion beams and high precision energy analyser for the ion beam.
- High precision measuring voltage divider.
- Insulating transformer for filament power supply
- Capacitor filter for 400 kV
- The High-Voltage power source for 30 kV – two units, 20 kV – two units, all by TREK Inc.
- The High-Voltage power sources, one for 400 kV and one for 100 kV, both by GLASSMAN HV Inc.
- The set of High-Voltage power sources for 5 kV – two units, 10 kV – four units, all by various producers.
- Oscilloscope for the measurements of the beam position and current profile.
- Computer system for the control and data acquisition for the HIBP diagnostics
- The similar hardware of the Heavy Ion Beam Probe Diagnostic on the TJ-II stellarator

3. DEVELOPMENT OF THE HEAVY ION BEAM PROBE (HIBP) DIAGNOSTICS FOR SMALL FUSION DEVICES

3.1. Plasma potential profiles

HIBP is capable to measure potential time evolution in the fixed sample volume (SV) and radial profiles as well.

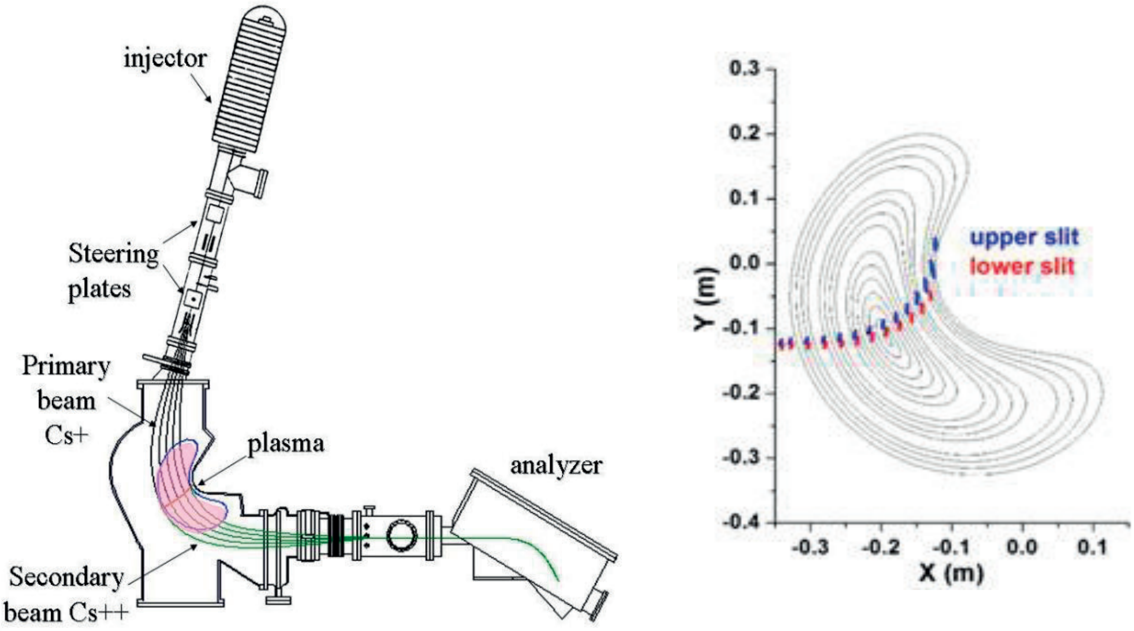

FIG. 5. HIBP experimental set-up at TJ-II. Black curves are trajectories of primary ($Cs^{+)}$ ions, green ones - of secondary ($Cs^{++)}$ ions. Inset shows detector lines for the poloidally resolved potential and density measurements.

The time evolution of the radial profiles from the Low Field Side (LFS) to the High Field Side ($-1<\rho<1$) is observed in TJ-II with 125 keV Cs^+ ions in a single shot. The typical scanning time is 10 ms. A few profiles are not complete at the plasma edge due to the low signal to noise ratio caused by the beam toroidal shift induced by plasma current variation during the discharge. In T-10, 4–6 repetitive pulses produce profile fragments with various beam Tl^+ energies from 80 to 300 keV, which unify to the radial profiles in LFS ($+0.2<\rho<1$), as shown in Figure 2.

The fine focused (<1 cm) and intense (100 μA) beams provide the measurements in the wide density interval $n_e=(0.3–5)\times10^{19}$ m^{-3}, while the advanced control system for primary and secondary beams provides the measurements in the wide range of the plasma current in T-10 and magnetic configurations in TJ-II, including Ohmic, ECR and NBI heated plasmas.

3.2 Plasma oscillations

Beam detector in the multi-slit electrostatic energy analyser is designed to measure simultaneously the data on plasma potential (by beam extra energy), plasma density n_e (by beam current) and B_{pol} (by beam toroidal shift) in poloidally shifted sample volumes. There are from 2 to 5 slits (spatial channels) in operation. The two slits measurement scheme is shown in Figure 1.
Low noise high gain (10^7 V/A) preamplifiers with 300 kHz bandwidth and 2 MHz sampling allows us to study broadband turbulence and quasi-coherent modes like Geodesic Acoustic Modes (GAM), Alfvén Eigenmodes (AE), suprathermal electron induced modes, etc.

3.2.1 Quasi-coherent modes: GAMs and AEs

HIBP is sensitive to the local plasma potential and density perturbation associated with GAM. GAM amplitude in plasma potential depends on the electron density and vary from the noise level (<10 V) up to ~100 V. Figure 3 (left) shows the Fourier Power Spectral Density (PSD) for the potential and density oscillations with a frequency resolution < 2 kHz. GAM is observed as a pronounced frequency peak in potential with a high contrast respect to the broadband turbulence, while the MHD mode is mainly seen in plasma density.

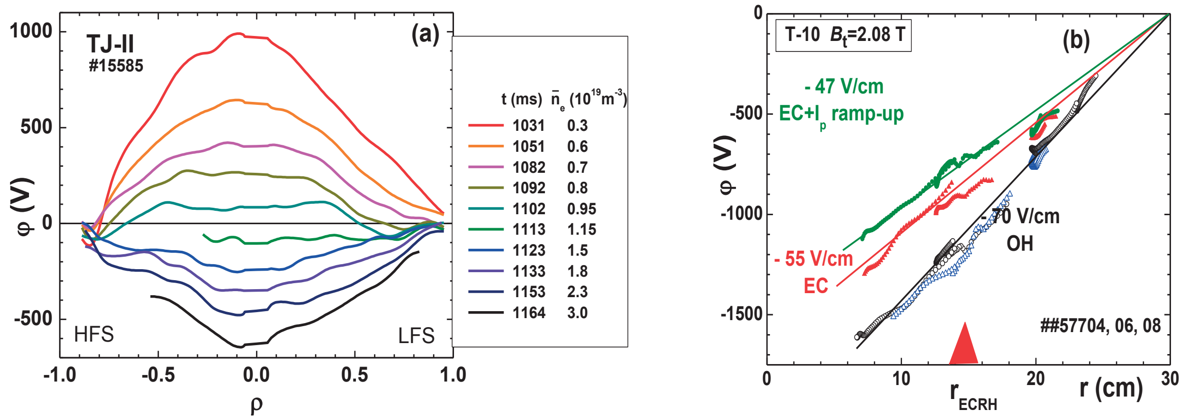

FIG. 6. Evolution of the electric potential profiles in the plasmas with ECR and NBI heating on TJ-II (a) and with Ohmic and ECR heating in T-10 (b).

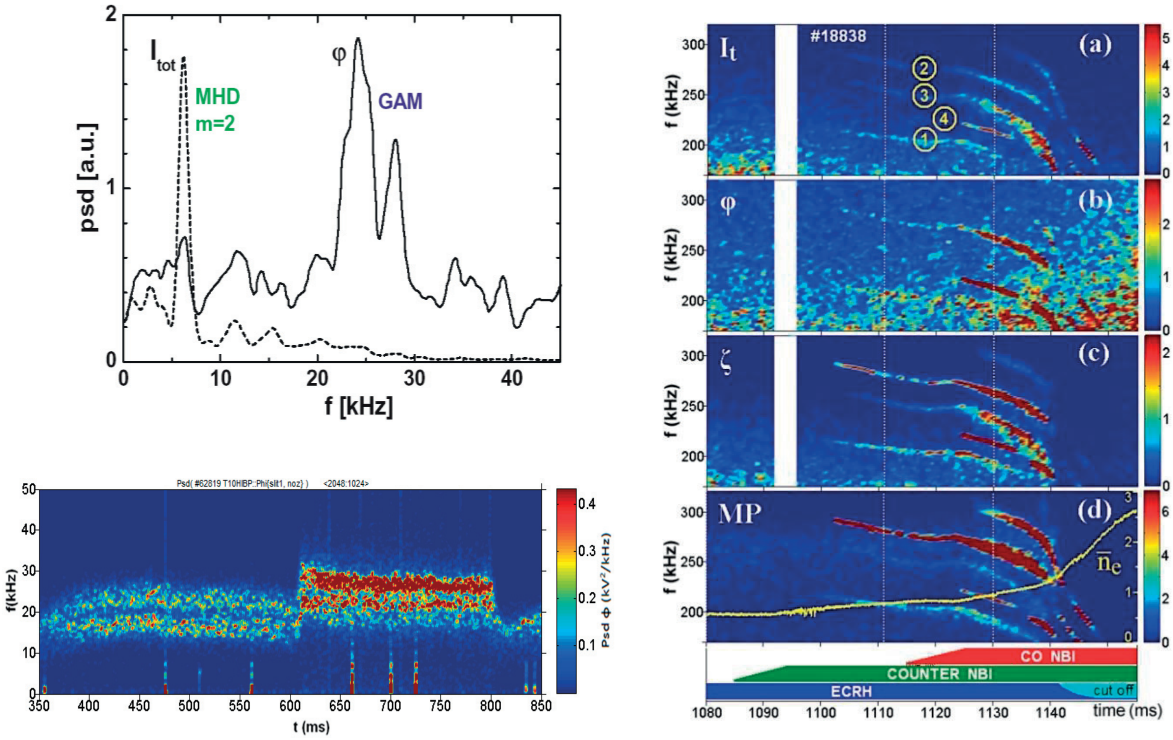

FIG. 7. Left: T-10 data. Left up. Potential and density power spectra for GAM. Left down potential spectrogram shows GAM evolution in the pulse with ECRH. The GAM intermittent structure is observed. Right: TJ-II data. PSD spectrograms of HIBP (ρ = -0.5) and Magnetic Probe (MP) signals in arbitrary unit. Alfvén Eigenmodes are pronounced: (a) on the total secondary beam current I_t proportional to n_e; (b) on the potential ψ; (c) on the toroidal shift of secondary beam ζ proportional to B_{pol}; (d) on the MP signal.

The high time resolution in a range of milliseconds allows us to resolve the GAM intermittent structure with a typical length of the wave packages ~1–2 ms. HIBP shows that GAMs on T-10 have a radially uniform spatial structure of potential perturbation and the π/2 phase shift between the plasma potential and density. Due to its capability to measure simultaneously potential, B_{pol} and density oscillations, HIBP is the most direct diagnostics to study Alfvén Eigenmodes, an electromagnetic waves, propagating along the magnetic field lines of plasma configuration and producing the oscillatory components of E_{r}, B_{pol} and plasma pressure. AEs are visible in all three HIBP parameters as presented in their spectrograms in Figure 3 (right). Various modes, marked with numbers are clearly detectable in the NBI heated phase of the discharge. The spatial scan of the sample volume allows us to find a radial location for each mode.

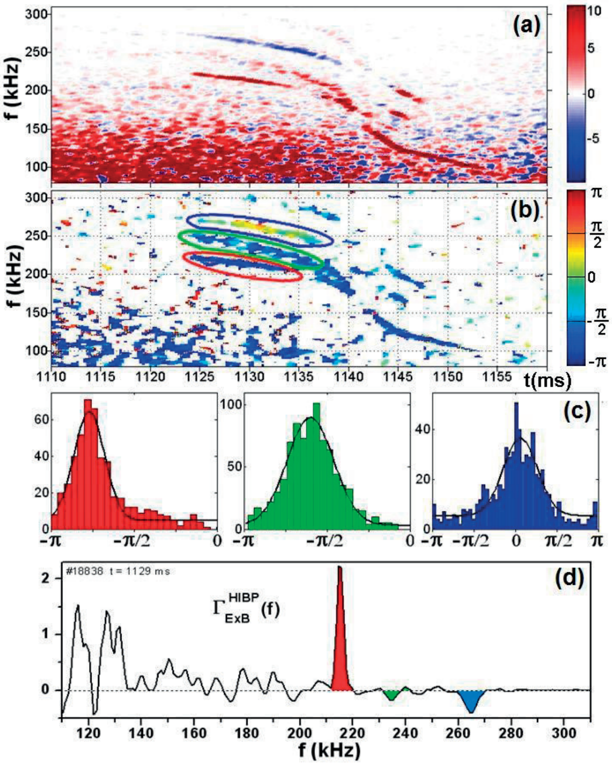

FIG. 8. a) Frequency resolved turbulent particle flux (in arb. units) in the NBI sustained dischargeof TJ-II. Red colour means outward flux, blue – inward flux.
b) Cross-phase $\theta_{ne\,Epol}$ between n_e and E_{pol} oscillations. Only the points with high $Coh_{ne\,Epol} > 0.3$ are shown. The colour bar is in radians. Three chosen AEs are marked by colour ovals.
c) The histograms of the cross-phase for each marked AEs with corresponding colours, indicating flux direction.
d) PSD of the turbulent particle flux, taken at some time instant, averaged over 1 ms.

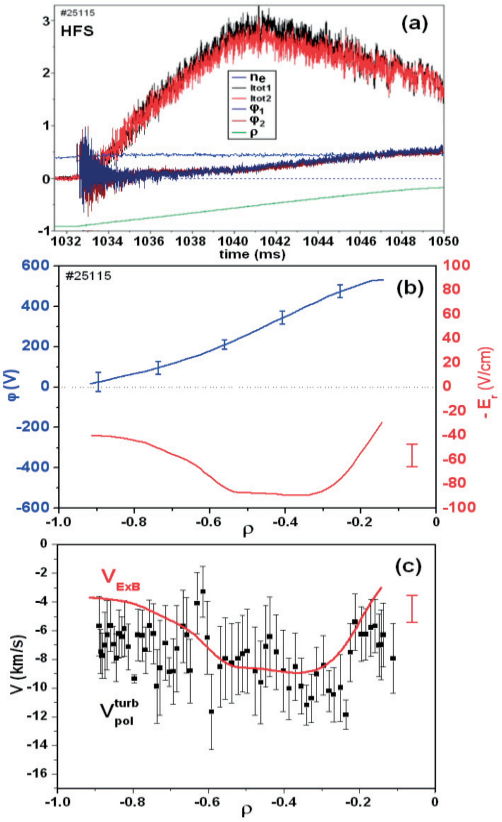

FIG. 9. Comparison of V_{phase}^{turb} and $V_{E\times B}$ measured by HIBP in TJ-II.
(a) raw signals of HIBP currents (red and black) and potentials (blue and brown) obtained during radial scan. The density time trace is shown as thin blue curvs, the SV radial position is in green;
(b) smoothed potential (blue) and E_r (red) radial profiles;
(c) V_{pol} and $V_{E\times B}$ radial profiles. Both of V_{pol} and $V_{E\times B}$ are directed to ion diamagnetic drift.

3.2.2 Turbulent particle flux

Multi-slits energy analyzer provides the oscillatory component of the plasma potential φ, and density $\tilde{n}_e(t)$ in poloidally shifted sample volumes, see Figure 1. Thus $E_{\mathrm{pol}} = (\varphi_1 - \varphi_2)/x$, $x \sim 1$ cm, and the electrostatic turbulent particle flux $\Gamma_{E\times B}(t) = 1/B_t \cdot \tilde{n}_e(t)\tilde{E}_{\mathrm{pol}}(t)$ is derived.

Frequency resolved turbulent particle flux, which is taken as $\Gamma_{E\times B}(f) = -2 / B_{tor} \cdot \mathrm{Re}(S_{nE})$, where S_{nE} is the Fourier cross-spectrum of density and E_{pol}, allows us to get a contribution of the broadband turbulence and that of the quasicoherent modes. Figure 7a shows the frequency resolved flux for the NBI discharge of TJ-II. It shows that the broadband turbulence at $f_{BB} <$ 250 kHz mainly produce the outward flux, denoted by red color. On top of that, the AEs are clearly visible in the spectrogram as a set of quasi-monochromatic modes. Figure 4a shows that the contribution of the specific modes may vary: there are outward, inward and zero flux presented for different AEs. The direction and the value of the flux contribution for specific AEs are theier specific characteristics. Their value depends on the cross-phase $\theta_{\mathrm{ne\ Epol}}$ between n_{e} and E_{pol} oscillations, as seen in Figure 7b, Figure 7c and Figure 7d.

3.2.3 Poloidal phase rotation for the broadband turbulence

The density oscillations cross-phase $\theta_{1,2}(f) = \arg\{P_{1,2}(f)\}$, where $P_{1,2}(f) = n_1^*(f) n_2(f)$ produces poloidal propagation velocity of perturbation or plasma rotation: $V_{\mathrm{phase}}^{\mathrm{turb}} = \Delta x \cdot 2\pi f / \theta_{1,2}$. Here we consider $\tilde{n}_e / n_e \approx \tilde{I}_{tot} / I_{tot}$, where $\tilde{I}_{tot} / I_{tot}$ is the relative oscillations of the beam current. Figure 8 shows the radial distribution of the plasma turbulence rotation for $0 < f < 150$ kHz in the TJ-II stellarator. Plasma potential profile is measured altogether with the density turbulence, see Figure 8b. Figure 8c shows that $V_{\mathrm{phase}}^{\mathrm{turb}}$ and $V_{E\times B}$ are in coincidence with an experimental accuracy over the whole radial interval.

Summary of the works performed:

- Calculation of HIBP probing beam trajectories and sample volume locations for the multislit energy analysers on the T-10 tokamak and TJ-II stellarator was performed.
- Calculation of ion trajectories inside the electrostatic energy analysers was done for the analysers, used in T-10 tokamak and TJ-II stellarator.
- The multislit beam detector for the energy analysers was designed.
- The steerable remote controlled support system for beam detector was designed.
- The multichannel preamplifier with high (250 kHz) bandwidth low noise (0.1 nA) compatible to the high vacuum conditions was designed.
- The multislit beam detector and high bandwidth low noise multichannel preamplifier were manufactured.
- The study of the plasma behavior in the T-10 tokamak and the TJ-II stellarator with the new HIBP beam detectors was performed.
- It provides the time evolution of the full radial mean profiles of plasma potential (or Er) in LFS on T-10 and in both LFS and HFS in TJ-II.
- The new multislit energy analyzers simultaneously measure the oscillatory component of three parameters: plasma potential, density and Bpol.

- Thus the poloidal mode number and rotation velocity of the density broadband turbulence and quasicoherent modes are retrieved.

- The frequency resolved turbulent particle flux is measured in the core plasma.

- Finally, HIBP becomes multipurpose diagnostics to study plasma electric potential and turbulence properties in the middle size toroidal devices.

ACKNOWLEDGEMENT

This research has been supported by Co-ordinated Research Project (CRP) of the International Atomic Energy Agency (IAEA) “Utilization of the Network of Small Magnetic Confinement Fusion Devices for Mainstream Fusion Research”, IAEA research contract RC 18033 “Development of the heavy ion beam probe (HIBP) diagnostics for small fusion devices”. The research described in sections 3.1 and 3.2 was funded by Russian Science Foundation, project 14-22-00193.

REFERENCES

[1] SOLOMATIN, R.Y., MELNIKOV, A.V., et al., Edge potential study in the T-10 tokamak, XLI Intenational conference on the plasma physics and controlled fusion, Zvenigorod (2014) http://www.fpl.gpi.ru/Zvenigorod/XLI/M.html#Sekcija%20MUoo.

[2] SOLOMATIN, R.Y., BUDAEV, V.P., GRASHIN, S.A., DZYATKO, E.V., ELISEEV, L.G., MELNIKOV, A.V., Investigation of the turbulence characteristics and turbulent fluxes in the sol of T-10 tokamak, 41st EPS Conference on plasma physics, http://ocs.ciemat.es/EPS2014PAP/pdf/P4.038.pdf

[3] BASHIR, M.F., SMOLYAKOV, A.I., ELFIMOV, A.G., MELNIKOV, A.V., MURTAZA, G., Electromagnetic effects on geodesic acoustic modes, Phys. Plasmas **21** 8 (2014).

[4] ZENIN V.N., ELISEEV L.G., KOZACHEK A.S., KRUPNIK L.I., LYSENKO S.E., MELNIKOV A.V. and PERFILOV, S.V., Study of poloidal structure of geodesic acoustic modes in the T-10 tokamak with heavy ion beam probing, Problems of atomic science and technology series, Phys. Plasmas **20** 94 (2014) 269-271.

[5] MELNIKOV, A.V., OCHANDO, M., ASCASIBAR, E., CASTEJON, F., ELISEEV, L., et al., Effect of magnetic configuration on frequency of nbi-driven Alfvén modes in TJ-II, Nucl. Fusion **54** (2014) 11.

[6] MELNIKOV, A.V., ELISEEV, L.G., LYSENKO, S.E., PERFILOV, S.V., ZENIN, V.N., Study of the gam radial structure and properties in the oh and ecrh plasmas in the T-10 tokamak, 15th Latin American Workshop on Plasma Physics (LAWPP2014), San Jose, Costa Rica, 27-31.01.2014. Rep. R-O09. http://plasma.ietec.org/abs/R-O09.pdf

[7] GUTIERREZ-TAPIA, C., MARTINELL, J., LOPEZ-BRUNA, D., MELNIKOV, A.V., Neoclassical modeling of the radial electric field and comparison with measurements in the TJ-II stellarator, 15th Latin American Workshop on Plasma Physics (LAWPP2014), San Jose, Costa Rica, 27-31.01.2014. Rep. R-PS05 http://plasma.ietec.org/abs/R-PS05.pdf

[8] MELNIKOV, A.V., BARCALA, J.M., KRUPNIK, L.I., HIDALGO, C., ELISEEV, L.G., et al., Control and data acquisition for dual hibp diagnostics in the TJ-II stellarator, 28th Symposium on Fusion Technology (SOFT 2014) Sept. 29 – Oct. 3, San Sebastián, Spain, P1.059. www.soft2014.eu

[9] MELNIKOV, A.V., DE PABLOS, J.L., BARCALA, J.M., KRUPNIK, L.I., HIDALGO, C., ELISEEV, L.G., et al, Dual heavy ion beam probing in the TJ-II stellarator, 28th Symposium on fusion technology (SOFT 2014) Sept. 29 – Oct. 3, San Sebastián, Spain, P1.060. www.soft2014.eu.

[10] MELNIKOV, A.V., LYSENKO, S.E., ELISEEV, L.G., PERFILOV, S.V., GRASHIN, S.A., SOLOMATIN, R.YU., KRUPNIK, L.I., ZENIN, V.N., Study of gam radial structure in oh and ecrh plasmas in the T-10 tokamak, 25th Fusion Energy Conference (FEC 2014) Saint Petersburg, Russia 13 - 18 October 2014. EX/P1-45. http://www-pub.iaea.org/iaeameetings/46091/25th-Fusion-Energy-Conference-FEC-2014

[11] IVANOV, N., ELISEEV, L., KAKURIN, A., MELNIKOV, A., PERFILOV, S., AND SOLOVIEV, V., Magnetic island and plasma rotation under external resonant magnetic perturbation in T-10 tokamak, 25th Fusion Energy Conference (FEC 2014) Saint Petersburg, Russia 13 - 18 October 2014. EX/P1-46. http://www-pub.iaea.org/iaeameetings/46091/25th-Fusion-Energy-Conference-FEC-2014

[12] MELNIKOV, A.V., ELISEEV, L.G., LYSENKO, S.E., PERFILOV, S.V., SHURYGIN, R.V., KRUPNIK, L.I., KOZACHEK, A.S., SMOLYAKOV, A.I., Radial homogeneity of geodesic acoustic modes in ohmic discharges with low b in the T-10 tokamak*,* JETP letters **100** (2015) 555-560

[13] SOLOMATIN, R.Y., MELNIKOV, A.V., et al, Characteristics of the plasma potential and turbulence at the plasma periphery in the T-10 tokamak, XLII International conference on the plasma physics and controlled fusion, Zvenigorod (2015).
http://www.fpl.gpi.ru/Zvenigorod/XLII/Zven_XLII.html

[14] SOLOMATIN, R.Y., BUDAEV, V.P., GRASHIN, S.A., DZYATKO, E.V., ELISEEV, L.G., MELNIKOV, A.V., Investigation of the turbulence characteristics and turbulent fluxes in the sol of T-10 tokamak, 42nd EPS Conference on Plasma Physics, P4.038.

[15] MELNIKOV, A.V., ACASIBAR, E., CAPPA, A., ELISEEV, L.G., et al, The study of Nbi-driven chirping mode properties and radial location by heavy ion beam probe in the tj-ii stellarator, 14th IAEA Technical Meeting (TM) on Energetic Particles in Magnetic Confinement Systems, 01-04-th September 2015, Vienna, Austria. Rep. O-18.
http://www-naweb.iaea.org/napc/physics/meetings/TM49508.html

[16] MELNIKOV, A.V., et al., The study of plasma electric potential and turbulence in T-10 tokamak and tj-ii stellarator and prospects for compass, 22-nd IAEA Technical Meeting (TM) on Research using Small Fusion Devices, Prague, Czech Rep., 12-14th October 2015, I-2.

[17] MELNIKOV, A.V., ELISEEV, L.G., LYSENKO S.E., PERFILOV, S.V., SHELUKHIN, D.A., VERSHKOV, V.A., ZENIN, V.N., KRUPNIK L.I., KHARCHEV, N. K. and HIBP team, Correlation properties of geodesic acoustic modes in the T-10 tokamak, J. Phys. Conference Series **591** (2015).

[18] GUTIERREZ-TAPIA ,C., MARTINELL, J.J., LOPEZ-BRUNA, D., MELNIKOV, A. V., Neoclassical modeling of the radial electric field and comparison with measurements in the tj-ii stellarator, J. Phys. Conference Series **591** (2015).

[19] MELNIKOV, A.V., BARCALA, J.M., KRUPNIK, L.I., HIDALGO, C., ELISEEV, L.G., CHMYGA, A.A., CHERCOLES, J., KOMAROV, A.D., KOZACHEK, A.S., KHREBTOV, S.M., LOPEZ, J., MOLINERO, A., MARTIN, G., DE PABLOS, J.L., PERFILOV, S.V., TASCHEV, YU.I., Control and data acquisition for dual hibp diagnostics in the tj-ii stellarator, Fus. Eng. Des. **96 – 97** (2015) 724–728.

[20] GUTIERREZ-TAPIA, C., MARTINELL, J.J., LOPEZ-BRUNA, D., MELNIKOV, A.V., ELISEEV, L., RODRGUEZ, C., OCHANDO, M.A., CASTEJON, F., GARCA, J., VAN MILLIGEN, B.P., FONTDECABA, J.M. Analysis of tj-ii experimental data with neoclassical formulations of the radial electric field, Plasma Phys. Control. Fusion **57** (2015).

[21] MELNIKOV, A.V, MARKOVIC, T., ELISEEV, L.G., GRYAZNEVICH, M., IMRISEK, M., KOVARIK, K., LYSENKO, S.E., MEDVEDEV, S.YU., PETERKA, M., SEIDL, J., STOCKEL, J., WEINZETTL, W. and the COMPASS team, Quasicoherent modes in the compass tokamak, Plasma Phys. Control. Fusion **57** (2015) 13.

[22] ELISEEV, L.G., IVANOV, N.V., KAKURIN, A.M., MELNIKOV, A.V., PERFILOV, S.V., Magnetic island and plasma rotation under external resonant magnetic perturbation in the T-10 tokamak, Phys. Plasmas **22** (2015).

[23] ELISEEV, L.G., IVANOV, N.V., KAKURIN, A.M., MELNIKOV, A.V., PERFILOV, S.V., LYSENKO, S.E., MALTSEV, S.G., and ZENIN, V.N., Study of the large-scale mhd mode and its effect on gam in the T-10 tokamak, 42nd EPS Conference on Plasma Physics P5.159, http://ocs.ciemat.es/EPS2015PAP/pdf/P5.159.pdf

[24] SOLOMATIN, R.Y., BUDAEV, V.P., GRASHIN, S.A., DZYATKO, E.V., ELISEEV, L.G., MELNIKOV, A.V. PERFILOV, S.V., ZENIN, V.N. Characteristics of turbulence and electric fields in the peripheral plasma of the T-10 tokamak, 42nd EPS Conference on Plasma Physics P5.160, http://ocs.ciemat.es/EPS2015PAP/pdf/P5.160.pdf

[25] MARKOVIČ, T., SEIDL, J., MELNIKOV, A., HÁČEK, P., HAVLICEK, J., HAVRÁNEK, A., HRON, M., HRONOVA, O., IMRÍŠEK, M., JANKY, F., KOVAŘÍK, K., MIKULÍN, O., PÁNEK, R., PAPŘOK R., PIPEK, J., VONDRÁČEK, P., WEINZETTL, V., Alfvén-wave character oscillations in tokamak compass plasma, 42nd EPS Conference on Plasma Physics P4.104, http://ocs.ciemat.es/EPS2015PAP/pdf/P4.104.pdf

[26] SEIDL, J., HRON, M., ADAMEK, J., VONDRACEK, P., HORACEK, J., HIDALGO, C., MELNIKOV, A., ELISEEV, L., MARKOVIC, T., STÖCKEL, J., BASU, D., HACEK, P., HAVLICEK, J., IMRÍŠEK, M., KOVARIK, K., WEINZETTL, V., PANEK, R. and COMPASS Team, Observation of geodesic acoustic mode-like oscillations on compass, 42nd EPS Conference on Plasma Physics P4.103, http://ocs.ciemat.es/EPS2015PAP/pdf/P4.103.pdf

[27] CASTEJÓN, F., AGUILERA, A. M., ASCASÍBAR, E., ESTRADA, T., HIDALGO, C., LÓPEZ-FRAGUAS, A., OCHANDO, M. A., YAMAMOTO, S., MELNIKOV, A.V., ELISEEV, L.G., PERFILOV, S.V., and the TJ-II team, Influence of magnetic well on electromagnetic turbulence in the TJ-II stellarator, 42nd EPS Conference on Plasma Physics O1.102, http://ocs.ciemat.es/EPS2015PAP/pdf/O1.102.pdf

[28] VERSHKOV, V.A, MELNIKOV, A.V., ELISEEV, L.G., et al Density fluctuations as an intrinsic mechanism of pressure profile formation, Nucl. Fusion **55** (2015) 063014

[29] GRYAZNEVICH, M., VAN OOST, G., STÖCKEL, J., KAMENDJE, R., KUTEEV, B.N., MELNIKOV, A., POPOV, T., SVOBODA, V. and the IAEA CRP teams, Contribution to fusion research from iaea coordinated research projects and joint experiments, Nucl. Fusion **55** (2015) 10.

[30] MELNIKOV, A.V., ELISEEV, L.G., PERFILOV, S.V., LYSENKO, S.E., SHURYGIN, R.V., ZENIN, V.N., GRASHIN, S.A., KRUPNIK, L.I., KOZACHEK, A.S., SOLOMATIN, R.YU., ELFIMOV, A.G., SMOLYAKOV, A.I., UFIMTSEV, M.V. and HIBP team, The features of the global gam in oh and ecrh plasmas in the T-10 tokamak, Nucl. Fusion **55** (2015) 8.

[31] MELNIKOV, A.V., ELISEEV, L.G., LYSENKO, S.E., PERFILOV, S.V., SHELUKHIN, D.A., VERSHKOV, V. A., ZENIN, V. N., KRUPNIK, L. I., KHARCHEV, N. K., UFIMTSEV, M.V. and HIBP team, Long-range correlations of geodesic acoustic modes in the t-10 tokamak, Problems of Atomic Science and Technology, Series: ThermoNucl. Fusion **38** 1 (2015) 49-56.

[32] MELNIKOV, A.V., ELISEEV, L.G., LYSENKO, S.E., PERFILOV, S.V., ZENIN, V.N., KRUPNIK, L.I., CHMYGA, A.A., KOMAROV, A.D., KOZACHEK, A.S., KHREBTOV, S.M., TASHCHEV, YU.I., ZHEZHERA, A.I., BARCALA, J.M., HIDALGO, C., LOPEZ, J., MOLINERO, A., DE PABLOS, J.L., Heavy ion beam probing – the diagnostics for internal measurements of the electric potential and turbulence in toroidal plasma devices, 1st EPS Conference on Plasma Diagnostics (ECPD2015), Frascati, Italy, 14 – 17 April 2015.

DEVELOPMENT OF DIAGNOSTICS AND EXPERIMENTAL INVESTIGATION OF RF PLASMA PRODUCTION AND CONFINEMENT IN STELLARATOR-TYPE DEVICES URAGAN-2M AND URAGAN-3M

V.S. VOITSENYA, V.V. CHECHKIN, L.I. KRUPNIK, V.E.MOISEENKO, V.K. PASHNEV

Kharkov Institute of Plasma Physics, National Science Center “Kharkov Institute of Physics and Technology” (IPP KIPT), Kharkov 61108, Ukraine

Abstract
In this report some results on development of new diagnostics and the results of experiments carried out during period 2012–2015 at the stellarator fusion devices Uragan-2M and Uragan-3M in Kharkov IPP are presented. The report consists of two parts concerning operation of both devices, correspondingly. In the case of Uragan-2M these are mainly efforts on development of new diagnostics, and in the case of Uragan-3M device these are results of experiments on plasma produced by RF power supplied by two RF antennas.

1. INTRODUCTION

Our investigations were provided in the framework of the Coordinated Research Project (CRP) of the International Atomic Energy Agency (IAEA) “Utilisation of a Network of Small Magnetic Confinement Fusion Devices for Mainstream Fusion Research” during the fulfillment of the 4-year activity. The work was directed to preparation of new diagnostics equipment for measuring plasma parameters and providing experiments at stellarator type devices Uragan-2M and Uragan-3M.

2. URAGAN-2M INSTALLATIONS

2.1. Common characteristics of the Uragan-2M torsatron

Uragan-2M is a torsatron ($l = 2$, $m = 4$, $R = 1.7$ m, $\langle a \rangle \leq 0.22$ m) with reduced helical ripples, moderate shear and magnetic well (up to $\delta V'/V' \approx -4.3\%$); maximal toroidal magnetic field is limited by $B_{max} < 2.4$ T, but presently maximal field is 0.5 T.

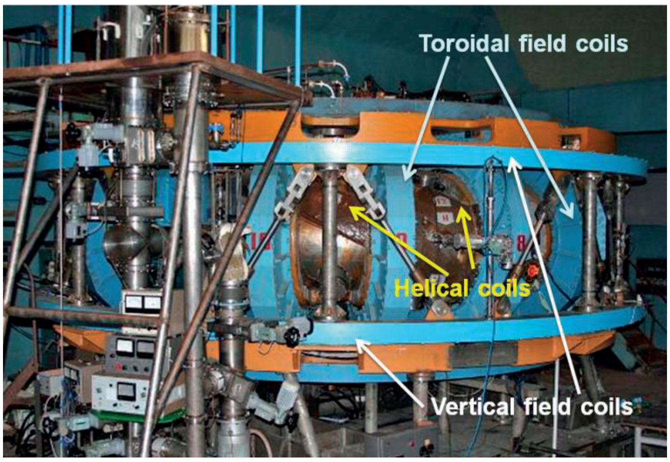

FIG. 1. Photo of U-2M. Arrows indicate the components of every system of magnetic coils: 16 coils for production of toroidal component of magnetic field, two pairs of helical coils for production of poloidal component of magnetic field, and 8 coils which produce vertical magnetic field that compensate vertical magnetic field of helical coils.

The most attractive regimes for investigation of plasma confinement are the low frequency regimes, when the helical ripple at the plasma boundary can be reduced down $\varepsilon_h(a) < 0.06$. For plasma production 3 different kind of RF antennas are installed inside toroidal vacuum chamber. The total view of the machine is shown in Figure 1.

The existence of magnetic configurations with closed magnetic surfaces was proved with the use of low energy electron beams and luminescent rod, before starting experiments with plasma. The results for two different magnetic configurations are presented in Figure 2.

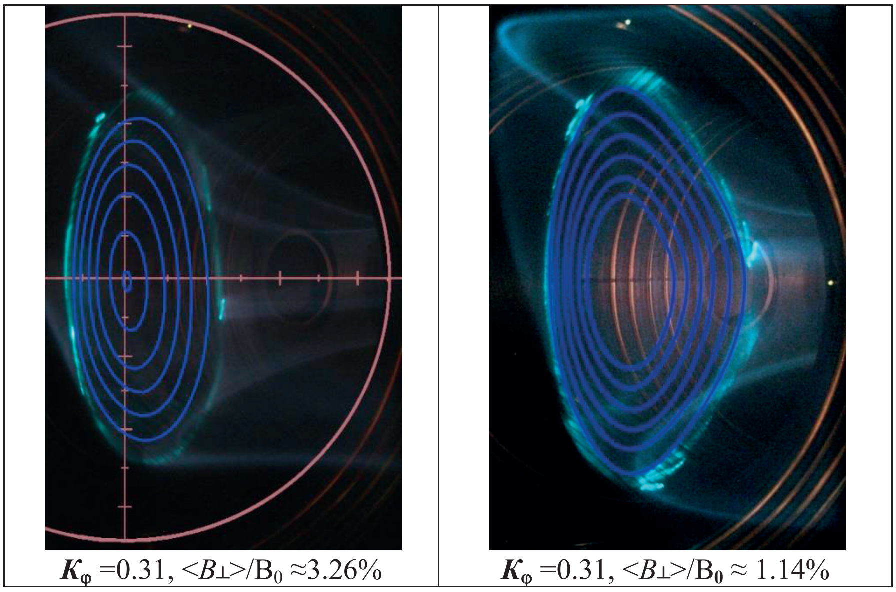

$\boldsymbol{K_\varphi}$ =0.31, $<B_\perp>/B_0 \approx 3.26\%$

$\boldsymbol{K_\varphi}$ =0.31, $<B_\perp>/\mathbf{B_0} \approx 1.14\%$

FIG. 2. Structure of measured magnetic surfaces in U-2M with all toroidal coils switched on.

Magnetic configuration has magnetic surfaces with maximal average radius $a \approx 20.5$ cm for $K_\varphi=0.31$, and $<B_\perp>/B_0 \approx 1.14\%$, $<B_\perp>/B_0 \approx 1.85\%$, $<B_\perp>/B_0 \approx 2.55\%$. Vertical magnetic field strongly influence the structure of magnetic surfaces: they move along the major radius and this is accompanying by a significant change of their size. Configurations with $K_\varphi=0.31$–0.32 has no magnetic islands and therefore are main that were recommended for providing experiments with plasma.

2.2. Control for efficiency of wall conditioning

Up to now there is no any limiter installed into U-2M vacuum chamber, therefore plasma that diffuses across magnetic field moves along open magnetic field line to the chamber wall, resulting in a backward flux of impurities from the wall. In this connection, high attention was focused on development of the methods of wall conditioning mostly suitable to the U-2M construction. In particular, in the framework of CRP new method for controlling the efficiency of wall conditioning with the use of a cryogenic trap was suggested and realized.

For plasma production RF power was used with 4 different kind of antennas installed in the vacuum chamber. All used radio-frequency generators are auto generators based on electronic tubes and adjusted for certain frequency bands (3–15 MHz, 140 MHz). Optical spectra are measured with the monochromators based on interference filter. The mass spectra are measured with the mass spectrometer which uses ion cyclotron resonance effect. Besides, pumped out gas is analysed with the help of the cryogenic trap with liquid nitrogen. The trap is periodically separated from the vacuum vessel and warmed up for further trapped gas analysis and pumping out. During the campaign different experiments have been performed. Table 1 presents the experiments and their duration.

TABLE 1. DETAILS OF ONE OF CONDITIONING CAMPAIGN AT U-2M

Duration of experiment, hours	Calendar days	Gas used	Neutral gas pressure, Torr	Magnetic field, kOe	Generators used*
165	32	H_2	1E-4	0.58	K1, U_a=3 kV; SGE, U_a =2 kV
87.5	30	He	5.8E-5	0.3	K1, U_a =3 kV; VHF, U_a=4 kV; SGE, U_a=2.5 kV
32.5	12	He+O_2	5.8E-5	0.3	K1, U_a=3 kV; VHF, U_a=3.8 kV
15	3	H_2+N_2	1E-4	0.15	K1, U_a=3 kV; VHF, U_a=4 kV; K2, U_a=5 kV
32	33	H_2	1.5E-4	4.0	K1, U_a=7 kV; K2, U_a=7 kV

** Notations: K1 and K2 are RF pulse generators “Kaskad”. K1 provides power for broad frame or crankshaft antenna during 10 ms at 4.5 MHz. K2 provides power for the four-strap antenna during 40 ms at 4.7 MHz. VHF is the VHF generator which operates in continuous mode at 135 MHz. SGE is the Small Generator of Evsukov (our staff member, a prominent engineer). It is a continuously operating RF generator with the frequency of 5.1 MHz.*

2.2.1. Experiments on RF wall conditioning in atmosphere of helium

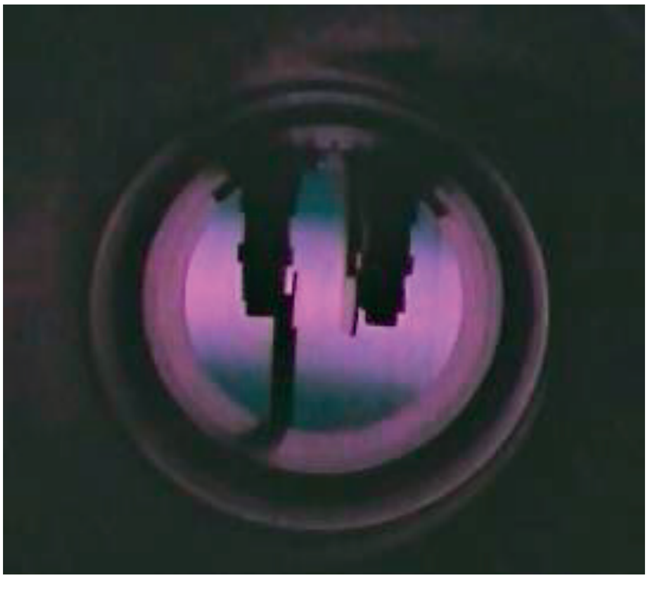

FIG. 3. Photo of RF discharge in helium made through side window.

Figure 3 shows the photo of RF discharge in helium atmosphere. Two different color layers are clearly seen in the discharge: pink layer in the middle and the green outer edge layer, what is connected with big difference in electron temperatures characterizing different parts of plasma volume. The frame antenna holders are seen at the front. In general, a RF discharge is created easier in this gas. The VHF discharge is much brighter in helium than that in hydrogen (Figure 4).

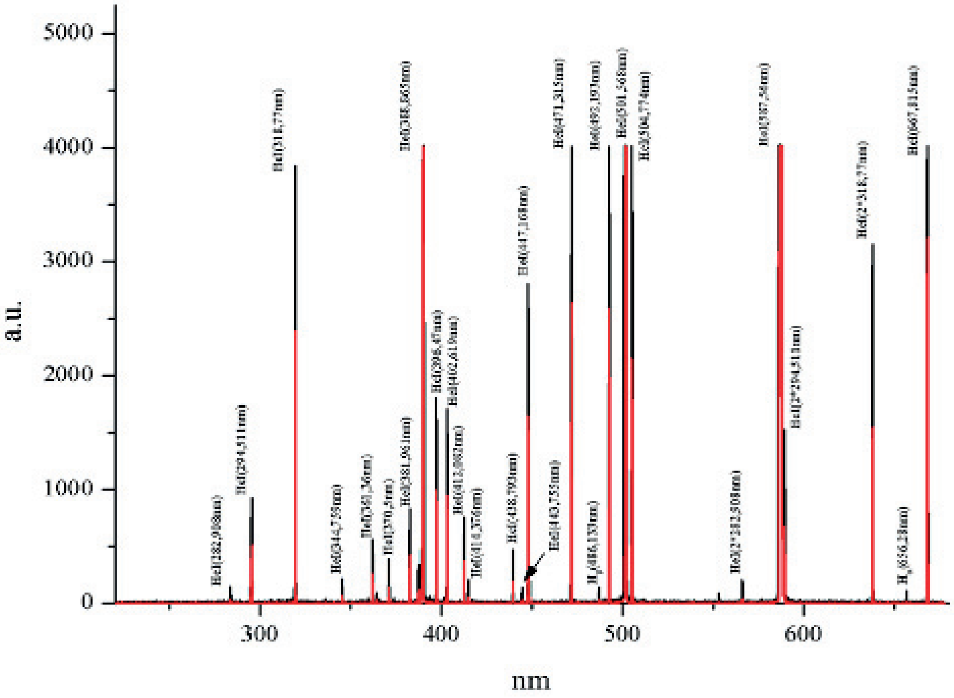

FIG. 4. Optical spectra of discharges in helium. Black lines – UHF, red lines – UHF+K1.

The optical spectrum of helium plasma is dominated by helium lines but some low intensity lines of hydrogen atoms can be also observed.

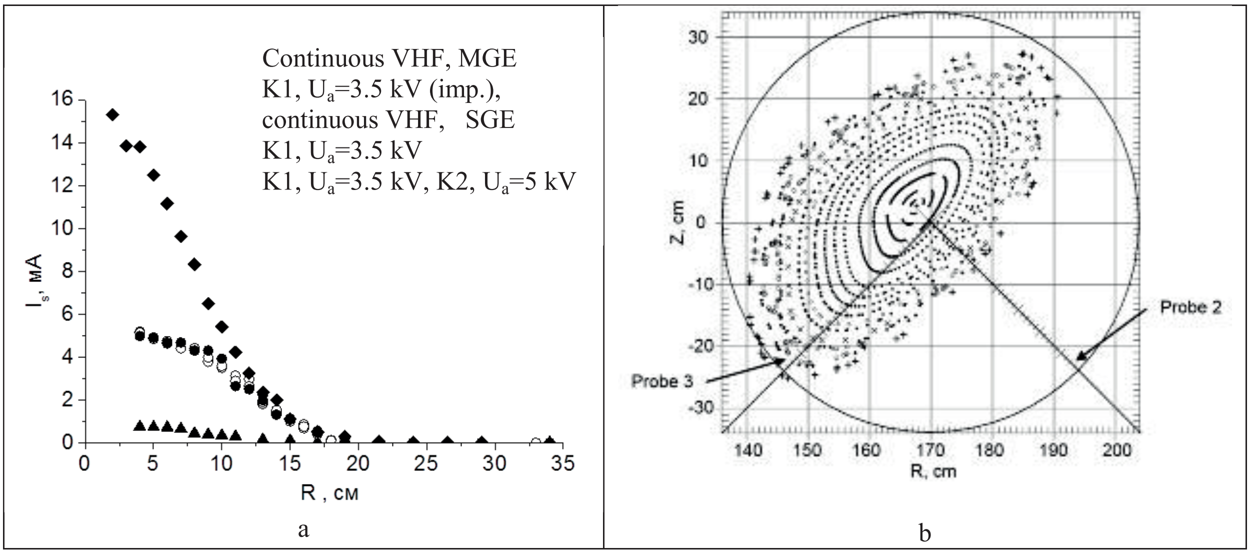

a b

FIG. 5. Ion saturation currents of Langmuir probe #2 for different discharges.

The movable Langmuir probes were used for collecting information about spatial distribution of plasma density. The ion saturation current versus the probe position is shown in Figure 5. For magnetic configuration chosen the last closed magnetic surface corresponds to the probe position R≈10 cm. One can see that plasma steps out the confinement volume for all discharges. The plasma density in VHF discharge is more than one order less than that in pulse discharges driven by the “Kaskad” generators.

In Figure 6 the mass spectra are shown immediately before conditioning VHF discharge in He accompanied by pulses of the K1 generator has started and during discharge, after 20 minutes RF discharge start. As seen, there appeared masses corresponding to CH_4 and C_3H_8, a little grow masses H_2 and CO_2, decrease masses He, H_2O, NH_3, and mass O_2 fully disappears.

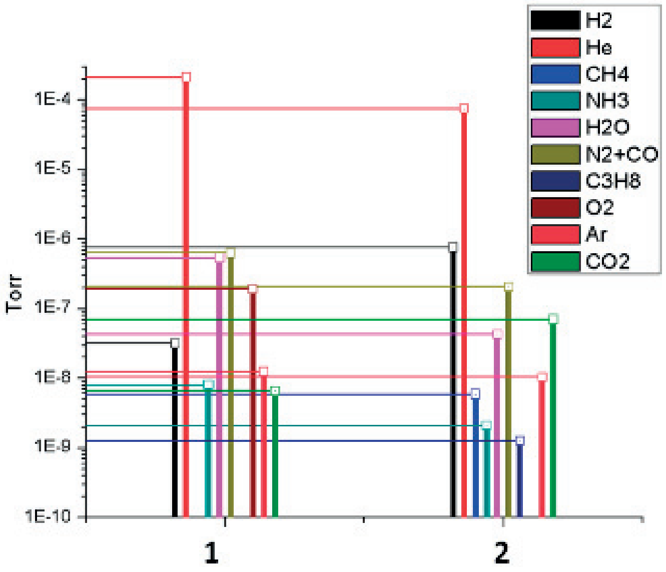

FIG. 6. Helium discharge mass spectrum. 1 – just before conditioning start; 2 – 20 minutes after discharge start.

2.2.3. Experiments on RF wall conditioning in atmosphere of helium and oxygen

The oxygen is puffed into the device using a leak valve to achieve 1/10 of the total pressure. After this the pressure is increased to regular value by helium feeding. During RF wall conditioning experiments in the atmosphere of helium and oxygen the panoramic optical spectra was measured (Figure 7).

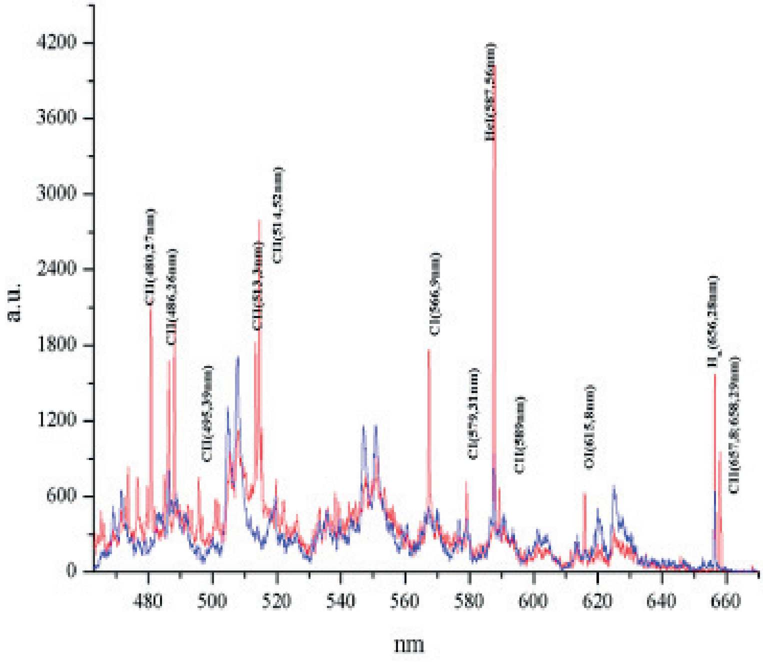

FIG. 7. Helium and oxygen discharge optical spectra. Red lines – K1, blue lines – UHF.

Optical spectra show a considerable amount of molecular bands which, in indirect way, may characterize the effectiveness of atomic oxygen generation. Also, mass spectrum (Figure 8) was measured at the beginning and at the end of the continuous VHF discharge.

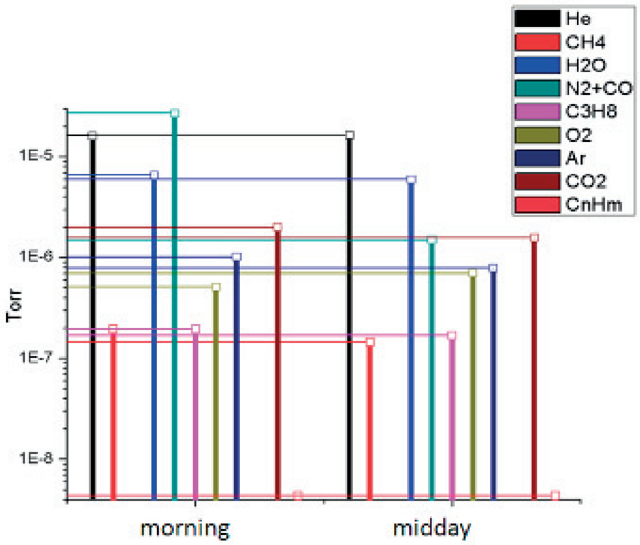

FIG. 8. Helium and oxygen RF discharge mass spectrum.

The mass spectrum shows some decrease of all measured impurities.

2.2.4. Experiments on RF wall conditioning in atmosphere of hydrogen and nitrogen

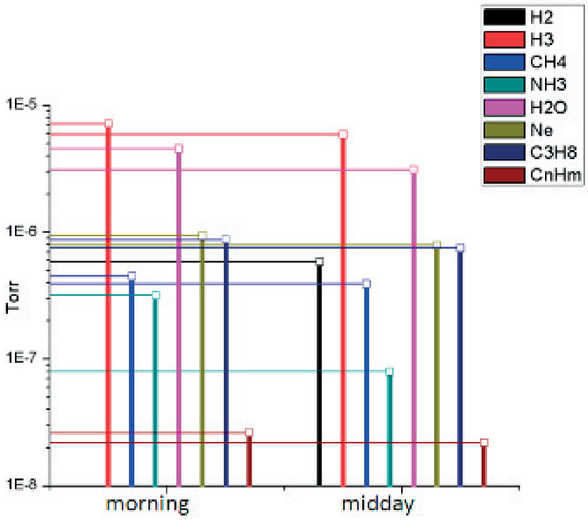

FIG. 9. Hydrogen and nitrogen RF discharge mass spectrum.

Measured during RF wall conditioning mass spectrum (Figure 9) shows cleaning process similar to the helium and oxygen.

2.2.5. Cryogenic Trap Operation

Uragan-2M is equipped with three high-vacuum cryogenic traps: two big traps with Venetian blends and one small cylindrical trap. There were no regular usages of these traps during the campaign. In eight occasions the small trap was filled with liquid nitrogen and after half-hour exposition during plasma discharge it was separated from the machine vessel and warmed up to the separated branch pipe of volume 52.000 cm^3. The gas pressure at this volume is measured and then the branch pipe is pumped. The results of measurement are present in Figure 10. The maximum amount of collected gas corresponds to wall conditioning in atmosphere of helium and oxygen, hydrogen and nitrogen and also to the case when the device is subjected to air.

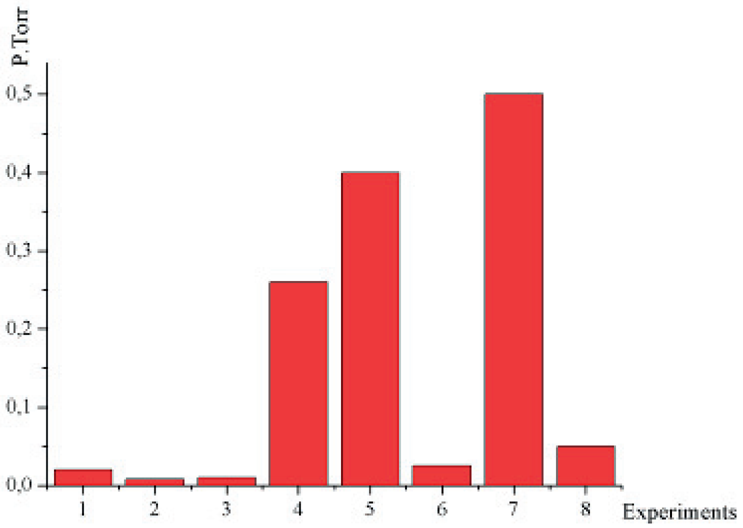

FIG. 10. Total pressure in the separated volume to which the cryogenic trap is warmed up: 1 - start of wall conditioning with He; end of wall conditioning with He after 10 calendar days; 3 –VHF wall conditioning with He; 4 one week later, VHF wall conditioning with He and O_2; 5 –two weeks later, end of wall conditioning with N_2 and H_2; 6 – three days later, wall conditioning with H_2; 7 – wall conditioning with H_2, after one week standby without pumping; 8 – regular wall conditioning with H_2.

2.2.6. Conclusion

The comparison of different working gases and regimes of wall conditioning demonstrated clearly significant advantage of the use of mixture of gases, He and O_2 or He and N_2 for the wall conditioning procedures at Uragan-2M stellarator.

2.3. Installation of HIBP equipment on the U-2M torsatron and carrying out of its adjustment and alignment

Beam-probe methods of diagnostics are on the important position in studying plasmas in fusion devices [1–4]. With the help of probing beams of neutrals and ions it is possible in modern fusion devices to obtain the information about the spatial distribution of the electric potential, plasma density and electron temperature, as well on their fluctuations and poloidal magnetic field (plasma current) with high spatial and temporal resolution.

The discovery of the regime for improved confinement of plasma (H-mode) on the tokamak ASDEX [5] led to the understanding of the important role of electric fields in the process of plasma confinement in tokamaks and stellarators [6,7]. A detailed knowledge of the structure of the electric field from the center plasma confinement volume to its periphery is the basis for understanding of the phenomenon of plasma confinement.

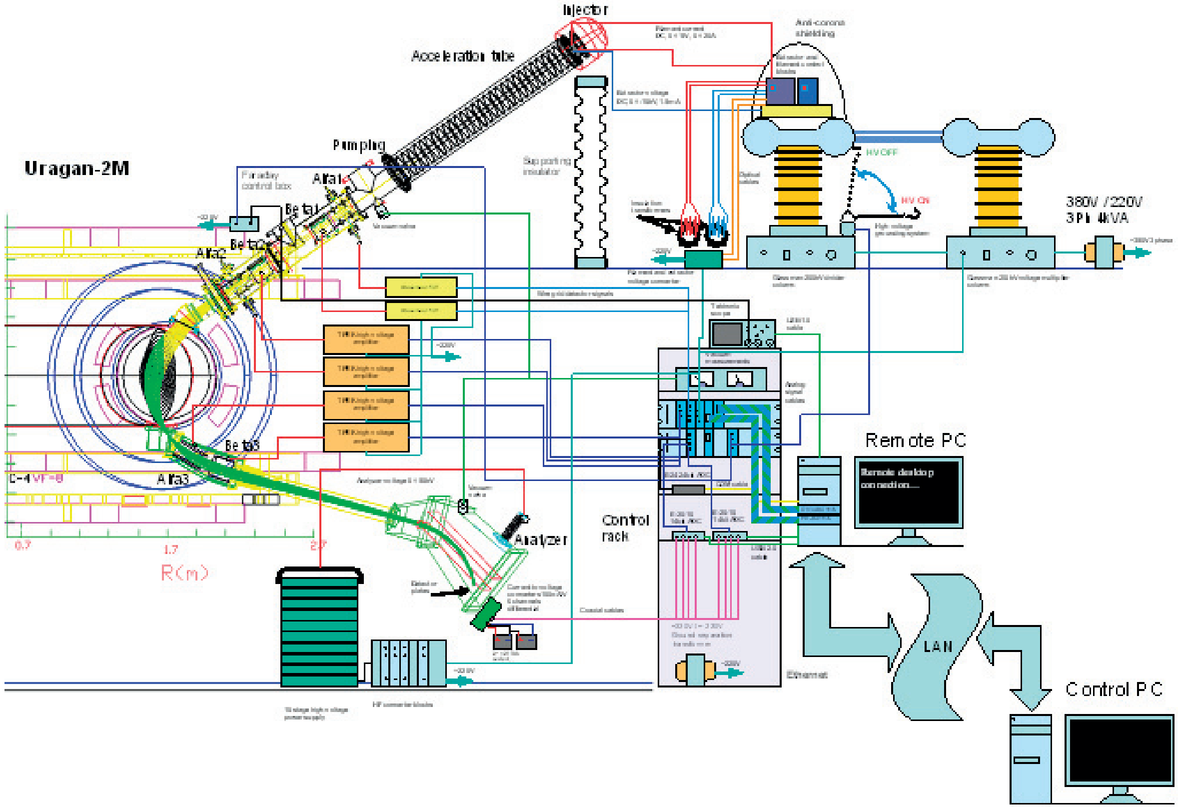

FIG. 11. The full principal scheme of the HIBP diagnostic complex for torsatron «U-2M».

Applying Heavy Ion Beam Probe (HIBP) method it is possible to have information on the distribution of the electric potential and its fluctuations along the whole plasma volume. This diagnostics can simultaneously measure a few parameters of plasma and their fluctuations with high spatial and temporal resolution – electric potential φ, electron density n_e, electron temperature T_e and poloidal magnetic field B_p [8–11].

Each HIBP diagnosis has its own unique settings, optimized for size and configuration of the magnetic field of a particular nuclear device (camera size and input and output ports, their location, configuration, amplitude and topology of the magnetic field). In the framework of this project we developed HIBP equipment for torsatron Uragan-2M, which gives possibility to measure the amplitude of the electric potential and its fluctuations in the space from the centre to the periphery of the plasma confinement volume synchronously with some other parameters.

2.3.1. Installation of the HIBP diagnostic system at torsatron Uragan-2M and carrying out of its adjustment and alignment

After all equipment was tested at the stand, the diagnostic system was assembled at the section of torsatron «Uragan-2M» (Figs 11 and 12). Injector unit is located on a special platform (Figure 12, position A), which was developed and fabricated in the framework of this project. The power sources (to +200 kV–10 kV) are displaced on the platform, as well as the system for heating of the ion emitter, and the grounding system. Figure 13 and Figure 14 show the main components of the HIBP diagnostics – injector and analyzer systems. To lock and to be able to fine-adjusting of the provisions of the injector, three fixing elements were developed and fabricated (Figure 13), which allow to adjust the angle of inclination up to ±5°.

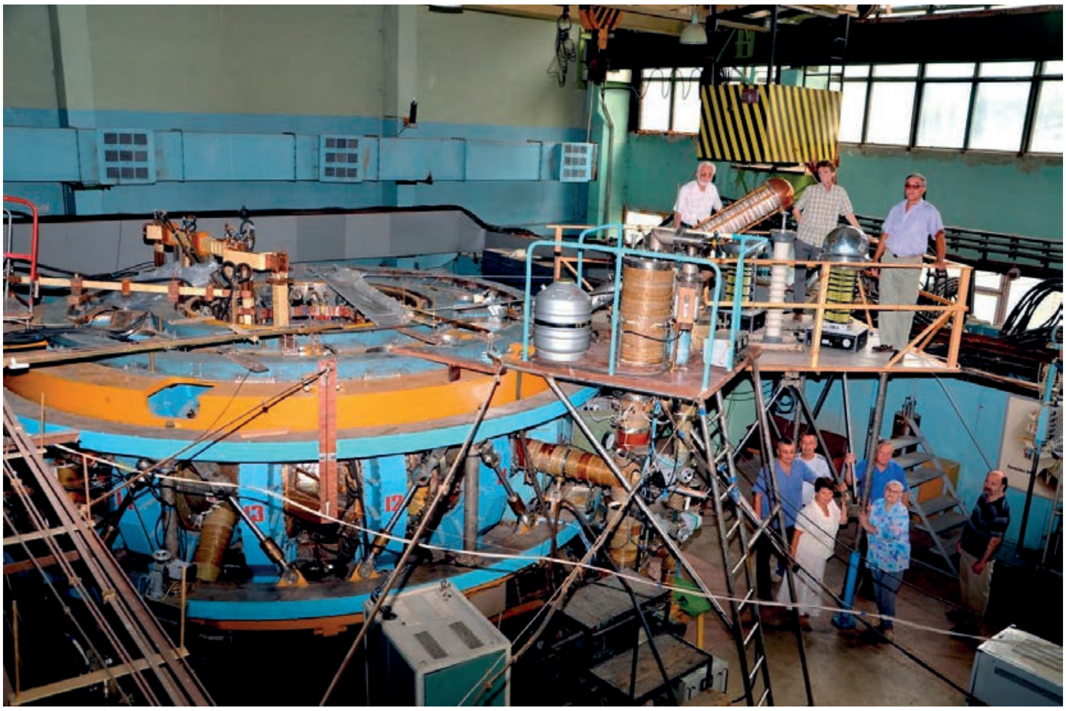

FIG. 12. Final view of the HIBP diagnostic system with all HIBP team and representatives of the IPP teams who were actively participated in assembling of the equipment. At the left is pumping control system. A high voltage part of the equipment is located on a special isolated platform.

FIG. 13. Injector part of the diagnostic complex. 1 - shield of emitter block, 2 - security rings of the accelerator tube, 3 - turbomolecular pump TV-301, 4 - vacuum valve, 5 - primary beam-line of the blocks of deflecting plates (α_1-β_1, α_2-β_2), 6 - backing tract, 7, 8 – support and HV insulator.

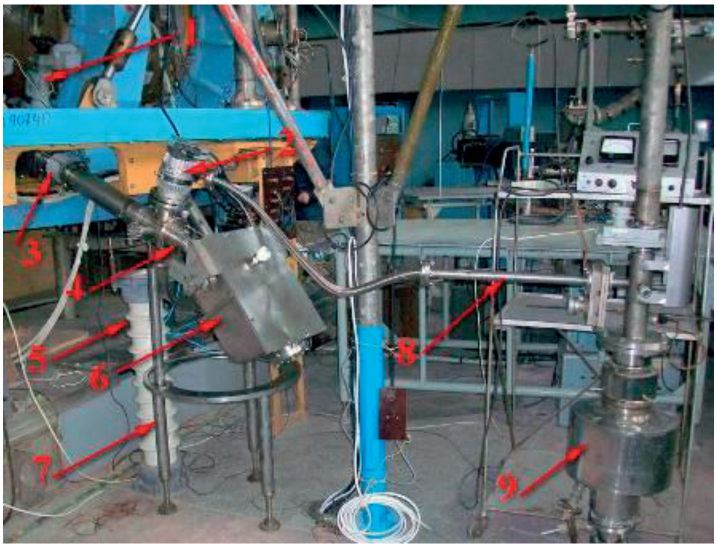

FIG. 14. Analyzer part of the diagnostic complex. 1 - valve («Uragan-2M»/analyzer), a 2 - turbomolecular pump TV-301, 3 - the first block of the air-bellow for the alignment of the analyzer, 4 - second air-bellow block, 5 – isolator of secondary beam-line, 6 - energy analyzer, 7 - support of the analyser, 8 - backing tract, 9 – vacuum trap with liquid nitrogen.

Figure 15 shows the picture of the secondary beam-line with its vacuum valve. The port of the camera of torsatron «Uragan-2M» (1) is fixed in transition socket (2) which provides passage of the secondary beam of ions to the detector plate of the analyzer according to calculations of trajectories of the secondary ion beam. For the electrical isolation of the secondary beam-line from the camera, a dielectric gasket (3) was placed. For the deflector plates α_3-β_3 (4) the adapter (6) is located with offset relative to the axis, and the flanges needed for the current output of the secondary ion beams to the energy analyzer. The adapter is designed to have the ability to change the angle of tilt of the analyzer to the horizon, to have a possibility for compensation of the angle of inclination of the secondary ion beam.

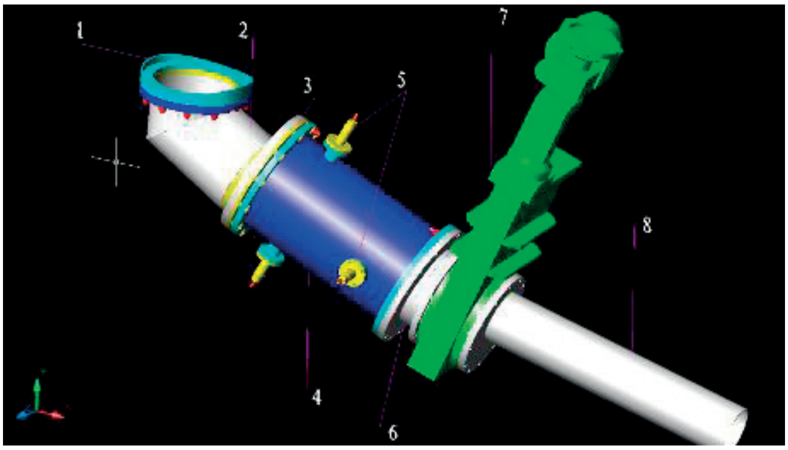

FIG. 15. Secondary beam-line with vacuum valve.

Figure 16a shows a grounding system, which is designed for the output circuit high voltage power supplier to the «ground» what is needed for draining the final electric charge from the main high-voltage electrode. Also this system is designed to lock on the high-voltage power supplier. The grounding system consists of an induction motor and the gearbox, which is driven by the bar to the main high-voltage electrode. The motor control is carried out with the help of two magnetic starters and phase-shift of the capacitor, which is used for the 220 V power supply system. The position of the rod is regulated with the help of the digital signal from the computer; the end positions of the rod are registered by two switches. Figure 16b shows the circuit of grounding system.

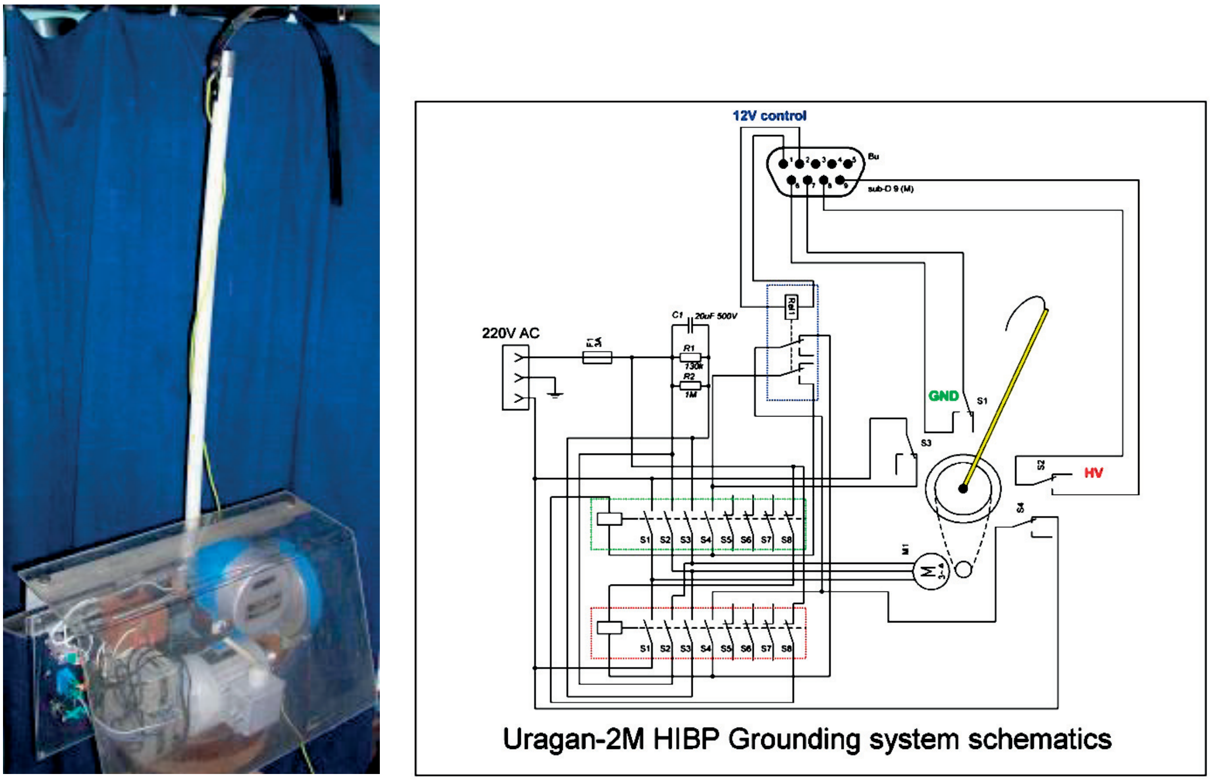

a) *b)*

FIG. 16. Uragan-2M HIBP grounding system.

The vacuum system of the diagnostic complex is based on the fore pump AB3-20, located under the torsatron «Uragan-2M». The design of fore-vacuum line allows carrying out parallel pumping of injector and analyzer parts of the complex, as well as each part separately. At the present time, injector and analyzer parts of the complex passed a vacuum test and vacuum of (6–7) x 10^{-7} Torr was achieved.

2.3.2. Manufacturing and installation of units and systems of control and collection of information complex

Power supply systems, control and information collector are placed in two racks. The rack No.1 contains: high voltage power supply “Glassman +200 kV”, power of the rack No.2, the power units for measurement of vacuum in the analyzer and injection parts of the diagnostic complex, a power supplier and control of fore pump AB3 -20 and turbopump TV-301. The rack No.2 conteins: power supply sources of the company Glassman +200 kV, +50 kV, +5 kV (2 PCs.), high-voltage amplifiers TREK 10 kV (4 PCs), computer control and blocks of systems of active management and collection of information diagnostic complex.

The system of monitoring and collecting information, which is performed on the basis of the boards of automation of the Russian company L-Card is represented in Figure 17. This system consists of modular station data collection LTR-EU-16-1 and attached to it blocks the control and management. There is a possibility to collect it from different modules to the specific needs or tu use other diagnostic or measuring tasks. The system is made on the basis of the signal to the processor Blackfin ADSP-BF537 (600 MHz), and has two high-speed interfaces for connection to PC USB 2.0 high-speed and Fast Ethernet (100BASE-TX). 2 modules DAC LTR34-8 maximum of 16 bits, which have on-Board buffer memory up to 2 million samples and are able to output the analog data in synchronous mode with a speed of more than 500 ksamples per second at 8 output channels each are installed in crate. These modules are used for remote control of injector and analyzer high voltages, current of emitter filament, extractor voltage and setting of scanning and corrective curves of voltages for electrostatic deflect and scanning plates on the high-voltage amplifiers TREK. Module LTR11 - 16 channel 14-bit ADC with a maximum sampling frequency of 400 kHz is installed to crate also. Measuring signals of an injector and analyzer voltages, current of the emitter heater, extractor voltage, primary beam current on the Faraday cylinder and the input diaphragm came to it. Since this module is designed with a serial poll channels, that is, sampling frequency is divided by the number of used channels, it can also be used for relatively low-frequency (20 kHz) measurement of the secondary beam current on the plate of the analyzer. Even before the modular gathering stations data includes module digital input-output LTR-43, with the help of which performed control cover of the Faraday cylinder and the system of emergency control and shutdown high voltage injector, but also the module LTR-51, frequency meter and meter time intervals, which are used when configuring General the control system, the office of the beam and the collection of information. To fix the diameter of primary ion beam at the entrance to the camera of Uragan-2M a wire detector is located connected with the digital oscilloscope Tektronix TDS-2004. It is also possible to connect it to the PC via the USB port. The software system of monitoring and data collection is done on the base of the software package Labview 2011 and codes, the driver card L-Card, which are supplied with modules.

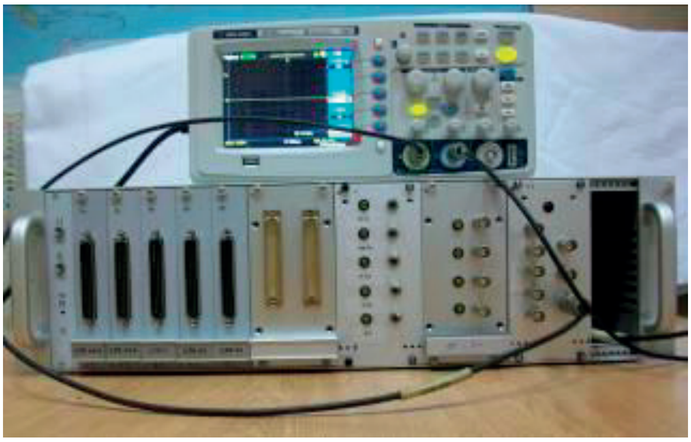

FIG. 17. The system of monitoring.

Figure 17 shows broadband highly sensitive converters of current-to-voltage signals from the detector plate analyzer. 10 converters with differential input on the basis of chipset OPA637 are installed in a metal shielding casing. The conversion ratio is 10^7 nA/V and the frequency bandwidth of the order of 250 kHz.

In the Figure 18 is the manufactured unit for remote control of turbomolecular pump of the injector and the analyzer. This unit is installed in a rack near the input door on torsatron Uragan-2M. It leverages remote inclusion of the pump, control of speed of rotation of the rotor and indication of the state of emergency in the operation of pumps.

FIG. 18. Unit for remote control of turbomolecular pump of the injector and the analyzer.

In the Figure 19 are presented the manufactured modules USB optical interface on the basis of chip FT232 and optical transceivers Agilent. This module can be used by connecting two computers or a computer - device remote through isolated optical cable. As an alternative, this system can be used to control the current of emitter filament and extractor voltage. Remote device on the high voltage side is based on microcontroller ATMEL (type ATMEGA32), which in itself has all the necessary components (ADC, asynchronous serial interface, PWM modulator and other).

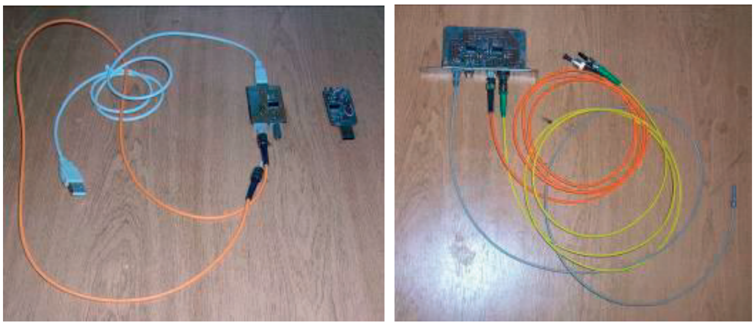

FIG. 19. USB optical interface.

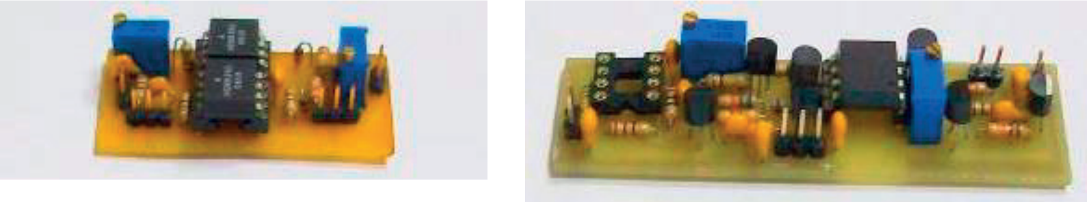

FIG. 20. Electronic components used for connection of analog signals and avoid briefly closed ground loops. Several variants schemes on various electronic components have been developed, manufactured and tested.

2.3.3. Detection system

Detection system consists from secondary beam-line and the energy analyzer of secondary ions with same platesfor secondary current measurement.

The secondary beam-line Figure 21 is placed at the U-2M facility among two angles – alfa = -30^{o} (from horizontal plane) and beta = 16^{o} (from vertical plane in a horizontal cross section). Secondary beam line is consists of two pares of the deflection plates placed in a rectangular metal housing. Afla3 plates is used to focus the secondary beam fan in the XY plane and the Beta3 plates in XZ plane to the entrance slits of the electrostatic energy analyzer. To do this, the secondary deflection voltages must be exactly synchronized with the primary Alfa2 scanning voltage.

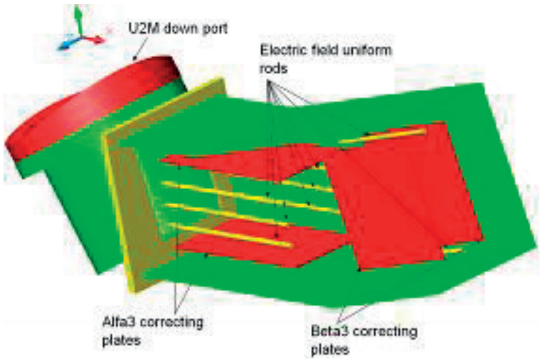

FIG. 21. Internal view of the secondary beam-line box.

2.3.4. Energy analyzer and its calibration

Proca-Green ("flat mirror") 30° electrostatic analyzer [4] usually used for high accuracy measurements of secondary ions energy and current in HIBP diagnostic systems.

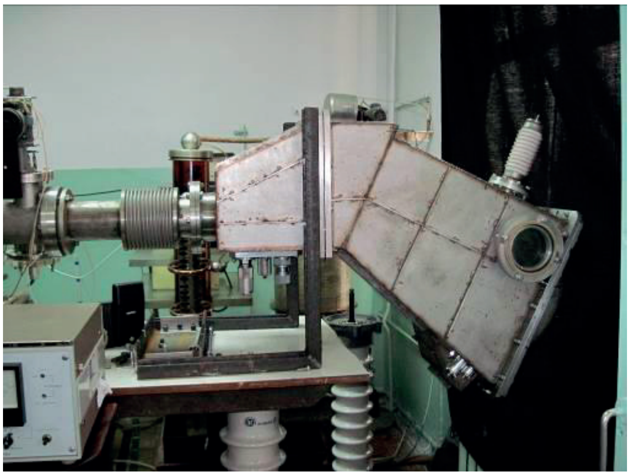

FIG. 22. Energy analyzer for installation on Uragan-2M.

Typical scheme of such 2-slits analyzer is shown on Figure 23.

Analyzer consists of 2 entrance slits, parallel plate capacitor ("flat mirror") and 8 detector plates (4 for each slit). Uniform transverse analyzer electric field deflecting ion beam to the angle, depending on ion energy. Position of deflected beam measured on collector plates. The bottom capacitor' plate is grounded; upper plate is under high voltage.

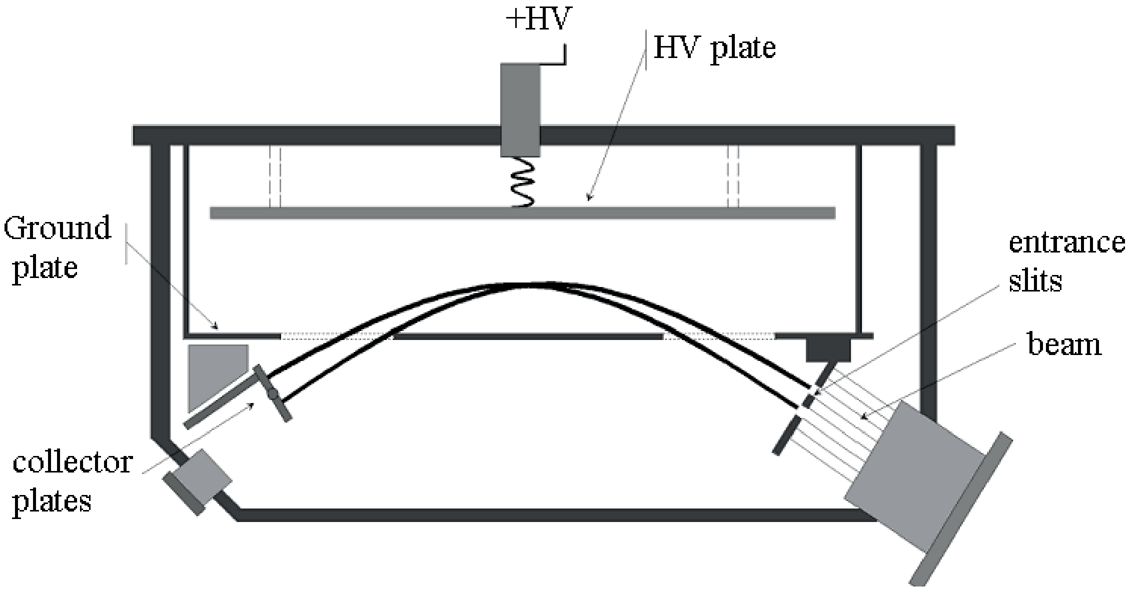

FIG. 23. Proca-Green energy analyzer.

Plasma potential value is measured as a difference between primary and secondary beams

energy: $\Phi = q_sV_A/(q_s - q_p)[(-i_b + i_t)/(i_b + i_t)F(\alpha) + G(\alpha)] - q_sV_B/(q_s - q_p)$ (1)

where:

$G= [x_d-(y_1 +y_2)\cdot ctg(\alpha)] / [2\cdot d\cdot \sin(2\alpha)\cdot \cos^2(\beta)]$ (2)

$F(\theta) = w(\sin30^o + \cos30^o tg\alpha)/[8\cdot d\cdot \sin^2\alpha\cdot \cos^2(\beta)]$ (3)

F and G are geometrical analyzer parameters named as gain function and dynamic function; i_b, i_t - currents to bottom and upper detector plates, V_A, V_B – analyzer and injector accelerating voltages, q_s, q_p – secondary and primary ion charges, x_d – distance between entrance slit and detector, y_1 and y_2 – distance between entrance and detector slits towards grounded plate, w – entrance slit width, α - poloidal (vertical) angle of ion beam, β-toroidal (horizontal) angle. So, the plasma potential can de measured if we know:

1) geometrical coefficients $F(\alpha)$ and $G(\alpha)$,
2) values of i_t, i_b, V_B, V_A, which can be measured.

Both geometrical coefficients must be obtained by special calibration. Figure 24 illustrates analytical curves of geometrical gain function $G(\alpha)$ for analyzer design. Gain function has 2 local extremes which are very important for measurements. Gain function between them has very weak dependence on α angle. It is possible to measure the ion energy in this angle range without exact information about poloidal (α) angle.

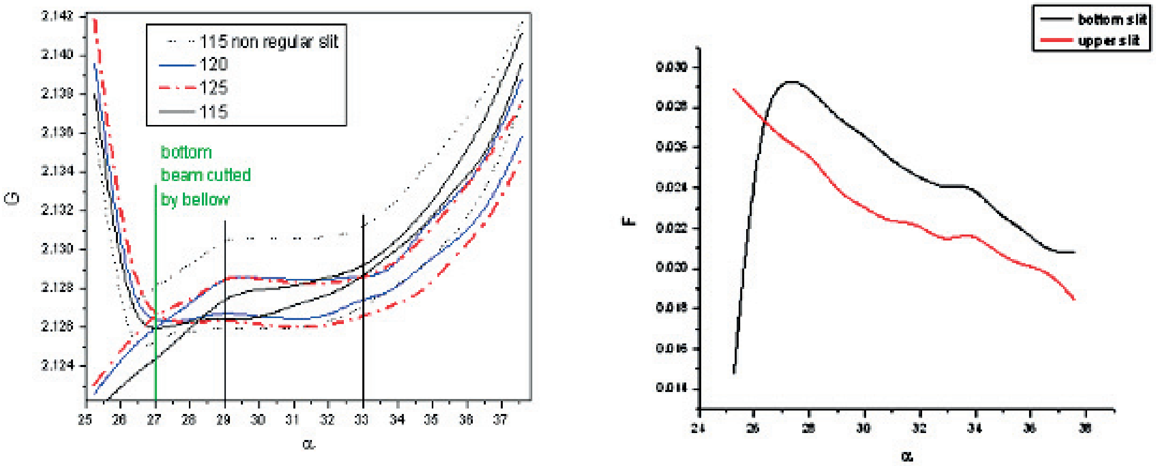

FIG. 24. The calibration curves of geometrical gain function G(α) and F(α).

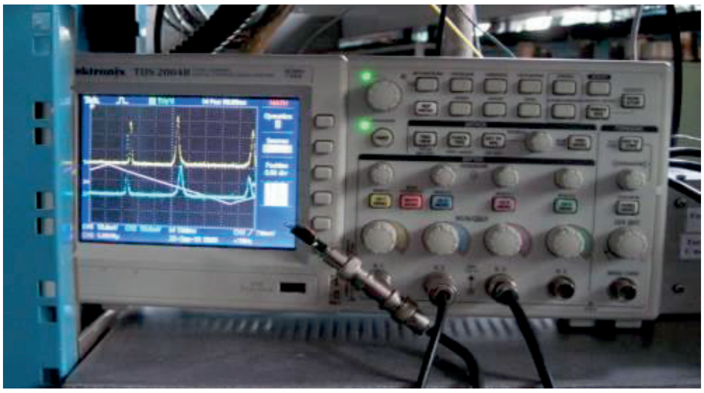

FIG. 25. First space profiles of the primary beam at Uragan-2M HIBP injector. Cesium beam energy is 50 kV, ion beam current is 50 μA, ion beam diameter is 3–4 mm.

Optimizing function G(α) and F(α) depend on analyzer geometry parameters, such as entrance-slit width, entrance slits and detector plates space positions with respect to the ground plate. After calibration this analyzer prepared to Uragan-2M diagnostic system is ready for operations with stellarator magnetic field from 0.8 to 2 T and for probing ion beam energy up to 150–450 keV.

2.4. Manufacture of the first stage of magnetic diagnostics for measuring plasma current and kinetic energy of plasma in U-2M

2.4.1. The peculiarities of magnetic diagnostics application at the U-2M torsatron

Magnetic diagnostics system is a set of magnetic sensors and electronic devices that enables one to determine a variety of important plasma characteristics owing to registration and processing of values of magnetic, which are generated by plasma currents outside the confinement volume [12–14]. Due to the existence of the stellarator vacuum magnetic configuration the performance capabilities of magnetic diagnostics in stellarator systems are significantly extended in comparison with tokamaks. As it has been demonstrated [15], magnetic diagnostics makes it possible to determine the longitudinal plasma current value, the plasma energy content, the power inputed into the plasma, the plasma energy confinement time, the shift and deformation of magnetic surfaces, the magnetic island structure, the MHD instability structure, etc. However, to obtain this information, it is necessary to place outside the plasma confinement volume a lot of sensors that register variations of magnetic fields generated by plasma currents in the confinement volume. The main difficulty in carrying out magnetic measurements is the account of the contribution of the image currents arising in the metal environment under the action of plasma currents. The image currents generate additional variable magnetic fields, which distort the plasma current magnetic fields registered by the magnetic sensors. The metal environment includes various metal structural elements, and also, metal vacuum-chamber walls.

The U-2M vacuum chamber presents a set of thin-walled sections (with a wall thickness up to 5 mm) connected together by bellows elements (with a wall thickness being about 1 mm). The vacuum chamber is placed into a toroidal metal casing (with a wall thickness up to 8 mm), on which the helical coils is mounted. According to the estimates, variable magnetic fields with impulse front greater than 10 ms can penetrate through this metal environment undistorted. For the reason that the heat time in the U-2M torsatron makes about 100 ms, the installation of magnetic sensors outside the vacuum chamber gives no way to obtaining information about the magnetic fields of plasma currents. Therefore, all magnetic diagnostics sensors must be placed inside the vacuum chamber. However, in most operating regimes of the U-2M torsatron, the last closed magnetic surface may be in contact with the vacuum chamber wall. So, inside the vacuum chamber of the U-2M torsatron, limiters have been installed to constrain the plasma within a distance of 1 to 2 cm from the wall chamber. These distances permit us to install magnetic sensors inside the vacuum chamber. However, the necessity to arrange the magnetic sensors within these narrow clearances complicates the design of magnetic plasma current registration systems. Besides, it is necessary to provide a thermal protection of the magnetic sensors, because the plasma creates heat loads on the constructional elements of the facility, which are in contact with the last magnetic surfaces of the confinement region. Furthermore, the electronic equipment that registers useful signals from the magnetic sensors should have the necessary time resolution to provide discrimination, amplification and integration of the useful signals.

2.4.2. The use, design and performance characteristics of magnetic sensors; electrical measurements circuits

Magnetic sensors systems were developed, manufactured and installed for carrying out the research program at the U-2M torsatron. The magnetic sensors enable one to register:

1) toroidal magnetic flux variations – with the use of diamagnetic loops;

2) variations with the poloidal angle in the zero, first and second harmonics of the poloidal magnetic field, as well as variations in the longitudinal plasma current and also, in the oscillation amplitude of the magnetic-filed poloidal component within the frequency range up to 200 kHz – through the use of 5 sets of 16 Mirnov coils placed in different cross sections along the length of the torus. The registration of toroidal magnetic flux variations and variations in zero harmonic of the poloidal magnetic field generated by the longitudinal plasma current makes it possible to determine the plasma energy content, the energy confinement time of plasma and the plasma-absorbed power. The registration of variations in the first and zero azimuthal harmonics of the poloidal magnetic field allow us to determine Pfirsch-Schluter currents, shift of magnetic surfaces, and MHD instability with first azimuthal harmonics. The registration of variations in the second poloidal magnetic field harmonic also enables one to determine the presence of magnetic islands, the deformation of magnetic surfaces, and the MHD instability with second azimuthal harmonics.

To protect the magnetic sensors from plasma-created thermal loads, in the regions close to the last magnetic surfaces, which may be in contact with the chamber walls, the magnetic diagnostic systems have additional stainless steel cover plates mounted on broad under plates being in contact with the vacuum chamber walls. This provides an efficient heat removal and protects the conductors and insulators of magnetic sensors from heat loads. All magnetic diagnostics elements are modular in design, in consequence of which they can be installed inside the vacuum chamber of the U-2M torsatron through the vacuum input ports, without vacuum chamber disassembly.

2.4.3. Diamagnetic loops

For registration of toroidal magnetic flux variations, two diamagnetic loops are installed inside the vacuum chamber of the U-2M torsatron. The external appearance of diamagnetic loops and their location inside the U-2M vacuum chamber are shown in Figure 26. Each of the diamagnetic loops consists of 21 turns of insulated wire, covering different areas. The turns are shielded against electrostatic inductions and placed in a protective casing made of stainless steel. The protective casing is mounted on electric insulators in order to prevent the flow of poloidal image currents through their surface, because these currents can cause strong electrical noise in the diamagnetic loops.

In diamagnetic measurements, the induced magnetic fields are compensated through the use of two diamagnetic loops covering different areas and are located in one cross section of the torus. The analog-digital (AD) techniques will be used to select the useful signal, which is the same for each loop. The block diagram of electrical signal measurements from the diamagnetic loops is shown in Figure 27. The electronic circuit of the AD converter is tuned so that in the absence of the useful signal the resulting signal from the diamagnetic loops should equal zero. Due to this, it becomes possible to exclude the influence of magnetic fields generated by image currents in the metal environment. A similar diamagnetic-flux measuring circuit is used successfully at the U-3M torsatron.

Before being installed in the vacuum chamber of the U-2M torsatron, the diamagnetic loops were calibrated and their characteristics were measured for their comparison under the conditions with and without metal environment. The metal environment was simulated with a stainless steel chamber, similar to a vacuum chamber of U-2M torsatron. Using a special test stand that could simulate poloidal plasma currents, the sensitivity of diamagnetic loops and their amplitude-frequency characteristics were measured inside and out of the simulator of U-2M torsatron chamber. The results of the studies are presented in Figure 28. It can be seen from the figure that at frequencies higher than the skin frequency $F\tilde{n}\hat{e} = \frac{\tilde{n}^2}{8\pi\sigma\Delta\grave{a}} = 500\tilde{A}\ddot{o}$ for the given chamber wall thickness (where *c* is the velocity of light, σ is the metal conduction, Δ is the wall thickness of the chamber, *a* is the chamber radius) the image currents flowing in the vacuum chamber, begins to affect on the values of signals registered by the diamagnetic loops. At frequencies below 300 Hz, the magnetic field of poloidal image currents begins penetrating through the metal wall of the chamber simulator, and the recorded signals from the two diamagnetic loops become the same. As a result, it appears possible to measure the magnetic fields of poloidal plasma currents without image current distortion with the time resolution being up to 500 μs. When measuring the signals of shorter duration, it is necessary to take into account the effect of the U-2M vacuum chamber. The findings of the investigation will be used in the data processing of the results of diamagnetic loop measurements of plasma-current magnetic fields.

FIG. 26. Side view of diamagnetic loops installed in U-2M vacuum vessel.

2.4.4. Mirnov coils

For registration of variations in the zero, first and second harmonics of the poloidal magnetic flux with the toroidal angle variation, sets of 16 Mirnov coils are planned to be installed in five sections of the torus. The photograph of the magnetic sensor – Mirnov coil module is given in Figure 29. The 16-Mirnov coil system and its arrangement inside the vacuum chamber of the U-2M torsatron are shown in Figs 29 and 30, respectively.

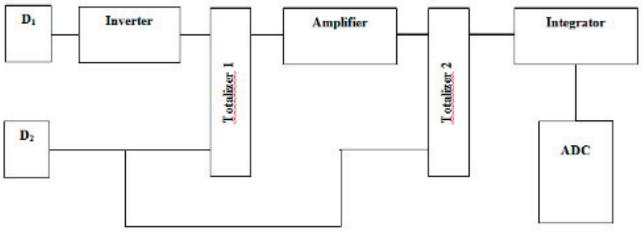

FIG. 27. Block diagram of diamagnetic measurements: D_1 – diamagnetic loop I; D_2 – diamagnetic loop II; ADC – analog-digital converter.

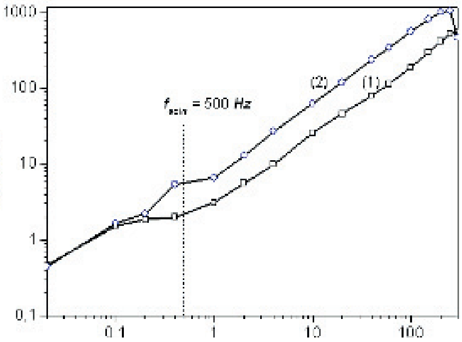

Frequency, kHz

FIG. 28. U signal recorded by diamagnetic loops as a function of the frequency of current simulating poloidal plasma currents in the U-2M chamber simulator. (1) – signal from the first diamagnetic loop covering a large area, (2) – signal from the second diamagnetic loop covering a smaller area.

On condition that $N/R << m/b$ (R – major radius of torus, a – minor radius, N – the number of magnetic field periods along the torus, m – the number of magnetic field periods at the small azimuthal angle, and b – the radius of the surface, over which the magnetic measurements are made), the measurement of poloidal magnetic field component variations gives objective information about the longitudinal plasma current structure.

It is planned to install 5 sets of 16 magnetic sensors in each of 5 cross sections of the U-2M torus.

FIG. 29. External view of the magnetic sensors – Mirnov coil module.

FIG.30. External view of the system with a set of 16 Mirnov coils.

The U-2M torsatron has the actual ratio b/a ≈ 1.5. This enables to select the poloidal harmonics of the plasma current magnetic field with m = 0, 1 and 2 from the general signal of the magnetic sensors. With the help of magnetic measurements in 5 sections of the torus will be possible to measure the perturbation of the magnetic field with n = 0 and n = 1. The magnetic sensors arrangement in specially selected cross sections will also make it possible to find the perturbations with n = 4. As a result, it will be possible to monitor the behavior of the magnetic field harmonic with m = 2 and n = 4. On the whole, the set of 80 magnetic sensors mounted in five cross sections along the torus will be able to investigate:

1) m = 0, n = 0 – longitudinal plasma current;
2) m = 1, n = 0 – horizontal plasma current shift, the magnetic field of Pfirsch-Schluter currents, vertical plasma current shift and time history of the radial electric field [16];
3) m = 2, n = 1 – the island structure of magnetic surfaces at $\iota/2\pi = 0.5$ (ι is the rotational transformation angle);
4) m = 1, m = 2, n = 4 – helical equilibrium plasma currents.

The magnetic sensors discussed above permit the registration of magnetic field variations in the frequency range from 10 Hz to 200 kHz. It allows registration of MHD oscillations with m = 0, m = 1, m = 2 and n = 0, n = 1, n = 2, n = 4.

During poloidal magnetic field measurements the image currents will be calculated using the numerical methods of signal processing on the basis of special model measurements in the vacuum chamber of the U-2M torsatron.

Prior to mounting the set of Mirnov coils in the U-2M torsatron, experiments were made to investigate the influence of the metal environment on measurements of the first and higher azimuthal harmonics of the poloidal magnetic field at frequencies ranging from 10 Hz to 300 kHz. Just as in the case of diamagnetic loops, the experiments also were performed with the vacuum chamber simulator similar to the vacuum chamber of the U-2M torsatron. A special test stand was manufactured to simulate the first azimuthal harmonic of the plasma-current magnetic field. Furthermore, magnetic sensors (Mirnov coils) with NS ≈ 200 cm^2 were manufactured and calibrated before mounting in the vacuum chamber of the U-2M torsatron (N = 600 – number of coil turns, S – cross section area of the coil). The special stand simulating plasma currents was used to determine the sensitivity of coils and to measure amplitude-frequency characteristics of magnetic sensors inside and out of the vacuum chamber simulator. The results of the studies are shown in Figure 31. This figure shows the frequency dependence of the ratio of the signal amplitude registered by the Mirnov coils to the current frequency and to the current of the coil that simulates the plasma currents with *m* = 1. The measurements were performed inside the metal chamber model and out of it. It can be seen from the figure that at frequencies above the skin frequency $f >> f_{skin} = \frac{\tilde{n}^2}{8\pi\sigma\Delta\grave{a}} = 500$ Hz for the given thickness of chamber simulator walls, the signal registered inside the chamber is nearly twice as large as that outside the chamber. This is due to the fact that image currents flows in the metal wall of the chamber simulator and the magnetic field of currents simulating the plasma current cannot penetrate through the metal environment. At frequencies below the skin frequency value, the simulating-current magnetic field penetrates through the metal walls of the chamber model, and as the frequency is reduced the measured signal becomes the same both in and out of the chamber. At frequencies higher than 100 kHz, resonance effects become apparent, being due to the presence of reactivity contributed by the metal environment to the magnetic sensor measuring circuits. The calculations have shown that the influence of the metal environment of the second, and higher azimuthal harmonics of the plasma current poloidal magnetic field is similar to the effect on the first azimuthal harmonic.

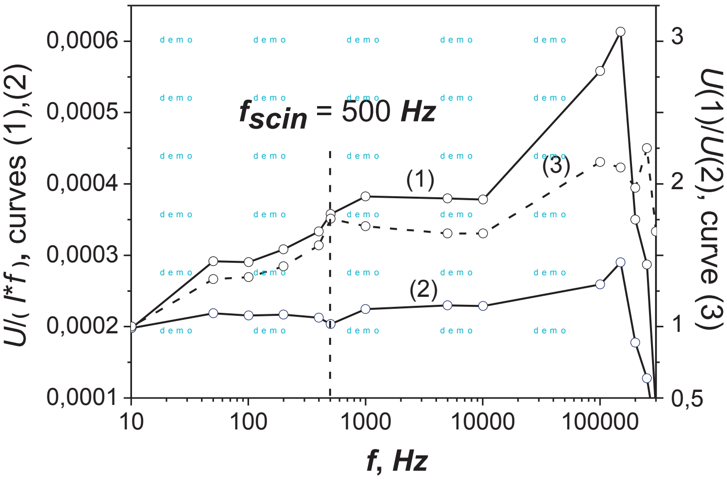

FIG. 31. Frequency dependence of the ratio of the U signal amplitude recorded by the magnetic sensors to the current frequency and to the current value of the m =1 plasma current-simulating coil. Coil arrangements: (1) - inside the metal chamber and (2) - outside the metal chamber. The dashed line (3) shows the U(1)/U(2) ratio of magnetic sensor signals in and out of the chamber model.

For registration of Mirnov coil signals, a special electronic equipment complex providing the required sensitivity and selectivity will be used. The block diagram of electrical measurements by a set of Mirnov coils is shown in Figure 32.

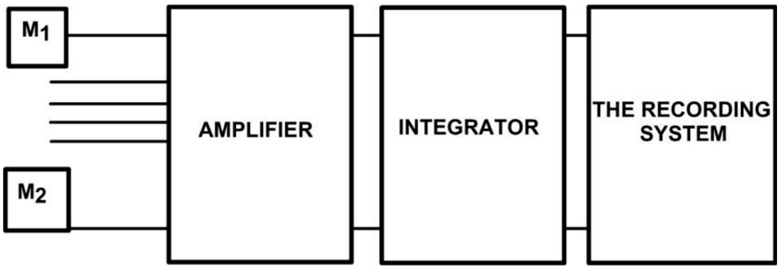

FIG. 32. Block diagram of electrical measurements by a set of Mirnov coils. M_1 *...* M_{16} *– Mirnov coils.*

The findings of model investigations will be used while processing the signals registered by Mirnov coils in the experiments at the U-2M torsatron.

2.4.5. Manufacture of the second stage of magnetic diagnostics for measuring plasma current and kinetic energy of plasma in U-2M

The main purposes of the magnetic measurements in U-2M during the second stage of works are:

1) Determination of plasma energy content in various operating regimes of U-2M;
2) Study of the MHD plasma activity and its influence on particle and energy losses from the confinement volume, as well as on spatial and frequency spectrum of plasma current fluctuations;
3) Investigation of the behavior of the longitudinal plasma current at different plasma parameters in various operating regimes of U-2M;
4) Study of the poloidal spectrum of the longitudinal plasma current resulting from the RF heating of the plasma;
5) Determination of the energy lifetime of the plasma, as well as the value of RF power inputted into the plasma.

Plasma equilibrium in stellarator type toroidal magnetic traps is provided by plasma currents flowing across the magnetic field (diamagnetic current) and the current removing the polarization (Pfirsch-Schlüter current). In stellarator magnetic configurations helical harmonics in the current removing the polarization are appeared, whose magnetic fields interact with real spectrum of stellarator helical fields. This complicates the behavior of the magnetic configuration and causes a change in stellarator rotational transform angle. The transverse magnetic field effects on the stellarator magnetic configuration and results in shift of internal magnetic surfaces, distortion of the magnetic surfaces located not far from separatrix, and change of the profile of stellarator rotational transform angle.

In most modern stellarator-torsatrons, such as U-2M torsatron, the current-free methods of plasma heating are used (RF methods). In the case of sufficiently frequent collisions between plasma particles, the longitudinal plasma current in such systems is small. In the case of rare collisions (basic mode of U-2M operation), in toroidal plasma a so-called bootstrap current will be generated, according to the neoclassical theory. Also the longitudinal plasma current can be generated as a result of the process of the RF plasma heating or neutral atoms beam injection (e.g., current drive). As was shown in [17], magnetic diagnostics allows to determine many important plasma parameters, such as: the value of the longitudinal plasma current, the value of the plasma energy content, the power inputted into the plasma, the plasma energy confinement time, shift and deformation of magnetic surfaces, the structure of magnetic islands, the structure of MHD instabilities, etc.

In the course of the experimental program on torsatron U-2M, the value of the plasma energy content, the plasma energy confinement time and the power inputted in the plasma will be determined by registration of variations of toroidal magnetic flux and zero harmonic of poloidal magnetic field created by longitudinal plasma current. Registration of plasma currents will be done during the transition process starting from a very small change of RF power. This allows us to calculate the plasma energy lifetime, as well as the value of the inputted RF power based on the time dependence of the rate of change of the plasma energy content.

The value of Pfirsch-Schlüter currents, the presence of magnetic islands, the shift of magnetic surfaces, the structure of MHD instabilities, corresponding to the first harmonic will be determined by registration of variations of first and zero harmonics of the poloidal magnetic field. Diamagnetic loops will be used to register variations of the toroidal magnetic flux. To register variations of zero, first and second harmonics of the poloidal magnetic flux over the toroidal angle, the set of 16 Mirnov coils will be used. Magnetic sensors will register variations in the toroidal magnetic flux, as well as variations in harmonics of poloidal magnetic field in the range of frequencies from 10 Hz up to 200 kHz.

To carry out the program of research on U-2M, magnetic sensors have been installed in the vacuum chamber of U-2M. Also, before being installed in the vacuum chamber of the U-2M torsatron, the magnetic sensors have been calibrated and their characteristics were measured for their comparison under the conditions with and without metal environment. Besides, the methods on taking into account the influence of the metal environment and induced magnetic fields on the results of magnetic measurements have been determined.

Another factor influencing the magnetic measurement is the instability of external magnetic fields generated by magnetic system U-2M, which leads to a substantial reduction in the accuracy of magnetic measurements. Therefore, in order to increase the accuracy of magnetic measurements in the second stage of works the details of penetration of external magnetic fields into the working chamber U-2M will be studied. Also before to start magnetic measurements, debugging, shielding and calibration of analogue to digital equipment and supply cables is planned, because of strong magnetic pickups created by RF antenna.

3. URAGAN-3M INSTALLATIONS

3.1. Common characteristics of the Uragan-2M torsatron

The main feature of the torsatron U-3M (l=3, m=9, R = 1m, ‹a›≈ 0.12 m, $\iota(a) \approx 0.3$, $B_{max} = 1.3$ T) is that all helical and vertical magnetic field coils are imbedded in large (5 m in diameter) vacuum chamber and thus the magnetic configuration with natural helical divertor is realized.

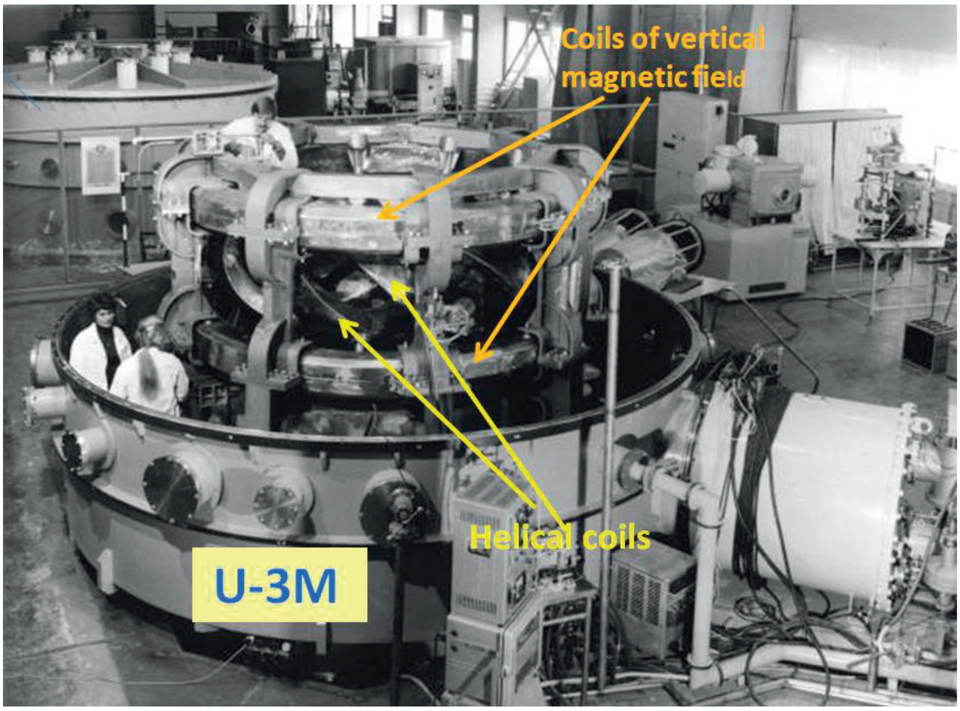

FIG. 33. Photo of Uragan-3M device with open upper part.

The main feature of the torsatron U-3M (l=3, m=9, R = 1m, ‹a›≈ 0.12 m, $\iota(a) \approx 0.3$, B_{max} = 1.3 T) is that all helical and vertical magnetic field coils are imbedded in large (5 m in diameter) vacuum chamber and thus the magnetic configuration with natural helical divertor is realized.

3.2. Optimization of RF discharge start in U-3M

3.2.1. Introduction

The Uragan-3M (U-3M) is a "classical" l/m=3/9 torsatron with a natural helical divertor. The major and average plasma radii are R = 1 m and $a \approx 12$ cm, toroidal magnetic field B_ϕ = 0.7 T is produced by the helical coils only, the transformation angle $\iota(a)/2\pi \approx 0.3$. The whole magnetic system is placed inside a large, 5 m diameter, vacuum tank, its volume being ~200 times as large as the plasma confinement volume. With a continuous hydrogen inlet at a pressure of ~10^{-5} Torr a currentless plasma is produced and heated by RF fields [18] in the Alfvén range of frequencies, $\omega \leq \omega_{ci}$, with using two types of unshielded antennas twisted along the helical windings: the frame type (FT) antenna, Figure 34a and the three-half-turn (THT) antenna, Figure 34b.

Both antennas excite the waves with a wide spectra of toroidal and poloidal wavenumbers. The widths of the spectra provide the sustainment of local Alfven resonances during the increase of plasma density by means of "relay-race" of subsequent toroidal modes [18].

The ~200 times difference in the volume of the vacuum tank and the plasma volume results in some peculiarities of plasma behavior, starting from the initial phase of the discharge and up to its termination, which will be discussed below.

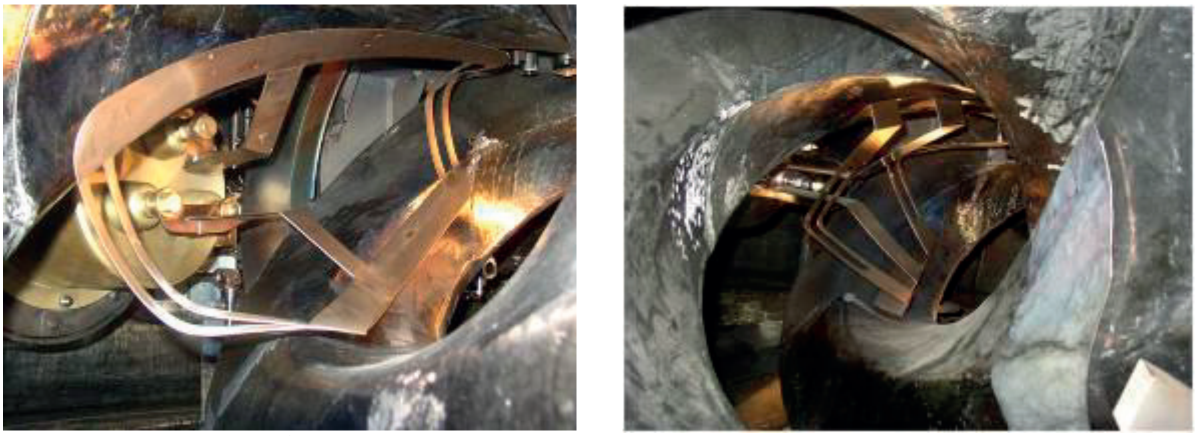

a) b)

FIG. 34. a) frame antenna, b) three-half-turn antenna installed inside helical coils.

3.2.2. Regimes of the U-3M operation

The FT antenna can produce and heat the plasma [19] however without pre-ionization (PI) the time delay of discharge ignition varies from shot to shot, and discharge repeatability is low. In particular, the THT antenna can be used for PI [20], in such a case it cannot be used for a further plasma heating. Recently it has been found that launching of 1 kW 2.45 GHz UHF power to the plasma confinement volume in the phase of confining magnetic field ramp-up creates some plasma which influences the plasma production by the FT antenna in such a way that repeatability of discharge start increases noticeably.

The present series of experiments aims to find an optimum scenario for the subsequent plasma heating by THT antenna. Depending on the magnitude of RF power P_{FT} fed to the FT antenna (for simplicity it will be characterized by the anode voltage of the RF oscillator U_{FT}) and initial hydrogen pressure p_{H2} in the U-3M tank, it is possible to implement two distinct regimes of FT antenna discharge with different behaviour of the line averaged electron density, radiation temperature, particle confinement time, and plasma loss to the divertor region [21]. For B_ϕ=0.7 T the corresponding operational frequency of the FT antenna is f=8.8 MHz$\omega/2\pi = 8.8$MHz and these two operational regimes differ by the values of RF oscillator anode voltage of ≈5.5 kV and ≈8.0 kV, which correspond to the P_{FT} power of 45 kW and 95 kW, respectively. This range depends on the initial gas pressure.

Figure 35 shows a typical time behaviour of the averaged plasma density (as measured by the 2 mm microwave interferometer) for these two regimes at the anode voltages U_{FT} = 8.0 kV and U_{FT} = 5.5 kV ($p_{H2} \approx 10^{-5}$ Torr). In this figure are also depicted the time behaviour of the absolute value intensity of the hydrogen line H_α. Figure 36 shows the temporal evolution of the radial profiles of the radiation electron temperature (in eV) obtained by means of the 2nd harmonic ECE diagnostic operated at X-mode (frequency range 33–37.5 GHz) for the same values of U_{FT}. Previously, it was shown [22] that even in the case of small optical thickness of the U-3M plasma, which can be approximated as $\tau(r) \propto T_e(r) \cdot n_e(r)$, the radial profile of the plasma radiation temperature can be estimated for a significant portion of plasma radius using the following relation: $T_e(r) = T_{\mathrm{ECE}}(r)\left(1 - e^{-\tau(r)}\right)^{-1}$. The applied conversion procedure of the ECE data into the $T_e(r)$ data ignores multiple reflections from the helical winding casing, the inner walls of the vacuum chamber and other structural elements of the U-3M. Nevertheless, this procedure allows, within an acceptable error, to estimate the electron temperature with an assumption on the plasma density profile and of the Maxwellian-like distribution function of plasma electrons.

One can see that the time (60 ms) when signal ECE drops (Figure 35b, U_{FT} = 5.5 kV) does strongly correlate with the time of achieving the maximum density (Figure 35b). After that time the discharge is maintained with rather low temperature plasma, but, nevertheless, this temperature is sufficient to ionize molecular hydrogen. In the case U_{FT} = 8.0 kV, on the contrary, RF waves penetrate deeper into the confinement volume (due to the low density of $\overline{n_e} \sim 1.1 \times 10^{12}$ cm^{-3}).

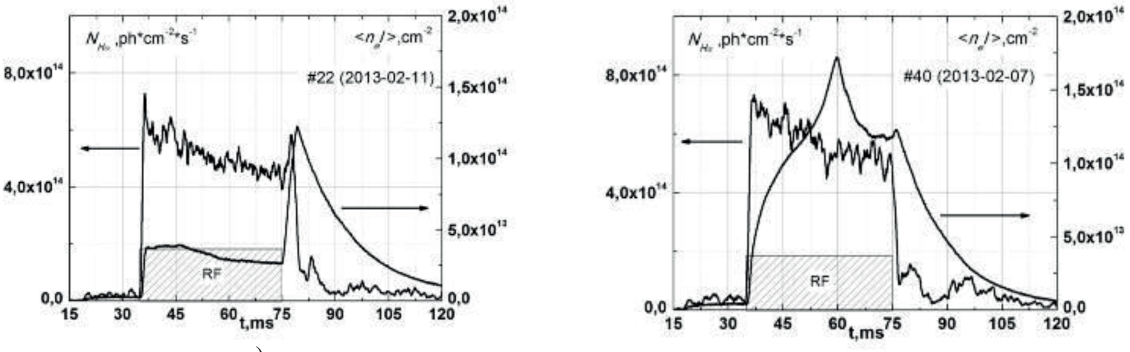

a) b)

FIG. 35. Temporal behavior of electron plasma line density <$n_e l$> from 2 mm microwave interferometer data and the absolute value intensity of the hydrogen line H_α at RF generator anode voltage 8.0 kV (a) and 5.5 kV (b).

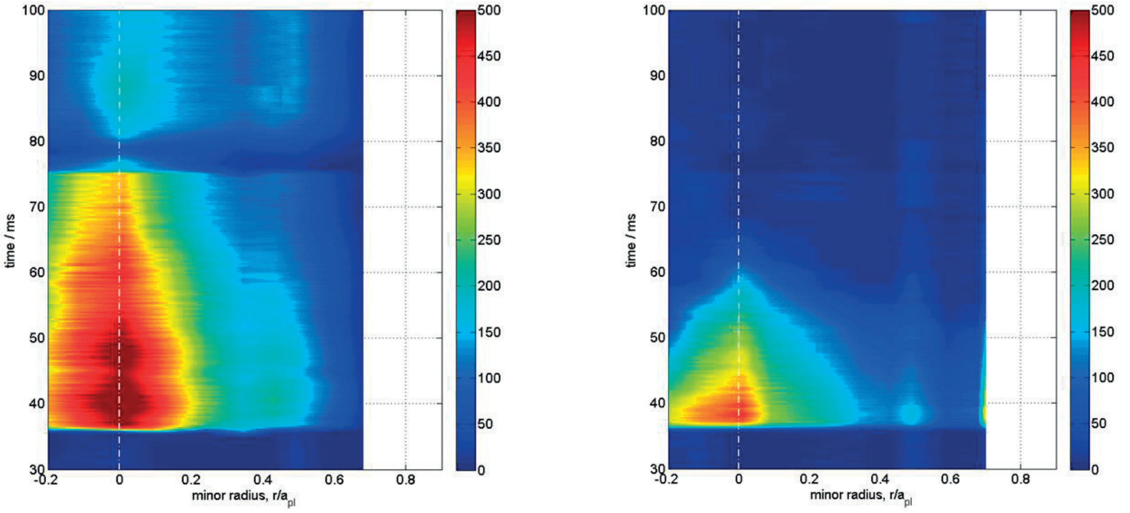

a) *b)*

FIG. 36. Temporal behavior of electron radiation temperature profile measured by X-mode second harmonic ECE diagnostic for RF generator anode voltages 8.0 kV (a) and 5.5 kV (b); radiation temperature is shown in eV with averaging through several plasma shots.

In the case U_{FT} = 8.0 kV, on the contrary case U_{FT} = 5.5 kV, RF waves penetrate deeper into the confinement volume (due to the low density of $\bar{n}_e \approx 1.1 \times 10^{12}$ cm^{-3}) and the electron temperature is high in confinement volume when RF is switched on. During strong density rump-up after RF switched off the electron temperature remains sufficient during some time to ionize the neutral gas (Figs 35a and 36a) [23]. The effect of the density rump-up was also observed in some experiments at the LHD heliotron and TJ-II stellarator [24,25] after switching off the heating pulse; in both these machines plasma confinement volume is significantly less than vacuum vessel volume.

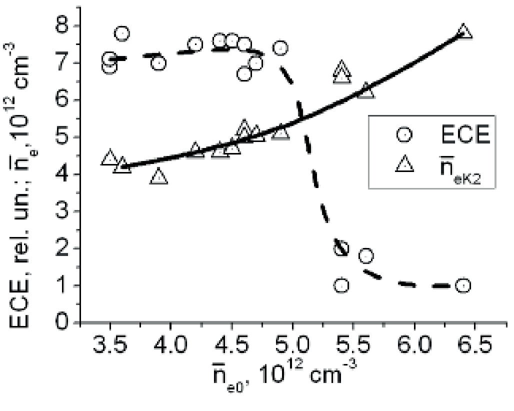

FIG. 37. Dependence of the maximum values of ECE intensity and the corresponding THT density on the initial start-up density produced by FT antenna.

In this scenario of operation the plasma is created by FT antenna and after that heated by THT antenna. The FT antenna is able to produce plasma with electron density up to 10^{19} m^{-3}, however, according to numerical simulations, Alfven waves excited by this antenna are absorbed at the external part of the plasma column [26]. The effect of initial density (produced by FTA) on the THT antenna operation is illustrated by Figure 37 which shows the dependences of electron radiation temperature (ECE intensity from the plasma center) and attainable density by THT antenna as a function of the start-up density produced by the FT antenna.

The threshold in the vicinity of $\overline{n_e}^{\mathrm{FTA}} \sim 4.5 \div 5.2 \times 10^{12}\ \mathrm{cm}^{-3}$ may be explained by the ECE emission locking at high plasma density values near the plasma center. One can see the clear threshold in the vicinity of $\overline{n_e}^{\mathrm{FTA}} \sim 4.5 \div 5.2 \times 10^{12}\ \mathrm{cm}^{-3}$ which characterizes the transition in U-3M operational modes.

Figs 37 and 38 show some data for discharge with operation of both antennas. Target plasma ($\overline{n_e}^{\mathrm{FTA}} \approx 4.5 \times 10^{12}\ \mathrm{cm}^{-3}\overline{\mathrm{n}_\mathrm{e}}^{\mathrm{FTA}} \sim 4.5 \div 5.2 \times 10^{12}\mathrm{cm}^{-3}$) was created and maintained during ≈6 ms by FT antenna. Plasma temperature and density increase by switching on the THT antenna. As a result of nonlinear effects [23, 27, 28], anomalous transport of plasma occurs. It can be seen in Figs 36a and 37b, that only central region of plasma column $r/a_p \lesssim 0.3$ retains a significant amount of the electron cyclotron emission intensity throughout the whole time of discharge.

At low density FT antenna regime plasma experiments an H-like mode discharge state was realized: with slowing down density decrease, and with the plasma energy content W_{dia} and ECE intensity growing monotonously (Figure 38). The H-like transition being triggered by a short-time enhanced fast ion (FI) loss [21]. The H-like state is characterized, in particular, by the reduced edge turbulent transport that correlates with the enhanced E_r shear at the plasma boundary.

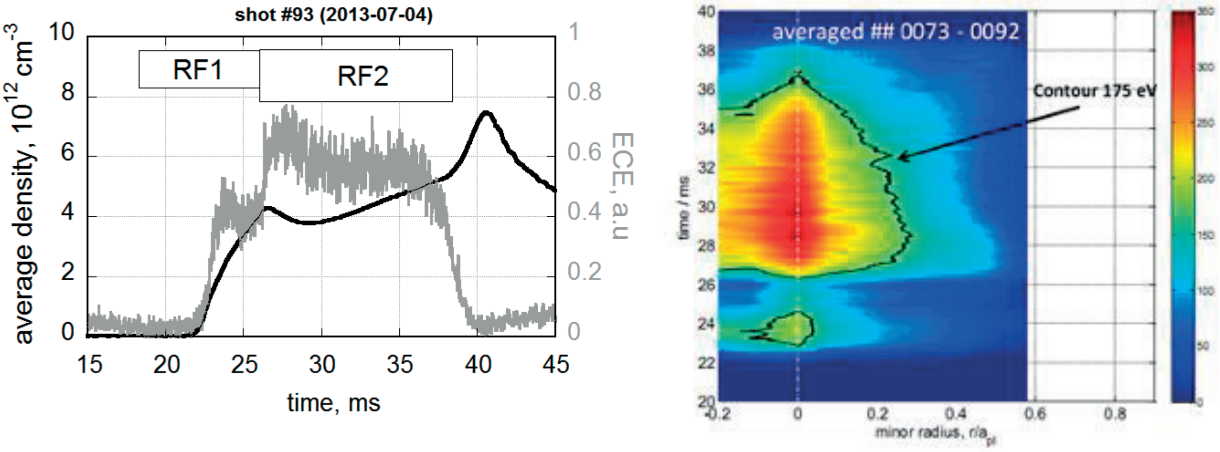

a) b)

FIG. 38. a) Temporal behavior of electron plasma line density $<n_e l>$ *and ECE radiation profile; RF generator anode voltages of FT antenna – 6.0 kV and for THT antenna – 10.0 kV. b) Temporal behavior of electron radiation temperature profile; RF generator anode voltages for FT antenna – 6.0 kV and for THT antenna – 10.0 kV; radiation temperature is shown in eV with averaging through several plasma shots.*

3.2.3. Conclusion

1. In Uragan-3M, when working with the frame antenna, two modes of RF discharge were identified, which are characterized by significantly different temporal behavior and absolute values of average plasma density and the ECE electron temperature, as well as by different particle confinement time.

2. By analysis of ECE, H_α and CV emissions profiles, a region of plasma confinement is indentified. It occupies plasma center and is surrounded by the region with substantially worse confinement.

3.3. Comparative measurements of divertor plasma flows

3.3.1. Introduction

Important distinctions of the $\ell=3$ / $m=9$ Uragan-3M torsatron are:

- a natural open helical divertor configuration;
- RF plasma production and heating in the Alfven range of frequencies ($\omega \lesssim \omega_{ci}$) using an unshielded frame-like antenna [29];
- indications of the H-like mode transition (Figure 39).

It has been shown recently that the diverted plasma is formed by a plasma escaping from the confinement volume and a plasma produced by fuelling gas ionization by the near antenna field outside the confinement volume. The flow of diverted plasma escaping from the confinement volume increases with RF power.

Similar to the Heliotron E and Heliotron J devices, a distinct vertical (up-down) asymmetry of the diverted plasma flows (DPFs) is observed in U-3M, and it has been shown that the asymmetry results from the direct (non diffusional) ion loss.

The objectives of the work under report were to find out effects of the electron loss on characteristics of the DPF vertical asymmetries in U-3M and effects of the H-like mode transition on diverted plasma parameters.

3.3.1. H-like mode transition in U-3M

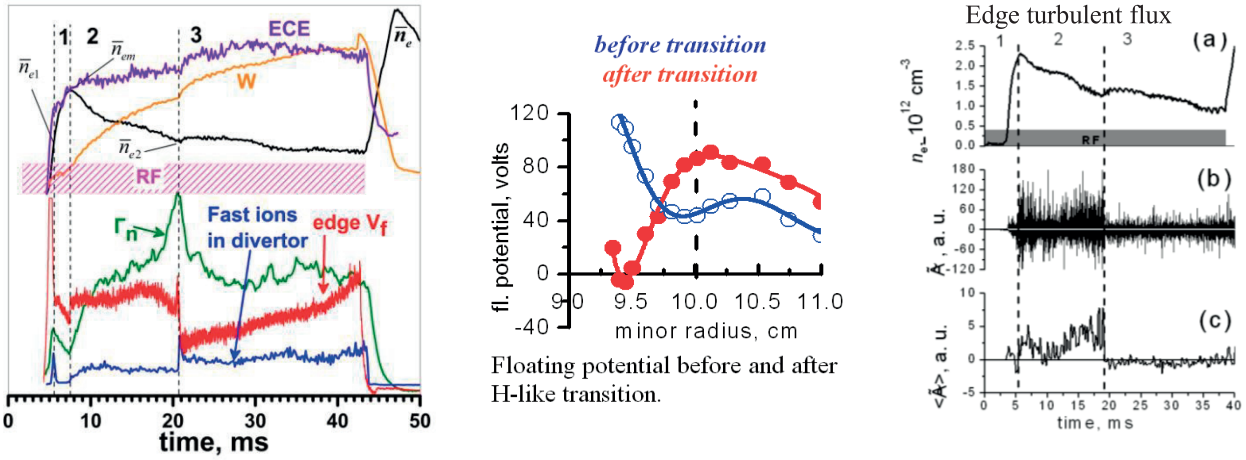

Floating potential before and after H-like transition.

a) b) c)

FIG. 39. a) time behavior of indicated signals; b) space distributions of plasma floating potential before and after H-like mode transition; c)time dependence of turbulent flow.

Slower processes (tens/units ms, Figure 39a) preceding the H-transition and preparing conditions for it (optimum conditions for RF heating and fast ion (FI) generation (FI: see CXN flux Γ_n):

- density $\bar{n}_e$ decay and (presumably) an absorbed RF power per one particle rize;
- energy content W and ECE rize;
- rize of FI ion ($\gtrsim$500 eV) content.

Faster processes (tens/hundreds μs) bearing a bifurcational character and indicating the transition in itself:

- short-time enhanced FI outflow to the divertor ("FI burst") on the ion ∇B side (Figure 39a);
- edge E_r becoming more negative with a stronger E_r shear (Figure 39b);
- stronger E_r shear suppresses the edge turbulence and turbulence-induced anomalous transport .

As a result, $\bar{n}_e$ decay termination and some $\bar{n}_e$ rize, speeding-up of W and ECE rise being indications of confinement improvement. τ_E is shown to increase from ~ 2.7 ms to ~ 5.1 ms.

3.3.2. Time evolution of diverted plasma flows

DPFs differ in their time behavior after RF pulse termination (three typical forms) and at the H-like mode transition. Typical examples: Ex-1, Ex-2, Ex-3 (Figure 40, N is probe number).

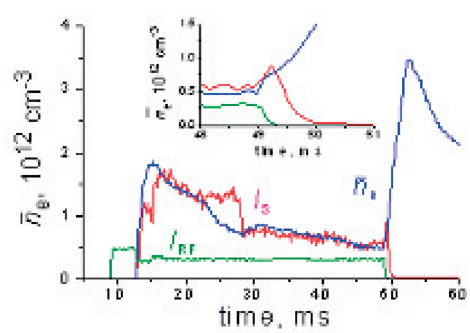

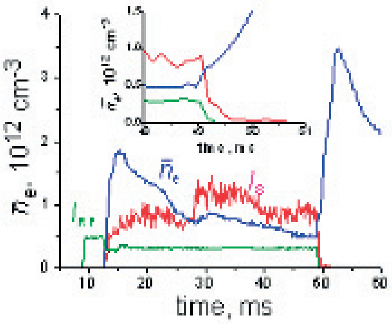

Ex-1: outboard, under midplane (*N* = 16)

Ex-2: outboard, over midplane (*N* = 6)

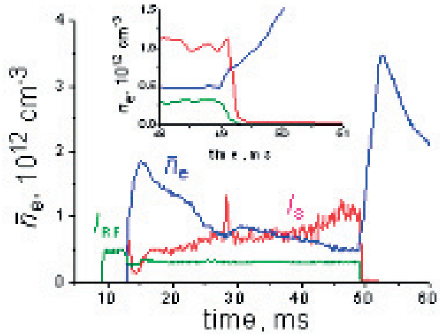

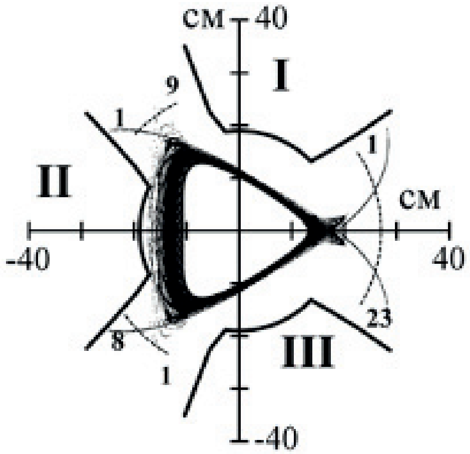

Ex-3: top (*N* = 3)

FIG. 40. Time behavior of RF pulse I_{RF} (green), mean plasma density $\bar{n}_e$ (blue) and ion saturation current I_s (red) in locations indicated on the right at the bottom.

Basing on DPF (ion saturation current I_S) behavior after RF off, two flow components are selected.

(1) In the outboard spacing between the helical coils under the midplane (Ex-1), the flow undergoes a short-time rise consistent with the start of $\bar{n}_e$ increase. It means that the main portion of this flow is formed by the plasma lost from the confinement volume.
(2) In the outboard spacing over the midplane (Ex-2) and the top spacing (Ex-3), the flows start to decay synchronously with the RF current drop. This means that predominant parts of these flows are produced by the RF field outside the confinement volume.

The H-like mode transition is preceded by slow (units/tens ms) changes in DPFs, while the transition in itself is accompanied by an abrupt change of the DPF (I_s) magnitude. The recorded period of the I_S “jump”, 150 µs for both flows under (Ex-1) and over (Ex-2) the midplane, is in fact determined by the ADC time resolution. In any case, it is appreciably less than characteristic times of DPF magnitude variation and density decay before the transition.

As the predominant fraction of the DPF in the outboard spacing under the midplane (Ex-1) outflows from the confinement volume, the sharp drop of this flow with the transition should indicate a plasma loss reduction and improvement of plasma confinement. At the same time, the transition-induced DPF increase over the midplane (Ex-2) results from the plasma density rize outside the LCFS.
The DPF response to the short-time burst of FI loss initiating the H-like mode transition is seen in D7 top (Ex-3).

3.3.3. Poloidal distributions of electron density and temperature in diverted plasma flows (from I-V characteristics)

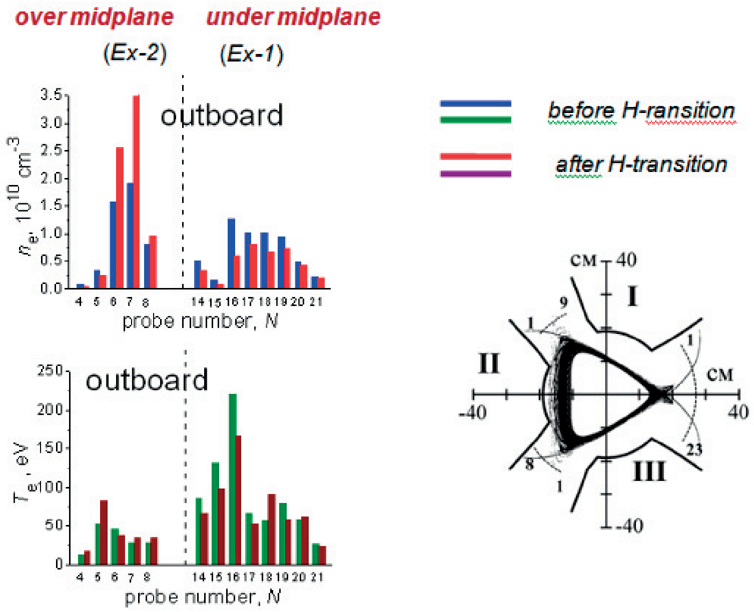

FIG. 41. Space distributions of electron density and temperature before and after H-like mode transition in the outboard side, as measured by electrostatic probes; locations of probes are shown on the right.

Higher n_e is seen on the ion ∇B drift side, i.e, over the midplane, (Figure 41, Ex-2). T_e is higher on the electron ∇B drift side, i.e., under the midplane, (Figure 41, Ex-1). Distinct reductions in n_e and T_e with transition are seen only in the outboard spacing under the midplane (Ex-1: no effect of the RF generated plasma outside the LCFS).

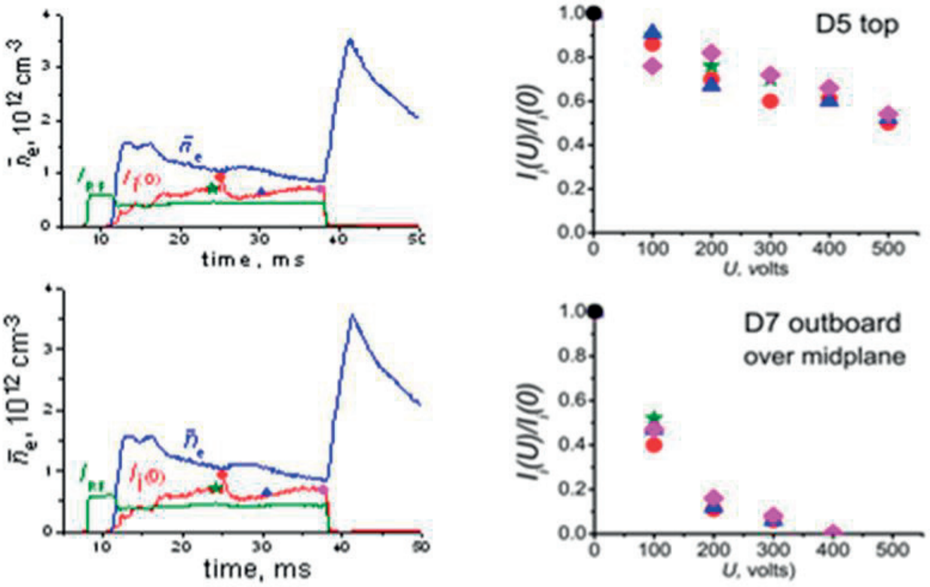

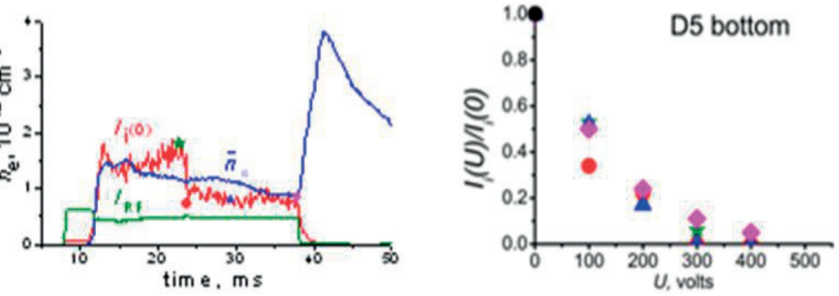

FIG. 42. Ion energy disribution for different time moments as indicated on oscillograms (left column).

3.3.4. Behavior of high energy ions in diverted plasma flows

To detect ions in DPFs, arrays of electrostatic grid ion energy analyzers with the retarding potential $U \leq 500$ V were used, and dependences $I_i(U)$, I_i being the current to the analyzer collector, were measured for several spacings between the helical coils in the symmetric poloidal cross sections D (Figure 42).

The ion energies in the DPFs on the ion ∇B drift side (top spacings) are appreciably higher than those on the electron side, this being a confirmation of the effect of direct ion loss. With the H-like mode transition the form of ion energy distributions practically does not change (at least at $U \leq 500$ eV).

3.3.5. Summary

The measured n_e (N) distributions confirm the effect of the DPF up-down asymmetry with the larger DPFs outflowing on the ion ∇B drift side due to the direct ion loss [23]. However, the plasma generated outside the confinement volume (Ex-2 and Ex-3) can also contribute to the larger DPFs on the ion side. A newly revealed asymmetry characteristic is that the maximum T_e in the DPFs on the electron ∇B drift side is substantially higher than that on the ion side, in part indicating the direct electron loss.

In both symmetric cross sections D and A the DPFs on the electron ∇B drift side with higher T_e undergo a short-time rize after RF off consistent with the start of the density $\bar{n}_e$ n_e rize (Ex-1). This means that the predominant part of the plasma in these flows escapes from the confinement volume, so that the hotter electrons in these flows really occur due to the direct loss from the confinement volume.

n_e reduction with the H-like transition in DPF maxima on the electron ∇B side (Ex-1) combined with DPF rize after RF off is an evidence of high temperature electron loss reduction and improvement of plasma confinement. A post transition n_e reduction (like Ex-1) is also observed in the DPF with colder electrons in A7 top (N=1, 2, 3). Most likely, this results from the FI content reduction after the transition. The total content of ions in the DPFs (current $I_i(0)$), is reduced with the H-like transition. For the higher-temperature group (T_{i2}), this could be attributed (at least partly) to the reduction of the higher-energy ion content in the confinement volume (confirmed by the CXN flux $\Gamma_n(t)$ behavior, see p. 5).

The ion energy distributions in the DPFs practically do not change with the transition (at least in the ≤ 500 eV range of energies).

3.4. Peripheral plasma characteristics under conditions of RF plasma production and heating in the Uragan-3M torsatron

3.4.1. Introduction

In the reported experiments the RF power was introduced into the plasma with the help of an unshielded frame-type antenna (FA) [18] with a broad spectrum of parallel wavelengths. Plasma characteristics (floating potential V_f, electron temperature T_e and local electron density n_e) were studied in the space between the last closed flux surface (LCFS, $\bar{a} \approx 10$ cm) and the helical coils and in the divertor flows in the gaps between the helical coils. Hereinafter this plasma is named as peripheral plasma (PP). A comparison was made of PP parameters far and near the antenna in two basic regimes of plasma production and heating in the confinement volume.

Due to peculiarities of the U-3M device, such as enclosing the whole magnetic system into a large vacuum chamber, a specific, inherent to the torsatron spatial structure of the edge magnetic field lines of force providing the helical divertor configuration and the RF method of plasma production and heating with a local disposition of RF antennae, the PP in U-3M is distinguished by a strong inhomogeneity in both toroidal and radial directions.

For measurements in the space between LCFS and helical coils, movable single Langmuir probes were used, one (MP-1) was moved horizontally far from FA (Figure 43a) and another one (MP-2) – vertically near FA (Figure 43b) and crossed the surface bounded by the antenna frame.

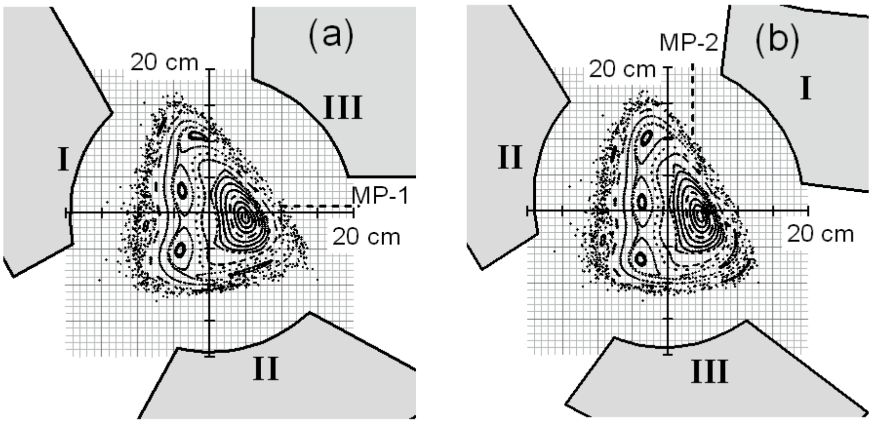

FIG. 43. Disposition of movable probes (a) PM-1 (far from the antenna) and (b) PM-2 (near the antenna) relatively cross sections of the helical coils I, II and III.

PP parameters in the divertor region were determined with the use of plane single Langmuir probe arrays (divertor probes, DP) arranged poloidally in the gaps between the helical coils in two symmetric poloidal cross sections of the U-3M torus D and A at the minor radius of 27 cm [29] (see below Figure 47).

In the active phase of the RF discharge two operating regimes can exist depending on the value of antenna current I_{RF} (proportional to the oscillator anode voltage U_a). These regimes differ by the values of the maximum average density $\bar{n}_e$ achieved in the active phase of discharge, intensity of the 2nd harmonic electron cyclotron radiation (ECE) from the central region and divertor plasma flow (PDF). From ECE measurements one can estimate radiation temperature T_e^{rad}. DPF is presented by the ion saturation current I_s to a DP and characterizes plasma loss from the confinement volume. To the regime I ("hot plasma heating", $U_a \gtrsim 6$ kV) a comparatively low density $T_e^{rad}(0) \sim (1\text{-}3)\times10^{12}$ cm^{-3}, high energetic electron content ($T_e^{rad}(0)$ up to 800 eV) and considerable plasma loss are inherent. The regime II ("cold plasma heating”) sets over the larger part of the RF pulse at $U_a < 6$ kV and is characterized by a higher density (up to $\bar{n}_{e\max} \approx (6–7)\times10^{12}$ cm^{-3}, lower ECE ($T_e^{rad} \lesssim 100$ eV) and lower plasma loss.

3.4.2. Plasma between LCFS and helical coils far from antenna

In Figure 44 are shown spatial (close to radial) $V_f(h)$ (Figure 44a), $T_e(h)$ (Figure 44b) and $n_e(h)$ (Figs 44c and d) plots measured in the regime I ($U_a = 8$ kV, $\bar{n}_e \sim 2\times10^{12}$ cm^{-3}, $T_e^{rad}(0) \lesssim 700$ eV). Here h is the probe MP-1 distance from the minor axis (see Figure 43a). For a better visuality, the $n_e(h)$ plot is presented in the linear (Figure 44c) and semilogarithmic (Figure 44d) coordinates. It is seen that at a distance from LCFS, in the $12 \lesssim h \leq 19$ cm interval, V_f and T_e change with h within (+20 – -5) V and (40 – 30) eV, respectively, and the density n_e grows monotonously from units 10^8 cm^{-3} at h = 19 cm to ~10^{10} cm^{-3} at h = 12 cm. With a further approach to LCFS, within the $10 \lesssim h \lesssim 12$ cm interval (the calculated LCFS position is $h \approx 10$ cm), in the transition region including the ergodic layer, a faster rize of the considered parameters occurs. The maximum values recorded in separate shots of V_r (up to 83 V), T_e (up to 80 eV) and n_e (up to 6×10^{12} cm^{-3}) are reached at $h \approx 9.7$ cm.

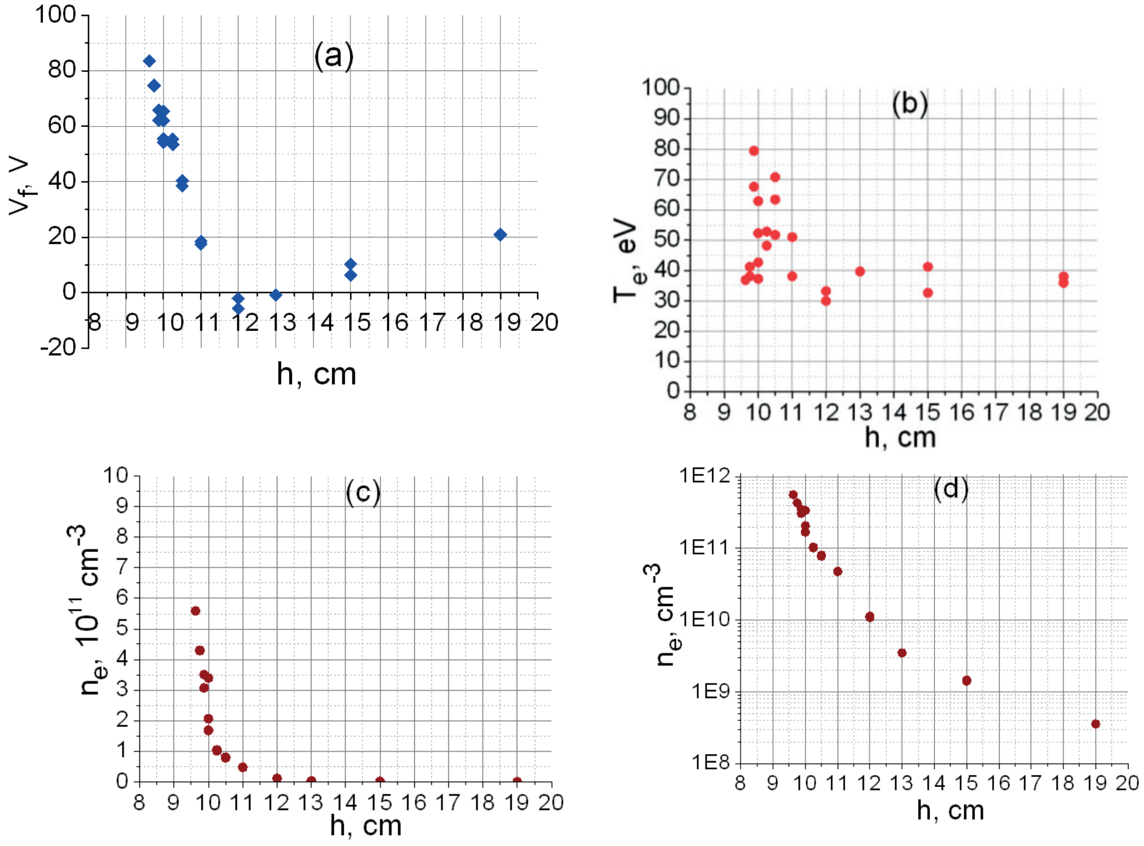

FIG. 44. Measured Plasma parameters.

A comparison with the regime I of corresponding dependences measured in the regime II (Figure 45) shows that within the shot-to-shot data spread there is no large difference in V_e, T_e and n_e measured at the distance $h > 12$ cm. In the transition region $10 \lesssim h \lesssim 12$ cm the potential V_f has the same values within the data spread as in the regime I. However, the maximum electron density in the regime II attains $n_e \approx 10^{12}$ cm^{-3} at h = 9.7 cm, obviously exceeding its value in the regime I (6×10^{11} cm^{-3}). At the same time, the maximum electron temperature in the transition layer stays at the same low level $T_e \approx 30$ eV in the regime II as at $h > 12$ cm in both regimes. The density rize and temperature fall in the layer of ~ 2 cm width adjacent to LCFS in the regime II represent the corresponding changes of electron density and temperature in the confinement volume when going from the regime I to regime II.

3.4.3. Plasma between LCFS and helical coils near antenna.

The PP parameters near FA differ appreciably from those measured far from the antenna by both their values and spatial distributions. This difference could result not only from the antenna disposition as a material object in the space between the helical windings and LCFS but from a stronger effect on the PP of the RF field generated by the antenna.

The characteristic values of the RF voltage on FA amount ~ 10 kV. Being isolated from the earth by d.c. current, the antenna as an electrode to which an RF voltage is applied must take a d. c. negative potential relative to the earth due to the sheath rectification effect [30]. Under the action of strong parallel RF electric field generated by FA, $E_z \gtrsim 100$ V/cm [31], the oscillatory velocity of electrons can exceed their thermal velocity, this resulting in deviation of the electron distribution function from the equilibrium (Maxwellian) one. Due to the sheath rectification of the RF potential, the probe MP-2 must gain an additional d.c. negative floating potential, its value depending on the electron temperature and amplitude of the RF potential induced on the probe [32].

The V_f (h) distribution measured by the probe MP-2 in the regime I is shown in Figure 45a (here h is the vertical distance to the torus midplane, with the calculated LCFS position $h \approx 10$ cm, see Figure 43b). This distribution really differs essentially from that taken far from the antenna (probe MP-1, see Figure 44a) both in the value and sign of V_f and in the form of the $V_f(h)$ curve. At some distances h the value of V_f falls lower than -100 V. In particular, V_f changes non-monotonously within (-10 – -140) V in comparison with (-5 – +80) V far from the antenna. In the regime II the interval of V_f values attains (0 – -160) V in comparison with (-10 – +100) V far from the antenna.

Due to the large negative potential V_f the ion branch of the I-V characteristic of the probe MP-2 is shifted toward a higher negative bias voltage V. As the amplitude of the saw-tooth oscillations V is small (the “swing” is ≤ 180 V), only a short, practically straight section of the I-V characteristic is accessible for some h, so it is impossible to fulfill any valuable analysis of the I(V) dependence, in particular, to estimate T_e and n_e.

However, in cases where the I(V) dependence at large negative biases exhibits signs of saturation in both sides from the ($11.5 < h < 13.5$ cm interval in Figure 45), such an estimation is possible. In this case, some “effective” electron temperature as determined via rough fitting of the “ideal” I-V characteristic occurs to be appreciably higher, approaching 200 eV, in comparison with $T_e \lesssim 40$ eV far from the antenna (Figure 44b).

Proceeding from the length of the straight section of the I-V characteristic and the value of the maximum attainable current I to the probe MP-2, the “effective” temperature T_e and density n_e near the antenna in the above-mentioned h-interval should also be higher in comparison with their values at similar distances far from the antenna (Figs 44b, 44c and 44d).

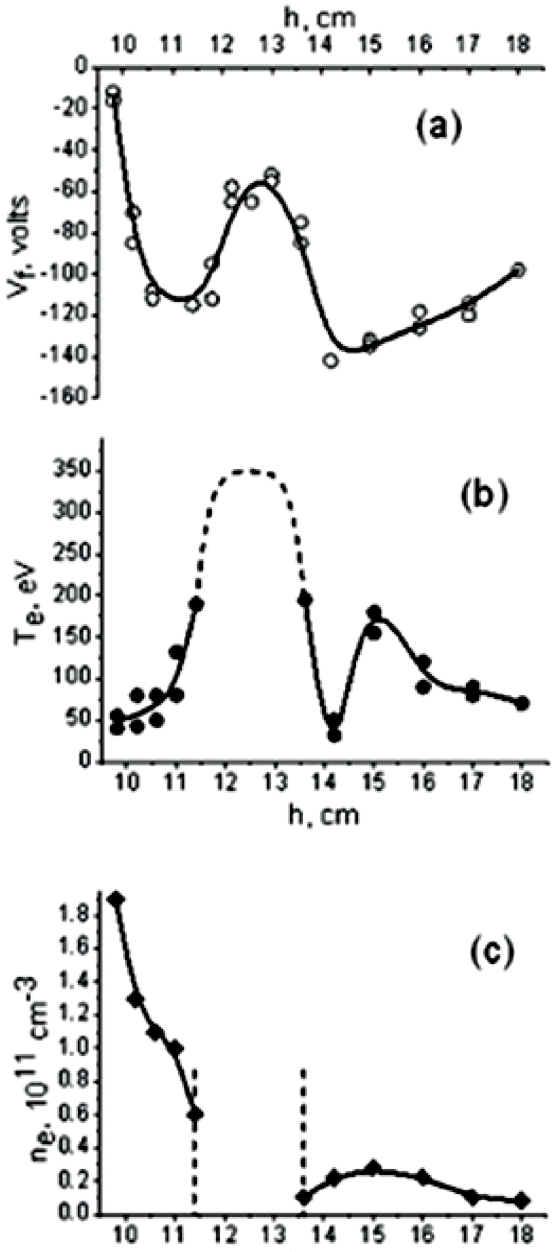

FIG. 45. I(V) dependence of the probe MP-2.

It is noteworthy that near the antenna, close to LCFS (h ≈ 10 cm), the density and temperature of electrons approach their values at similar distances h far from the antenna. This means that the direct effect of the near antenna field on the mentioned PP characteristics becomes weak when approaching the boundary of the confinement region and the influence of the RF field of the waves exited and propagating inside this region remains determinative.

3.4.4. Plasma in divertor flows

In Figs 46 and 47 poloidal distributions are presented of the density $n_e(N)$ and temperature $T_e(N)$ of electrons in the spacings between the helical coils in the symmetric poloidal cross sections D (Figure 46) and A (Figure 47) far from the antenna, N is the probe number in a DP array. The measurements were made in the regime I.

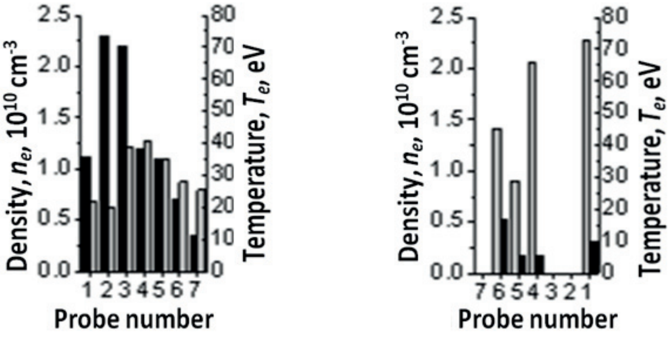

D Top **D bottom**

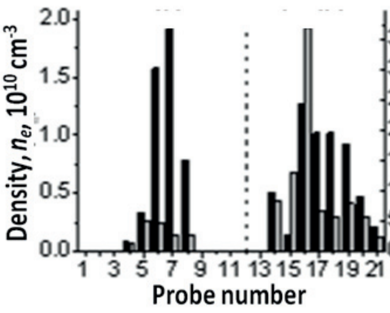

D outboard

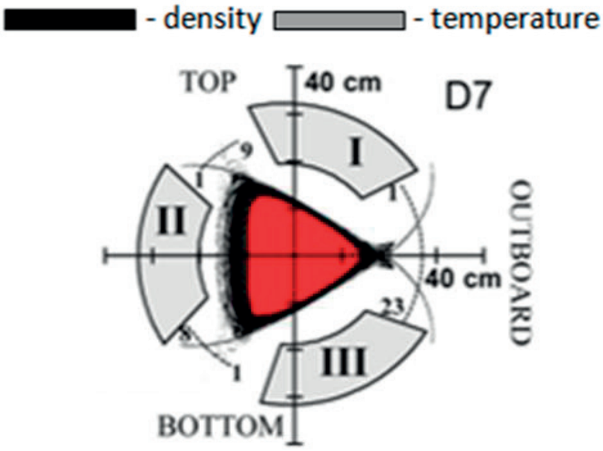

FIG. 46. Plasma density and temperature.

When comparing the values of density in maxima of the $n_e(N)$ distributions with the density $n_e(h)$ measured by the probe MP-1 away from the divertor flows, it is seen that the maximum n_e values in the flows which attain ~ 2×10^{10} cm^{-3} considerably exceed the density between LCFS and the helical coils out of the transit layer near the plasma boundary. Besides, the electron temperature in the divertor flows can reach hundreds eV (up to 375 eV in the outboard spacing of the cross section D under the midplain, i. e., on the electron B×∇B drift side (Figure 46). At the same time, the electron temperature measured by the probe MP-1 away from the divertor flows and transit layer does not exceed 30–40 eV. So, a conclusion may be done that a predominant part of the plasma in the divertor flows is formed by particles escaping from the transit layer that adjoints directly the confinement volume.

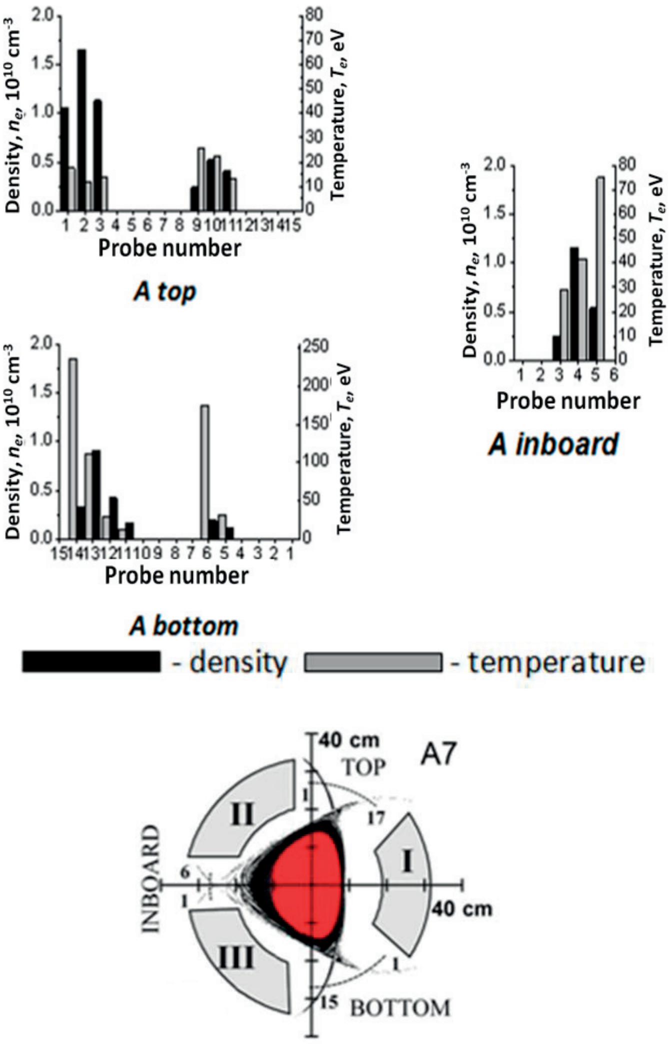

FIG. 47. Plasma density and temperature.

The presence of a higher plasma density in divertor flows on the ion B×∇B drift side (Figs. 46 and 47) confirms the effect of the divertor flow vertical asymmetry in U-3M [29]. A higher electron temperature in the flows on the electron B×∇B drift side that is comparable with that in the confinement region is an evidence of the direct (non-diffusional, collisionless) loss of electrons and is one more manifestation of the divertor flow vertical asymmetry.

3.5. Suppression of appearance of runaway electrons

Both stellarator-type fusion devices in Kharkov, Uragan-2M and Uragan-3M, operate at room temperature and their magnetic field systems are power-supplied with the pulse duration 3–4 s with several minute interval between pulses. Because of torsatron magnetic configuration, during rize of current in helical windings a circuital electric field is generated at both current-up and currant-down phases of magnetic field pulse. If gas pressure in the vacuum chamber is not high, as it usually takes place in experiments on plasma heating and confinement, this curl field generates a flux of high energy (runaway) electrons with energy up to ~2 MeV in the case of Uragan-3M device. The consequence of appearance of high energy electrons is the rize of electron cyclotron emission, hard X rays, and longitudinal plasma current. Also, appearance of high energy electrons can result in destruction of the surface of material (in vessel construction or vessel walls) where they are outcropping. Just such event has one happened at tokamak Tore Supra in France.

Similar situation, i.e., appearance of conditions for acceleration of electrons, is typical for any torsatron/heliotron fusion facility operating in pulse regime. To overcome the negative (and uncontrolled) effects of runaway electrons in TJ-2 facility a special device is used [33], which is placed in the plasma confinement volume all the time except a short interval during experiment with plasma where time derivative of magnetic field is close to zero. For this moment it was mechanically taken off from its stationary position.

The examples of data obtained in typical conditions of U-3M are shown below. As one can see, the phenomena are observed only at initial and final stages of magnetic field pulse. The rough estimations give the mean energy of runaway electrons near 2 MeV.

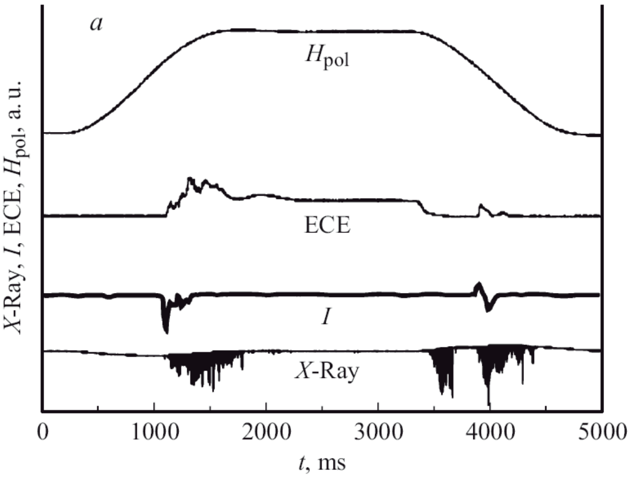

FIG. 48. Time dependence in relative units of: vertical component of magnetic field generated by currents in magnetic coils, electron-cyclotron emission (ECE) at frequency 60 GHz, toroidal plasma current, and hard X ray emission during magnetic field pulse in U-3M device with antenna voltage +100 V.

To suppress appearance of high energy electrons in U-3M it was suggested to supply some fixed voltage to one of RF antennae (of the two ones used for plasma production and heating during plasma experiments). The voltage could be positive or negative relative to the grounded vacuum vessel and was varied from one pulse of magnetic field to another. Thus, dependence of phenomena on voltage amplitude was obtained. As was found, the sign and amplitude of voltage play a determining role in behavior of phenomena shown in Figs 48 and 51.

Combining these data and data for other values of voltage, the graphs shown in Figs 51a and 51b are presented.

As seen, there is no simple correlation for appearance of hard X rays and ECE radiation for both stages of magnetic field intensity variation: ramp-up and ramp-down. The ramp-up signals are more resistant to applying voltage than ramp-down signals. This difference can probably be connected with existence of some low density plasma that survives by the time when magnetic field begins to decrease. Also, there is big difference between dependences on voltage of hard X ray and ECE intensities.

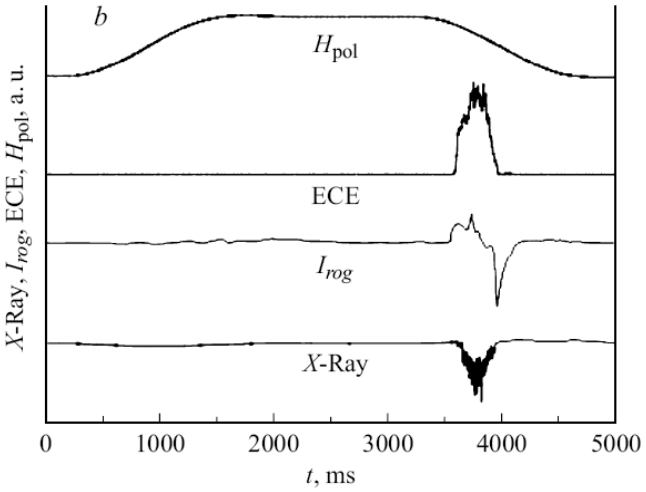

FIG. 49. Similar to Figure 1, with antenna voltage +20 V.

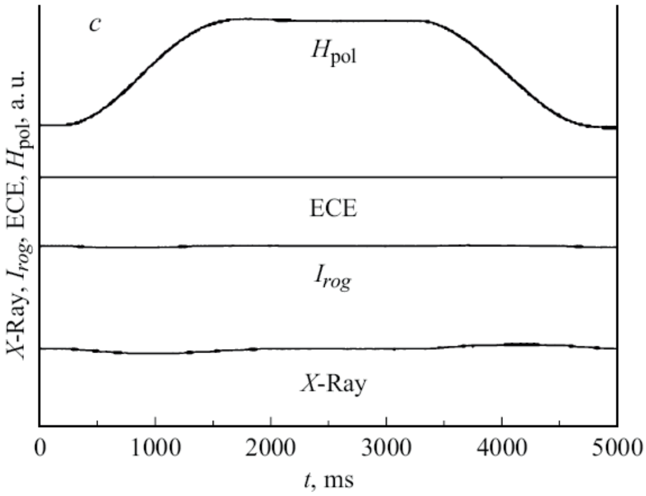

FIG. 50. Similar to Figure 1, with antenna voltage -210 V.

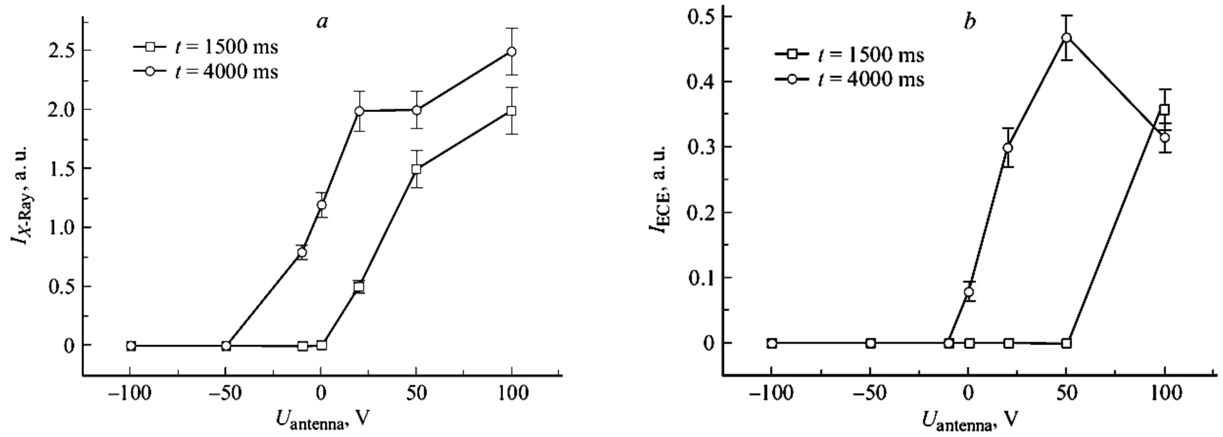

FIG. 51. Intensity of hard X ray emission (a) and radiation at frequency 60 GHz (b) at two stages of magnetic field pulse (rize and decay) depending on sign and amplitude of voltage applied to the antenna.

REFERENCES

[1] DNESTROVSKIJ, YU.N., MELNIKOV, A.V., KRUPNIK, L.I., NEDZELSKIJ, I.S., Development of heavy ion beam probe diagnostics, IEEE Transactions on Plasma Science **22** 4 (1994) 310.

[2] KRUPNIK, L.I., MELNIKOV, A.V., NEDZELSKIJ, I.S., Development of beam probe diagnostics and recent measurements on the tj-i and t-10 tokamaks, Fusion Eng. Des. **34 - 35** (1997) 639.

[3] DESHKO, G.N., ZHEZHERA, A.A., CHMYGA, A.D., KOMAROV, A.S., KOZACHOK, A.S., KRUPNIK, L.I., MELNIKOV, A.V., PERFILOV, S.V., OTTE, M., SHUBERT, M., The heavy ion beam probing development for wega stellarator, Fus. Sci. Technol. **50** (2006) 276.

[4] KRUPNIK, L.I., MEL'NIKOV, A.V., NEDZEL'SKII, I.S., SAMOKHVALOV, N.V., SCHWELBER-GER, J., CONNOR, K.A., Plasma diagnostics using a heavy-ion beam in the u-2m stellarator, Plasma Phys. Rep. **20** (1994) 173.

[5] WAGNER, F., BECKER, G., BEHRINGER, K., CAMPBELL, D., EBERHAGEN, A., ENGELHARDT, W., FUSSMANN, G., GEHRE, O., GERNHARDT, J., GIERKE, G., HAAS, G., HUANG, M.(a), KARGER, F., KEIHACKER, M., KLUBER, O., KORNHERR, K., LACKNER, K., LISITANO, G., LISTER, G.G., MAYER, H.M., MEISEL, D., MULLER, E.R., MURMANN, H., NIEDERMEYER, H., POSCHENRIEDER, W., RAPP, H., RÖHR, H., SCHNEIDER, F., SILLER, G., SPETH, E., STÄBLER, A., STEUER, K.H., VENUS, G., VOLLMER, O., YU, Z., Regime of improved confinement and high beta in neutral-heated divertor discharges of the asdex tokamak, Phys. Rev. Lett. **49** (1982) 1408.

[6] ITOH, K., and ITOH, S., The Role of the Electric Field in Confinement, Plasma Phys. Contr. Fusion **38** (1996) 1.

[7] GROEDNER, R.J., BURRELL, K.H., SERAYDARIAN, R.P., Role of the edge electric field and poloidal rotation in the l-h transition, Phys. Rev. Lett. 64 (1990) 3015.

[8] ASKINAZI, L.G., KORNEV, V.A., LEBEDEV, S.V., TUKACHINSKY, A.S., ZHUBR, N.A., DREVAL, N.B., KRUPNIK, L.I., Heavy ion beam probe development for plasma potential measurements on the tuman-3m tokamak, Rev. Sci. Instrum. **75** (2004) 3517.

[9] MELNIKOV, A.V., HIDALGO, C., ELISEEV, L.G., ASCASIBAR, E., GHMYGA, A.A., DYABILIN, K.S., KRASILNIKOV, I.A., KRUPIN, V.A., KRUPNIK, L.I., KHREBTOV, S.M., KOMAROV, A.D., KOZACHEK, A.S., LOPEX-BRUNA, D., LYSENKO, S.E., MAVRIN, V.A., DE PABLOS. J.L., PASTOR, I., PERFILOV, S. V., PEDROSA, M. A., SHURYGIN, R. V., VERSHKOV, V. A., T-10 team and tj-ii team, plasma potential and turbulence dynamics in toroidal devices (survey of t-10 and tj-ii experiments), Nucl. Fusion **51** (2011) 083043.

[10] MELNIKOV, A.V., VERSHKOV, V.A., GRASHIN, L.G., ELISEEV, L.G., LYSENKO, S.E., MAVRIN, V.A., PERFILOV, S.V., SHELUKHIN, D.A., MAVRIN, V.A., DE PABLOS. J.L., PASTOR, I., PERFILOV, S.V., PEDROSA, M.A., SHURYGIN A.V., KRUPNIK, L.I., KOMAROV, A.D., KOZACHEK, A.S., ZHEZHERA, A.I., Measurements of plasma potential, radial electric field and turbulence rotation velocity in the T-10 tokamak, 37th EPS Conf. on Plasma Physics, Dublin, Ireland, 21-25 June 2010, ECA, 34A Rep. O5.128 http://ocs.ciemat.es/EPS2010PAP/html/

[11] MELNIKOV, A.V., VERSHKOV, V.A., GRASHIN, L.G., ELISEEV, L.G., LYSENKO, S.E., MAVRIN, V.A., MEREZHKIN, V.G., PERFILOV, S.V., SHELUKHIN, D.A., SHURYGIN A.V., KRUPNIK, L.I., KOMAROV, A.D., KOZACHEK, A.S., ZHEZHERA, A.I., Study of plasma potential, its fluctuations and turbulence rotation in the T-10 tokamak, Problems of Atomic Science and Technology, Phys. Plasmas **6** (2010) 40.

[12] SHAFRANOV, V.D., Determination of the parameters $ß_p$ and l_i in tokamaks for arbitrary shape of the plasma pinch, Phys. Plasmas **13** (1971) 757.

[13] ZAKHAROV, L.E., SHAFRANOV, V.D., Equilibrium of the plasma with current in the toroidal systems, Zhurnal Tekhnicheskoj Fiziki **43** (1973) 225 (in Russian).

[14] BRAAMS, B.J., Equilibrium of the plasma column in the tokamaks, Preprint IPP s/r, Garching, (1985).

[15] PASHNEV, V.K., NEMOV, V.V., Use of magnetic diagnostics in stellarators, Nucl. Fusion **33**

3 (1993) 435.

[16] MOROZOV, A.I., SOLOV’YOV, L.S., Geometry of magnetic field, Plasma theory issues, Gosatomizdat publ., Moscow, **2** (1963) 3 (in Russian).

[17] PASHNEV, V.K., Influence of the radial electric field on the structure of plasma current in a toroidal trap, VI Ukrainian Conference and School on Plasma Physics and Controlled Fusion, Alushta, Crimea, Ukraine, 14-20 September 1998.

[18] SHVETS, O.M., DIKIJ, I.A., KALINICHENKO, S.S., LYSOJVAN, A.I., NAZAROV, N.I., RANYUK, T.YU., GREKOV, D.L., STEPANOV, K.N., TOLOK, V.T., Absorption of Alfven waves and plasma production in the omega and uragan-3 toroidal devices, Nucl. Fusion **26** (1986) 23.

[19] MOISEENKO, V.E., BEREZHNYJ, V.L., BONDARENKO, V.N., BURCHENKO, P.YA., CASTEJON, F., CHECHKIN, V.V., CHERNYSHENKO, V.YA., DREVAL, N.B. , GARKUSHA, I.E., GLAZUNOV, G.P., GRIGOR’EVA, L.I., HARTMANN, D., HIDALGO, R., KOCH, R., KONOVALOV. V.G., KOTSUBANOV, V.D., KRAMSKOI, YE.D., KULAGA, A.E., LOZIN, A.V., LYSSOIVAN, A.I., MIRONOV, YU.K., MYSIURA, I.N., PAVLICHRNKO, R.O., PASHNEV, V.K., ROMANOV, V.S., SHAPOVAL, A.N., SKIBENKO, A.I., SLAVNYI, A.S., SOROKOVOY, E.L., STADNIK, YU.S., TARAN, V.S., TERESHIN, V.I., VOITSENYA, V.S., Rf plasma production and heating below ion-cyclotron frequencies in uragan torsatron, Nucl. Fusion **51** (2011).

[20] LOZIN, A.V., MOISEENKO, V.E., GRIGOR’EVA, L.I., KOZULYA, M.M., KRASYUK, A,YU,, KULAGA, A.E., KRAMSKOY, E.D., LYSSOIVAN, A.I., MAZNICHENKO, S.M., MIRONOV, YU.K., PAVLICHENKO, R.O., ZAMANOV, N.V., ROMANOV, V.S., CHENYSHENKO, V.YA., CHECHKIN, V.V., and URAGAN-3M team, Usage of three-halfturn antenna at the uragan-3m device, Problems of Atomic Science and Technology, Phys. Plasmas **1** (2013) 27.

[21] CHECHKIN, V.V., PANKRATOV, I.M., GRIGOR’EVA, L.I., BELETSKII, A.A., KASILOV, A.A., BURCHENKO, P.YA., LOZIN, A.V., TSYBENKO, S.A., SLAVNYJ, A.S., LITVINOV, A.P., KULAGA, A.E., PAVLICHENKO, R.O., ZAMANOV, N.V., MIRONOV, YU.K., ROMANOV, V.S., PASHNEV, V.K., MAZNICHENKO, S.M., VOLKOV, YE.D., Rf discharge dynamic with passing over l- and h- like mode states in the URAGAN-3M torsatron, Problems of Atomic Science and Technology, Phys. Plasmas **6** (2012) 3.

[22] PAVLICHENKO, R.O., KULAGA, A.E., ZAMANOV, N.V., LOZIN, A.V., MIRONOV, YU.K., ROMANOV, V.S., CHECHKIN, V.V., GRIGOR’EVA, L.I., Behaviour of electron cyclotron emission for optically thin plasmas during various Rf plasma production scenarios at Uragan-3M torsatron, Problems of Atomic Science and Technology, Phys. Plasmas **1** (2013) 270.

[23] BESEDIN, N.T., KASILOV, S.V., PANKRATOV, I.M., PYATAK, A.I., STEPANOV, K.N., Numerical simulation of particle and energy transport in uragan-3m torsatron, stellarators and other helical confinement systems, Collection of Papers Presented at the IAEA TCM, Garching, Germany, 10-14 May 1993, Vienna, IAEA (1993) 277.

[24] FUJIWARA, M., KAWAHATA, K., OHYABU, N., KANEKO, O., KOMORI, A., YAMADA, H., ASHIKAWA, N., BAYLOR, L.R., COMBS, S.K., DE VRIES, P., EMOTO, M., EJIRI, A., FISHER, P. W., FUNABA, H., GOTO, M., HARTMANN, D., IDA, K., IDEI, H., IIO, S., IKEDA, K., INAGAKI, S., INOUE, N., ISOBE, M., KADO, S., KHLOPENKOV, K., KOBUCHI, T., KRASILNIKOV, A. V., KUBO, S., KUMAZAWA, R., LEUTERER, F., LIANG, Y., LYON, J.F., MASUZAKI, S., MINAMI,T., MIYAJIMA, J., MORISAKI, T., MORITA, S., MURAKAMI, S., MUTO, S., MUTOH, T., NAGAYAMA, Y., NAKAJIMA, N., NAKAMURA, N., NAKANISHI, H., NARIHARA, K., NISHIMURA, K., NODA, N., NOTAKE, T., OHDACHI, S., OKA, Y., OKAJIMA, S., OKAMOTO, M., OSAKABE, M., OZAKI, T., PAVLICHENKO, R.O., PETERSON, B.J., SAGARA, A., SAITO, K., SAKAKIBARA, S., SAKAMOTO, R., SANUKI, H., SASAO, H., SASAO, M., SATO, K., SATO, M., SEKI, T., SHIMOZUMA, T., SHOJI, M., SUGAMA, H., SUZUKI, H., TAKECHI, M., TAKEIRI, Y., TAMURA, N., TANAKA, K., TOI, K., TOKUZAWA, T., TORII, Y., TSUMORI, K., WATANABE, K. Y., WATANABE, T., WATERI, T., YAMADA, I., YAMAGUCHI, S., YAMAMOTO, S., YOKOYAMA, M., YOSHIDA, N., YOSHIMURA, Y.,

ZHAOL, Y., AKIYAMA, R., HABA, K., IIMA, M., KODAIRA, J., TAKITA, T., TSUZUKI, T., YAMAUCHI, K., YONEZU, H., CHIKARAISHI, H., HAMAGUCHI, S., IMAGAWA, S., INOUE, N., IWAMOTO, A., KITAGAWA, S., KUBOTA, Y., MAEKAWA, R., MITO, T., MURAI, K., NISIMURA, A., TAKAHATA, K., TAMURA, H., YAMADA, S., YANAGI, N., ITOH, K., MATSUOKA, K., OHKUBO, K., OHTAKE, I., SATOH, S., SATOW, T., SUDO, S., TANAHASHI, S., YAMAZAKI, K., HAMADA, Y., MOTOJIMA, O., Overview of lhd experiments, in Fusion Energy 2000, Proc, 18th Fusion Energy Conf., Sorrento, Italy, October 2000, IAEA-CN-77-OV1/4 (2000).

[25] RAPISARDA, D., ZURRO, B., TRIBALDOS, V., BACIERO, A., and the TJ-II team, The role of a fast ion component on the heating of the plasma bulk, Plasma Phys. Control. Fusion **49** (2007) 309.

[26] LYSSOIVAN, A.I., MOISEENKO, V.E., PLYUSNIN, V.V., KASILOV, S.V., BONDARENKO, V.N., CHECHKIN, V.V., FOMIN, I.P., GRIGOR’EVA, L.I., KONOVALOV, V.G., KOVAL’OV, S.V., LITVINOV, A.P., MIRONOV. YU.K., NAZAROV, N.I., PAVLICHENKO O.S., PAVLICHENKO, R.O., SHAPOVAL, A.N., SKIBENKO, A.I., VOLKOV, E.D., A study of three-half-turn and frame antennae for ion cyclotron range of frequency plasma heating in the uragan-3m torsatron, Fus. Eng. Des. **26** (1999) 185.

[27] MIKHAILENKO, V.S. and STEPANOV, K.N., Theory of weak parametric plasma turbulence, Zh. Eksp. Teor. Fiz. **87** (1983) 161 (in Russian).

[28] OLSHANSKY, V.V., TARASOV, M.I., SITNIKOV, D.A., Dynamics of electrostatic fluctuations in the edge plasma in the u-3m torsatron, Plasma Phys. Rep. **36** (2010) 859.

[29] CHECHKIN, V.V., GRIGOR’EVA, L.I., SMIRNOVA, M.S., SOROKOVOJ, E.L., VOLKOV, E.D., RUDAKOV, V.A., RUBTSOV, K.S., NAZAROV, N.I., LOZIN, A.V., TSYBENKO, S.A., Plasma flow asymmetries in the natural helical divertor of an l=3 torsatron and their relation to particle losses, Nucl. Fusion, **42** (2002) 192.

[30] GODYAK, V.A., KUZOVNIKOV, A.A., O ventil’nykh svojstvakh rf razryadov, Fizika Plazmy **1** (1975) 496 (in Russian).

[31] CARTER, M.D., LYSSOIVAN, A.I., MOISEENKO, V.E., NAZAROV, N.I., SHVETS, O.M., and STEPANOV, K.N., Plasma production using radiofrequency fields near or below the ion cyclotron range of frequencies, Nucl. Fusion **30** (1990) 723.

[32] GODYAK, V.A., IVANOV, A.N., KUZOVNIKOV, A.A., changes in the variable potential of the Langmuir probe to the effect of alternating voltage, Zh. Tekh. Fiz. **37** 6 (1967) 1063 (in Russian).

[33] MAAβBERG, H., BURHENN, R., GASPARINO, U., KUHNER, G., RINGLER, H. and DYABILIN, K.S., Experimental and neoclassical electron heat transport in the LMPF regime for the stellarators w-7a, l-2, w-7as, Plasma Phys. Control. Fusion **35** (1993) B319.

DESIGN, DEVELOPMENT AND APPLICATION OF HIGH TEMPERATURE SUPERCONDUCTORS IN FUSION DEVICES

M. GRYAZNEVICH

* Tokamak Energy LTD, Culham Science Centre, Abingdon, OX13 3DB UK

Abstract

Design, development and application of High Temperature Superconductors in Fusion Devices have been carried out on GOLEM, ST25 and ST25-HTS tokamaks. HTS magnet for high-field (3–5T) ST60 tokamak is being designed.

1. INTRODUCTION

Our investigations on the design, development and application of High Temperature Superconductors (HTS) in Fusion Devices are provided in the framework of the current Co-ordinated Research Project (CRP) of the International Atomic Energy Agency (IAEA) “Utilization of the Network of Small Magnetic Confinement Fusion Devices for Mainstream Fusion Research” during the fulfilment of the 4-year activity.

Tokamak Energy Ltd aims to accelerate the development of fusion energy by working with compact, high performance spherical tokamaks. The company’s strategy is to work close to the mainstream of tokamak fusion where a huge base of knowledge and expertise has been built up over many years, and to focus on spherical tokamaks and high temperature superconducting magnets (HTS). Spherical tokamaks can achieve high beta (ratio of plasma pressure to magnetic pressure) and are inherently compact. For the tokamak magnets, Tokamak Energy uses second generation YBCO high temperature superconductors manufactured as tapes. These YBCO tapes have a remarkable ability to carry exceptionally high current density in a strong magnetic field and can operate efficiently at 20–30K rather than 4K or lower for conventional low temperature superconductors.

So far Tokamak Energy has built two small tokamaks with 25cm major radius, one with conventional copper magnets, the other with high temperature superconducting magnets (ST25 HTS). The ST25 HTS has sustained plasma for 29 hours with excellent stability of the magnets. The next device, presently being constructed at Tokamak Energy’s engineering facility, is the ST40, a spherical tokamak with a field of up to 3T, plasma current up to 2MA and the major radius of 40–60 cm. The ST40 will demonstrate exceptional high field operation for a compact device and will achieve plasma temperatures of 8–10 keV by the end of 2017.

Tokamak Energy has a policy of open publication for most of its work, although in some cases the company files patent applications, particularly on HTS magnet technology, prior to publication. 16 papers have been published in refereed journals in the last 5 years. Results have been presented at all major Fusion Conferences and Meetings. One Ph.D. has been completed and we have 2 Ph.D. students at present.

To provide training and education activities to members of the network, tokamak ST25 is fully equipped for remote operations for research, educational and training purposes.

2. DESIGN, DEVELOPMENT AND APPLICATION OF HIGH TEMPERATURE SUPERCONDUCTORS IN FUSION DEVICES

2.1. First tests of PF HTS coils on GOLEM tokamak, CTU, Prague, Czech Republic and on ST25, Tokamak Energy Ltd, Culham, UK.

The main objective of our research is to develop new technology for tokamak magnets utilizing the flexibility of a small tokamak to be a test bed for the development of HTS magnets. As the price of HTS is still high, application of it in a small device will require moderate funds due to compact assembly and relatively low required fields. Due to easier access, the cryostat design can be simplified for initial tests and non-expensive liquid nitrogen or moderate amount of liquid He can be used for cooling. Typically flexible experimental schedule may allow easy access for modifications and tests. Collaboration with other CRP members is possible and proved to be efficient.

Joint development of HTS magnets for tokamaks in collaboration with Oxford Instruments UK, GOLEM and IPP Prague resulted in:

- Development of new concept of advanced magnets in fusion devices, based on High Temperature Superconductors. Design of tokamaks with HTS magnets;
- Studies of properties of HTS: critical current dependence on magnetic field, temperature, stresses, irradiation properties etc;
- Preliminary design of cryostat, feeds and power supplies for initial tests in collaboration with Oxford Instruments (UK), Forma Machinery (Latvian Republic) and IPP Prague.
- Operations of HTS PF coils on ST25 tokamak have been performed after successful tests of HTS PF coils on GOLEM tokamak. First tests of HTS coils on Golem tokamak in collaboration with CCFE (UK), Oxford Instruments (UK), the Czech Technical University in Prague and IPP Prague Figure 1, left. Fist tests on industrial-made HTS coils on ST25, Culham, UK; Figure 1, right.
- Design, manufacture and tests of different types of cryostats for HTS magnets, Figure 2.

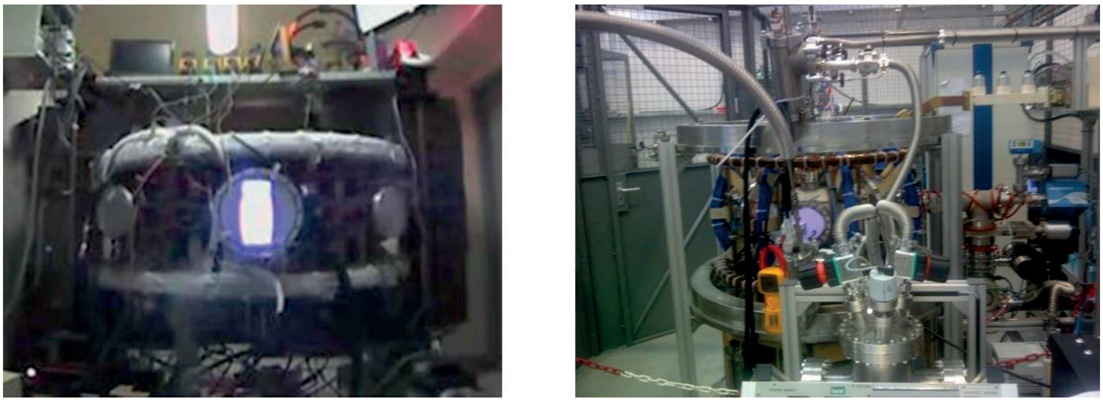

FIG. 1. First application of HTS in tokamak magnets: GOLEM August 2011, left; ST25 2.5 sec plasma discharge, 4 October 2013, right. Reproduced from Ref. [1] with permission.

Extended tests of HTS coils installed on tokamak Golem have been carried out. Tests of advanced cryostats and different feeds designs have been performed and optimised cryostats, Figure 2, and current leads, Figure 3, have been installed on Golem in collaboration with CTU and OI. Studies of quench characteristics of HTS magnets in a tokamak environment have been performed and analysis of HTS tape damaged during a controlled quench “up-to-destruction” has been done. The cause of the damage has identified to be due to delamination of the tape at non-sufficient cooling and hot-spot formation (Figure 4).

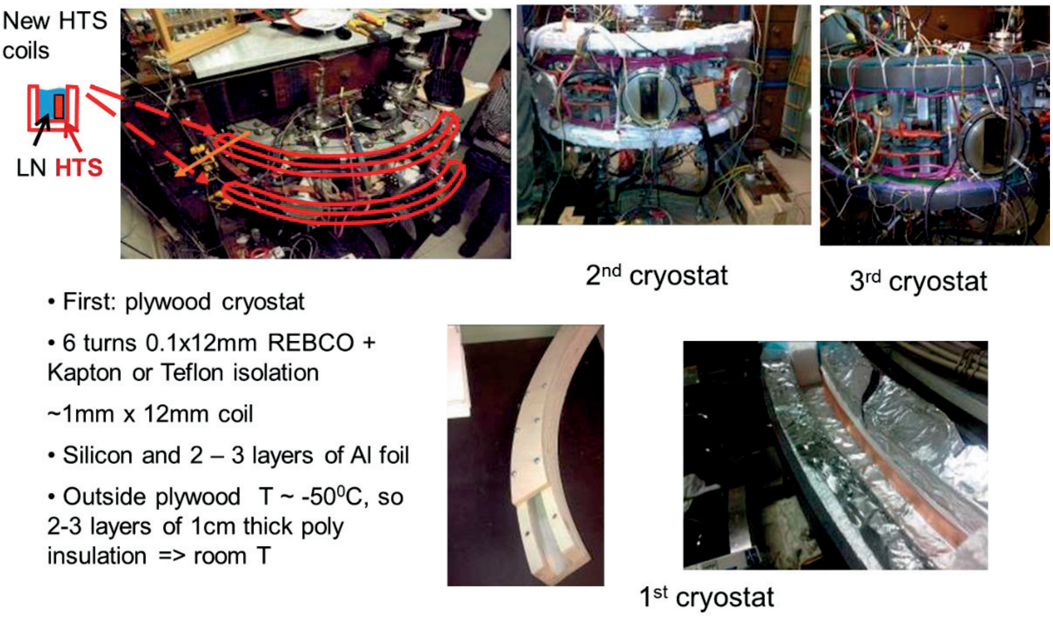

- First: plywood cryostat
- 6 turns 0.1x12mm REBCO + Kapton or Teflon isolation

~1mm x 12mm coil

- Silicon and 2 – 3 layers of Al foil
- Outside plywood T ~ -50⁰C, so 2-3 layers of 1cm thick poly insulation => room T

FIG. 2. Tests of different types of cryostats on GOLEM.

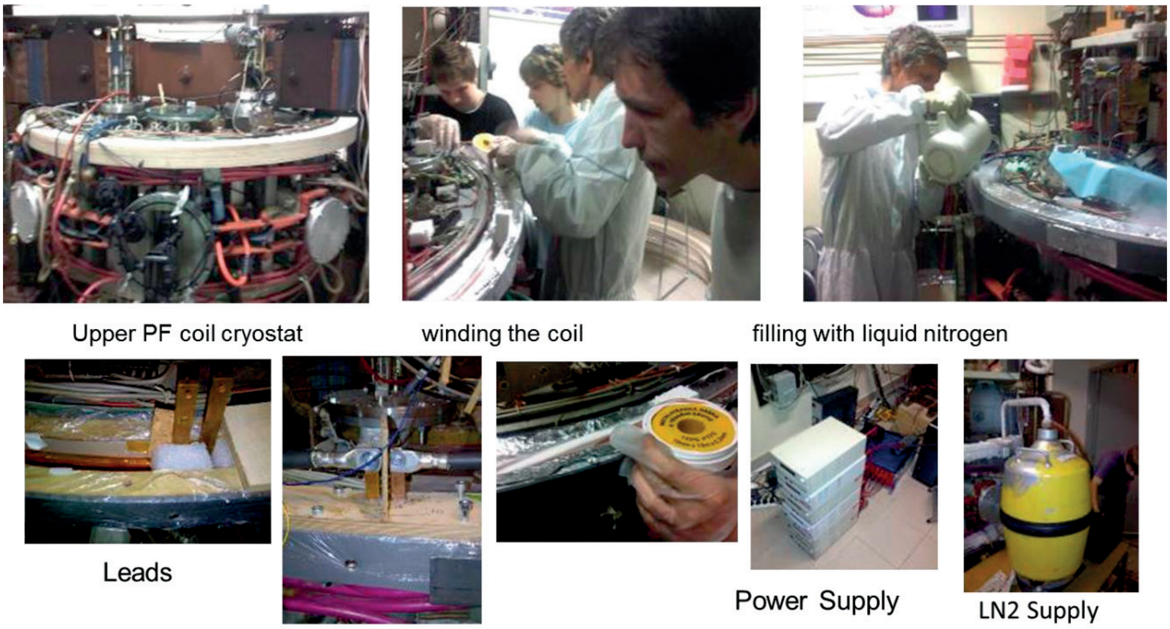

FIG. 3. Tests of different types of cryostats and current leads on GOLEM.

Comparative analysis of different HTS tapes has been done and parameters on SuperPower and Fujikura tapes have been compared. Currently both tapes are used for irradiation studies at two nuclear reactors.

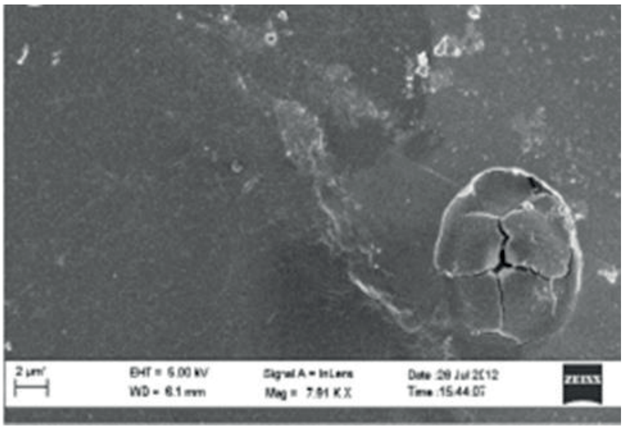

FIG. 4. SEM image of the hot spot in the YBCO tape used in PF coils of GOLEM.

2.2. First full-HTS tokamak, ST25-HTS.

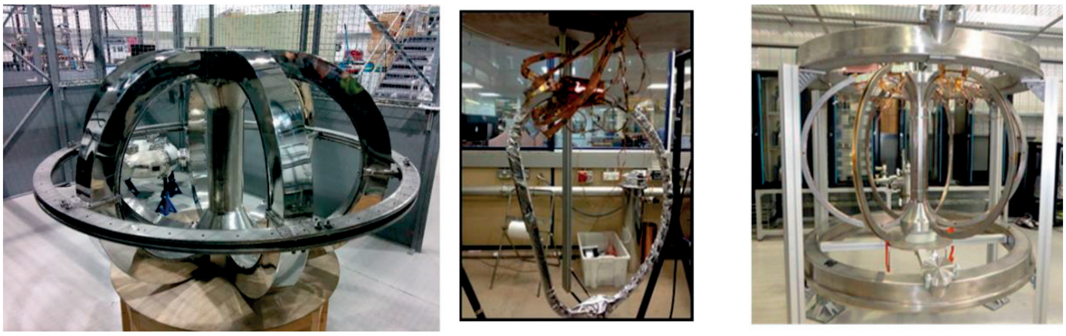

FIG. 5. From left to right: TF cryostat made by MetalCraft UK; Winding of TF coils completed by Oxford Instruments, UK; HTS magnets: assembly, Tokamak Energy Ltd, UK.

FIG. 6. ST25(HTS): world's first all-HTS tokamak.

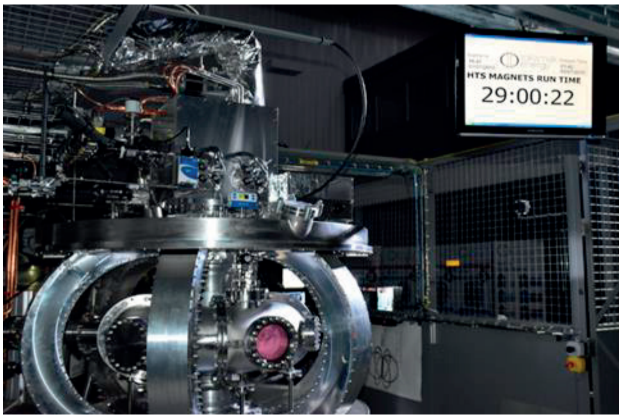

FIG. 7. ST25(HTS): world's longest discharge in a tokamak.

The first full-HTS tokamak has been constructed jointly by TE Ltd and OI UK in 2014, Figs. 5 and 6.

- Built in collaboration with Oxford Instruments UK, using SuperPower HTS 12mm YBCO tape.
- First cool-down in July 2014.
- First plasma (RF driven) 29 July 2014. Demonstrated 24 hour operation on 30th October 2014 and >29 h in July 2015, Figure 7.
- Coil temperature: 8–30K. Current in the HTS tape 100–400A.
- Multiple diagnostics to determine HTS behavior quench detection and control.
- Present status: the 6-limb TF magnet is being converted to cryo-free operation using Sumitomo cold head. Now under upgrade to increase toroidal field (designed to operate up to 1T).

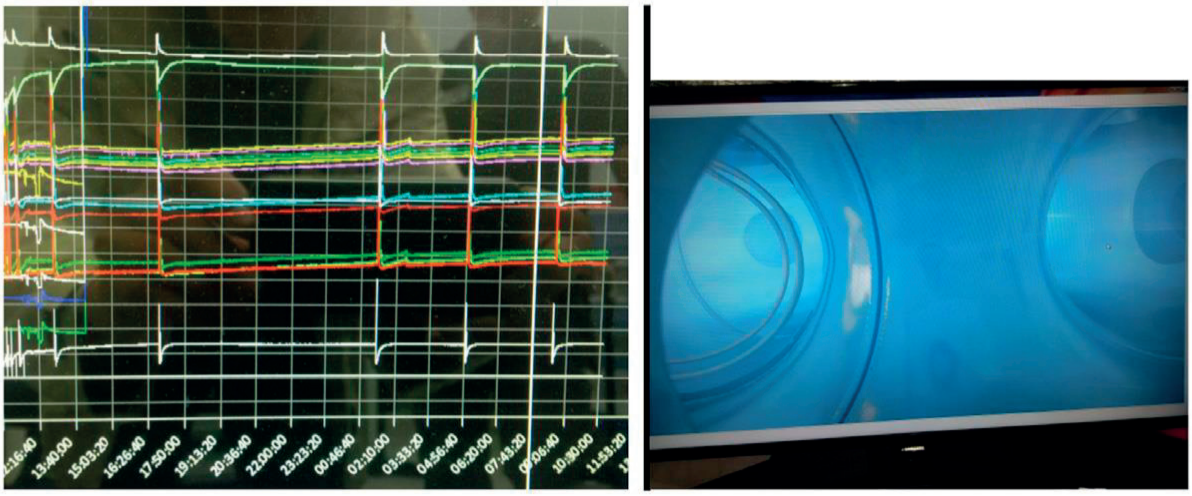

FIG. 8. Left: typical waveforms from continues plasma discharge in HTS tokamak. Top two: reflected and injected RF power (<1kW in this case), next—temperatures in different HTS TF coils. Axis X—in hours, beginning of the discharge at ~11:30 am. Right: typical discharge with RF antenna seen at the left. Reproduced from Ref. [1] with permission.

Within the CRP programme, experiments have been performed on two small tokamaks, ST25 and HTS-ST tokamak, Figs 1 (right) and 6. Both devices have a circular plasma crosssection, R/a =0.25/0.12 cm, I_p up to 10 kA, TF=0.1–0.3 T in ST25, Figure 1, right, and 0.1–1 T in fully-HTS tokamak ST-HTS, Figure 6. These tokamaks use various RF power sources (EBW, ICRH) to provide fully non-inductive current derive. Experience gained from operation of the ST25 and the first fully-HTS tokamak ST-HTS contribute to the design of the next step tokamaks (i.e. DEMO) magnets and also are providing physics results on the EBW current drive in long pulses or CW as they are equipped with different RF launch geometries (steerable low- and the unique up to date high-field launch of RF power from two 2.45 GHz, 3 kW magnetrons). RF-driven plasma with pulse duration of 25 s is routinely available on the ST25 tokamak, with Cu TF magnets powered by the Maxwell supercapacitors power supplies. The full-HTS tokamak HTS-ST has already performed 29 h operations (Figs 7 and 8). Several spikes in the waveforms in Figure 8 correspond to temporary loss of the RF coupling to the plasma, and can be avoided. Video of the discharge can be found at www.tokamakenergy.co.uk. Results of these studies have been presented at SOFT 2014, FEC 2012 and 2014 and other meetings. Paper "Contribution to Fusion Research from IAEA Coordinated Research Projects and Joint Experiments" has been published in 2015 in Nuclear Fusion. Paper "Progress in application of High Temperature Superconductor in Tokamak Magnets" has been published in Fusion Energy and Design 2013.

2.3. Future development of HTS magnets for tokamaks.

Comparative experiments on small tokamaks using HTS magnets have been performed on ST25, HTS-ST and GOLEM tokamaks. These studies provided background for the future development of HTS magnets for tokamaks.

In the HTS development area several studies have been performed and on-going:

- Feasibility studies and chooses of suitable HTS conductor. Comparative analysis of different HTS tapes.
- Extended tests of HTS coils on tokamak Golem.
- Studies of quench characteristics of HTS magnets in a tokamak environment on tokamak GOLEM.
- Preliminary tests of advanced cryostats and feeds designs.
- Detailed studies of HTS properties relevant to applications in Fusion devices.
- Design studies of the next step high field HTS tokamak ST60. Conceptual design studies of the HTS magnets for the ST Pilot Plant Prototype tokamak ST140.
- Publication and presentation of results of advanced feasibility studies and detailed tests at International Conferences.

GOLEM and ST25-HTS magnets were wound with a non-cabled tape, but:

- No extra protective copper connected in parallel, so vulnerable to localised quench damage.
- During first operations on ST25 (HTS), current in the toroidal magnet was limited to 100 s of amps, so the design resulted in lots of turns, high inductance and voltage limits run down time, makes it vulnerable to localised quench damage.

So, for the next designs it was found to be necessary to connect numerous tapes and copper in parallel to form a high-current cable.

At present, HTS Magnet Development for next step tokamaks is being carried out in the following areas of research:

- Demonstration of reproducible low resistance joints (<10 nanoOhm) - enables use of short lengths of tape which are much cheaper to manufacture;
- Demonstration of technology to support “laying up of tape”– enables major reduction in quantity, and hence cost, of HTS tape;
- Validation of quench protection/survival – a good solution to the problem of quench (sudden loss of superconductivity) will enable a smaller device size;
- Progress towards demountable joints including demonstration of a basic demountable joint – demountable joints will allow us to replace the central column and hence allow reduced neutron shielding leading to a smaller device size;
- Robust concept for minimal centre column – leading to reduced device size.

For the HTS application in a Fusion Power Plant it is important to develop a strategy to remove the neutron and resistive produced heat from the HTS magnet. The heat is dominated by neutrons. So, there are significant impacts on the design of future STs with HTS magnets:

- selection of coolant and pressure
- provision of cooling channels (bulk and heat exchange, mechanical)
- efficiency of the cryo-plant (recycled power) is essential for the economic operations of an ST Power Plant.

The radiation degradation is not an issue for the ST60, and fairly unimportant for ST140 Pilot Plant. In a commercial reactor, degradation of HTS performance with time is an issue. Degradation of insulation can also be limiting factor, however, performance of artificially pinned HTS in neutron flux is still unknown and the theory predict significant advantages.

Many of these areas will require future collaboration. Areas of possible collaboration include:

- Specification and negotiation with suppliers
- Creative applied physics/engineering
- Experiment design
- Mechanical engineering/FEA
- Low noise electronics (analogue?)
- Power electronics/electrical engineering
- Digital electronics
- AC loss modelling
- Thermal modelling
- Irradiation tests
- Shielding calculations
- Quench detection, protection and management.

The block diagram of the TE Ltd research programme for the design of the HTS magnets for the high-field ST60 device is presented in Figure 9.

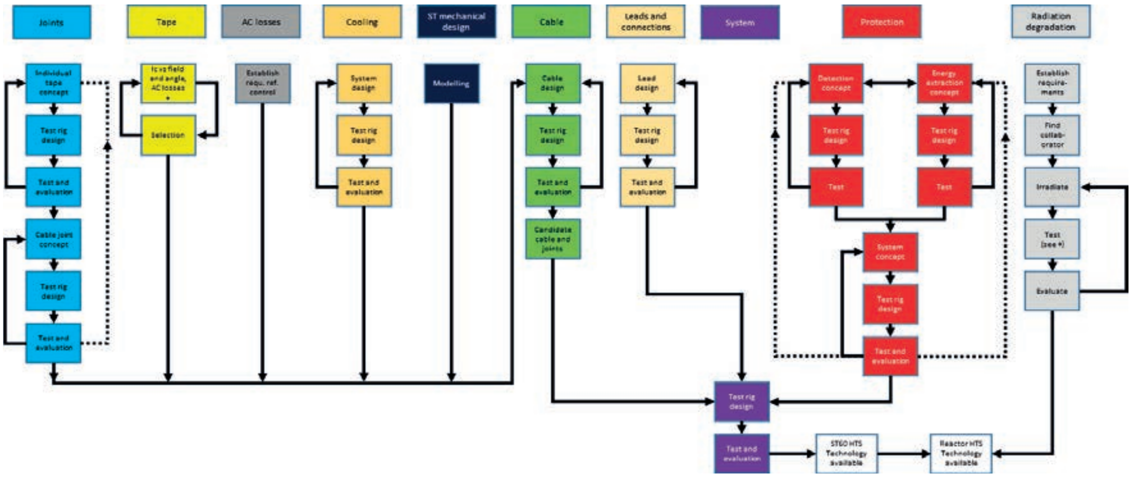

FIG. 9. Block diagram of the TE Ltd research programme for the design of the HTS magnets for the high-field ST60 device.

ACKNOWLEDGEMENT

This research has been supported by the IAEA CRP "Utilization of the Network of Small Magnetic Confinement Fusion Devices for Mainstream Fusion Research", No. F1.30.14.

REFERENCES

[1] GRYAZNEVICH, M., VAN OOST, G., STÖCKEL, J., KAMENDJE, R., KUTEEV, B.N., MELNIKOV, A., POPOV, T., SVOBODA, V. and the IAEA CRP teams, Contribution to fusion research from iaea coordinated research projects and joint experiments, Nucl. Fusion **55** (2015).

[2] GRYAZNEVICH, M., SVOBODA, V., STOCKEL, J., SYKES, A., TODD, T.T., KINGHAM, D., MELHEM, Z., BALL, S., CHAPPELL, S., DURAN, I., KOVARIK, K., MARKOVIC, T., ONDREJ, G., LILLEY, M.K., DE GROUCHY, P. and KIM, H-T, First results from tests of high temperature superconductor magnets on tokamak, Proceedings of the 24th IAEA Conference on Fusion Energy 2012, San Diego, October 8 – 13 2012, (IAEA, 2013) FTP/P7-26.

[3] GRYAZNEVICH, M., SVOBODA, V., STOCKEL, J., SYKES, A., SYKES, N., KINGHAM, D., HAMMOND, G., APTE, P., TODD, T.N., BALL, S., CHAPPELL, S., MELHEM, Z., ĎURAN, I., KOVARIK, K., GROVER, O., MARKOVIC, T., ODSTRCIL, M., ODSTRCIL, T., SINDLERY, A., VONDRASEK, G., KOCMAN, J., LILLEY, M.K., DE GROUCHY, P., KIM, H.T, Progress in application of high temperature superconductor in tokamak magnets, Proc. of 27th Symposium on Fusion Technology September 24 – 28 2012, Liege, Belgium P2.81 http://www.soft2012.eu/papers-and-contributions.

[4] BROMOVÁ, E., ĎURAN, I., EL-AHMAR, S., GROVER, O., GRYAZNEVICH, M., JANKOWSKI, J., KOCMAN, J., KOVAŘÍK, K., MARKOVIČ, T., ODSTRČIL, M., ODSTRČIL, T., OSZWALDOWSKI, M., PLUHAŘ, O., STÖCKEL, J., SVOBODA, V., ŠINDLERY, A., VONDRÁŠEK, G., ŽÁRA, J., Recent results from the Golem tokamak. "Indeed, you can teach an old dog some new tricks". Proc. 39th EPS Conference & 16th Int. Congress on Plasma Physics, Stockholm, 2 – 6 July 2012, Europhysics Conferences Abstracts, **36** F (2012) P2.059

[5] GRYAZNEVICH, M., SVOBODA, V., STOCKEL, J., SYKES, A., KINGHAM, D., TODD, T.N., MELHEM, Z., BALL, S., CHAPPELL, S., ĎURAN, I., KOVARIK, K., GROVER, O., MARKOVIC, T., ODSTRCIL, M., ODSTRCIL, T., SINDLERY, A., VONDRASEK, G., KOCMAN, J., First results from tests of high temperature superconductor magnets on tokamak. Proc. 39th EPS Conference & 16th Int. Congress on Plasma Physics, Stockholm, 2 – 6 July 2012, Europhysics Conferences Abstracts, Vol. **36** F (2012) P2.052.

LIST OF CRP PARTICIPANTS

AHMAD Zahoor	Pakistan Atomic Energy Commission (PAEC) **Pakistan**
CHAPPELL Steve	Oxford Instruments plc **United Kingdom**
FERNANDEZ Horacio	Instituto Superior Técnico (IST) **Portugal**
GAO Zhe	Tsinghua University **China**
GRYAZNEVICH Mikhail	Tokamak Solutions UK Ltd **United Kingdom**
HIROSE Akira	University of Saskatchewan **Canada**
KHORSHID Pejman	Islamic Azad University **Iran - Islamic Republic of**
MELNIKOV Alexander	National Research Center Kurchatov Institute **Russian Federation**
POPOV Tsviatko	Faculty of Physics **Bulgaria**
RIBEIRO Celso	Instituto Tecnológico de Costa Rica **Costa Rica**
SHAPOVALOV Gennadiy	Republican State Enterprise National Nuclear Center of the Republic of Kazakhstan (RSE NNC RK) **Kazakhstan**
STOCKEL Jan	Academy of Sciences of the Czech Republic (ASCR) **Czech Republic**
SVOBODA Vojtech	Faculty of Nuclear Science and Physical Engineering (FNSPE) **Czech Republic**
VAN OOST Guido	Ghent University **Belgium**
VOROBYEV Gennady	St. Petersburg State University (SPbSU) **Russian Federation**
VOYTSENYA Volodymyr	National Science Center "Kharkov Institute of Physics and Technology" (NSC KIPT) **Ukraine**

RESEARCH COORDINATION MEETINGS OF THE CRP

- 19 – 22 December 2011, IAEA, Vienna, Austria.
- 19 – 22 March 2013, IAEA, Vienna, Austria.
- 23 – 26 Febrary 2016, IAEA, Vienna, Austria.

ORDERING LOCALLY

In the following countries, IAEA priced publications may be purchased from the sources listed below or from major local booksellers.

Orders for unpriced publications should be made directly to the IAEA. The contact details are given at the end of this list.

BELGIUM

Jean de Lannoy
Avenue du Roi 202, 1190 Brussels, BELGIUM
Telephone: +32 2 5384 308 • Fax: +32 2 5380 841
Email: jean.de.lannoy@euronet.be • Web site: http://www.jean-de-lannoy.be

CANADA

Renouf Publishing Co. Ltd.
22-1010 Polytek Street, Ottawa, ON K1J 9J1, CANADA
Telephone: +1 613 745 2665 • Fax: +1 643 745 7660
Email: order@renoufbooks.com • Web site: http://www.renoufbooks.com

Bernan Associates
4501 Forbes Blvd., Suite 200, Lanham, MD 20706-4391, USA
Telephone: +1 800 865 3457 • Fax: +1 800 865 3450
Email: orders@bernan.com • Web site: http://www.bernan.com

CZECH REPUBLIC

Suweco CZ, s.r.o.
SESTUPNÁ 153/11, 162 00 Prague 6, CZECH REPUBLIC
Telephone: +420 242 459 205 • Fax: +420 284 821 646
Email: nakup@suweco.cz • Web site: http://www.suweco.cz

FRANCE

Form-Edit
5 rue Janssen, PO Box 25, 75921 Paris CEDEX, FRANCE
Telephone: +33 1 42 01 49 49 • Fax: +33 1 42 01 90 90
Email: fabien.boucard@formedit.fr • Web site: http://www.formedit.fr

Lavoisier SAS
14 rue de Provigny, 94236 Cachan CEDEX, FRANCE
Telephone: +33 1 47 40 67 00 • Fax: +33 1 47 40 67 02
Email: livres@lavoisier.fr • Web site: http://www.lavoisier.fr

L'Appel du livre
99 rue de Charonne, 75011 Paris, FRANCE
Telephone: +33 1 43 07 43 43 • Fax: +33 1 43 07 50 80
Email: livres@appeldulivre.fr • Web site: http://www.appeldulivre.fr

GERMANY

Goethe Buchhandlung Teubig GmbH
Schweitzer Fachinformationen
Willstätterstrasse 15, 40549 Düsseldorf, GERMANY
Telephone: +49 (0) 211 49 874 015 • Fax: +49 (0) 211 49 874 28
Email: kundenbetreuung.goethe@schweitzer-online.de • Web site: http://www.goethebuch.de

HUNGARY

Librotrade Ltd., Book Import
Pesti ut 237. 1173 Budapest, HUNGARY
Telephone: +36 1 254-0-269 • Fax: +36 1 254-0-274
Email: books@librotrade.hu • Web site: http://www.librotrade.hu

INDIA

Allied Publishers
1st Floor, Dubash House, 15, J.N. Heredi Marg, Ballard Estate, Mumbai 400001, INDIA
Telephone: +91 22 4212 6930/31/69 • Fax: +91 22 2261 7928
Email: alliedpl@vsnl.com • Web site: http://www.alliedpublishers.com

Bookwell
3/79 Nirankari, Delhi 110009, INDIA
Telephone: +91 11 2760 1283/4536
Email: bkwell@nde.vsnl.net.in • Web site: http://www.bookwellindia.com

ITALY
Libreria Scientifica "AEIOU"
Via Vincenzo Maria Coronelli 6, 20146 Milan, ITALY
Telephone: +39 02 48 95 45 52 • Fax: +39 02 48 95 45 48
Email: info@libreriaaeiou.eu • Web site: http://www.libreriaaeiou.eu

JAPAN
Maruzen-Yushodo Co., Ltd.
10-10, Yotsuyasakamachi, Shinjuku-ku, Tokyo 160-0002, JAPAN
Telephone: +81 3 4335 9312 • Fax: +81 3 4335 9364
Email: bookimport@maruzen.co.jp • Web site: http://maruzen.co.jp

RUSSIAN FEDERATION
Scientific and Engineering Centre for Nuclear and Radiation Safety
107140, Moscow, Malaya Krasnoselskaya st. 2/8, bld. 5, RUSSIAN FEDERATION
Telephone: +7 499 264 00 03 • Fax: +7 499 264 28 59
Email: secnrs@secnrs.ru • Web site: http://www.secnrs.ru

UNITED STATES OF AMERICA
Bernan Associates
4501 Forbes Blvd., Suite 200, Lanham, MD 20706-4391, USA
Telephone: +1 800 865 3457 • Fax: +1 800 865 3450
Email: orders@bernan.com • Web site: http://www.bernan.com

Renouf Publishing Co. Ltd.
812 Proctor Avenue, Ogdensburg, NY 13669-2205, USA
Telephone: +1 888 551 7470 • Fax: +1 888 551 7471
Email: orders@renoufbooks.com • Web site: http://www.renoufbooks.com

Orders for both priced and unpriced publications may be addressed directly to:

IAEA Publishing Section, Marketing and Sales Unit
International Atomic Energy Agency
Vienna International Centre, PO Box 100, 1400 Vienna, Austria
Telephone: +43 1 2600 22529 or 22530 • Fax: +43 1 2600 29302
Email: sales.publications@iaea.org • Web site: http://www.iaea.org/books

International Atomic Energy Agency
Vienna
ISBN 978–92–0– 110416-8
ISSN 1011–4289